

PhD thesis

# Organic Coupling Reactions by Heterogeneous Photocatalysis

Prepared by: Qingning Yang

**Department of Chemical Engineering** 

**University College London, UK** 

**Supervisor: Prof. Junwang Tang** 

25/Sep/2023

# **Declaration**

I, Qingning Yang, confirm that the work presented in this thesis is my own. Where informatin has
been derived from other sources, I confirm that this has been indicated in the thesis.
Signature
Date

## I. Acknowledgements

Firstly, I would like to express sincere gratitude to my supervisor Prof. Junwang Tang for providing continuous guidance and support to my research. I am also very grateful to my subsidiary supervisor Dr Ryan Wang for letting me use instruments and equipment in his lab.

A huge mention must go to all members of the Solar Energy and Advanced Materials research group at UCL, Dr Jijia Xie, Dr You Wang, Dr Qiushi Ruan, Dr Chaoran Jiang, Dr Chi Ching Lau, Dr Tina Miao, Dr Madasamy Thangamuthu, Dr Christopher Windle, Dr Jiefang Sun, Dr Jianfeng Ye, Dr Mustafa Bayazit, Dr Hui Wang, Dr Xiyi Li, Lungiao Xiong, Chao Wang, Youxun Xu, Enqi Chen, Zhe Yuan for their supports both technical and personal.

I would also like to thank other researchers at UCL, Dr Lu Chen, Jingyi Wang, Dr Xiaoyu Han (the DFT calculation in Chapter 5 is credited to Dr Xiaoyu Han), Dr Yang Lan, Xuze Guan, Dr Han Wu, Dr Xueming Xia, Dr Abil E Aliev, Martyn Towner and Martin Vickers, who always offered scientific discussions and helped me address issues related to characterisations and equipment.

Finally, I am deeply indebted to my parents in China for their financial support and unconditional love.

#### II. Abstract

Carbon—carbon (C—C) bond formation is one of the most important research areas in modern organic synthesis. Different cross—coupling reactions, e.g. Suzuki Miyaura coupling (SMC) reaction, Sonogashira reaction, Heck reaction and Stille reaction, have been intensively studied and recognised as the very useful processes for constructing C—C bonds. In conventional methods, transition metal catalysts are often used to promote these coupling reactions, and in order to achieve the redox process and overcome the energy barrier, high temperature is always required. Recent research trend has moved to develop a green, sustainable and efficient process for C—C coupling reactions. Photocatalytic technology has been considered as an emerging technique for organic synthesis because the light energy can trigger the electron transfer process, hence carrying out the C—C coupling reaction at ambient temperature with potential high efficiency.

In this thesis, three coupling reactions have been investigated, including pinacol coupling reaction, homo-coupling of benzyl chloride and Suzuki-Miyaura cross-coupling reaction. I first reported pinacol coupling of benzaldehyde, which has been successfully carried out with a 96% selectivity. When adjusting experimental conditions, such as pH, light source, and selection of a catalyst, benzaldehyde can be transformed into benzaldehyde dimethyl acetal or benzyl alcohol with 92% and 85% selectivity, respectively. The reaction mechanism was then studied using isotopic labelling and it reveals the difference between the tuning selectivity of hydrogenation and pinacol coupling in the presence/absence of titanium dioxide (P25).

I then investigated bibenzyl synthesis using copper-loaded zinc oxide (ZnO) via a homo-coupling route. Here, copper (Cu) exhibits the best performance to promote the coupling of aromatic halides over other transition metals, and Cu-modified ZnO shows a remarkable 92% selectivity compared to a previous report (57% using Cu/TiO<sub>2</sub>). The low-cost photocatalyst has great stability that there

is no obvious decay after 9 runs. It also shows that selective coupling of a series of benzyl chloride derivatives can be achieved using this Cu/ZnO catalyst, demonstrating the heterogeneous photocatalytic C–C coupling as an attractive process for applications. The high selectivity is attributed to the enhanced adsorption of reactants, stabilisation of intermediates (benzyl radicals) for the selective coupling by the Cu loading and the moderate oxidation ability of the ZnO support, besides the promoted charge separation and transfer by Cu species.

Finally, Suzuki-Miyaura coupling of aryl bromides was investigated using low concentration palladium (Pd) supported catalyst. Covalent triazine framework-1 (CTF-1) was chosen as the photocatalyst, and a second co-catalyst, copper, was introduced. The concentration of the bimetallic Pd Cu nanoparticles (NPs) was then optimised separately. Compared to the monometallic sample Pd<sub>0.2</sub>/CTF-1, a 16-fold increase in yield was observed over Pd<sub>0.2</sub>Cu<sub>1</sub>/CTF-1, and this activity is comparable against 1.5% Pd loading, providing a new strategy to achieve Suzuki-Miyaura coupling with less cost photocatalyst. The high performance is attributed to the synergistic between PdO and CuOx. Palladium functions as a reduction site to activate the carbon-bromine (C-Br) bonds, while copper species accelerate the oxidative half-reaction during the photocatalytic process and further improve the charge separation and transfer in the system.

#### III. Impact statement

The formation of carbon-carbon bonds is crucial in organic chemistry as it allows the creation of larger and more complex molecules, which are the basis for the synthesis of many important compounds, such as pharmaceuticals and natural products. Traditional methods for C-C bond formation often require harsh reaction conditions, toxic reagents, and generate significant amounts of waste, which poses a significant challenge to environmental sustainability. Therefore, the development of alternative, greener methods for C-C bond formation, such as heterogeneous photocatalysis, has attracted considerable attention in recent years. Though the development of heterogeneous photocatalytic C-C coupling has shown great promise as an environmentally friendly and sustainable approach for a variety of coupling reactions, current limitations include its inability to apply to complex reactions (e.g. carbon-chlorine bond cleavage), the use of expensive components in photocatalysts (e.g. palladium, platinum and gold), and the difficulty in understanding the reaction mechanism (reaction intermediates and photo charge dynamics). These challenges hinder the practical application of this technology in organic synthesis, emphasizing the need for further research to address these issues and unlock the full potential of heterogeneous photocatalytic carbon-carbon coupling.

In my project, the main strategy is developing robust and low-cost photocatalytic systems to efficiently drive various C–C coupling reactions and then study the mechanism behind the photocatalytic process. Copper was found to be an excellent co-catalyst that can break carbon-chlorine (C–Cl) bond on benzyl chlorides for its homo-coupling and reduce palladium usage in Suzuki-Miyaura coupling of aryl bromides. My finds also proposed that the selectivity in these coupling reactions depends on not only the co-catalyst but also the selection of semiconductors. For example, copper-decorated titanium dioxide (TiO<sub>2</sub>) and ZnO samples can break C–Cl bond

on benzyl chlorides. However, the moderate oxidation ability of ZnO can lead to an ideal yield of bibenzyl product (92%), which is the first example of heterogeneous photocatalytic bibenzyl synthesis from benzyl chlorides. This offers an insight that in order to achieve high selectivity and yield of coupling products, both sides of photoredox cycles need to be carefully designed. Moreover, instead of using Pd and gold (Au) bimetallic co-catalyst, copper can replace gold and dramatically improve the activity of SMC of aryl bromides. With in-situ X-ray photoelectron spectroscopy (XPS), in-situ electron paramagnetic resonance (EPR), density functional theory (DFT) calculation and Mulliken population analysis, the charge dynamic in these photocatalytic systems were studied, offering a detailed understanding of the reaction mechanism. Overall, these findings provide new approaches and ideas for heterogeneous photocatalytic C-C coupling, including photocatalytic system designing, novel coupling reaction applications and in-depth mechanism, which can lead to the development of more efficient and sustainable methods for constructing C-C bonds and be potentially utilised in industrial settings.

#### IV. Publication

- 1). Li, Jiaquan, Fuping Li, Qi Yang, Shaobin Wang, Hongqi Sun, Qingning Yang, Junwang Tang, and Shaomin Liu. Tailoring collaborative N–O functionalities of graphene oxide for enhanced selective oxidation of benzyl alcohol. *Carbon* 182 (2021): 715-724.
- 2). Yang, Qingning, Xiyi Li, and Junwang Tang. Tuning selectivity among acetalisation, pinacol coupling, and hydrogenation reactions of benzaldehyde by catalytic and photochemical pathways at room temperature. *Materials Today Energy* 23 (2022): 100890.
- 3). Yang, Qingning, Xiyi Li, Lu Chen, Xiaoyu Han, Feng Ryan Wang, and Junwang Tang. Effective activation of strong C–Cl bond for highly selective photosynthesis of bibenzyl via homocoupling. *Angewandte Chemie* (2023): e202307907.
- 4). Yang, Qingning, Xiyi Li, Chao Wang, Youxun Xu, and Junwang Tang. CuOx and PdO codecorated CTF-1 for efficient Suzuki-Miyaura coupling reaction (in preparation)

# V. Table of Contents

Declaration	2
I. Acknowledgements	3
II. Abstract	4
III. Impact statement	6
IV. Publication	8
V. Table of Contents	9
VI. List of Table	14
VII. List of Scheme	15
VIII. List of Figure	18
IX. Definition of Abbreviations	26
Chapter 1 Introduction	29
1.1 Background	29
1.2 Motivation	29
1.3 Aim and objectives	31
1.4 Structure of the report	31
Chapter 2 Literature review	33
2.1 Introduction	33
2.2 Fundamentals of photocatalysis	33
2.2.1 Homogeneous photocatalyis and heterogeneous photocatalysis	33

2.2.2 Semiconductors and heterogeneous photocatalysis	34
2.3 Heterogeneous photocatalysis in organic chemistry	36
2.4 Evaluation for photocatalytic organic transformation	37
2.5 C-C bond formation by heterogeneous photocatalysis	40
2.6 Inorganic materials for organic C–C coupling reactions	40
2.6.1 Wide bandgap semiconductor	40
2.6.2 Narrow bandgap semiconductor	46
2.6.2.1 Metal oxides	46
2.6.2.2 Metal sulfides	49
2.6.2.3 Carbon materials	54
2.6.2.4 Other inorganic materials	56
2.6.3 Methods to improve inorganic photocatalysis	59
2.6.3.1 Localised surface plasmon resonances	60
2.6.3.2 Interband transitions	67
2.6.3.3 Band engineering	68
2.7 Organic materials for organic C–C coupling reactions	70
2.7.1 Carbon nitride	70
2.7.2 Other organic materials	76
2.8 Organic-inorganic composites for organic C–C coupling reactions	78
2.8.1 Dye-metal oxide composite	78

2.8.2 Metal-organic framework 80
2.9 Conclusion and outlook
Chapter 3 Characterisations Methodology
3.1 Gas Chromatography-Mass Spectrometry
3.2 Powder X-ray Diffraction
3.3 Photoluminescence Spectroscopy (PL)
3.4 Ultraviolet-Visible Spectroscopy (UV-vis)
3.5 Fourier-transform Infrared Spectroscopy (FTIR)
3.6 Nuclear Magnetic Resonance (NMR)
3.7 Transmission Electron Microscopy (TEM)
3.8 X-ray Photoelectron Spectroscopy (XPS)
3.10 Electron Paramagnetic Resonance (EPR)
3.11 Temperature-programmed Desorption (TPD)
Chapter 4 Control Selectivity Among Acetalisation, Pinacol Coupling and Hydrogenation
Reactions of Benzaldehyde via Catalytic and Photochemical Pathways at Ambient Temperature
92
4.1 Introduction
4.2 Experimental section
4.2.1 Characterisation of bare P2594
4.2.2 Catalytic performance evaluation

4.3 Results and discussion	97
4.4 Substrate scope	106
4.4 Conclusion	110
Chapter 5 Effective Activation of Strong C-Cl Bonds for Robust	Homo-Coupling in
Photosynthesis of Bibenzyl	112
5.1 Introduction	112
5.2 Experimental Section	114
5.3 Result and Discussion	117
5.3.1 Catalytic Performance	117
5.3.2 Substrate Scope	131
5.3.3. Catalyst characterizations	144
5.3.4. Reaction Mechanism	150
5.4 Conclusion	163
Chapter 6 CuOx and PdO Co-decorated CTF-1 for Efficient Suzuki-Miyaur	a Coupling Reaction
	165
6.1 Introduction	165
6.2 Experimental section	167
6.3 Results and discussion	169
6.3.1 Materials characterisation.	169
6.3.2 Photocatalytic activity	174

6.3.3 Substrates scopes	183
6.3.4 Reaction mechanism	193
6.4 Conclusion	201
Chapter 7 Overall conclusion and future works	203
Chapter 8 Reference	208

# VI. List of Table

Table 1 Experimental conditions for the transformations of benzaldehyde 1 <sup>a</sup>	97
Table 2 pH influence on the transformations of benzaldehyde 1 <sup>a</sup>	99
Table 3 Scope of different aldehydes	06
Table 4 Performance of bibenzyl synthesis over different photocatalysts	19
Table 5 Control experiments for photocatalytic Ullmann homo-coupling of benzyl chloride 1	52
Table 6 Energy data of benzyl chloride and benzyl radicals on different model surface for DI	FT
	57
Table 7 Mulliken charge of C7H7Cl	61
Table 8 Optimised reaction conditions and control experiments of SMC reaction ov	/er
Pd <sub>0.5</sub> Cu <sub>1</sub> /CTF-1	82

# VII. List of Scheme

Scheme 1 The mechanism of photocatalysis: after irradiation and the excitation of electrons (a)
surface e-/h+ recombination; (b) bulk e-/h+ recombination; (c) reduction reactions; (d) oxidation
reactions <sup>[6]</sup> 36
Scheme 2 Proposed mechanism of the photocatalytic Ullmann cross-coupling reaction over
Pd@TiO <sub>2</sub> under UVA and visible light irradiation <sup>[36]</sup>
Scheme 3 Conversions (dark bars) of benzene iodides and yields (light bars) of biphenyl obtained
after several catalytic cycles of reactions (A) and (B) and the demonstration of the catalytic farming
cycle <sup>[37]</sup> 42
Scheme 4 Photocatalytic Ullmann coupling of iodobenzenes over a blended catalyst system [38] 43
Scheme 5 Proposed electron transfer process in the system during light activation <sup>[39]</sup>
Scheme 6 Illustration of reaction intermediates and pathways of dehalogenative coupling of benzyl
bromide over Cu/TiO <sub>2</sub> <sup>[41]</sup>
Scheme 7 Proposed mechanism for the heterogeneous Lewis Acid catalytic reductive cyclization
of <i>trans</i> -chalcones <sup>[42]</sup> 46
Scheme 8 Proposed mechanism of SMC reaction over Ag@Cu <sub>2</sub> O core-shell NPs <sup>[48]</sup> 49
Scheme 9 Mechanism of visible light photoredox catalytic C-H arylation of aryl bromide over
ZnSe/CdS core/shell QDs <sup>[50]</sup>
Scheme 10 Mechanism illustration for the hydrogenation and pinacol coupling of aryl aldehydes
and ketones over CdSe/CdS QDs <sup>[51]</sup>
Scheme 11 Near-field scattering light harvesting model to enhance light absorption of CdS QDs
for photocatalytic hydrogen evolution and C–C coupled hydrobenzoin over CdS/SiO <sub>2</sub> <sup>[52]</sup>

Scheme 12 Illustration for two reaction pathways of benzaldehyde transformation under light
irradiation <sup>[53]</sup>
Scheme 13 Illustration of the photocatalytic reaction pathways over $Zn_xIn_2S_{3+x}^{[54]}$
Scheme 14 Proposed mechanism of photocatalytic SMC over Pd/ MoS <sub>2</sub> <sup>[55]</sup>
Scheme 15 Proposed mechanism of photocatalytic Pinacol coupling over CNTs under UV
irradiation <sup>[57]</sup>
Scheme 16 Proposed mechanism of photocatlytic coupling reaction of phenylacetylene over Cu-
$Cu_2O-C^{[61]}$
Scheme 17 Proposed mechanism of the photocatalytic hydrogenation coupling of acetone into 2,3-
dimethyl-2,3-butanediol <sup>[64]</sup>
Scheme 18 Proposed mechanism of the photocatalytic Sonogashira C-C cross-coupling reaction
over Pd <sub>3</sub> Cu <sub>1</sub> /SiC <sup>[67]</sup>
Scheme 19 The proposed reaction mechanism for the SMC reaction over Pd/TiO <sub>2</sub> <sup>[72]</sup>
Scheme 20 Proposed mechanism for photocatalytic SMC reaction over Au-Pd/ZrO <sub>2</sub> under visible
light irradiation <sup>[81]</sup> 65
Scheme 21 Photocatalytic selective oxidation of primary amines to imines over O <sub>2</sub> by 2P-TiO <sub>2</sub> .
500 <sup>[90]</sup>
Scheme 22 Esterification of NHI with alcohol over N-TiO <sub>2</sub> -30 <sup>[91]</sup>
Scheme 23 Mechanism of photocatalytic Suzuki-Miyaura coupling reaction over HUY@S-
TOH/AuPd under visible irradiation <sup>[79]</sup>
Scheme 24 Oxidative coupling reaction with nitroalkanes over mpg-C <sub>3</sub> N <sub>4</sub> <sup>[92]</sup>
Scheme 25 Reaction of benzana trifluoromethylation <sup>[93]</sup>

Scheme 26 Photocatalytic [4+2] cycloaddition of <i>trans</i> -anethole with 2,3-dimethyl-1,3- butadie	ne
over g-C <sub>3</sub> N <sub>4</sub> <sup>[94]</sup>	71
Scheme 27 Mizoroki–Heck type reactions of olefins and alkyl bromides <sup>[95]</sup>	71
Scheme 28 Proposed mechanism of photocatalytic Ullmann coupling and aromatic alcoh	ol
oxidation over Pd/CN-450 <sup>[98]</sup>	72
Scheme 29 Proposed mechanism of photocatalytic SMC over PdCu/UTCN <sup>[101]</sup>	74
Scheme 30 Proposed explanation for the favourable promotional effect of Pd, Ni and Cu <sup>[102]</sup>	75
Scheme 31 Metal-free heterogeneous photochemical synthesis <sup>[104]</sup>	75
Scheme 32 Illustration for the generation of alkyl radicals from redox-active esters <sup>[105]</sup>	76
Scheme 33 Proposed photocatalytic mechanism of the Suzuki cross-coupling reaction ov	er
Cu <sub>2</sub> O/PBI <sup>[111]</sup>	79
Scheme 34 Proposed mechanism of SMC reaction over CoPc/NiO photocatalyst <sup>[113]</sup>	79
Scheme 35 Mechanism of photocatalytic SMC over (a) Pd@NH <sub>2</sub> -Uio-66(Zr) and (b) CuPd@NH	[ <sub>2</sub> -
Uio-66(Zr) [115]	30
Scheme 36 (a) Synthesis of Cu <sub>3</sub> P/hBN Composites from HKUST MOF (b) Mechanism	of
photocatalytic cycle <sup>[116]</sup>	31
Scheme 37 Four different pathways for benzaldehyde transformations and corresponding produ	ct
yield (%)9	94
Scheme 38 Purposed mechanisms for photochemical pinacol coupling of benzaldehyde (left pane	ી)
and photocatalytic hydrogenation of benzaldehyde (right panel)	)5
Scheme 39 Proposed mechanism for photocatalytic reductive homo-coupling of benzyl chloric	de
over Cu/ZnO catalyst	63

# VIII. List of Figure

Figure 1 Polypyridyl ruthenium and iridium complexes as homogeneous photocatalysts [2,3] 34
Figure 2 Band structures of insulator, semiconductor and metal <sup>[5]</sup>
Figure 3 (a) Preparation process of Pd-NiFe <sub>2</sub> O <sub>4</sub> /rGO; (b) PL spectra of (a) pure NiFe <sub>2</sub> O <sub>4</sub> , (b)
NiFe <sub>2</sub> O <sub>4</sub> /rGO-4, (c) Pd- NiFe <sub>2</sub> O <sub>4</sub> /rGO-4 upon 425 nm excitation <sup>[45]</sup>
Figure 4 (a) Ultraviolet-visible (UV-vis) spectra results of WO <sub>3-x</sub> , Pd/WO <sub>3-x</sub> and Pd/WO <sub>3-x</sub> after
8min UV irradiation; (b) Proposed mechanism of SMC reaction over Pd/WO <sub>3-x</sub> <sup>[47]</sup>
Figure 5 Mechanism of LSPR when light incident on a metal nanoparticle causes the conduction
band electrons to oscillate
Figure 6 (a) temporal study of biphenyl yield by various catalysts; (b) The wavelength-dependent
study on the yield of biphenyl; (c) Proposed photocatalytic reaction mechanism over the
Pd/Au/PN-CeO <sub>2</sub> catalysts under visible irradiation <sup>[80]</sup>
Figure 7 (a) Preparation process of Pd/SiO <sub>2</sub> /Au/ZrO <sub>2</sub> ; (b) Simulation of two situations in near-field
enhancement <sup>[85]</sup> 66
Figure 8 (a) Enhanced catalytic performance of metal NPs on ZrO <sub>2</sub> support as a result of irradiation
with UV light and with visible light from an incandescent lamp and an LED lamp for benzylamine
coupling reaction. (b) Proposed mechanisms of the photocatalytic reactions with nonplasmonic
metal NP photocatalysts <sup>[89]</sup>
Figure 9 Structure of PDA and its inspiration species mussels, shellfish and geckos [109]
Figure 10 Bragg's Law86
Figure 11 XRD result of TiO <sub>2</sub> (bare P25)
Figure 12 UV-vis spectrum of P25

Figure 13 (a) structure of Brønsted acid site on P25 surface. (b) mechanism of acetalisation of
benzaldehyde98
Figure 14 UV-Vis spectrum of methanol and benzaldehyde
Figure 15 (a) GC-spectrum for isotopic labelling test; (b)Isotopic labelling of pinacol coupling
reaction of benzaldehyde. a: Substrate 1 (1 mmol), methanol solvent (15 ml), 365 nm LED, pH 12,
25 °C, 2h. b: Substrate 1 (1 mmol), CD <sub>3</sub> OD solvent (15 ml), 365 nm LED, pH 12, 25 °C, 2h . 102
Figure 16 Isotopic labelling result of hydrogenation of benzaldehyde
Figure 17 UV-vis spectrum of substrate 6
Figure 18 UV-vis spectrum of substrate 7
Figure 19 UV-vis spectrum of substrate 8
Figure 20 UV-vis spectrum of substrate 9
Figure 21 UV-vis spectrum of substrate 10
Figure 22 UV-vis spectrum of substrate 11
Figure 23 XRD patterns of bare ZnO, 1.5% M/ZnO (M=Cu, Pd, Ag, In, Rh, Au, Ni, Pt, Ru, Ir, Fe,
Co) samples
Figure 24 Photocatalytic benzyl chloride coupling using a series of selected metals decorated ZnO,
1.5 wt% M/ZnO (M=Cu, Pd, Ag, In, Rh, Au, Ni, Pt, Ru, Ir, Fe, Co). Reaction conditions: 10mM
reactant, 10 mg photocatalyst in 5 ml solvent (2-propanol: water = 1:1) under 365 nm LED
irradiation for 6 h in Ar at room temperature
Figure 25 GC spectra of products over 1.5% M/ZnO (M= Cu, Pd, Ag)
Figure 26 Temporal study of photocatalytic benzyl chloride conversion over 1.5 wt% Cu/ ZnO.
Reaction conditions: 10mM reactant, 10 mg photocatalyst in 5 ml solvent (2-propanol: water =
1:1) under 365 nm LED irradiation for 6h, Ar, room temperature

Figure 27 Temporal study of photocatalytic benzyl chloride conversion using Pd/ ZnO. Reaction
conditions: 10mM reactant, 10 mg photocatalyst in 5 ml solvent (2-propanol: water = 1:1) under
365 nm LED irradiation for 6h, Ar, room temperature
Figure 28 Temporal study of photocatalytic benzyl chloride conversion using Ag/ ZnO. Reaction
conditions: 10mM reactant, 10 mg photocatalyst in 5 ml solvent (2-propanol: water = 1:1) under
365 nm LED irradiation for 6h, Ar, room temperature
Figure 29 XRD patterns of 5% Ag/ZnO after reaction sample
Figure 30 Effect of Cu loading on the photocatalytic coupling of benzyl chloride. Reaction
conditions: 10mM reactant, 10 mg photocatalyst in 5 ml solvent (2-propanol: water = 1:1) under
365 nm LED irradiation for 6 h in Ar at room temperature
Figure 31 Solvent effect on the photocatalytic coupling of benzyl chloride. Reaction conditions:
10mM reactant, 10 mg photocatalyst in 5 ml pure solvent under 365 nm LED irradiation for 2h in
Ar at room temperature
Figure 32 Water contents on the photocatalytic coupling of benzyl chloride. Reaction conditions:
10mM reactant, 10 mg photocatalyst in 5 ml solvent (2-propanol with different water contents)
under 365 nm LED irradiation for 2h in Ar at room temperature
Figure 33 Stability test of 1.5 wt% Cu/ZnO. Reaction conditions: 10mM reactant, 10 mg
photocatalyst in 5 ml solvent (2-propanol: water = 1:1) under 365 nm LED irradiation for 6 h in
Ar at room temperature
Figure 34 Scaling-up experiment with higher benzyl chloride concentration. Reaction conditions:
40mM reactant, 50 mg photocatalyst in 50 ml solvent (2-propanol: water = 1:1) under 365 nm
LED irradiation for 40 h, Ar, room temperature

Figure 35 Extension to different substrates. Photocatalytic homo-coupling of various be	enzylic
chlorides to the corresponding bibenzyl using Cu/ZnO photocatalyst. <sup>a</sup> Reaction conditions:	10mM
reactant, 10 mg photocatalyst in 5 ml solvent (2-propanol: water = 1:1) under 365 nn	n LED
irradiation for 6 h, Ar, room temperature. <sup>b</sup> Analysed by GC−FID, and all conversions ≥ 99	%, the
percentage indicates its yield, the equation for calculating yield is shown in Equation 2	133
Figure 36 (a) <sup>1</sup> H NMR of 2a, and (b) <sup>13</sup> C NMR of 2a	134
Figure 37 (a) <sup>1</sup> H NMR of 3a, and (b) <sup>13</sup> C NMR of 3a	135
Figure 38 (a) <sup>1</sup> H NMR of 4a, and (b) <sup>13</sup> C NMR of 4a	136
Figure 39 (a) <sup>1</sup> H NMR of 5a, and (b) <sup>13</sup> C NMR of 5a	137
Figure 40 (a) <sup>1</sup> H NMR of 6a, and (b) <sup>13</sup> C NMR of 6a	138
Figure 41 (a) <sup>1</sup> H NMR of 7a, and (b) <sup>13</sup> C NMR of 7a	139
Figure 42 (a) <sup>1</sup> H NMR of 8a, and (b) <sup>13</sup> C NMR of 8a	140
Figure 43 (a) <sup>1</sup> H NMR of 9a, and (b) <sup>13</sup> C NMR of 9a	141
Figure 44 (a) <sup>1</sup> H NMR of 10a, and (b) <sup>13</sup> C NMR of 10a	142
Figure 45 (a) <sup>1</sup> H NMR of 11a <sup>a</sup> , and (b) <sup>13</sup> C NMR of 11a	143
Figure 46 XRD patterns of bare ZnO, 5%Cu/ZnO samples (before, activated and post real	action)
	144
Figure 47 TEM and EDS mapping (Zn, Cu, O) image of 1.5 wt% Cu/ZnO post-reaction	sample
	145
Figure 48 EPR spectra of 1.5% Cu/ZnO samples (before, activated and post reaction)	146
Figure 49 EPR spectra of 5% Cu/ZnO samples (before and post reaction)	147
Figure 50 TEM image of Cu/ZnO post reaction sample	147
Figure 51 in-situ EPR spectra of 1.5% Cu/ZnO post reaction sample	148

Figure 52 Deconvolution of XPS spectra in the Cu 2p <sub>3/2</sub> region for 1.5% Cu/ZnO samples (before,
activated and post reaction)
Figure 53 Deconvolution of XPS spectra in the Cu 2p <sub>3/2</sub> region for 5% Cu/ZnO samples (before,
activated and post reaction)
Figure 54 TPD spectra of benzyl chloride on bare ZnO and 1.5% Cu/ZnO 6h reaction sample 151
Figure 55 UV-vis spectra of bare ZnO, 1.5% Cu/ZnO after 6 hour reaction sample
Figure 56 Electron capture experiments. Reaction conditions: 10mM reactant, with/without NaIO <sub>3</sub> ,
10 mg photocatalyst in 5 ml solvent (2-propanol: water = 1:1) under 365 nm LED irradiation for
1.5h
Figure 57 Images of reaction solutions for identifying reaction intermediates. A: benzyl chloride
in isopropanol/water mixture. C and E: photoreduction of benzyl chloride using 1.5% Cu/ZnO
after irradiated by 365nm LED for 2 h and 4 h, respectively under deaerated conditions. B, D and
F: photos after adding the same amount of AgNO3 into A, C and E
Figure 58 benzyl radical and benzyl chloride on selected surfaces of ZnO(100)
Figure 59 benzyl radical and benzyl chloride on selected surfaces of Cu/ZnO(100)
Figure 60 benzyl radical and benzyl chloride on selected surfaces of Cu/TiO <sub>2</sub> (101)
Figure 61 EPR spectra for capture experiment of alkoxy radicals from 2-propanol over TiO <sub>2</sub> , ZnO
and no catalyst. The EPR measurement was conducted at room temperature, with a modulation
frequency of 100 kHz, a microwave frequency of 9.46 GHz, a sweep time of 60 s, a microwave
power of 10 mW, and swept from 330 to 345 mT. irradiation for 20s using 465 nm LED 159
Figure 62 Temporal study of photocatalytic benzyl chloride conversion using Cu/TiO <sub>2</sub> . Reaction
conditions: 10mM reactant, 10 mg photocatalyst in 5 ml solvent (2-propanol: water = 1:1) under
365 nm LED irradiation for 7h, Ar, room temperature

Figure 63 PL spectra of bare ZnO and Cu/ZnO post reaction sample
Figure 64 XRD patterns of bare CTF-1 and Pd <sub>0.2</sub> Cu <sub>1</sub> /CTF-1 samples
Figure 65 FTIR spectra of bare CTF-1 and Pd <sub>0.2</sub> Cu <sub>1</sub> /CTF-1 samples
Figure 66 <sup>13</sup> C ssNMR spectrum of CTF-1
Figure 67 Deconvolution of XPS spectrum of the C 1s in bare CTF-1
Figure 68 Deconvolution of XPS spectra of the N 1s in bare CTF-1
Figure 69 Effect of Pd loading on the photocatalytic SMC reaction of 4-bromoanisole over CTF
1 photocatalysts. Reaction conditions: 0.05 mmol 4-bromoanisole, 1.3 equiv phenylboronic acid
4 equiv K <sub>2</sub> CO <sub>3</sub> , 5 ml solvent (EtOH: H <sub>2</sub> O=1:1), 5 mg photocatalyst, 365 nm multi-channel LED
15 h, Ar, room temperature
Figure 70 Effect of Cu loading on the photocatalytic SMC reaction of 4-bromoanisole over
Pd <sub>0.5</sub> /CTF-1 photocatalysts. Reaction conditions: 0.05 mmol 4-bromoanisole, 1.3 equiv
phenylboronic acid, 4 equiv K <sub>2</sub> CO <sub>3</sub> , 5 ml solvent (EtOH: H <sub>2</sub> O=1:1), 5 mg photocatalyst, 365 nn
multi-channel LED, 15 h, Ar, room temperature
Figure 71 Effect of preparation order of Pd and Cu co-catalysts on CTF-1 for the photocatalytic
SMC reaction of 4-bromoanisole. Reaction conditions: 0.05 mmol 4-bromoanisole, 1.3 equiv
phenylboronic acid, 4 equiv K <sub>2</sub> CO <sub>3</sub> , 5 ml solvent (EtOH: H <sub>2</sub> O=1:1), 5 mg photocatalyst, 365 nn
multi-channel LED, 15 h, Ar, room temperature
Figure 72 Optimisation of Cu loading on Pd <sub>0.2</sub> /CTF-1 for the photocatalytic SMC reaction of 4
bromoanisole. Reaction conditions: 0.05 mmol 4-bromoanisole, 1.3 equiv phenylboronic acid, 4
equiv K <sub>2</sub> CO <sub>3</sub> , 5 ml solvent (EtOH: H <sub>2</sub> O=1:1), 5 mg photocatalyst, 365 nm multi-channel LED, 15
h, Ar, room temperature

Figure 73 Stability test of $Pd_{0.2}Cu_1/CTF-1$ . Reaction conditions: 0.05 mmol 4-bromoanisole, 1.3
equiv phenylboronic acid, 4 equiv K <sub>2</sub> CO <sub>3</sub> , 5 ml solvent (EtOH: H <sub>2</sub> O=1:1), 5 mg photocatalyst,
365 nm multi-channel LED, 20 h, Ar, room temperature
Figure 74 UV-vis spectra results of bare CTF-1 and $Pd_{0.5}Cu_1/CTF-1$
Figure 75 Extension to different substrates. Photocatalytic SMC reaction of various aryl bromides
to the corresponding coupling products using $Pd_{0.2}Cu_1/CTF-1$ photocatalyst. <sup>a</sup> Reaction conditions:
0.05 mmol 4-bromoanisole, 1.3 equiv phenylboronic acid, 4 equiv K <sub>2</sub> CO <sub>3</sub> , 5 ml solvent (EtOH:
$H_2O=1:1$ ), 5 mg photocatalyst, 365 nm multi-channel LED, 15 h, Ar, room temperature. ${}^b$ Analysed
by GC–MS, and all conversions ≥ 99%, the percentage indicates its yield
Figure 76 (a) <sup>1</sup> H NMR of 1a, and (b) <sup>13</sup> C NMR of 1a
Figure 77 (a) <sup>1</sup> H NMR of 2a, and (b) <sup>13</sup> C NMR of 2a
Figure 78 (a) <sup>1</sup> H NMR of 3a, and (b) <sup>13</sup> C NMR of 3a
Figure 79 (a) <sup>1</sup> H NMR of 4a, and (b) <sup>13</sup> C NMR of 4a
Figure 80 (a) <sup>1</sup> H NMR of 5a, and (b) <sup>13</sup> C NMR of 5a
Figure 81 (a) <sup>1</sup> H NMR of 6a, and (b) <sup>13</sup> C NMR of 6a
Figure 82 (a) <sup>1</sup> H NMR of 7a, and (b) <sup>13</sup> C NMR of 7a
Figure 83 (a) <sup>1</sup> H NMR of 8a, and (b) <sup>13</sup> C NMR of 8a
Figure 84 TEM and EDS mapping image of Pd <sub>0.2</sub> Cu <sub>1</sub> /CTF-1 post-reaction sample
Figure 85 Deconvolution of XPS spectra of the Pd 3 <i>d</i> region for Pd <sub>0.2</sub> Cu <sub>1</sub> /CTF-1samples (before
and after reaction)
Figure 86 Deconvolution of XPS spectra of the Cu 2p for Pd <sub>0.2</sub> Cu <sub>1</sub> /CTF-1samples (before and after
reaction)
Figure 87 EPR spectra of Pd <sub>0.2</sub> Cu <sub>1</sub> /CTF-1samples

Figure 88 In-situ XPS spectra of the Pd 3d region for Pd <sub>0.2</sub> Cu <sub>1</sub> /CTF-1 samples (Xe lamp off an
on for 20min)
Figure 89 in-situ XPS spectra in the Cu 2p region for Pd <sub>0.2</sub> Cu <sub>1</sub> /CTF-1 samples (Xe lamp off an
on for 20min)
Figure 90 In-situ EPR spectra of Pd <sub>0.2</sub> Cu <sub>1</sub> /CTF-1 sample
Figure 91 PL spectra for bare CTF-1, Pd <sub>0.2</sub> /CTF-1, Cu <sub>1</sub> /CTF-1 and Pd <sub>0.2</sub> Cu <sub>1</sub> /CTF-120
Figure 92 Proposed mechanism for photocatalytic SMC reaction of 4-bromoanisole over
Pd <sub>0.2</sub> Cu <sub>1</sub> /CTF-1

# IX. Definition of Abbreviations

The following table describes the significance of various abbreviations and acronyms used throughout the thesis. The page on which each one is defined or first used is also given.

Abbreviation	Meaning	Page
C-C bond	carbon-carbon bond	4
SMC	Suzuki Miyaura coupling	4
P25	Titanium dioxide	4
ZnO	Zinc oxide	4
Cu	Copper	4
Pd	Palladium	5
CTF-1	Covalent triazine framework-1	5
NPs	Nanoparticles	5
C–Br	Carbon-bromine bond	5
C-Cl	Carbon–chlorine bond	6
$TiO_2$	Titanium dioxide	6
Au	Gold	7
XPS	X-ray photoelectron spectroscopy	7
EPR	Electron paramagnetic resonance	7
DFT	Density functional theory	7
e-/h+	Electron/hole pairs	30
C=O	Carbon oxygen double bond	30
CB	Conduction band	33
VB	Valence band	33
$E_{g}$	Bandgap energy	34
ATRA	Atom-transfer radical addition	34
$CO_2$	Carbon dioxide	36
Ci	Initial concentration of reagent	37
Cr	Concentrations of reagent at a specific time during reaction	37
Cp	Concentrations of target products at a specific time during reaction	37
TON	Turnover number	37
TOF	Turnover frequence	37
AQY	Apparent quantum yield	38
$n_{electron}$	Number of electrons participating in the reaction	38
$n_{photon}$	Total number of incident photons under a specific wavelength condition	38
UV	Ultraviolet	39
UVA	Ultraviolet A	40
LEDs	Light-emitting diodes	40
C–I	Carbon-iodine bond	40
THF	Tetrahydrofuran	41
$Al_2O_3$	Aluminium oxide	41
CNTs	Carbon nanotubes	42
DMF	Dimethylformamide	42
AQE	Apparent quantum efficiency	42
SET	Single electron transfer	44
$Sm_xO_y$	Samarium oxide	44
$Bi_2O_3$	Bismuth(III) oxide	44

BiVO <sub>4</sub>	Bismuth vanadate	45
MFe <sub>2</sub> O <sub>4</sub>		45
WO <sub>3-x</sub>	Ferrimagnetism spinel ferrites	45
rGO	Tungsten trioxide	45
NIR	Reduced graphene oxide Near-infrared	45
LSPR		
	Localised surface plasmon resonances Ultraviolet visible	46 47
UV-vis		
Ag	Silver	47
Cu <sub>2</sub> O	Copper(I) oxide	47
CdS	Cadmium sulfide	48
$ZnIn_2S_4$	Zinc indium sulfide	48
$MoS_2$	Molybdenum disulfide	48
QDs	Quantum dots	48
ZnSe	Zinc selenide	48
CdSe	Cadmium selenide	49
$SiO_2$	Silicon dioxide	50
$H_2$	Hydrogen	50
Xe	Xenon	50
$2H$ - $WS_2$	Tungsten disulfide	52
DMSO	Dimethyl sulfoxide	52
MOF	metal-organic frameworks	53
PECET	photo-excited conduction electron transfer	53
FeOx	Iron oxide	53
N	Nitrogen	53
ZIF	Zeolitic imidazolate frameworks	54
CsPbBr <sub>3</sub>	Lead halide perovskites	55
$KNb_3O_8$	potassium niobium oxide	55
NaTaO <sub>3</sub>	Sodium tantalum trioxide	55
Na <sub>2</sub> Ti <sub>3</sub> O <sub>7</sub>	Sodium titanate	55
CO	Carbon Monoxide	55
Ag-AgBr	Silver-decorated silver bromide	56
β-SiC	Cubic silicon carbide	56
LDHs	layered double hydroxides	57
$CeO_2$	Cerium(IV) oxide	60
$ZrO_2$	Zirconium dioxide	60
SBA-15	mesoporous silica	63
$Nb_2O_5$	niobium oxide	65
CND	carbon nanodiamond	65
$C_3N_4$	Conjugated carbon nitride	69
CN-C	Crystallized carbon nitride nanobelts	70
NRCN	N-rich carbon nitride	71
UTUC	Ultrathin 2D carbon nitride nanosheets	71
AE	Atom economy	72
BCN	Boron carbon nitrides	73
COFs	Covalent organic frameworks	74
B-BO <sub>3</sub>	conjugated microporous poly (benzoxadiazole) network	75
PDA-CL	Polydopamine nanofilms	75
HPS	Hyper-cross-linked polystyrene	75
PBI	Perylene bisimide	76
Cu <sub>3</sub> P	Copper phosphide	79 79
hBN	Hexagonal boron nitride nanostructures	79
117714	Tieragonar boton intride nanostructures	1)

$O_2$ -·	Superoxide radical anion	79
CDC	Cross-dehydrogenative coupling	80
GC-MS	Gas Chromatography-Mass Spectrometry	83
EI	Electron ionisation	83
PXRD	Powder X-ray Diffraction	83
PL	Photoluminescence spectroscopy	85
FTIR	Fourier-transform infrared	86
NMR	Nuclear magnetic resonance spectroscopy	87
TEM	Transmission electron microscopy	87
TPD	Temperature-programmed desorption	89
KOH	Potassium hydroxide	94
Ar	Argon	94
mmol	millimoles	95
mg	milligram	95
ml	millilitre	95
M	Molar concentration	95
$CD_3OD$	Deuterated methanol	100
PC50	Anatase TiO <sub>2</sub>	101
wt%	Weight percentage	111
In	Indium	112
Rh	Rhodium	112
Pt	platinum	112
Ru	Ruthenium	112
Ir	Iridium	112
$O_2$	Oxygen	112
Ni	Nickel	112
Fe	Iron	112
Co	Cobalt	112
GGA	Generalised gradient approximation	114
PAW	Projected augmented wave	114
ICP-OES	Inductively coupled plasma atomic optical emission spectroscopy	124
MeCN	Acetonitrile	125
HCl	Hydrogen chloride	126
EDS	Energy dispersive spectroscopy	142
NaIO <sub>3</sub>	Sodium iodate	151
$AgNO_3$	Silver nitrate	152
t-BuNO	2-nitroso-2-niethylpropane	156
equiv	Equivalent	173
$K_2CO_3$	Potassium carbonate	173
EtOH	Ethanol	173
XAFS	in-situ X-ray absorption fine structure spectroscopy	204

## **Chapter 1 Introduction**

## 1.1 Background

Organic transformations are vital in producing valuable compounds, such as pharmacies, cosmetics, food and fragrance, which are very demanding<sup>[1]</sup>. Many different processes are used in the industry to produce those products on a large scale. Mature industrial organic synthesis routes and manufacturing processes have been set up in the industry, but they have not been changed for a reasonably long period as it is complicated to change those large-scale processes once established. However, many reactions on the industrial scale are still using unsustainable, energy-inefficient processes and some reagents, catalysts, solvents and by-products involved in the processes are harmful and toxic. Thus, there is a real need for the industry to find alternatives which are more environmentally friendly and eco-compatible to replace those conventional processes.

#### 1.2 Motivation

The construction of C–C bonds is a fundamental aspect of organic chemistry, as it is the basis for the synthesis of many complex organic molecules, including natural products, pharmaceuticals, and materials. The ability to selectively and efficiently form C–C bonds allows chemists to design and synthesise molecules with specific properties and functions. In conventional methods, C–C bond formation reactions can be performed using transition metal-catalysed reactions and organocatalysis. Despite their advantages, such as high selectivity and high reaction efficiency, these methods often require harsh reaction conditions and expensive catalysts. In addition, the potential toxicity of the metal catalysts and their environmental impact is another problem worth tackling.

Heterogeneous photocatalysis is an emerging area in C–C bond formation and organic synthesis<sup>[2]</sup>. The use of photocatalysts, which can harness light energy to drive chemical reactions, has gained significant attention in recent years due to their potential for sustainable and environmentally friendly synthesis of complex organic molecules. Heterogeneous photocatalysts, in particular, have several advantages over homogeneous photocatalysts, such as easier catalyst separation, improved stability, and increased recyclability. These advantages have led to the development of a wide range of heterogeneous photocatalysts for C-C bond formation, including metal oxides, semiconductors, and carbon-based materials. In addition to the potential advantages of heterogeneous photocatalysis mentioned earlier, it is essential to address the specific challenges and gaps in the field. One key challenge is the design and synthesis of highly efficient and stable heterogeneous photocatalysts tailored for C-C bond formation. The development of photocatalysts with enhanced light absorption, efficient charge separation, and reduced recombination rates is critical to achieving high catalytic activity. Furthermore, the integration of green and sustainable principles in the synthesis and design of heterogeneous photocatalysts should be a focal point of the research. Exploring earth-abundant and eco-friendly materials as photocatalysts could address concerns regarding the potential toxicity and environmental impact of conventional transition metal-based catalysts. A comprehensive study encompassing both experimental and theoretical approaches will be essential to unravel the mechanistic aspects of C-C bond formation using heterogeneous photocatalysts. By gaining insights into the reaction mechanisms and intermediates, it becomes possible to develop rational strategies for enhancing selectivity and controlling the formation of specific C-C bonds. Overall, the emerging field of heterogeneous photocatalysis offers new opportunities for developing sustainable and efficient methods for C-C bond formation and organic synthesis.

## 1.3 Aim and objectives

Based on the above discussion, the project aims to utilise heterogeneous photocatalysis to achieve the targeted organic transformations or synthesise value-added compounds with high selectivity operated at ambient conditions. The project first aims to achieve pinacol coupling of benzaldehyde. Then, a more challenging dehalogenative homo-coupling of alkyl chlorides will be targeted. After that, achieving Suzuki-Miyaura coupling with low-concentration Pd co-catalyst will be investigated. Therefore the objectives include the following:

- (1). Designation and optimisation of the co-catalysts to modify the robust and cheap photocatalysts (e.g. TiO<sub>2</sub>) to retard the recombination of photo-induced electron/hole pairs (e<sup>-</sup>/h<sup>+</sup>) and to activate the carbon oxygen double (C=O) bond in aldehydes or C-X (X=Br, Cl) in aromatic halides.
- (2). Optimisation of reaction conditions such as temperature, pH, solvent, light source and additives to tune selectivity towards the targeted direction.
- (3). Isotopic labelling and radical trapping experiments will be conducted to investigate the mechanism behind the photocatalytic organic transformations.
- (4) Correlation of the photocatalytic system with the selectivity will be elucidated.

## 1.4 Structure of the report

This report first introduced the background and motivation of this project: Organic C–C Coupling Reactions by Heterogeneous Photocatalysis in Chapter 1. General knowledge of photocatalysis and different reported cases of heterogeneous photocatalytic C–C bond formation are reviewed in Chapter 2. Methodologies for characterisation and compound analysis have

been described in Chapter 3. In Chapter 4, the pinacol coupling of benzaldehyde is described. Next, efficient homo-coupling of alkyl chlorides by Cu-decorated ZnO with a detailed mechanistic study is discussed in Chapter 5. Low concentration PdO with second co-catalyst CuOx modified CTF-1 for Suzuki-Miyaura coupling of aryl bromides is shown in Chapter 6, and the functions of both co-catalysts are also investigated. The conclusion of the work and discussion of future work are introduced in Chapter 7, respectively.

## **Chapter 2 Literature review**

#### 2.1 Introduction

Following the short introduction of my PhD project in Chapter 1, this Chapter reviews the emerging photocatalysis, including the fundamentals of photocatalysis and tuning selectivity in heterogeneous photocatalytic organic reactions. The investigations on the C–C coupling reactions over different heterogeneous photocatalysts are then classified into C–C homo-coupling and C–C cross-coupling and summarised in detail.

## 2.2 Fundamentals of photocatalysis

#### 2.2.1 Homogeneous photocatalyis and heterogeneous photocatalysis

Photocatalysis, as a multifunctional process, involves knowledge of materials science, chemical engineering and physics. Due to its environmentally friendly advantage, photocatalysis has gained enormous attention in the past few decades. There are two types of photocatalytic systems, homogeneous systems and heterogeneous systems. Homogeneous catalysis is a system where the catalysts dissolve in the solvent and remain in the same phase as the reactants, while heterogeneous systems using a solid phase photoactive catalyst instead.

For homogeneous photocatalysis, the catalyst can be either organic compounds or transition metal complexes. Each molecule can function as a photocatalyst if the lifetime of the molecule's excited state is long enough for the electron transfer to compete with the relaxation. The most successful and widely used homogeneous photocatalysts are polypyridyl ruthenium and iridium complexes [2,3] (**Figure 1**). The advantage of a homogeneous system is that all the active sites are fully used during reactions. Still, it has to face the problem that complicated separation methods are required to

purify reaction mixtures, and due to degradation, the homogeneous photocatalyst cannot be reused in most cases<sup>[4]</sup>. Compared to homogeneous photocatalysis, heterogeneous catalysts can be easily separated and recycled at any time during experiments. Due to this advantage, heterogeneous systems are more favourable for application in the industry considering the economic viability of a process. Though in heterogeneous photocatalysis only active sites on the catalyst surface can work during the reaction, this drawback can be improved by increasing the surface area of photocatalysts.

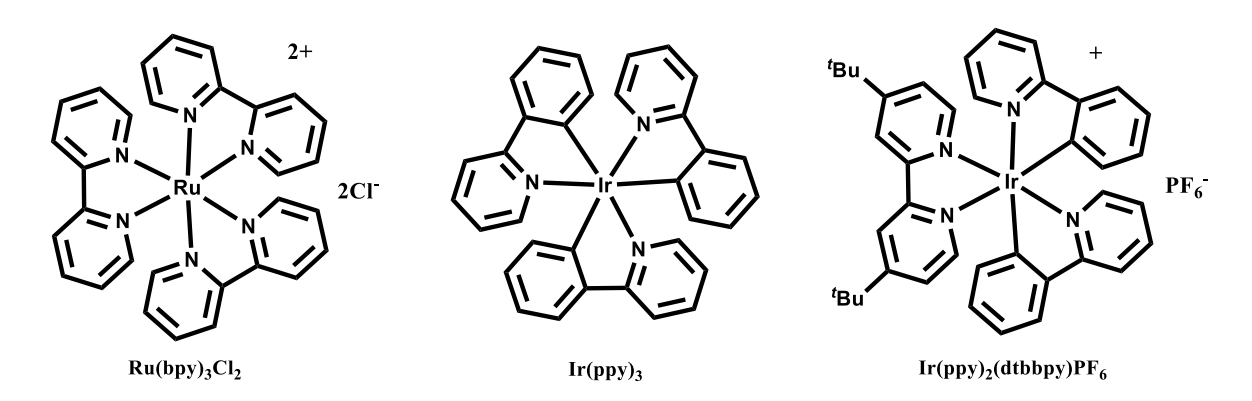


Figure 1 Polypyridyl ruthenium and iridium complexes as homogeneous photocatalysts [2,3]

#### 2.2.2 Semiconductors and heterogeneous photocatalysis

In solid materials, a large number of atomic orbitals overlap with each other, leading to the formation of molecular orbital energy levels. Those molecular orbital energy levels are continuous and the grouping of those energy levels are defined as energy bands.

In metals, either the conduction band (CB) is partially occupied or the valence band (VB) is partially empty, and these two bands overlap with each other. Electrons below the Fermi level can receive energy from any source and then jump to a higher energy level which is above the Fermi

level in the conduction band and then become free electrons. On the other hand, for insulators and semiconductors, the gap between the highest occupied energy level at the top of the valence band and the lowest unoccupied energy level at the bottom of the conduction band is called bandgap. In insulators, the valence band is completely occupied while the conduction band is empty, and their bandgaps are normally quite large ( $E_g > 4.5 \, eV$ ), which makes it impossible for electrons to be excited from the valence band to the conduction band. For semiconductors, as a result of a smaller bandgap, the electrons in the valence band can absorb energy and migrate to the conduction band<sup>[5]</sup> (**Figure 2**). Based on the above discussion, when a suitable light source is applied, semiconductors will be a great candidate for heterogeneous photocatalysis.

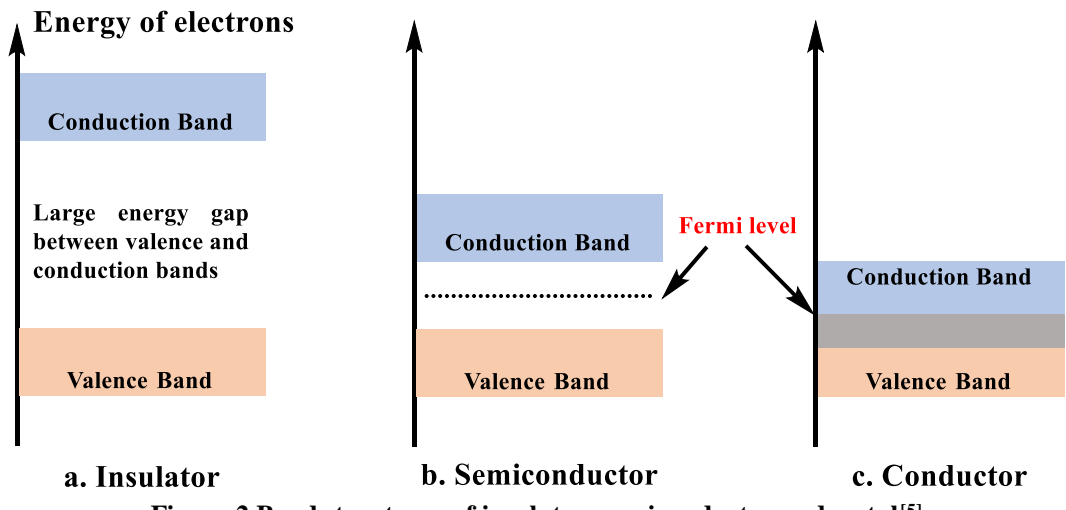
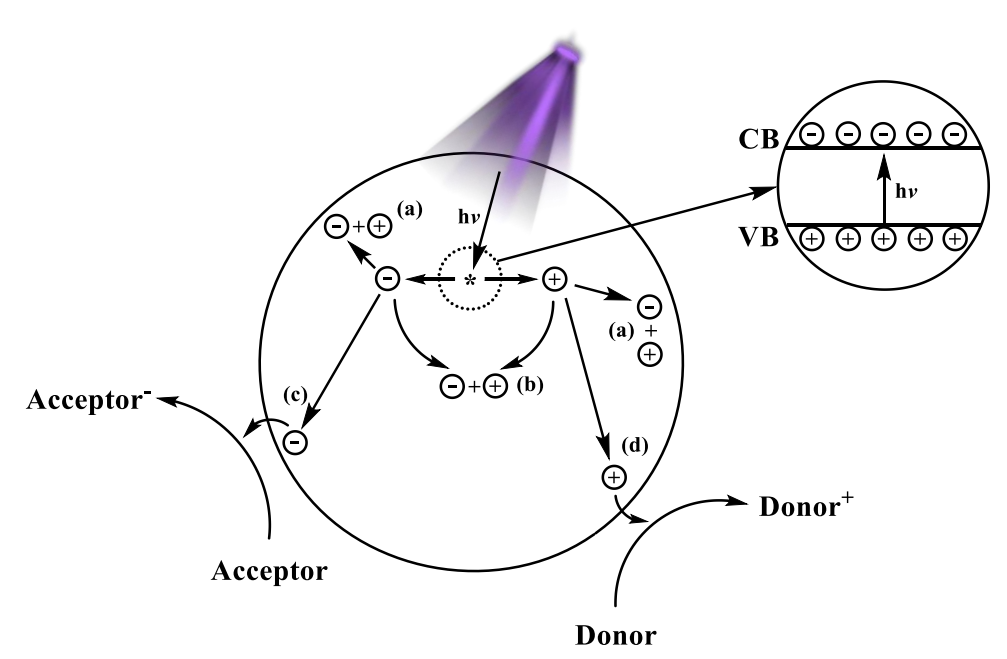


Figure 2 Band structures of insulator, semiconductor and metal<sup>[5]</sup>

In heterogeneous photocatalysis, the solid state photocatalyst plays two roles during the catalytic process: (1) charge generator after absorbing light energy and (2) reactive sites for reactants that adsorbed on the catalyst surface. The fundamental principle of photocatalytic process using heterogeneous catalysts is demonstrated in **Scheme 1**. Heterogeneous photocatalysis starts with the interaction between semiconductor materials and light irradiation. When photons from the light source have energy that exceeds the semiconductor's bandgap energy, the electrons in the valence

band absorb the photon energy, becoming excited and moving to the conduction band, leaving behind positively charged holes in the valence band. As a result, this process generates electron-hole pairs that participate in redox reactions, enabling the photocatalyst to carry out various chemical transformations under light illumination. For a given semiconductor, the positions of its band edges determine the potential of CB electrons and the potential of VB holes, which will then limit the thermodynamics of the photocatalytic oxidation and reduction half-reactions<sup>[6]</sup>.



Scheme 1 The mechanism of photocatalysis: after irradiation and the excitation of electrons (a) surface e-/h+recombination; (b) bulk e-/h+recombination; (c) reduction reactions; (d) oxidation reactions<sup>[6]</sup>

## 2.3 Heterogeneous photocatalysis in organic chemistry

During the past decades, the utilisation of heterogeneous photocatalysis in significant organic transformations has been reported many times, including cycloadditions, cross-coupling reactions, and atom-transfer radical addition (ATRA). However, the main issue related to product selectivity remains since photocatalysis has been utilised in organic transformation. In an ideal heterogeneous

photocatalytic selective transformation process, the photocatalyst attracts and adsorbs a substrate on its surface. Subsequently, the substrate undergoes rapid oxidation or reduction, leading to the formation of a stable product. After the reaction, the product desorbs from the catalyst, ensuring that it will not undergo further oxidation or reduction. The attraction, adsorption of the substrate, and desorption of the product are indeed crucial aspects of heterogeneous photocatalysis to achieve high selectivity. However, in reality, heterogeneous photocatalytic selective organic transformations are much more complex than the ideal process described above [7]. The efficiency and selectivity of photocatalytic reactions depend on various factors, such as the nature of the photocatalyst, the specific properties of the substrate and product, reaction conditions, and the presence of co-catalysts or additives. Additionally, competing reactions and side reactions may occur, leading to the formation of undesired by-products<sup>[8,9]</sup> Due to those aforementioned situations, photocatalysis has been considered as a non-selective process for a long time and previous research in this area largely ignored the investigation on this aspect. In recent years, selective photocatalysis has become a highly valuable research direction and provided emerging prospects for the field of advanced photocatalysis [10],[11]. Many investigations in selective photocatalysis have been reported, and several new applications have been explored and recognized, such as selectively transforming carbon dioxide (CO<sub>2</sub>) to fuels<sup>[12–15]</sup>, selective removing or degrading dilute pollutants<sup>[16–19]</sup>, achieving industrial selective catalytic reactions<sup>[20–</sup> 22]

### 2.4 Evaluation for photocatalytic organic transformation

The equations for the conversion rate, yield, and target product selectivity are shown below<sup>[23]</sup> (**Equation 1**):

conversion (%) = 
$$\left[\frac{Ci - Cr}{Ci}\right] \times 100$$
 (2 - 1)

selectivity (%) = 
$$\left[\frac{Cp}{Ci - Cr}\right] \times 100$$
 (2 – 2)

yield (%) = 
$$\frac{Cp}{Ci} \times 100 = conversion$$
 (%)  $\times$  selectivity (%) (2 - 3)

# Equation 1 Equations for calculating conversion, selectivity and yiled of target products in photocatalytic organic conversion

Where Ci is the initial concentration of reagent and Cr and Cp are the concentrations of reagent and target products at a specific time during the reaction, respectively.

For most organic reactions, the yield of desired product within a certain reaction time is often used to measure the efficiency of the synthetic procedure. Although high conversion of reactant and high selectivity towards target products are both important to achieve an excellent yield, the enhancement of selectivity is more complicated. Currently, improving selectivity in photocatalytic organic synthesis remains a formidable challenge, and common strategies that help improve selectivity in photocatalysis can be classified into two categories. One is the modifications of photocatalysts, including electronic structure (band engineering<sup>[24–26]</sup>, e.g. doping), geometric structure (selective growth of crystal facets, nanosheet, nanorod or porous morphology)<sup>[23,27,28]</sup> and surface modification (co-catalyst and vacancy sites)<sup>[29,30]</sup>. The other one is the manipulation of experimental conditions, including aeration, solvent selection, additives usage and others (temperature, light source, pH value and reaction time).

When comparing different works reported by different research groups, as all the works were conducted under different conditions (reaction volume, reaction time, amount of catalyst). it is convincing to simply compare the yield or conversion. Turnover number (TON) and turnover

frequency (TOF) are used to directly compare the catalytic performance in different studies, where TON indicates the number of moles of substrate that per unit of catalyst can convert before becoming inactivated, and TOF refers to the turnover per unit time. The equations for the TON and TOF are shown below **Equation 2**<sup>[31]</sup>:

$$TON = \frac{n_{reactant}}{n_{catalyst}}$$
 (2 - 4)

$$TOF = \frac{TON}{t} \tag{2-5}$$

#### **Equation 2 Equations for calculating TON and TOF**

Where  $n_{reactant}$  is the molecular number of converted reactant,  $n_{catalyst}$  is the number of catalyst active sites involved in the reaction, and t is the reaction time.

The apparent quantum yield (AQY) is also used to evaluate the photocatalytic efficiency because it can demonstrate the efficiency of light absorption, charge separation and surface redox reaction. The equation for calculating AQY is shown below **Equation 3** $^{[31]}$ :

$$AQY = \frac{n_{electron}}{n_{photon}} \tag{2-6}$$

#### **Equation 3 Equations for calculating AQY**

Where  $n_{electron}$  is the number of electrons participating in the reaction while  $n_{photon}$  is the the total number of incident photons under a specific wavelength condition.

### 2.5 C-C bond formation by heterogeneous photocatalysis

C–C bond formation is one of the most important research contents in modern organic synthesis, and it can normally be classified into two groups, C–C homo-coupling and C–C cross-coupling. Since several decades ago, different homo-coupling reactions such as Ullmann reaction, pinacol reaction and Glaser reaction and cross-coupling reactions such as Suzuki Miyaura reaction, Sonogashira reaction, Heck reaction, Stille reaction have been studied intensively and recognised as a very useful tool for constructing C–C bond. In thermal catalysis, transition metal catalysts are often used to promote these coupling reactions. In order to achieve the redox process and overcome the energy barrier, higher temperature is required (typically 75-200 °C)<sup>[32-34]</sup>. Another main drawback is the biotoxicity of the heavy metal involved in the process, which has been a severe issue for a long time in the pharmaceutical industry<sup>[35]</sup>. Recent research has been focused on developing a new system which is greener, more sustainable and more efficient for C–C coupling reactions. Photochemical and photocatalytic technology have been considered as a new green technique for organic synthesis because the light energy can trigger the electron transfer process, hence carrying out the C–C coupling reaction at ambient temperature.

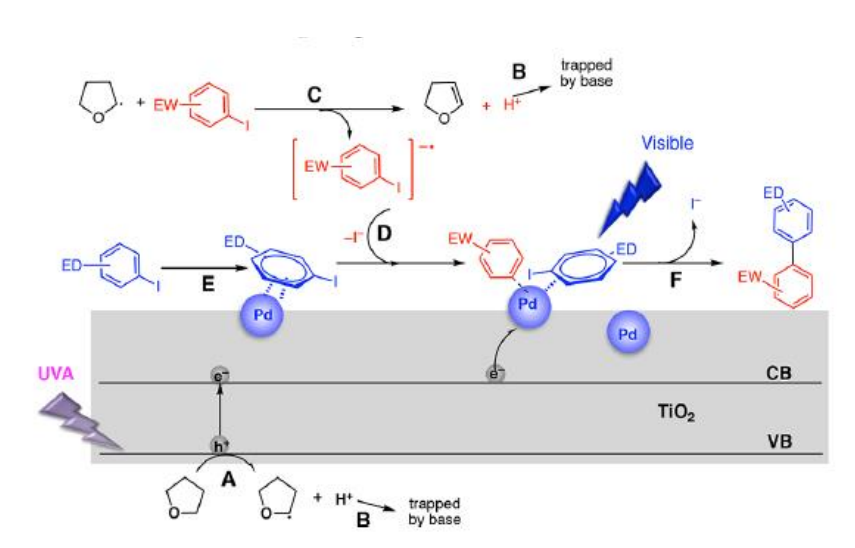
### 2.6 Inorganic materials for organic C-C coupling reactions

## 2.6.1 Wide bandgap semiconductor

Wide bandgap semiconductors (TiO<sub>2</sub>, ZnO etc.) absorbs light energy in the ultraviolet (UV) region and have been widely applied to various photocatalystic reactions (hydrogen evolution, CO<sub>2</sub> reduction and pollutant degradation) due to their excellent intrinsic properties such as less cost, environmentally friendly and high efficiency. C–C cross-coupling reactions, such as Suzuki-

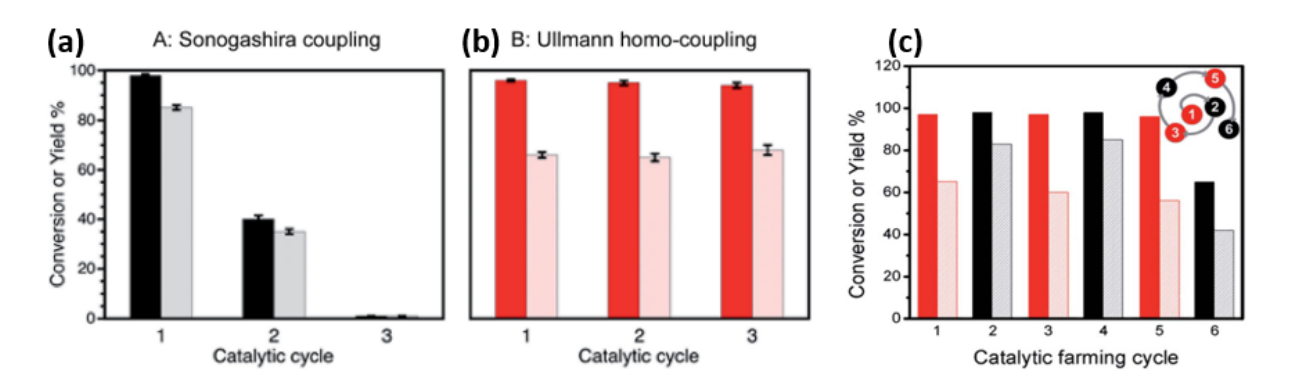
Miyaura reaction, Heck reaction, were awarded the Nobel prize in 2010 for their important contribution to the area of organic synthesis. Pd has been recognised as the preferred catalytic site for a range of C–C coupling reactions due to its high efficiency, selectivity and stability. Various C–C coupling reactions have been carried out under irradiation in the UV region over TiO<sub>2</sub> based photocatalysts and the selectivity can be easily tuned by several methods (e.g. co-catalyst loading, hybrid composite).

Ullmann cross-coupling between aryl iodides with electron-donating groups and aryl iodides with electro-withdraw groups could be realised over Pd@TiO<sub>2</sub> under irradiation of a two-colour system (**Scheme 2**)<sup>[36]</sup>. In the presence of only 368 nm ultraviolet A (UVA) irradiation, except the target cross-coupling product (10% selectivity), the other two byproducts homo-coupling product and dehalogenation product would generate too. However, adding 465 nm blue light-emitting diodes (LEDs) would result in rapid reactant conversion and enhanced cross-coupling selectivity (80% selectivity). According to the proposed mechanism, 368 nm light is responsible for initiating carbon-iodine (C–I) cleavage, while the 465 nm functions to transfer electrons from Pd NPs to the remaining iodide, hence tuning the selectivity.



Scheme 2 Proposed mechanism of the photocatalytic Ullmann cross-coupling reaction over  $Pd@TiO_2$  under UVA and visible light irradiation [36]

An interesting catalytic farming strategy using Pd-deposited TiO<sub>2</sub> NPs (Pd/TiO<sub>2</sub>) has been investigated<sup>[37]</sup>, where the photocatalytic Sonogashira coupling and Ullmann homocoupling of benzene iodides could be achieved under visible light and UV light irradiation, respectively. The photocatalytic performance of Sonogashira coupling dropped significantly after 2 cycles, indicating poor stability, while the activity of the Ullmann coupling reaction using the same photocatalyst well remained after 3 cycles. XPS showed that Pd<sup>2+</sup> was reduced during the Sonogashira coupling reaction. By performing Ullmann coupling afterwards, the Ullmann coupling solvent tetrahydrofuran (THF) could restore the oxidation state of reduced Pd<sup>0</sup>. Therefore, the stability of Pd/TiO<sub>2</sub> photocatalyst for Sonogashira coupling could be improved. The strategy is illustrated in **Scheme 3**. This catalytic farming strategy was further expanded to other reactions, such as alkene isomerisation and alkene hydrogenation, providing an innovative approach to prolonging catalyst lifetime.



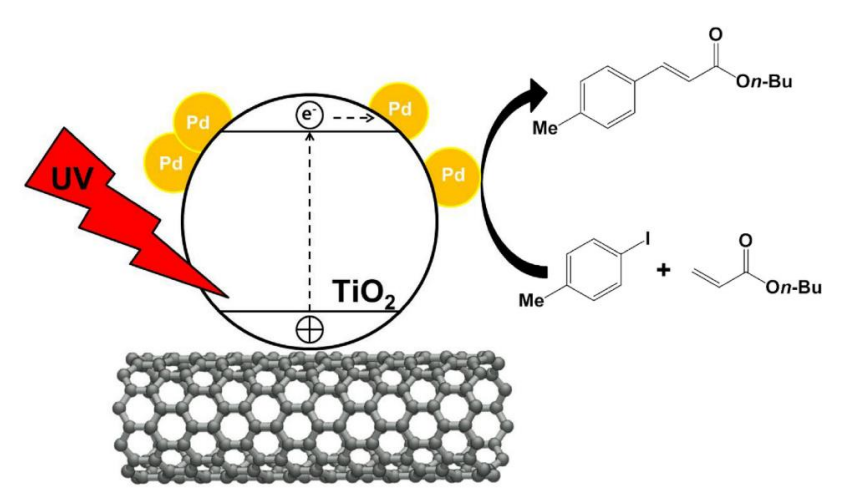
Scheme 3 Conversions (dark bars) of benzene iodides and yields (light bars) of biphenyl obtained after several catalytic cycles of reactions (A) and (B) and the demonstration of the catalytic farming cycle $^{[37]}$ 

A novel blended catalytic system consisting of  $TiO_2$  photocatalyst and a Pd-Au loaded aluminium oxide (Al<sub>2</sub>O<sub>3</sub>) bimetallic catalyst (Pd(2.0)Au(1.0)/Al<sub>2</sub>O<sub>3</sub>) has been reported<sup>[38]</sup>, and biaryls were

synthesised in methanol via Ullmann homo-coupling with 15-84% yields from different aryl halides after 1 h (8 examples; X=I, Br, Cl). The separation preparation of co-catalysts on Al<sub>2</sub>O<sub>3</sub> dramatically harnessed the production of byproduct arene compared to the direct co-catalyst loading on TiO<sub>2</sub> surface (**Scheme 4**).

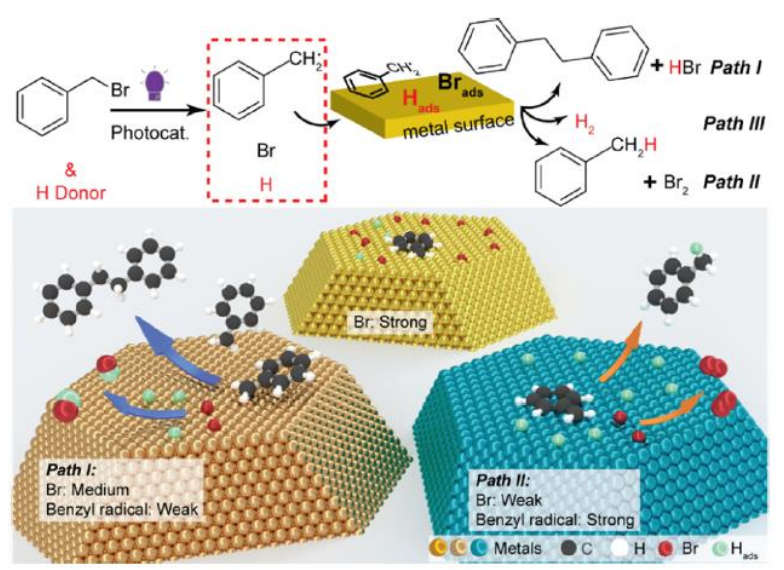
Scheme 4 Photocatalytic Ullmann coupling of iodobenzenes over a blended catalyst system<sup>[38]</sup>

A Pd-decorated TiO<sub>2</sub> and carbon nanotube composite (Pd-TiO<sub>2</sub>-CNT) was synthesised via a solgel method (**Scheme 5**)<sup>[39]</sup>. TiO<sub>2</sub> and Pd NPs were well dispersed on the surface of CNTs, and this photocatalyst exhibited good performance in driving Heck cross-coupling (6 examples, yield 87%-99%, DMF, 12 h) and decarboxylative coupling (8 examples, yield 45%-81%, DMSO, 12 h) of aryl iodides under UV irradiation. The enhanced nucleophilicity of Pd NPs and the synergy between TiO<sub>2</sub> and CNTs were responsible for the improved photocatalytic performance. A similar photocatalyst, Pd-doped mesoporous TiO<sub>2</sub> NPs (Pd/TiO<sub>2</sub>)<sup>[40]</sup>, was also reported for the Heck reaction of iodobenzene with styrene in dimethylformamide (DMF) under sunlight irradiation (9 examples, yield 76%-94%, 3 days).



Scheme 5 Proposed electron transfer process in the system during light activation<sup>[39]</sup>

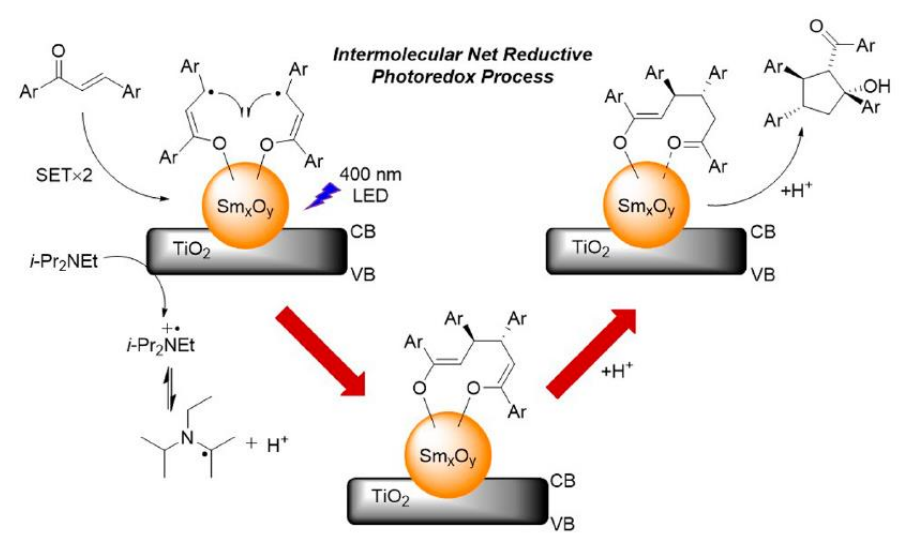
Copper is also a commonly used co-catalyst in photocatalytic organic transformation, and in some cases, Cu exhibits better selectivity compared to Pd. Bibenzyl was synthesised with a high yield (95%) and a remarkable apparent quantum efficiency (AQE) of 15% from benzyl bromide via a photocatalytic dehalogenative homo-coupling pathway over Cu-loaded TiO<sub>2</sub> upon 365 nm irradiation (water-isopropanol solution, 2 h) (**Scheme 6**)<sup>[41]</sup>. The co-catalyst selection was based on the density functional theoretical (DFT) calculation of adsorption energies of reaction intermediates (benzyl radical and Br atom) and 3 potential reaction paths in the system were studied using Pd/TiO<sub>2</sub> and Cu/TiO<sub>2</sub>.



Scheme 6 Illustration of reaction intermediates and pathways of dehalogenative coupling of benzyl bromide over  $\text{Cu/TiO}_{7}^{[41]}$ 

The above examples all follow the classical semiconductor photoexcitation mechanism, including the excitation of TiO<sub>2</sub> by UV light and the generation of photo-induced electron-hole pairs. Those excited electron-hole pairs then migrate to the loaded metal NPs (Pd, Cu etc.) on the surface of the semiconductors and then complete the chemical reactions, where the reaction pathway depends on the adsorption/desorption of substrate on the metal cocatalyst surface, indicating that metal cocatalyst loading plays an important role in product selectivity.

Single electron transfer (SET) is also a common mechanism in photocatalytic systems. For example, a samarium oxide nanoparticle-decorated titanium dioxide nanocomposite  $(Sm_xO_y@TiO_2 \text{ with } 4.7 \text{ wt\% } Sm)$  was reported to be an efficient photoredox-Lewis acid catalyst in achieving photoreductive cyclisations (70% yield) and [2+2] photocycloadditions (71% yield) under 400 nm irradiation (**Scheme 7**)<sup>[42]</sup>. The Lewis acidity of lanthanide could be harnessed and the catalyst-caused product contamination could also be eliminated.



Scheme 7 Proposed mechanism for the heterogeneous Lewis Acid catalytic reductive cyclization of trans-chalcones [42]

#### 2.6.2 Narrow bandgap semiconductor

#### 2.6.2.1 Metal oxides

Bismuth(III) oxide (Bi<sub>2</sub>O<sub>3</sub>) (bandgap 1.3 eV) was reported to successfully carry out atom transfer radical addition (ATRA) reactions between organo-bromides and different terminal olefins under visible light irradiation<sup>[43]</sup>. Compared to previous research results in homogeneous photocatalysis, this work offered a greener approach which required no participation of additives, and the loading amount of commercial Bi<sub>2</sub>O<sub>3</sub> was as low as 1% to offer good yields for ATRA products (18 examples, yield 45%-90%, DMSO).

Several semiconductors, such as bismuth vanadate (BiVO<sub>4</sub>), ferrimagnetism spinel ferrites (NiFe<sub>2</sub>O<sub>4</sub>) and tungsten trioxide (WO<sub>3-x</sub>), have been proven as suitable candidates to accommodate Pd NPs for the Suzuki Miyaura coupling (SMC) reaction under visible irradiation. Monoclinic BiVO<sub>4</sub> microspheres (bandgap 2.4 eV) were successfully synthesised<sup>[44]</sup>. Due to the pure monoclinic phase and larger grain size of BiVO<sub>4</sub> and improved surface charge transfer from Pd

loading, the Pd–BiVO<sub>4</sub> exhibited higher photocatalytic performance compared to other BiVO<sub>4</sub> catalysts. Furthermore, this photocatalyst exhibited excellent activity in the organic dyes decomposition and the SMC reaction of aryliodides (15 examples, yield 78%-94%, ethanol-water solution, 24 h) under irradiation from blue LEDs, providing a possibility of sustainable organic transformations using low energy density indoor light source.

Ferrimagnetism spinel ferrites (MFe<sub>2</sub>O<sub>4</sub>, M=Ni, Zn, Mn, Cu, Co) showed promising photocatalytic performance due to their narrow bandgaps near 2 eV. Pd-NiFe<sub>2</sub>O<sub>4</sub>/reduced graphene oxide (Pd-NiFe<sub>2</sub>O<sub>4</sub>/rGO) was developed, and this photocatalyst could be synthesised via a one-step green hydrothermal method (**Figure 3**)<sup>[45]</sup>. Due to efficient electron transfer, the heterojunction structure with Pd mediated on the interfacial layer exhibited significant photocatalytic activity improvement in the dyes degradation and SMC of a series of aryl halides (9 examples, yield 25%-99%, ethanol-water solution, 0.5-2 h). Moreover, this photocatalyst showed excellent recyclability and could be conveniently recovered by simply applying an external magnet.

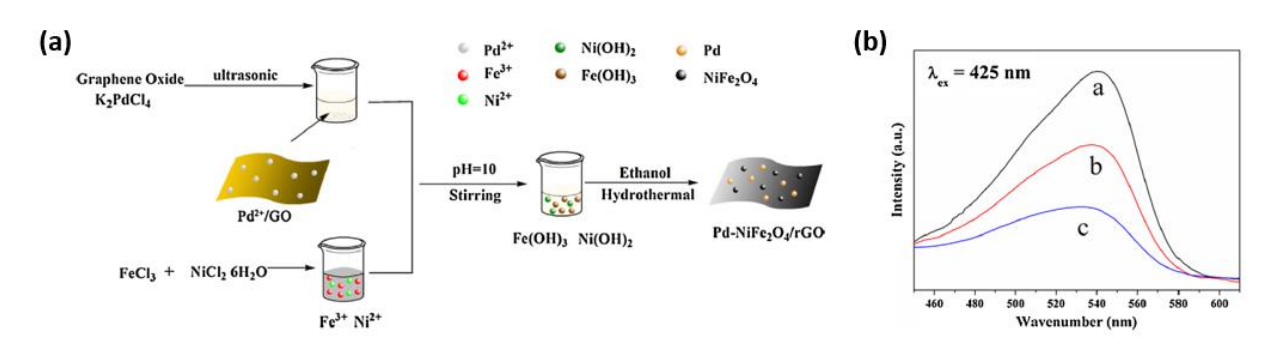
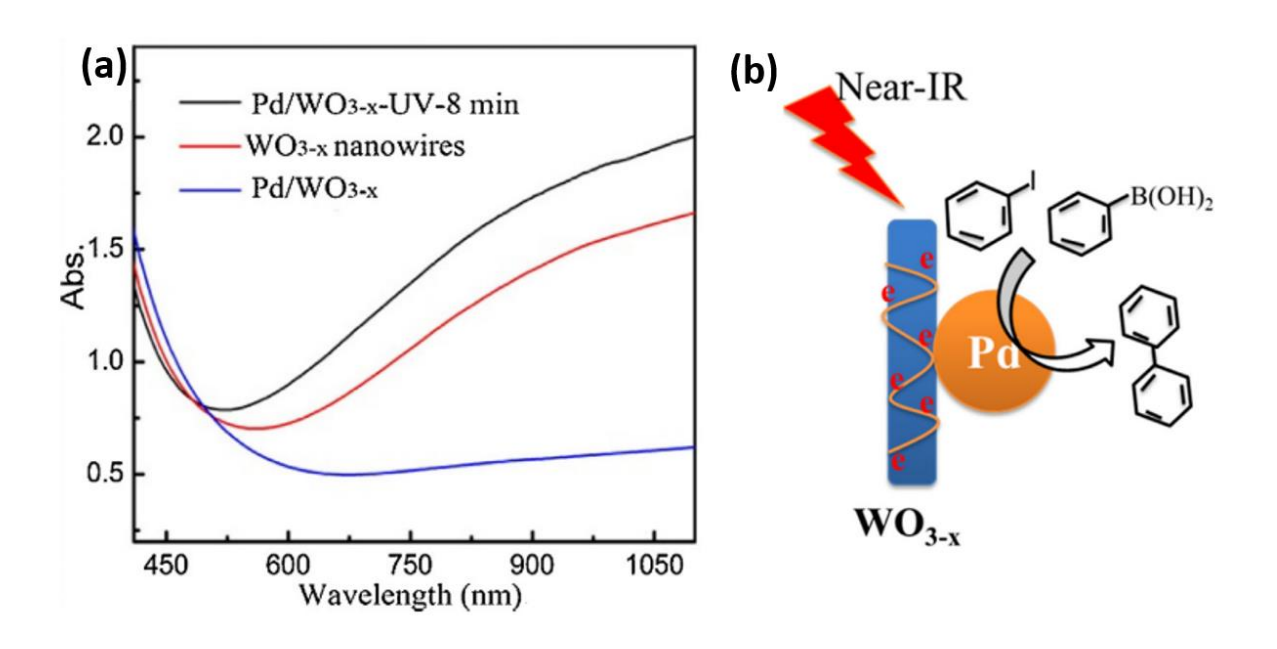


Figure 3 (a) Preparation process of Pd-NiFe<sub>2</sub>O<sub>4</sub>/rGO; (b) PL spectra of (a) pure NiFe<sub>2</sub>O<sub>4</sub>, (b) NiFe<sub>2</sub>O<sub>4</sub>/rGO-4, (c) Pd- NiFe<sub>2</sub>O<sub>4</sub>/rGO-4 upon 425 nm excitation<sup>[45]</sup>

 $WO_{3-x}$  nanowires exhibited strong plasmonic light absorption even in the near-infrared (NIR) region<sup>[46]</sup>. The strong absorption in the visible and near-infrared (NIR) region is a consequence of the collective oscillation of free electrons (from oxygen vacancies) on the surfaces of  $WO_{3-x}$ 

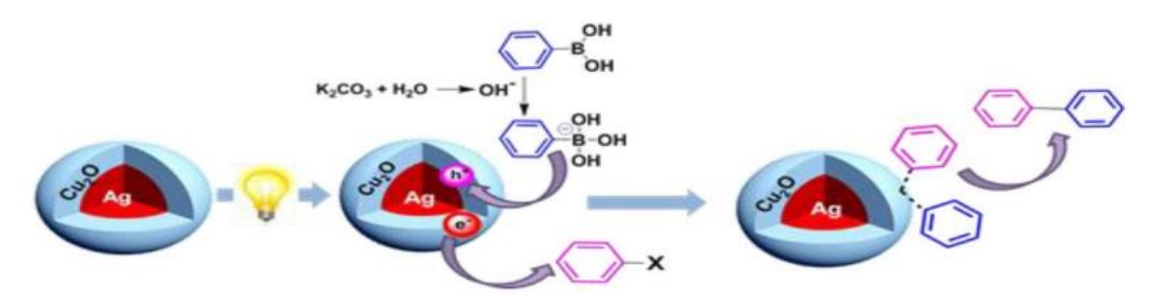
nanowires<sup>[47]</sup>. By loading Pd on WO<sub>3-x</sub> nanowires (Pd/WO<sub>3-x</sub> nanowires), this photocatalyst could greatly promote the SMC of iodobenzene under the long wavelength (>650 nm) irradiation (**Figure 4**). This performance could be attributed to the photothermal effect from the localised surface plasmon resonances (LSPR) on the surface of WO<sub>3-x</sub> nanowires and the third-party co-catalyst influenced by the LSPR, in this case, Pd metals. Unlike most other LSPR-related strategies that use LSPR metals in the system, this work provided a new LSPR-based strategy (LSPR metal oxide nanostructures) that can utilise near-infrared light for organic C–C formation.



 $\label{eq:continuous} Figure~4~(a)~Ultraviolet-visible~(UV-vis)~spectra~results~of~WO_{3-x}, Pd/WO_{3-x}~and~Pd/WO_{3-x}~after~8min~UV~irradiation;~(b)~Proposed~mechanism~of~SMC~reaction~over~Pd/WO_{3-x}^{[47]}$ 

In-situ generated Ag@Cu<sub>2</sub>O core-shell NPs have been reported as the first palladium-free catalyst for SMC in heterogeneous photocatalysis (bromobenzene, yield 75%, ethanol-water solution, 5 h)(**Scheme 8**)<sup>[48]</sup>, offering a cheap, easy-to-prepare system with reduced reaction time and

minimised side products for SMC and Suzuki type cross-coupling reactions under visible irradiation.



Scheme 8 Proposed mechanism of SMC reaction over Ag@Cu<sub>2</sub>O core-shell NPs<sup>[48]</sup>

#### 2.6.2.2 Metal sulfides

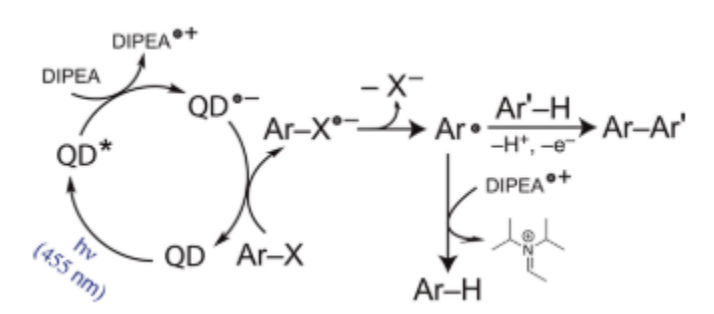
Metal sulfide is a big group of photocatalyst material, and most metal sulfides are visible light responsive with bandgaps smaller than  $3.0\,\text{eV}$ . Common metal sulfides, including cadmium sulfide (CdS), zinc indium sulfide (ZnIn<sub>2</sub>S<sub>4</sub>) and molybdenum disulfide (MoS<sub>2</sub>), have been proven to efficiently drive different organic C–C reactions upon visible light irradiation.

Semiconductor quantum dots have the advantages of homogeneous catalysts, such as high surface volume ratio and great homogeneity in reaction solvent, while maintaining the high stability of heterogeneous catalysts. CdS is a widely studied quantum dots (QDs), which plays an important role in synthesising core-shell QDs due to its excellent charge transfer and ideal band positions.

CdS QDs have been used and showed excellent ability in tuning the selectivity of benzyl alcohol to either benzaldehyde (99% selectivity) or C–C coupled products (primarily hydrobenzoin, 91% selectivity) after 10 h under 405 nm irradiation<sup>[49]</sup>. The selectivity to primary coupling product hydrobenzoin was achieved by in-situ photo-depositing more Cd<sup>0</sup> on the surfaces of QDs and also

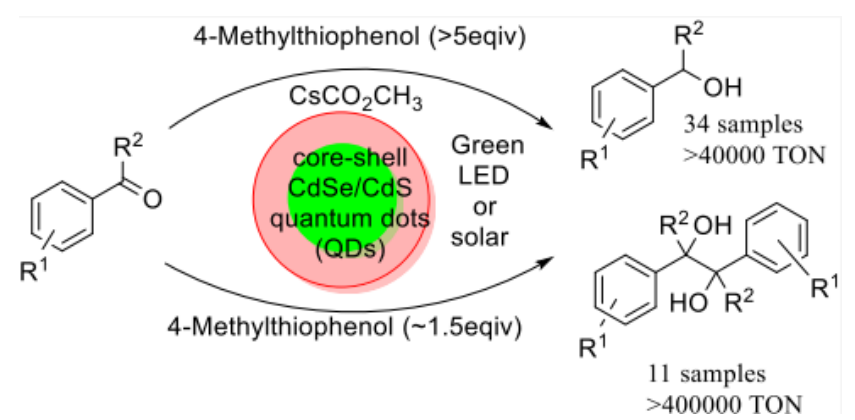
increasing benzyl alcohol concentration. The Cd<sup>0</sup> functions as an electron source to reduce benzyl alcohol to the radical intermediate and then form the coupling products. Quantum efficiency for both pathways was determined to be around 1%.

Zinc selenide (ZnSe)/CdS core/shell QDs were synthesised and this photocatalyst exhibited excellent activity for C–H arylation reactions of aryl bromides under 455 nm irradiation<sup>[50]</sup>. ZnSe/CdS core/shell QDs activated C–Br bond via a single electron transfer pathway and in the presence of a trapping reagent, such as substituted pyrroles, the benzene radical would couple with the trapping reagent instead of undergoing the dehalogenation pathway (4 examples, yield 36% - 42%, hexane, 48-76 h) (**Scheme 9**). This high performance was due to QDs' high surface area and homogeneity in the solvent.



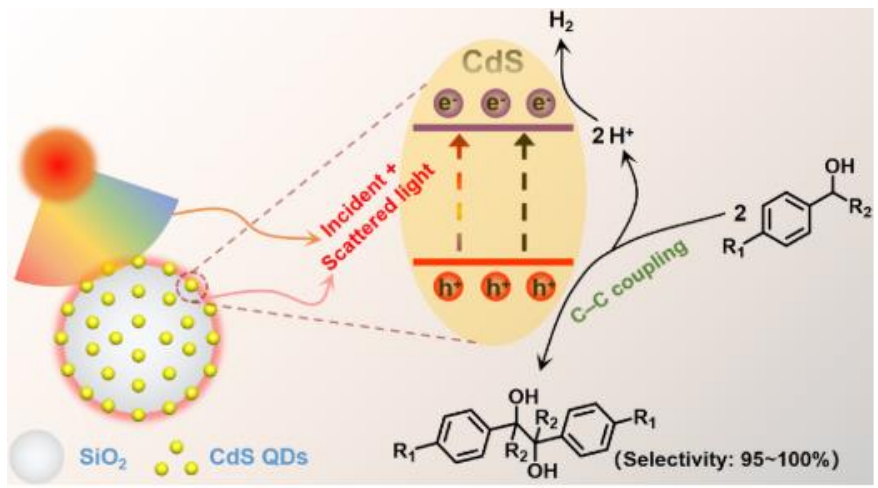
Scheme 9 Mechanism of visible light photoredox catalytic C–H arylation of aryl bromide over ZnSe/CdS core/shell QDs<sup>[50]</sup>

Pinacol coupling of aryl aldehydes and ketones (11 examples, yield 54% -99%) was achieved using cadmium selenide (CdSe)/CdS core-shell QDs as the photocatalyst under irradiation from green LEDs<sup>[51]</sup>. Thiophenols acted as both the hydrogen donor and hole scavenger, and the amount of thiophenols was critical in tuning the selectivity to either the hydrogenation product or pinacol coupling product (**Scheme 10**). The CdSe/CdS QDs had a turnover number as high as 400000 and could be reused up to 10 times without visible activity decay.



Scheme 10 Mechanism illustration for the hydrogenation and pinacol coupling of aryl aldehydes and ketones over CdSe/CdS QDs  $^{[51]}$ 

Silicon dioxide (SiO<sub>2</sub>)-supported CdS quantum dots (CdS/SiO<sub>2</sub>) were synthesised by assembling quantum dots onto the spherical SiO<sub>2</sub> to achieve light harvesting and efficient charge generations(**Scheme 11**)<sup>[52]</sup>. Photocatalytic hydrogen evolution with selective organic synthesis is attractive as both H<sub>2</sub> and value-added compounds can be generated at ambient conditions and this CdS/SiO<sub>2</sub> showed boosted hydrogen (H<sub>2</sub>) evolution and C–C coupling of benzyl alcohol into hydrobenzoin (6 examples, yield 52%-92%, MeCN, 12 h) under Xenon (Xe) lamp irradiation. Furthermore, this work offered a new design protocol by utilising a near-field scattering-promoted optical absorption model to manipulate the light-harvesting property of semiconductor QDs.

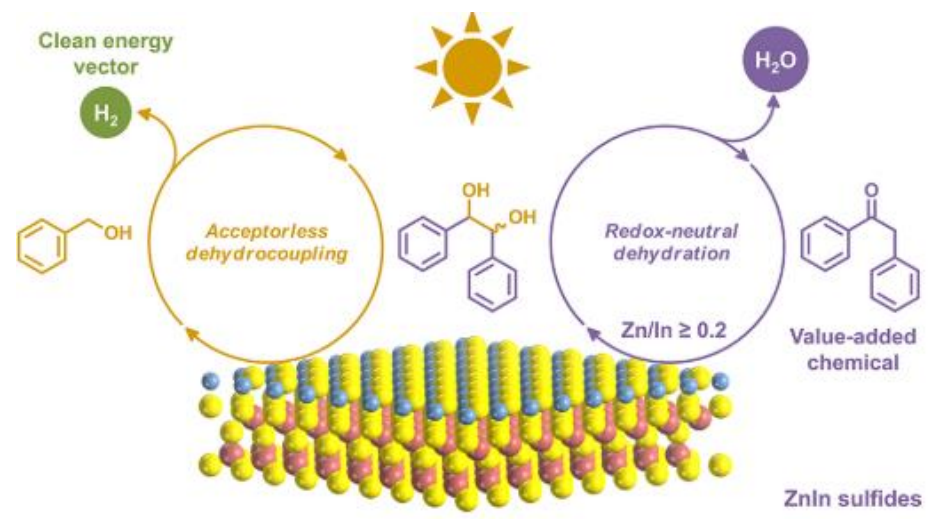


Scheme 11 Near-field scattering light harvesting model to enhance light absorption of CdS QDs for photocatalytic hydrogen evolution and C–C coupled hydrobenzoin over CdS/SiO<sub>2</sub><sup>[52]</sup>

ZnIn<sub>2</sub>S<sub>4</sub> nanosheets have also been reported to drive the pinacol coupling of aryl aldehydes under visible light irradiation (7 examples, yield 16%-99%, MeCN, 0.5-6 h)<sup>[53]</sup>. The 2D ZnIn<sub>2</sub>S<sub>4</sub> nanosheets were synthesised via a fast microwave-assisted solvothermal method, and such photocatalytic strategy could be applied to furfural to produce jet fuel precursor, hydrofuroin, exhibiting potential in practical applications (**Scheme 12**).

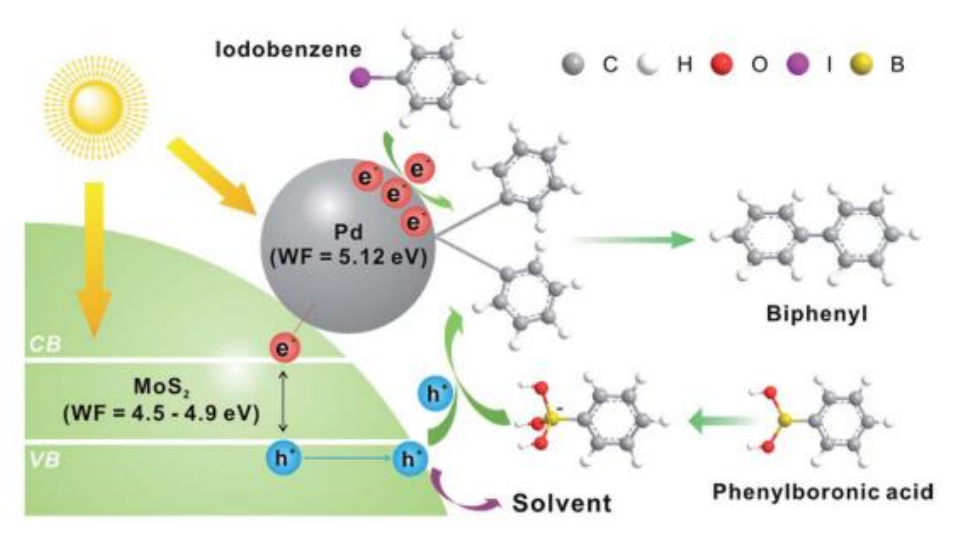
Scheme 12 Illustration for two reaction pathways of benzaldehyde transformation under light irradiation<sup>[53]</sup>

Another Zn<sub>x</sub>In<sub>2</sub>S<sub>3+x</sub> with various x also has been reported<sup>[54]</sup>. With a ratio of Zn<sub>0.6</sub>In<sub>2</sub>S<sub>3.6</sub>, the photocatalyst displayed high hydrogen production from benzyl alcohol under blue LEDs irradiation. By adjusting the conduction band bottom potentials of ZnIn sulfide catalysts, the generation of coupling products, deoxybenzoin (64% yield) or benzoin (61% yield), could be controlled in MeCN after 12 h. The key factor in tuning the selectivity to deoxybenzoin was to adjust the Zn/In ratio, and when it was greater than 0.2, the dehydrogenation of intermediate hydrobenzoin would happen, resulting in the production of dexoxybenzoin (**Scheme 13**).



Scheme 13 Illustration of the photocatalytic reaction pathways over  $Zn_xIn_2S_{3+x}^{[54]}$ 

A hybrid structure between  $MoS_2$  nanosheets (bandgap 1.9 eV) and Pd nanodots was developed and  $MoS_2$  nanosheets exhibited higher visible light absorption because of the higher dispersity and light-matter interaction in distilled water compared to  $MoS_2$  microsheets<sup>[55]</sup>. As a result, the Pd- $MoS_2$  photocatalyst could achieve the Suzuki-Miyaura coupling of iodobenzene and phenylboronic acid with a 95% yield (ethanol-water solution, 2 h) and an impressive TOF as high as 5100 h<sup>-1</sup> (**Scheme 14**).



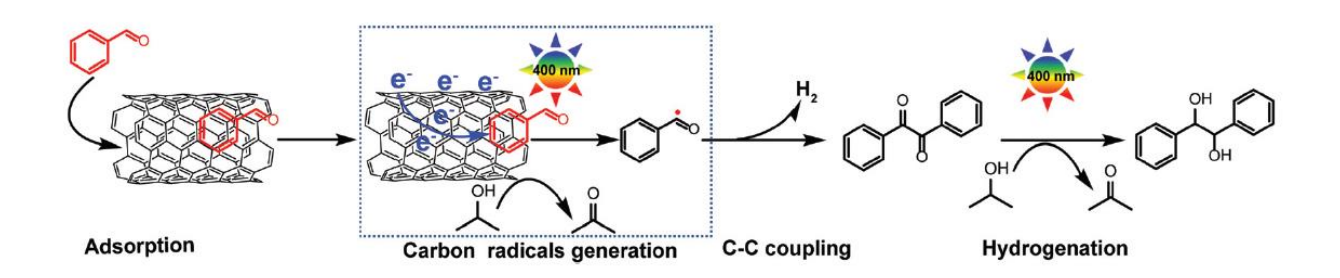
Scheme 14 Proposed mechanism of photocatalytic SMC over Pd/ MoS<sub>2</sub><sup>[55]</sup>

Pd NPs were loaded on exfoliated tungsten disulfide (2H-WS<sub>2</sub>) nanosheets<sup>[56]</sup>, producing extraordinary photocatalytic activity for SMC under visible light irradiation. Pd NPs were decorated via a sonic wave-assisted nucleation method without reductants, and a larger Pd size resulted in higher photocatalytic performance. The reaction solvent was also studied and protic organic solvents (e.g. methanol, ethanol and isopropanol) were proved more suitable for photocatalysed SMC than polar aprotic solvents (e.g. DMF, dimethyl sulfoxide), which were often recognised as more efficient in conventional SMC by Pd catalysts.

#### 2.6.2.3 Carbon materials

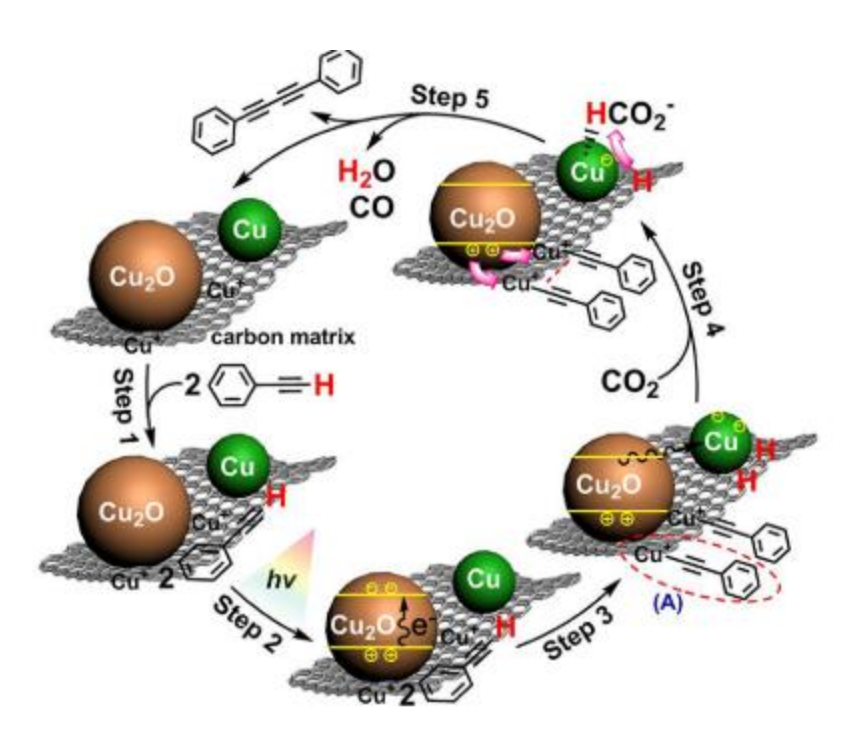
Carbon materials are suitable for heterogeneous catalysis due to their high stability, unique electronic properties, and tunable surface area. As a result, carbon nanotubes and other metalorganic frameworks (MOFs)-derived carbon/metal oxide composites have been developed for various photocatalytic C–C bond formations.

Metal-free carbon nanotubes have been reported to efficiently achieve pinacol coupling of benzaldehyde to produce chiral hydrobenzoins with > 87% yield (2-propanol, 6 h) under UV irradiation (320-400 nm)<sup>[57]</sup>. The mechanism has been studied and a photo-excited conduction electron transfer (PECET) was proposed, displaying the potential applications of CNTs in photosynthesis.



 $Cu_xO$  nanoparticles supported on carbon nanotubes ( $Cu_xO/CNT$ ) were developed<sup>[58]</sup>. Under dark conditions, Glaser homo-coupling of phenylacetylene was realised by this photocatalyst. However, the selectivity was tuned to Sonogashira coupling reaction upon light irradiation, which could be attributed to the cleavage of C–I bond on iodobenzene in the presence of light energy.

Core-shell Iron oxide (FeOx)@nitrogen-doped carbon cubes were synthesised to support Pd NPs for photocatalytic Ullmann homo-coupling reaction with oxidation of benzyl alcohol<sup>[59]</sup>. The support FeOx@Nitrogen doped carbon (FeOx@N-C) core-shell cubic nanostructure was fabricated by annealing Fe<sub>2</sub>O<sub>3</sub>@ZIF-8 under inert gas. The catalyst could easily be separated from the solution by applying an external magnetic field and it could be reused for up to 6 cycles without visible decay. Homo-coupling of terminal alkynes was achieved using a composite of Cu@In<sub>2</sub>O<sub>3</sub> core-shell structure on N-doped graphitic carbon cuboctahedral cages (Cu@In<sub>2</sub>O<sub>3</sub>@N-C)<sup>[60]</sup>. The structure was obtained upon carbonization of the In-loaded Cu-MOF-199, and excellent performance of homo-coupling of various alkynes over this Cu-included composite was examples, yield over 90%). observed(7 Graphitic-Carbon-layer-supported Cu-Cu<sub>2</sub>O nanocomposites (Cu-Cu<sub>2</sub>O-C) were synthesised using Cu-MOF-74 as precursor. Photocatalytic coupling reaction of phenylacetylene was observed over Cu-Cu<sub>2</sub>O-C with CO<sub>2</sub> as the oxidant (Scheme 16)<sup>[61]</sup>. The synergistic effect was the key for such 3 components consisted nanocomposite in photocatalytic C–C bond formation, including strong interaction between active sites and carbon support, enhanced charge separation and transfer and improved substrate adsorption.



Scheme 16 Proposed mechanism of photocatlytic coupling reaction of phenylacetylene over Cu-Cu<sub>2</sub>O-C<sup>[61]</sup>

#### 2.6.2.4 Other inorganic materials

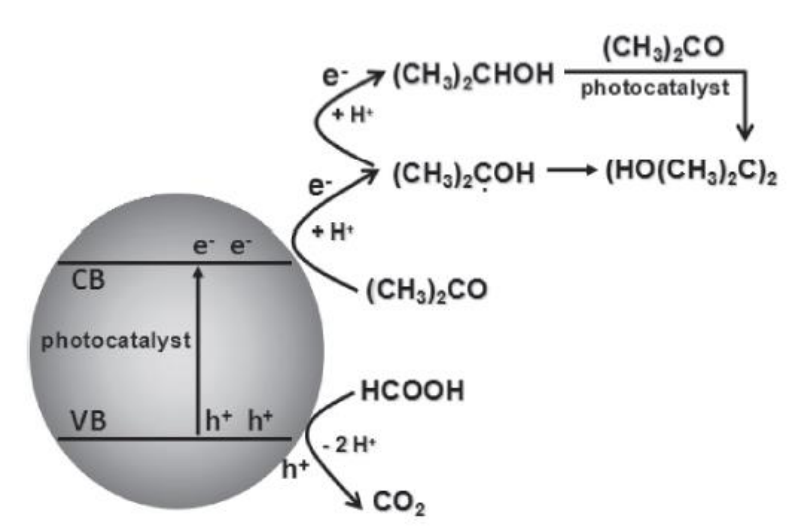
Perovskites are a class of semiconductors that have been underdeveloped in photocatalytic organic transformations. Compared to traditional semiconductors, they can offer inherent advantages such as easy recoverability and larger particle size.

Lead halide perovskites (CsPbBr<sub>3</sub>) have been reported for the first time as suitable photosensitisers for synthesising bibenzyl from benzyl bromide (83% yield, toluene, 20 h) under 447 nm irradiation at ambient conditions with TON as high as 17500<sup>[62]</sup>. These examples broadened the applicability and showed the potential of perovskite materials in photocatalysis.

Perovskites have also been reported to achieve C–C coupling reactions under UV light irradiation. Au nanoparticle functionalised potassium niobium oxide (AuNP/KNb<sub>3</sub>O<sub>8</sub>) has been synthesised<sup>[63]</sup>. It showed great photocatalytic activities for Ullmann homo-coupling of a series of substituted iodobenzenes (5 examples, yield 66%-99%, ethanol, 1-24 h) under UVA irradiation. Furthermore,

this AuNP/KNb<sub>3</sub>O<sub>8</sub> could be reused for up to three runs, offering a cost-effective alternative for organic coupling reactions and extending the photocatalytic application of perovskites.

The pinacol coupling of acetone has also been investigated. The reaction was carried out using formic acid as the hydrogen source over sodium tantalum trioxide (NaTaO<sub>3</sub>) or sodium titanate (Na<sub>2</sub>Ti<sub>3</sub>O<sub>7</sub>) under 365 nm irradiation<sup>[64]</sup>, and the selectivity to 2,3-dimethyl-2,3-butanediol over these two photocatalysts were 56% and 39%, respectively. The generation of carbon monoxide (CO) from formic acid decomposition could be alleviated in the presence of acetone (**Scheme 17**).

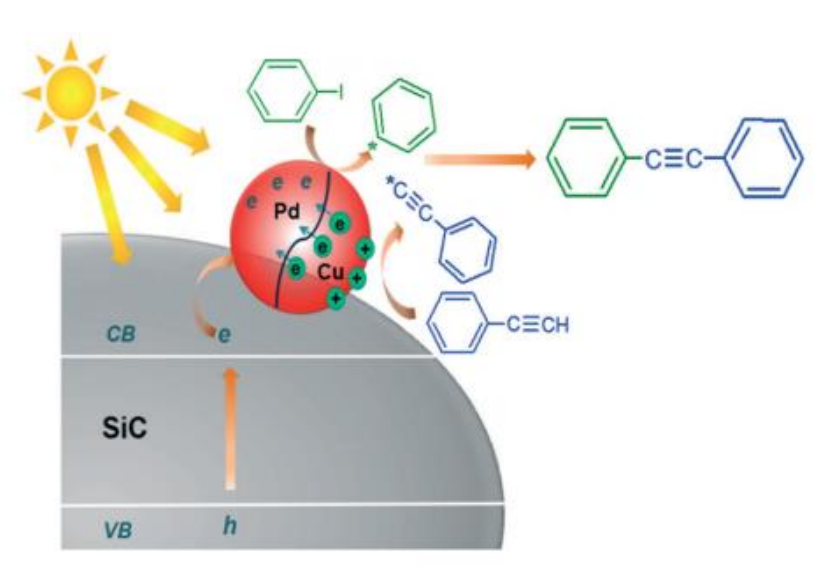


 $Scheme\ 17\ Proposed\ mechanism\ of\ the\ photocatalytic\ hydrogenation\ coupling\ of\ acetone\ into\ 2,3-dimethyl-2,3-but ane diol^{[64]}$ 

Silver-decorated silver bromide (Ag-AgBr) exhibited high visible light absorption due to the narrow bandgap of AgBr (2.6 eV) and the localised surface plasmon resonance (LSPR) of Ag NPs<sup>[65]</sup>. Palladium NPs and graphene oxide were both decorated onto the Ag-AgBr to synthesise the plasmonic composite GO-Pd@Ag-AgBr for efficient SMC of aryl halides (14 examples, yield 6%-99%, ethanol, 0.5-2 h) under Xe lamp irradiation equipped with a 400 nm long pass filter. The influence of different wavelength ranges was studied by applying different cut-off filters, and 400-

510 nm, 510-570 nm and 570-620 nm were responsible for 12.2%, 44.4% and 38.9% of the product yield, respectively.

Cubic silicon carbide ( $\beta$ -SiC) has a narrow bandgap of 2.4 eV, which made it a suitable candidate for visible light driven organic transformation. A Mott-Schottky heterojunction consisting of Pd NPs and  $\beta$ -SiC has been developed for the SMC reaction (11 examples, yield 50%-99%, DMF-water solution, 80 min-5 h)<sup>[66]</sup>. Upon visible light irradiation, the intrinsic catalytic activity of Pd was significantly improved due to the fast Mott-Schottky charge transfer (photo-electrons), and electron-rich Pd NPs were responsible for the cleavage of C–X (X=I, Br) in aryl halides while SiC activated the C–B bond in phenylboronic acids (TOF 1053 h<sup>-1</sup>, selectivity 100%). This Pd/SiC photocatalyst was applied to Sonogashira reaction of aryl halides and desired corresponding coupling products were successfully synthesised (14 examples, yield 40%-97%, DMF, 8-12 h)<sup>[67]</sup>. SiC materials were then further studied by the same group, and Pd<sub>3</sub>Cu<sub>1</sub> alloy was prepared and loaded onto SiC (Pd<sub>3</sub>Cu<sub>1</sub>/SiC) for visible light Sonogashira C–C cross-coupling reaction. Enhanced activity was attributed to the synergistic effect between Pd and Cu (Scheme 18).



Scheme 18 Proposed mechanism of the photocatalytic Sonogashira C–C cross-coupling reaction over  $Pd_3Cu_1/SiC^{[67]}$ 

Considerable attention to layered double hydroxides (LDHs) has been drawn due to their applications in photocatalysis. With a bandgap of 2.47 eV, ZnCr layered double hydroxide (LDH) was hybridised with graphene oxide (GO) and tested for photocatalyzed C–C coupling reactions. After decorating AuPd alloy on its surface, robust SMC reaction activity could be observed over this GO/LDH@AuPd material<sup>[68]</sup>. Such blended architectured composite structure enhanced the roles of individual components in the photocatalytic process.

#### 2.6.3 Methods to improve inorganic photocatalysis

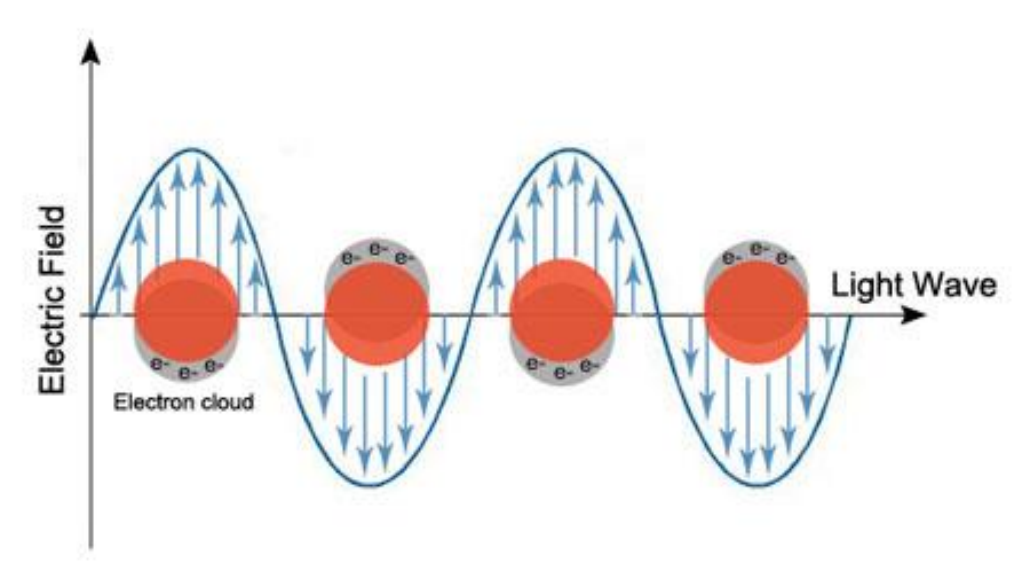
Based on the solar radiation spectrum, visible and infrared light takes up more than 90% of solar energy. UV photons also carry more energy than visible light, resulting in unselective photochemical pathways, lowering the selectivity of desired products<sup>[69–71]</sup>. Due to the two reasons, in recent years, some research interests in heterogeneous photocatalytic C–C coupling reactions have shifted to the visible region because the low energy of visible light can allow broad use in diverse settings and achieve organic transformations under mild conditions.

However, wide bandgap semiconductors such as  $TiO_2$  can only absorb light within the ultraviolet (UV) region, which means all the solar energy from visible light and infrared light is wasted. It is desired to modify wide bandgap semiconductor photocatalysts to enable better visible light responses, thereby improving solar energy utilisation and expanding their applications in the visible region.

Three strategies are often utilised to grant these wide bandgap semiconductors visible responding properties: (1) Localised surface plasmon resonances (LSPR) effect; (2) Interband transitions; (3) Band engineering.

#### 2.6.3.1 Localised surface plasmon resonances

Localised surface plasmon resonances (LSPR) is an effect between light and NPs with a particle size comparable to or smaller than the incoming light, resulting in the collective electron density oscillating to form a surface resonance (**Figure 5**).

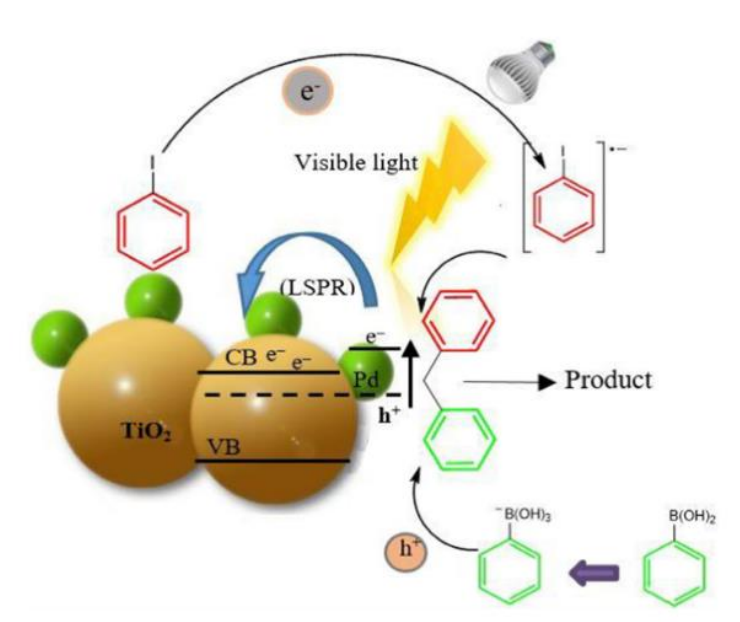


 $Figure \, 5 \, Mechanism \, of \, LSPR \, when \, light \, incident \, on \, a \, \, metal \, nan oparticle \, causes \, the \, conduction \, band \, electrons \, to \, oscillate$ 

The most commonly used LSPR metals are gold, silver and copper due to their extensively studied LSPR effect in the visible region. Palladium has been proven as a suitable co-catalyst on wide bandgap semiconductors for different organic C–C coupling reactions under UV irradiation. However, several photocatalysts, such as Pd/TiO<sub>2</sub><sup>[72,73]</sup> and Pd/ZnO<sup>[74]</sup>, have been reported to

successfully drive SMC reaction, Ullmann coupling reaction, Buchwald-Hartwig coupling reaction and Hiyama cross-coupling reaction under visible light irradiation. Pd NPs mainly exhibit high LSPR effects within the deep UV region<sup>[75]</sup>, but more evidence has been found that the LSPR position of Pd could be red-shifted depending on the particle size and local environment<sup>[76]</sup>.

For example, TiO<sub>2</sub> is a semiconductor with a 3.2 eV bandgap, which cannot absorb light energy in the visible region. By anchoring Pd NPs on TiO<sub>2</sub>, the Pd/TiO<sub>2</sub> photocatalyst was able to afford SMC reaction<sup>[72,77]</sup>. The scheme is illustrated in **Scheme 19**, where through LSPR effects, the photogenerated electrons could migrate from Pd NPs to TiO<sub>2</sub> conduction band to break the carbon halogen bond while the arylboronic acids were oxidised by the positively charged holes. The single electron transfer process was also promoted by Mott–Schottky heterojunction between the Pd-TiO<sub>2</sub> interface, which enhanced the LSPR of Pd NPs in the visible region, therefore offering higher activity. The size of palladium (in the size range of 20–30 nm) played a significant role in redshifting its LSPR position to around 500 nm.



Scheme 19 The proposed reaction mechanism for the SMC reaction over Pd/TiO<sub>2</sub><sup>[72]</sup>

Gold is one of the most used LSPR metals. However, the control experiments in publications suggested that Au NPs could not carry out organic C–C coupling reactions on their own in photocatalysis. Conversely, Palladium exhibits excellent catalytic properties but in most cases, Pd has a weak visible light absorption. In order to test the potential synergy between Pd and Au to achieve organic C–C coupling under visible light irradiation, a series of Au/Pd plasmonic bimetallic or alloy nanostructure have been decorated on wide bandgap semiconductors (TiO<sub>2</sub><sup>[78],[79]</sup>, cerium(IV) oxide<sup>[80]</sup>, zirconium dioxide<sup>[75],[81],[82]</sup>) and SiO<sub>2</sub><sup>[83]</sup>,

Plasmonic Au-Pd alloy decorated TiO<sub>2</sub> has been synthesised to drive the SMC of iodobenzene substrates under irradiation from blue LEDs (11 examples, yield 14% -94%, ethanol-water solution, 5 h)<sup>[78]</sup>. The synergy of each co-catalyst both contributed to the activity as the strong LSPR from Au enhanced the visible light absorption while Pd promoted the break of the carbon-halogen bonds. Pd and Au were loaded on the surface of porous nanorods cerium(IV) oxide (PN-CeO<sub>2</sub>)<sup>[80]</sup>, and this multifunctional Pd/Au/PN-CeO<sub>2</sub> was reported to be the first example to efficiently achieve SMC of aryl chlorides at ambient temperatures under irradiation in the visible region (5 examples, yield 15.3%-98.3%, DMF, 0.5-6 h), and the synergies between each component were responsible for this high performance. By conducting the experiments at each wavelength (400 nm to 650 nm) for 6.5 h, the yields of biphenyl were highly correspondent to the LSPR absorptions of Au NPs. Since Au/PN-CeO<sub>2</sub> alone could not achieve satisfying yields for SMC reaction, it was reasonable to suggest that Au was a visible light absorber and the excited photo-electrons were transferred from Au NPs to Pd NPs to enhance the photocatalytic activity. Compared to commercial CeO<sub>2</sub>, the PN-CeO<sub>2</sub> with strong basicity exhibited weak visible light adsorption, and LSPR of Au was believed to be the major electron source (Figure 6). Also, DFT calculation was carried out to prove the activation of chlorobenzene on the surface of Pd NPs. Compared to the C-Cl bond length of

1.760 Å in the gas phase, the C–Cl bond length of chlorobenzene adsorbed on the surface of Pd cluster (Pd<sub>6</sub>) and negatively charged Pd cluster (Pd<sub>6</sub><sup>-</sup>) was 1.779 Å and 1.826 Å, respectively, suggesting the advantage of negatively charged Pd cluster on activating chlorobenzene. Mulliken population analysis was conducted to further prove the electron transfer between Pd and chlorobenzene. -0.208 e of the Mulliken charge was obtained for the chlorobenzene/Pd<sub>6</sub><sup>-</sup> model, indicating electrons were transferred from Pd<sub>6</sub><sup>-</sup> to chlorobenzene.

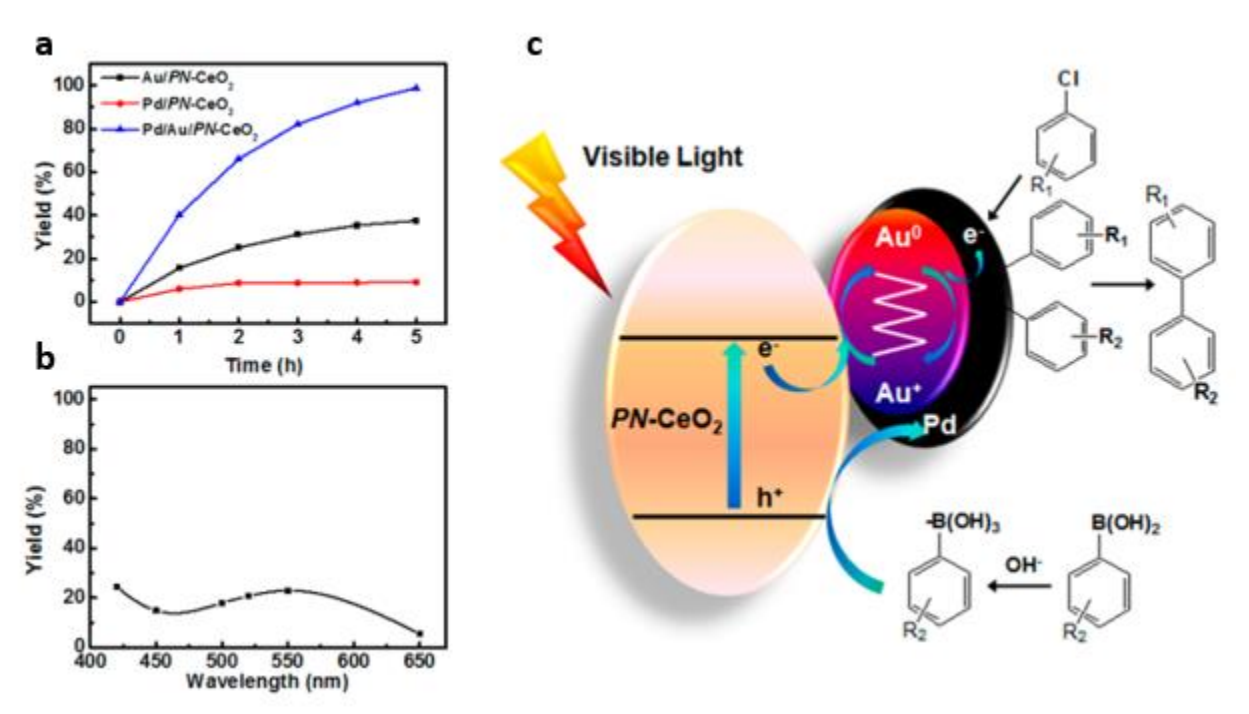
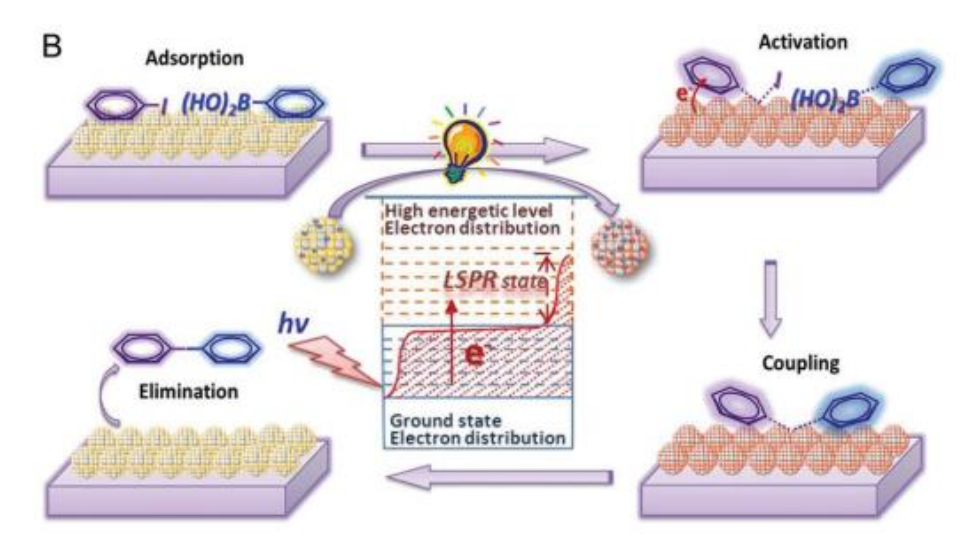


Figure 6 (a) temporal study of biphenyl yield by various catalysts; (b) The wavelength-dependent study on the yield of biphenyl; (c) Proposed photocatalytic reaction mechanism over the  $Pd/Au/PN-CeO_2$  catalysts under visible irradiation<sup>[80]</sup>

The first visible-driven heterogeneous photocatalytic SMC was reported in 2013, where Palladium and Gold NPs were deposited on the surface of zirconium dioxide (ZrO<sub>2</sub>) (4 examples, yield 86%-96%, DMF-water solution, 2-22 h)<sup>[75]</sup>. Apart from the SMC reaction of iodobenzene, other reactions, such as selective oxidation of aromatic alcohols to corresponding aldehydes and ketones,

phenol oxidation and oxidative addition of benzylamine, could also be achieved using this Au-Pd@ZrO<sub>2</sub>. Due to the wide bandgap of ZrO<sub>2</sub> (5 eV), it was assumed that ZrO<sub>2</sub> did not contribute to the activity. The loading of Au provided strong LSPR in the visible region, and therefore the hot electrons transferred to Pd would dramatically enhance the intrinsic catalytic activity of Pd. The highest quantum yield of this Au-Pd@ZrO<sub>2</sub> under visible irradiation could reach 8.1%, which was much higher than the TiO<sub>2</sub> in the UV region (1.5%), providing new insight into utilising Au LSPR with other transition metals for various organic reactions in photocatalysis.

This bimetallic Au-Pd decorated ZrO<sub>2</sub><sup>[81]</sup> was reported later by another group for the SMC of aryl halides with a broader substrate scope (13 examples X=I, Br, yield 25% -99%, DMF-water solution, 2-22 h) and a deeper investigation of the reaction mechanism using density functional theory (DFT) calculations (Scheme 20). After generating hot electrons from the LSPR effect under visible light irradiation, the adsorption of reactant molecules on NPs would be enhanced due to the large surface charge heterogeneity. The oxidative addition of aryl halide was well-known to be the ratedetermining step for SMC, and after conducting DFT on the electron transfer from the NPs' surface to iodobenzene, the result suggested that when the molecule received an electron, the C-I bond length would elongate from 0.214 nm to 0.3 nm, indicating an easier cleavage. The same group further extended the applications of this Au-Pd/ZrO<sub>2</sub> to various organic C-C coupling reactions under irradiation in visible region<sup>[82]</sup>, including Sonogashira coupling, Stille coupling, Hiyama coupling, Buchwald-Hartwig coupling and Ullmann coupling (22 examples, yield 15%-99%). Given that Au NPs alone could not achieve most of the reactions, it could be evidently suggested that Pd NPs were the active species, and photo-electrons induced carbon halogen bond cleavage occurred on the surface of Pd NPs instead of Au NPs.



Scheme 20 Proposed mechanism for photocatalytic SMC reaction over Au-Pd/ZrO $_2$  under visible light irradiation  $^{[81]}$ 

Hybridization of plasmonic metal NPs and Pd catalytic sites could also work on silica materials.

Pd-Au/SiO<sub>2</sub> hybrid catalyst was synthesised, and Au nanorods were proven to efficiently enhance the Pd-induced SMC reaction under visible light irradiation<sup>[83]</sup>. The Pd-Au-SiO<sub>2</sub> samples with different Pd/Au ratios were investigated as the optical properties and exposure of active species was highly dependent on the ratio of Pd/Au. Silver is an alternative plasmonic metal in such bimetallic system, and enhanced activity in SMC reaction was observed over this Pd/Ag decorated mesoporous silica (Pd/Ag/SBA-15)<sup>[84]</sup>.

Two possible mechanisms are behind these plasmonic bimetallic nanostructures in photocatalytic C–C bond formation under visible light illumination. One is the direct hot-electron transfer and the other is the near-field enhancement effect. For the above examples of plasmonic bimetallic or alloy decoration, the plasmonic Au NPs and catalytic Pd sites directly contacted each other, indicating a direct transfer of hot electrons from the LSPR effect to the conduction band of the active catalyst under visible irradiation. Near-field enhancement was therefore studied to fully understand the mechanism in this plasmonic system.

Antenna–reactor system of Pd/SiO<sub>2</sub>/Au/ZrO<sub>2</sub> was prepared where a 2 nm thick SiO<sub>2</sub> layer was added between Pd and Au to prevent direct hot-electron transfer (**Figure 7**)<sup>[85]</sup>. The near-field enhancement effect was studied in two categories: (1) between Au NPs and Pd NPs; (2) between Pd NPs and substrates. The activity of SMC reaction could be dramatically enhanced under visible light irradiation in the presence of Au NPs (situation 1), but the reaction would be suppressed with excessive Au loading potentially by the interaction between the neighbouring electromagnetic hot spots (situation 2). Moreover, reaction enhancement was more obvious for substrates with higher electron cloud density at Pd sites, offering enriched knowledge regarding the near-field enhancement effect in photocatalytic reactions.

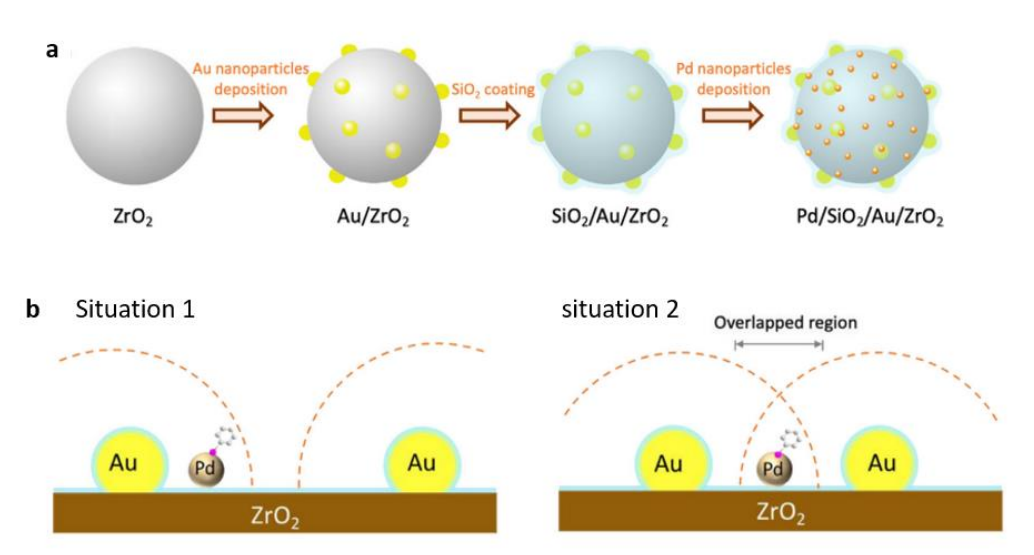


Figure 7 (a) Preparation process of  $Pd/SiO_2/Au/ZrO_2$ ; (b) Simulation of two situations in near-field enhancement<sup>[85]</sup>

The utilization of plasmon-induced hot-electron can be further improved by adding reduced graphene oxide (rGO) interface between Au and Pd<sup>[86,87]</sup>. Two interface-controlled photocatalysts Pd-rGO-AuNPs and Pd/Au@rGO-10/SiO<sub>2</sub> have been developed and both systems exhibited higher photocatalytic performance for SMC reaction in the presence of rGO layer. The function of

rGO was believed to be an electron mediator between Au and Pd and the excellent conductivity of rGO could intensively accelerate hot electron transfer.

#### 2.6.3.2 Interband transitions

Apart from LSPR effects, some previous research works have found that the visible light harvesting of metals originated from interband transition. The supported Pd NPs on different wide bandgap materials were screened for Sonogashira C–C coupling, namely, titanium dioxide (TiO<sub>2</sub>), niobium oxide (Nb<sub>2</sub>O<sub>5</sub>) and carbon nanodiamond (CND)<sup>[88]</sup>. Excellent activity was achieved from iodobenzene under 465 nm irradiation at mild temperature, which could be attributed to the excited electrons from interband transition of Pd NPs on the surface.

The interband electronic transitions of nonplasmonic transition metals (Pd, Pt, Ir and Rh) were investigated in detail(**Figure 8**)<sup>[89]</sup>. The metal NPs were dispersed on  $ZrO_2$  powder (M@ $ZrO_2$ ) because  $ZrO_2$  could only absorb light shorter than 370 nm. Light irradiation clearly enhanced the catalytic performance of all the metal NPs for the benzylamine coupling reaction. The activity under visible light irradiation meant M@ $ZrO_2$  samples had visible absorption, which was from the bound electrons exciting individual electrons to high energy levels ( $\psi_g$  to  $\psi_{hv}$ ). This was the interband electronic transition from those noble metals, and if the excited electron had sufficient energy, it would break through the energy barrier and jump to the lowest unoccupied molecular orbital of a reactant molecule which was adsorbed on the metal surface. Longer wavelengths would cause a decreased energy in the excited electron, but it could contribute to the reaction through photothermal effect. This nonplasmonic photocatalyst set was also extended to other reactions including SMC reaction and enhanced activity was realised due to the interband transitions.

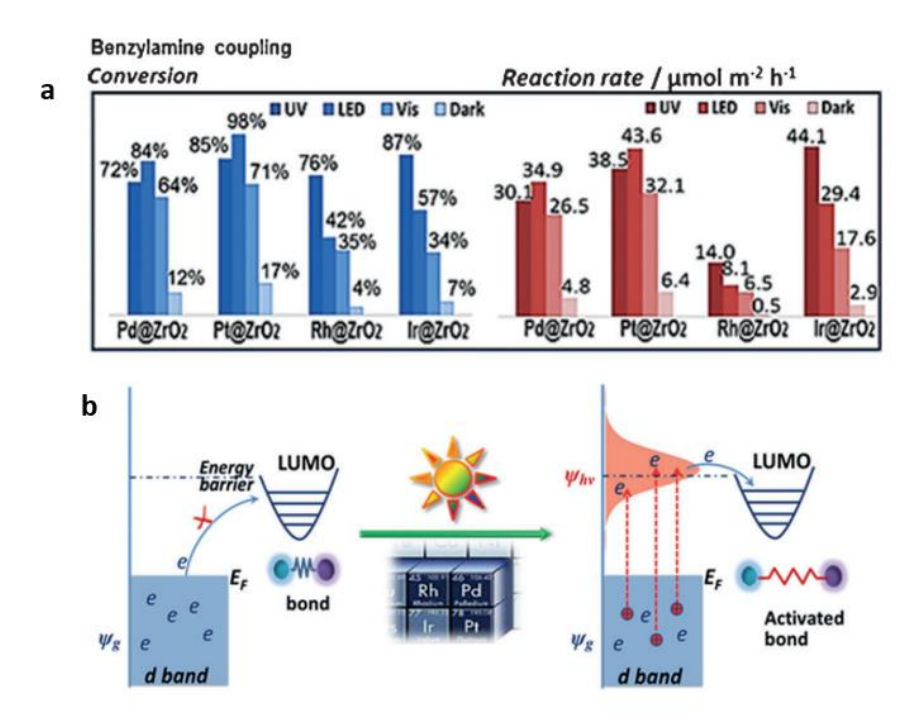


Figure 8 (a) Enhanced catalytic performance of metal NPs on  $ZrO_2$  support as a result of irradiation with UV light and with visible light from an incandescent lamp and an LED lamp for benzylamine coupling reaction. (b) Proposed mechanisms of the photocatalytic reactions with nonplasmonic metal NP photocatalysts [89]

### 2.6.3.3 Band engineering

The band engineering approach can modify the bandgap of wide bandgap semiconductors, therefore offering visible light absorption property, and doping is a commonly used method for such purposes.

A phosphorus-doped TiO<sub>2</sub> photocatalyst (2P-TiO<sub>2</sub>-500) was fabricated<sup>[90]</sup>. After calcination, this boric acid-induced hydrolysis of tetrabutyl titanate could produce well-distributed P-TiO<sub>2</sub> NPs in the presence of triphenylphosphine. According to the Tauc plot from UV–vis diffuse reflectance spectra, the bandgap of 2P-TiO<sub>2</sub>-500 reduced from 3.2 eV to 2.98 eV compared to commercial TiO<sub>2</sub>, thus enabling visible light absorption. Photocatalytic oxidative coupling of benzylamines could be realised under blue LED irradiation (7 examples, yield 85%-100%, MeCN, 6.5 h) (Scheme 21).

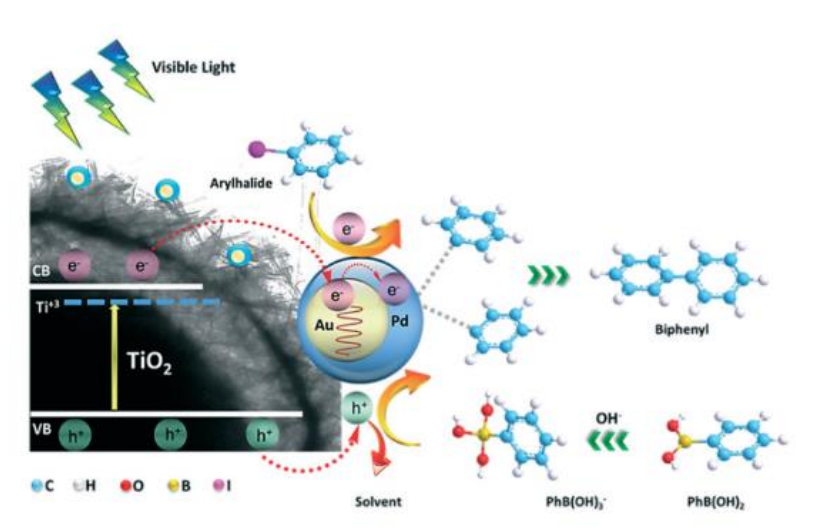
Scheme 21 Photocatalytic selective oxidation of primary amines to imines over O<sub>2</sub> by 2P-TiO<sub>2</sub>-500<sup>[90]</sup>

Anionic nitrogen doping in TiO<sub>2</sub> structure (N-TiO<sub>2</sub>) is also an effective strategy to boost light absorption in the visible region. N-doped yellow TiO<sub>2</sub> (N-TiO<sub>2</sub>-30) hollow spheres were developed<sup>[91]</sup>. The inner hollow architecture could enhance surface area and also provide a microreactor environment. A gram scale of esterification of alcohol and N-hydroxyimides to active esters was achieved in a one-pot reactor by this photocatalyst under visible illumination (15 examples, yield 20%-92%, MeCN, 18-24 h) (**Scheme 22**).

Scheme 22 Esterification of NHI with alcohol over N-TiO<sub>2</sub>-30<sup>[91]</sup>

Surface egineering is another way to decrease bandgap of semiconductors. a hydrogenated urchin-like yolk@shell TiO<sub>2</sub> was synthesised and decorated by Au and Pd (HUY@S-TOH@AuPd)<sup>[79]</sup>. the Ti<sup>3+</sup> on the surface could decrease the bandgap of TiO<sub>2</sub> and enable visible light adsorption. Meanwhile, The urchin-like structure dramatically improved surface area for both light harvesting and co-catalyst anchoring, and the yold@shell mesoporous structure enhanced the multiple scattering thus improving the light absorption (**Scheme 23**). Pd received photo-electrons from hydrogenated titania (minor), and with the hot electrons injected from LSPR of Au NPs (major),

the rate-determining step was further accelerated. Therefore high photocatalytic performance of SMC (18 examples, yield 61%-99%, ethanol-water solution) was achieved under visible light irradiation with a TOF as high as 7095 h<sup>-1</sup>.



 $Scheme~23~Mechanism~of~photocatalytic~Suzuki-Miyaura~coupling~reaction~over~HUY@S-TOH/AuPd~under~visible~irradiation^{[79]} \\$ 

### 2.7 Organic materials for organic C–C coupling reactions

The research works mentioned above are mainly inorganic materials with different modifications for photocatalyzed C–C coupling reactions. In recent years, different organic materials (conjugated polymers etc.) have been reported to act as outstanding supports for a variety of coupling reactions under light irradiation.

#### 2.7.1 Carbon nitride

Conjugated carbon nitride  $(C_3N_4)$  is a typical organic polymer material with promising visible light response (bandgap 2.7 eV) and photocatalytic activities. Different C–C coupling reactions have been carried out over various carbon nitrides.

Mesoporous graphitic carbon nitride (mpg- $C_3N_4$ ) was firstly reported for oxidative coupling of N-phenyl-1,2,3,4-tetrahydroisoquinoline with nitromethane under visible light irradiation (**Scheme** 

**24**)<sup>[92]</sup>. Later the application of this polymer was extended to the fluoroalkylation of arenes (**Scheme 25**)<sup>[93]</sup>, Diels–Alder cycloaddition reactions (**Scheme 26**)<sup>[94]</sup> and Mizoroki-Heck reaction (**Scheme 27**)<sup>[95]</sup>.

$$R^1$$
 $R^1$ 
 $R^1$ 
 $R^2$ 
 $Q_2, hv$ 
 $R^2$ 
 $Q_2, hv$ 
 $R^1$ 
 $Q_2N$ 
 $R^2$ 
 $Q_2N$ 
 $R^2$ 

Scheme 24 Oxidative coupling reaction with nitroalkanes over mpg-C<sub>3</sub>N<sub>4</sub><sup>[92]</sup>

Scheme 25 Reaction of benzene trifluoromethylation<sup>[93]</sup>

Scheme 26 Photocatalytic [4+2] cycloaddition of trans-anethole with 2,3-dimethyl-1,3- butadiene over g-  $C_3N_4^{[94]}$ 

Scheme 27 Mizoroki–Heck type reactions of olefins and alkyl bromides<sup>[95]</sup>

Different C–C coupling reactions were achieved by the impressive intrinsic properties of mpg- $C_3N_4$  under visible illumination. With the help of metal loadings, the application of g- $C_3N_4$  was further expanded (SMC reaction, Ullmann homo-coupling reaction etc.)

g-CNX polymers (X represents nucleobase) with tunable texture, surface and optical properties have been prepared from urea and nucleobases<sup>[96]</sup>, and with the optimised synthetic recipe, the

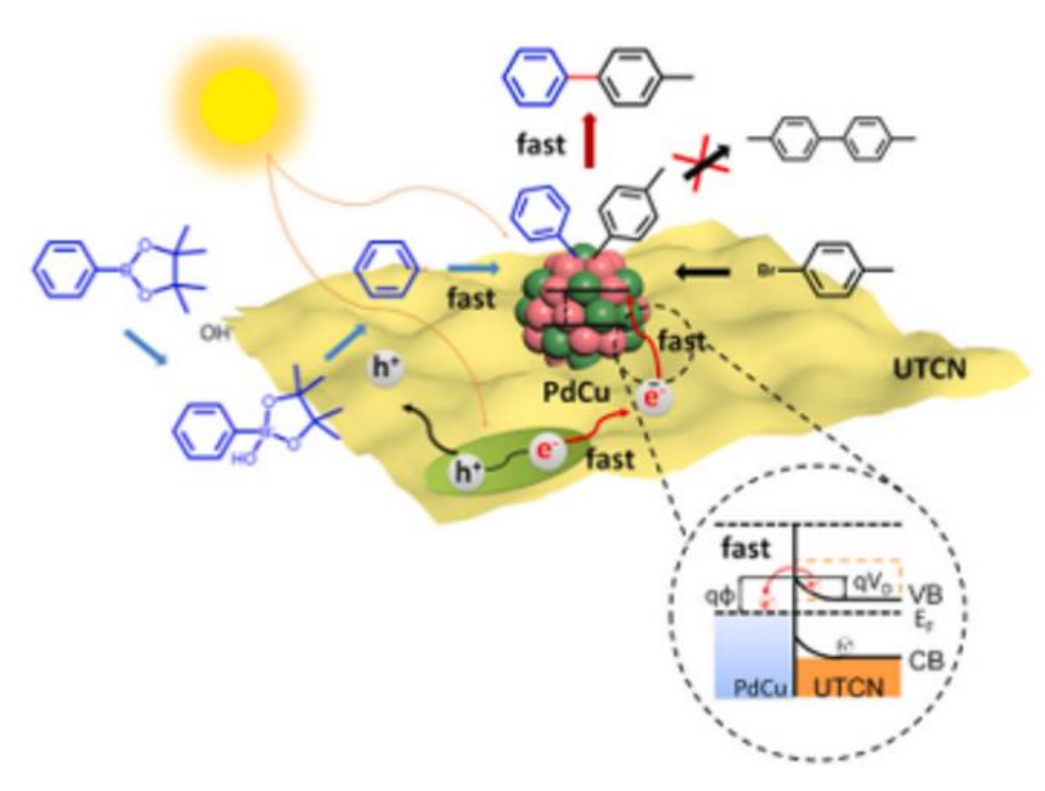
photocatalyst exhibited  $282 \, \mu molh^{-1}$  and 7.1% apparent quantum yield for hydrogen evolution reaction under visible light irradiation. Furthermore, after loading 3 wt% of Pd, the Pd/g-CNX could successfully drive SMC of iodobenzene with a yield of 97%.

Similar Pd-based Mott–Schottky heterojunction was prepared on crystallized carbon nitride nanobelts (Pd/CN-C) for Ullmann homo-coupling under visible light irradiation (14 examples, yield 3%-99%, MeCN, 10 h)<sup>[97]</sup>. Pd/g-C<sub>3</sub>N<sub>4</sub> was chosen as a reference sample and high crystallinity of carbon nitride could not only boost visible light absorption but also enhance the photoinduced charge transfer and separation due to the more extended  $\pi$ -conjugation system in the structure. Crystallized carbon nitride with N defect and O dopant co-modifications (CN-450) was developed and reported later by the same group. After loading Pd NPs on CN-450, this Pd/CN-450 photocatalyst was proven to efficiently drive Ullmann-type coupling reactions. Unlike the previous report, solvent ethanol was replaced by aromatic alcohol. Therefore two organic reactions (Ullmann coupling of aryl bromide and oxidation of aromatic alcohol) could be achieved in one photocatalytic cycle (**Scheme 28**)<sup>[98]</sup>.



Scheme 28 Proposed mechanism of photocatalytic Ullmann coupling and aromatic alcohol oxidation over  $Pd/CN-450^{[98]}$ 

Pd-based alloy was also decorated on carbon nitride materials. AuPd alloy was immobilised on g-C<sub>3</sub>N<sub>4</sub> and this AuPd/g-C<sub>3</sub>N<sub>4</sub> could successfully carry out visible light-driven SMC reaction with a high turnover frequency of 7920 h<sup>-1</sup> (12 examples, yield 39%-99%, ethanol-water solution, 0.5-2 h)<sup>[99]</sup>. N-rich carbon nitride (NRCN) was also reported as an alternative support to accommodate AuPd alloy. Due to the smaller size and more amino groups in NRCN, this AuPd@NRCN exhibited excellent activity for photocatalytic Ullmann reaction and Heck reaction under visible light irradiation<sup>[100]</sup>. PdCu alloy with low crystallinity was loaded on the surface of large-area ultrathin 2D carbon nitride nanosheets (PdCu/UTUC)<sup>[101]</sup>. The UTUC was synthesised by exfoliation from bulk g-C<sub>3</sub>N<sub>4</sub> using a twice thermal exfoliation and repolymerization method. Efficient photocatalytic SMC transformations of various aryl iodide were realised with a TOF of 418.2 h-1, which is 8 times higher compared to similar Pd decorated g-C<sub>3</sub>N<sub>4</sub>. The large specific surface area allowed enhanced photoinduced charge migration and separation, and the alloy showed a reduced Schottky barrier at the alloy/carbon nitride interface, resulting in an improved activity (Scheme 29).



Scheme 29 Proposed mechanism of photocatalytic SMC over PdCu/UTCN<sup>[101]</sup>

Non-noble metal as co-catalyst for selective C–C bond formation offers an eco-friendly platform. Recently, nickel decorated g-C<sub>3</sub>N<sub>4</sub> (Ni/gCN) was reported for homo-coupling of benzyl halide<sup>[102]</sup>. Compared to palladium or copper co-catalysts, nickel exhibited a 13 times higher activity due to fast C-X dissociation rate and rapid removal of active halogen anions (**Scheme 30**). However, though the photocatalyst could successfully drive homo-coupling of benzyl bromides, decreased yields were observed when using benzyl chlorides as substrates.  $Cu_2O$  decorated g-C<sub>3</sub>N<sub>4</sub> ( $Cu_2O$  NPs@ g-C<sub>3</sub>N<sub>4</sub>) was developed for the synthesis of ynone, aminoindolizines, and pyrrolo [1, 2-a] quinoline under visible light irradiation<sup>[103]</sup>. This approach was proven following green chemistry principles based on the calculation of atom economy (AE) and E-factor (**Equation 4**).

$$AE = \frac{molecular\ weight\ of\ desired\ product}{sum\ of\ molecular\ weight\ of\ all\ materials\ produced} \times 100 \tag{2-7}$$

$$E - factor = \frac{mass\ of\ total\ waste}{mass\ of\ product}$$
 (2 - 8)

#### Equation 4 equations for aton economy and E-factor

Scheme 30 Proposed explanation for the favourable promotional effect of Pd, Ni and Cu<sup>[102]</sup>

Metal-free heterogeneous photochemical synthesis for decarboxylation of carboxylic acids was reported using boron carbon nitrides (BCN) (**Scheme 31**)<sup>[104]</sup>. Control experiments explained valuable carbon radical intermediate formation. It provided an alternative to homogeneous catalysts and demonstrated potential application in drug fabrication.

R-COOH

PC = BCN

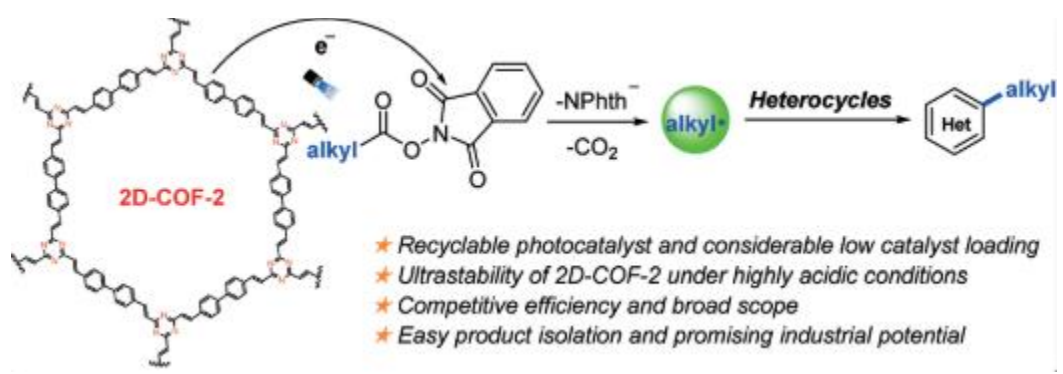
$$R^{\bullet}$$
 $R^{\bullet}$ 
 $R$ 

Scheme 31 Metal-free heterogeneous photochemical synthesis<sup>[104]</sup>

#### 2.7.2 Other organic materials

Covalent organic frameworks (COFs) are a novel category of porous polymers that possess a crystalline structure, which are fabricated by covalently connecting small-size organic molecules using the technique of dynamic covalent chemistry.

An olefin-linked two-dimensional covalent organic framework (2D-COF-2) was synthesised<sup>[105]</sup>. This ultrastable 2D-COF was smoothly applied in the visible-driven decarboxylative alkylations of heterocycles in the presence of NHPI esters. 2D-COF-2 exhibited high tolerance in highly organic acidic conditions and great recyclability, offering a greener approach to synthesising privileged alkylated heterocycles (**Scheme 32**). Under photothermal conditions with temperatures up to 100°C, asymmetric Henry reaction was carried out by metal-loaded (Pd or Au) porphyrincontaining homochiral covalent organic framework (CCOF-CuTPP)<sup>[106]</sup>, and this strategy provided a general and effective way to fabricate more multifunctional composite catalysts in the future.



Scheme 32 Illustration for the generation of alkyl radicals from redox-active esters<sup>[105]</sup>

Various organic polymers have also been reported as visible light photocatalysts for SMC reactions. For example, 8-hydroxyquinoline-based polymers with strong light absorption ranging from 300 nm to 700 nm have been synthesised via Friedel–Crafts polymerisation method<sup>[107]</sup>. This porous organic material had a large surface area (up to 848 m<sup>2</sup>g<sup>-1</sup>) with irregular morphology and disordered structure. After Pd modification, the Pd/P13 photocatalyst displayed excellent photocatalytic performance for SMC reaction under blue light irradiation with a 1931 h<sup>-1</sup> TOF (11 exmaples, yield 82%-99%). A conjugated microporous poly (benzoxadiazole) network (B-BO<sub>3</sub>) was also synthesised for SMC coupling of aryl iodide<sup>[108]</sup>. Polydopamine nanofilms (PDA-CL) were prepared from the inspiration of mussels (**Figure 9**), and this nanofilm showed potential as light-harvesting materials to support Pd NPs for the visible-light-induced SMC (16 examples, 0-99% yields, DMF-water solution, 2-10 h)<sup>[109]</sup>.

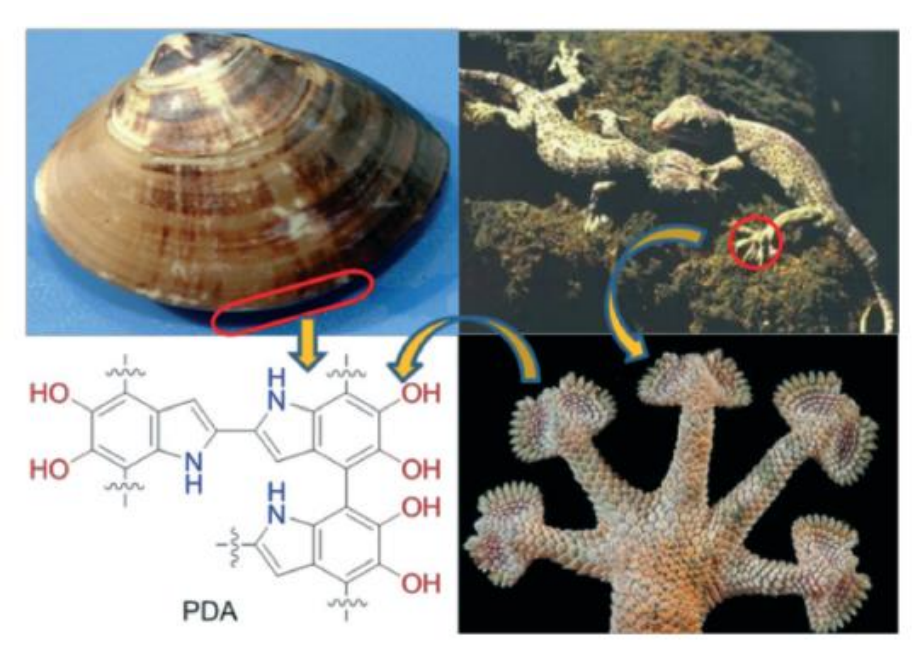


Figure 9 Structure of PDA and its inspiration species mussels, shellfish and geckos [109]

Moreover, hyper-cross-linked polystyrene (HPS) supported Au-Pd bimetallic nanoparticles were reported<sup>[110]</sup>. Au core with an extremely thin Pd shell (Au-Pd/HPS) allowed this system to increase the activity (71.6% yield compared to 22.4% yield when using Pd/HPS) for SMC reaction of 4-

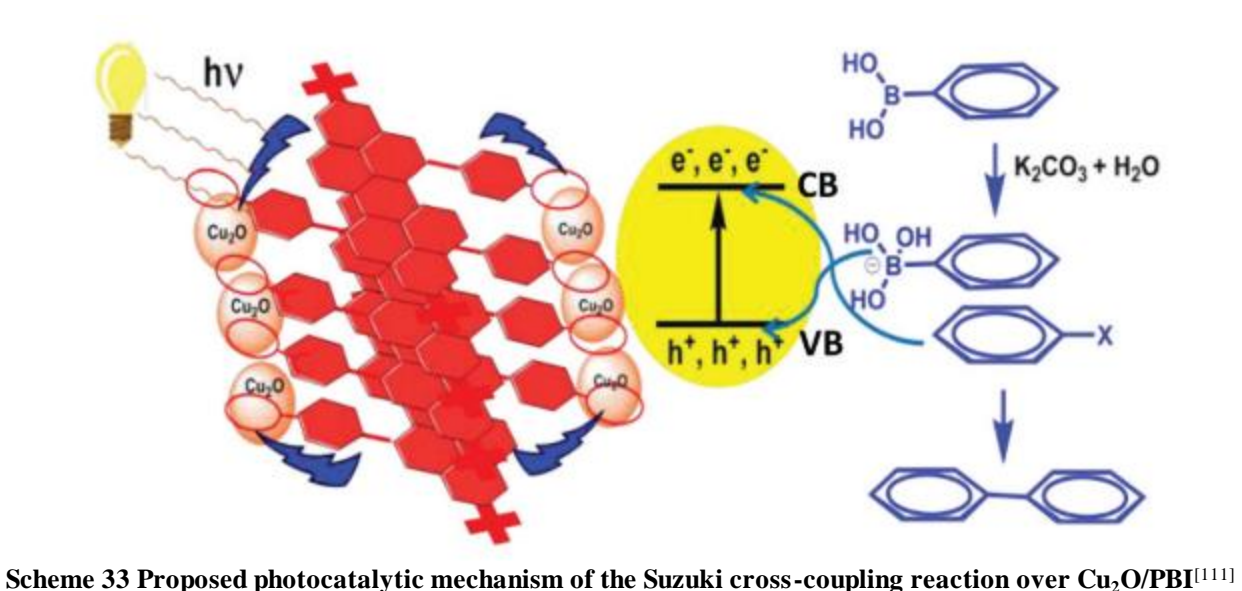
bromoanisole under visible light irradiation. HPS-based catalysts usually functioned as a cocktail system where Pd existed in different forms (Pd(II) and Pd(0)), which allowed a detailed mechanism investigation, and increasing the share of Pd(0) in such cocktail systems to push the heterogeneous mechanism of SMC.

#### 2.8 Organic-inorganic composites for organic C–C coupling reactions

# 2.8.1 Dye-metal oxide composite

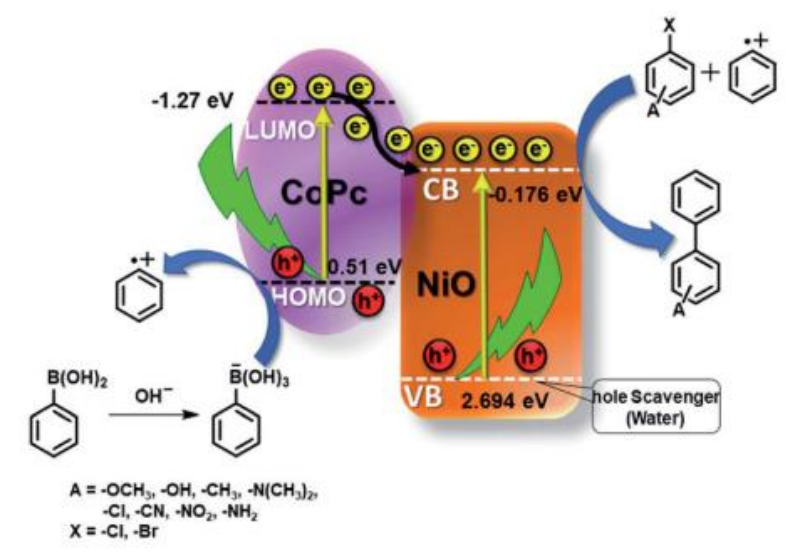
Functionalization of inorganic materials with organic molecules is a very useful method to obtain inorganic materials with great properties as support for photocatalytic C–C bond formation.

Cu<sub>2</sub>O was studied as the semiconductor nanomaterial and a supramolecular ensemble photocatalytic system consisting of perylene bisimide (PBI) derivatives and Cu<sub>2</sub>O NPs was therefore developed (**Scheme 33**)<sup>[111]</sup>. This system was used in visible-driven SMC reactions and exhibited relatively good activity under ambient conditions (6 examples, yield 65% -79%, ethanolwater solution). However, a poor recyclability of this nobel-metal-free system was observed, and there was a 30% loss in the product yield after 4 runs. This supramolecular ensemble strategy was extended to CuO NPs and TICT-AIEE active pyrazine derivative was used in this case<sup>[112]</sup>. Sonogashira coupling was carried out with a wide variety of substrates under visible light irradiation, and a single-electron transfer mechanism was proposed for the photocatalytic process.



Another palladium-free hybrid photocatalyst was developed by grafting cobalt(II) phthalocyanine complex on nickel oxide (CNO-10)<sup>[113]</sup>, and this photocatalyst was even able to break C–Cl bond on chlorobenzene to achieve SMC reaction (12 examples, yield 52%-92%, DMF-water solution, 8 h). A possible mechanism is shown in **Scheme 34**. However, the exact mechanism was unknown

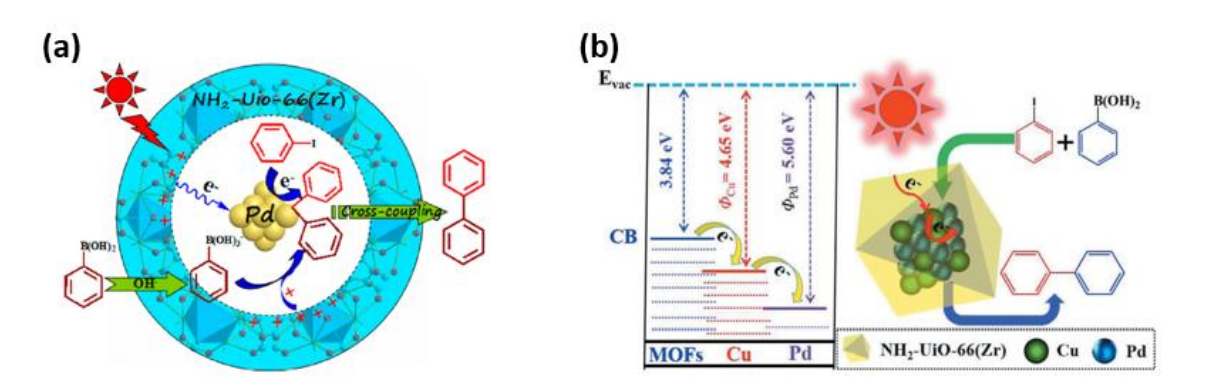
at this stage, requiring further investigation.



Scheme 34 Proposed mechanism of SMC reaction over CoPc/NiO photocatalyst[113]

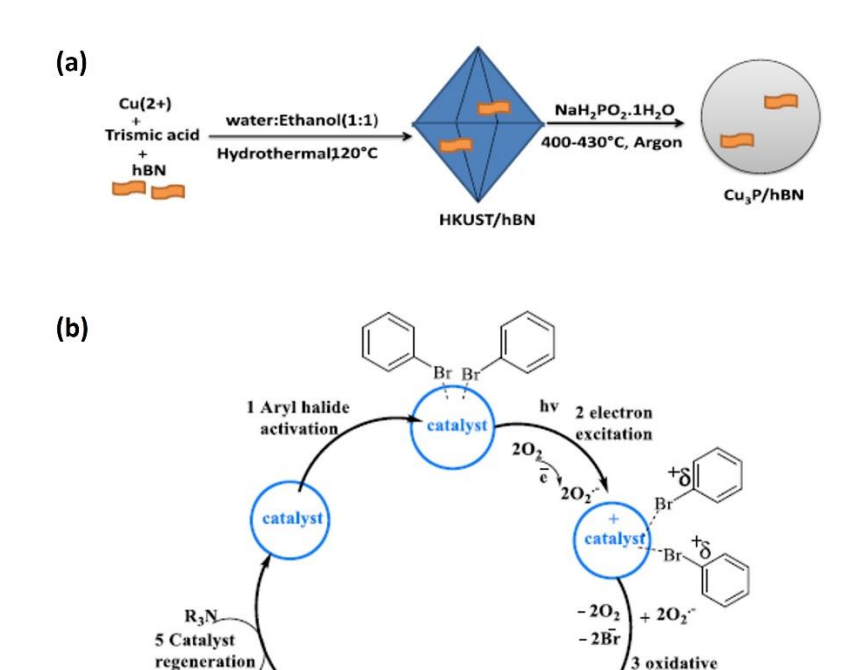
#### 2.8.2 Metal-organic framework

Metal-organic frameworks (MOFs) are crystalline 3D micro-mesoporous hybrid materials. MOFs have uniform nanopores and organic ligands, which function as cages to control the size of the confined nanoclusters, and anchors to stabilise these metal nanoclusters, respectively. Due to its advantage of homogeneous and heterogeneous photocatalysts, various MOFs have been developed for photocatalytic C-C bond formations. Pd nanoclusters encapsulated NH<sub>2</sub>-Uio-66(Zr) was developed and this photocatalyst showed excellent photocatalytic activity for SMC of iodobenzene (5 examples, yield 20.5%-99%, DMF-water solution, 45 min-2 h)<sup>[114]</sup>. Similar to semiconductors, upon light irradiation, the organic ligands in MOFs could absorb the light energy and transfer the excited electrons to Pd clusters through a ligand-to-metal charge transfer (LMCT). Later, a bimetallic CuPd@NH<sub>2</sub>-Uio-66(Zr) was reported by the same research group<sup>[115]</sup>. Compared to the monometallic Pd@NH<sub>2</sub>-Uio-66(Zr), the CuPd@NH<sub>2</sub>-Uio-66(Zr) displayed a photocatalytic performance in the coupling of a variety of iodobenzenes with different functional groups and phenylboronic acids (Scheme 35). The introduced Cu acted as a mediator, which could further promote the charge transfer from NH<sub>2</sub>-Uio-66(Zr) to Pd. This study demonstrated the potential of using Metal@MOFs in photocatalytic organic coupling reactions.



Scheme 35 Mechanism of photocatalytic SMC over (a) Pd@NH $_2$ -Uio-66(Zr) and (b) CuPd@NH $_2$ -Uio-66(Zr)  $_{[115]}^{[115]}$ 

A visible light response photocatalytic system consisting of metal-organic framework derived p-Type copper phosphide ( $Cu_3P$ ) and hexagonal boron nitride nanostructures (hBN) was prepared, and this  $Cu_3P/hBN$  heterogeneous catalyst was tested to successfully drive the homo-coupling of bromobenzene. In most publications, the break of C-X (X=I, Br, Cl) bond was considered a reductive activation process requiring the absence of oxygen. However, the  $Cu^{2+}$  active sites on  $Cu_3P/hBN$  improved the adsorption of bromobenzene on the catalyst surface, and the photoexcited electrons would oxidase oxygen molecules to form superoxide radical anion ( $O_2$ ), which would oxidatively activate C-Br bond and further lead to biphenyl formation (**Scheme 36**)<sup>[116]</sup>.



Scheme 36 (a) Synthesis of  $\text{Cu}_3\text{P/hBN}$  Composites from HKUST MOF (b) Mechanism of photocatalytic cycle<sup>[116]</sup>

4 Reductive elimination

catalys

addition

The C–C coupling reaction between nitromethane and *N*-phenyltetrahydroisoquinoline was achieved by a 2-photon responsive ZJU-56-0.2 under 660 nm light irradiation<sup>[117]</sup>. NIR-light was proven to minimise the generation of byproducts in comparison with UV light source. The cross-dehydrogenative coupling (CDC) reaction of CH<sub>3</sub>NO<sub>2</sub> was carried out under 450 nm irradiation and aerobic conditions over MOF UiO-68Se<sup>[118]</sup>. These works broadened the application of MOFs in photocatalytic C–C coupling reactions.

#### 2.9 Conclusion and outlook

Organic C–C coupling reactions by heterogeneous photocatalysis is an emerging area to synthesise value-added chemicals, including biomaterials and natural products, fine chemicals, and medicines. These reactions are usually carried out over transition metal or homogeneous catalysts to achieve high selectivity and yield. However, homogeneous catalysts are unfavourable for industrial-scale production due to various issues related to cost, stability, reusability, and separation. Heterogeneous photocatalysts are great alternatives to tackle those drawbacks existing in homogeneous catalysis for the C-C coupling reactions. Two types of organic C-C coupling reactions have been achieved using heterogeneous photocatalysts, C-C cross-coupling (Suzuki, Stille, Sonogashira, Hiyama etc.) and C-C homo-coupling (Ullmann, homo-coupling of halogenated arenes etc.). In this chapter, I summarised the progress in heterogeneous photocatalytic organic C–C coupling reactions according to the category of photocatalysts used. The heterogeneous photocatalysts can be classified into 4 main categories, inorganic materials with wide bandgap or narrow bandgap, organic materials and organic-inorganic composites with a more detailed classification under each main branch. The main factors that largely influence selectivity for these coupling reactions are (1) light harvesting; (2) co-catalyst selection; (3) reaction conditions. UV light is too strong so sometimes photochemical pathways would take place

for reactions involving simple structured substrates, resulting in poor yield of targeted coupling products. To improve light harvesting, efforts have been focused on modifying wide bandgap semiconductors to enhance their visible light absorption since visible takes a large share in the diverse light spectra. As for co-catalyst selection, Pd is the most studied due to its promising activity for a wide range of coupling reactions. In most cases, monometallic Pd loading is enough to achieve the target reaction even with wide bandgap semiconductors under visible light irradiation (interband transition). A plasmonic metal is needed to grant or further improve visible light absorption since LSPR effect is stronger compared to interband transition. Pd-based plasmonic bimetallic or alloy co-catalysts are therefore developed. Non-noble-metal is another research area, and Ni and Cu exhibit good activity for reactions such Ullmann coupling and homocoupling of benzyl halides. Reaction conditions play a big part in achieving organic C-C coupling reactions. Solvent selection, pH, gas phase and additives are critical for higher selectivity and conversion. The reaction mechanism, which depends on the photocatalytic system used for a specific coupling reaction, can potentially be classical semiconductor mechanism, single electron transfer, radical-mediated pathway, interband electronic transition and LSPR effect.

Though great progresses regarding heterogeneous photocatalytic C–C coupling have been made in the past decade, some challenges and problems still need to be tackled. Firstly, most of the studies have focused on reactions such as Suzuki-Miyaura cross-coupling, in which one of the two substrates has to be easily activated (e.g. boronic acid in SMC). Further efforts are urgently required to broaden the reaction application, and this will bring to the second topic. The development of robust photocatalysts is highly desired, including (1) the design of metal-free or noble metal free photocatalysts for explored reactions; (2) the design of novel photocatalysts for new reactions to activate two sluggish substrates and tune selectivity to targeted pathways. Lastly,

the detailed mechanism behind those coupling reactions should be investigated by cutting-edge characterisations involving (1) light harvesting and photo-electron generation; (2) electron transfer process at the interface; (3) adsorption and activation of substrate and desorption of products. These investigations will benefit the development of efficient photocatalytic systems for C–C coupling reactions.

# **Chapter 3 Characterisations Methodology**

# 3.1 Gas Chromatography-Mass Spectrometry

Gas Chromatography-Mass Spectrometry (GC-MS) is an instrumental technique which combines a gas chromatograph (GC) and a mass spectrometer (MS) to separate, identify and quantify complex mixtures of chemicals. The compounds must be volatile and stable at high temperature to be analysed by the machine. The liquid sample is injected to the GC from the inlet and then vaporized. The vapour flew with helium carrier gas through a chromatographic column and the mixture of compounds would be separated due to its interaction with the stationary phase and the mobile phase, in other words, the column and the carrier gas. There is a heated transfer line at the end of the column where the compounds would be converted to ions and then enter the ion source. There are different methods to produce ion and the most commonly used method is electron ionisation (EI). In a typical process, the molecular sample is hit by a beam of electrons and ionised to molecular ions (each molecule lost one electron). In a mass spectrum, these ions would form a peak which reveals the molecular weight of the compound. The molecular ion would become several smaller ions when it receives a large amount of energy and these smaller ions can act as "fingerprints" to identify the structure of the molecule. These positively charged ions are then separated by a mass analyser and there are a few types of analysers with different mass related properties. Frequently used analysers are quadrupoles and ion traps. After the separation, ions would enter a detector where they are amplified as signals and these signals are then operated by computers to form visual displays. Column used in this thesis is Rxi-5SilMS Column.

# 3.2 Powder X-ray Diffraction

The non-interrupted repeating of a unit cell leads to the formation of a single crystal in three dimensions. Powder X-ray Diffraction (PXRD) is an analytical technique commonly used to

identify the phase of crystalline materials. It could provide information about the crystalline structure, bond lengths and angles. A narrow beam of X-ray is released from a cathode ray tube where it is filtered to produce monochromatic radiation. The collimated radiation is directed to pass through the tested sample, which is finely ground, homogenized before mounted on the machine. When conditions meet the requirement of Bragg's Law  $(n\lambda=2d\sin\theta)$  (Figure 10), constructive interference and a diffracted ray would be produced via the interaction between the X-ray and the sample. This law demonstrates the relationships of the wavelength of electromagnetic radiation with a diffraction angle and the lattice spacing in the analysed sample. These diffracted X-rays are then detected and counted. The powdered material has random orientations and because of that, every possible diffraction directions of the lattice would be detected if the sample is scanned through the range of 20 angles, minerals have a set of its own unique d-spacings thus the mineral could be identified by comparison the standard reference patterns with the d-spacings which are converted from the diffraction peaks. The model used is Stoe STADI-P instrument ( $2\theta = 2^{\circ}-40^{\circ}$ ,  $0.5^{\circ}$  each step at 5.0 s/step) using Mo Ka1 (wavelength 0.70930, 50 kV and 30 mA)

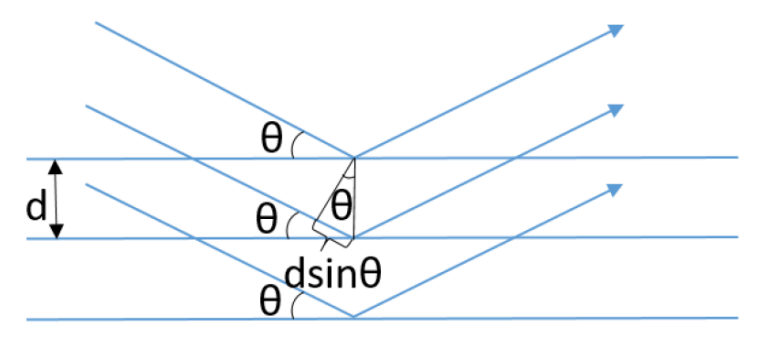


Figure 10 Bragg's Law

# 3.3 Photoluminescence Spectroscopy (PL)

Photoluminescence spectroscopy refers to the emission of light by materials upon absorption of photons. The process involves the excitation of valence electrons by incident photons, followed by the descent of some excited electrons to one of the several vibrational levels of the ground electronic state, resulting in the emission of a photon. In the context of photocatalysis, the intensity of photoluminescence is indicative of the extent of recombination between excited electrons and holes. The model used in this project is the Renishaw InVia Raman microscope, with excitation laser beams of either 325m or 514 nm and a 200-800 nm wavelength range. Both Raman spectrum and PL spectrum can be obtained from the Raman instrument. The difference between both is that when a laser illuminates the sample, Raman spectrum is collected from the scattering of sample while PL spectrum contains the absorption/emission process of laser energy.

# 3.4 Ultraviolet-Visible Spectroscopy (UV-vis)

Ultraviolet-visible (UV-vis) spectroscopy is a technique to acquire the absorbance spectra of either a solid material or a compound in solution. Those sample materials can absorb light energy or electromagnetic radiation, thus completing the excitation of electrons from the ground state to the first singlet excited state. The UV-vis region is a wavelength range of 200-800 nm which means it covers the energy range from 1.5 eV to 6.2 eV in the electromagnetic spectrum. The principle of the absorbance spectroscopy is the Beer-Lambert Law:  $A = \epsilon bc$ , where A is absorbance,  $\epsilon$  is the molar absorptivity of the compound or molecule in solution (M-1cm-1), b is the path length of the cuvette or sample holder, c indicates the concentration of the solution (M). In this project, the data was collected from Shimadzu UV-2550 spectrophotometer fitted with an integrating sphere, and **Equation 5** shows how to convert absorbance data from reflectance data in UV-vis.

Absorbance 
$$(A) = -\log_{10} Reflectance(R)$$
 (3 – 1)

Equation 5 Convert absorbance from reflectance in UV-vis

#### 3.5 Fourier-transform Infrared Spectroscopy (FTIR)

Fourier-transform infrared (FTIR) spectroscopy is a commonly used analytical technique for characterising polymer samples. It involves directing an infrared light beam onto a sample and measuring the amount of light absorbed at each frequency. The mechanism of FTIR spectroscopy is based on the interaction of infrared radiation with the molecular bonds within the sample, which causes them to vibrate and absorb energy at specific frequencies. The molecular structure of polymers is complex, and FTIR spectroscopy can provide valuable information about the types of functional groups present in the polymer chains, the degree of polymerization, and the polymer morphology. Analyzing the absorption spectrum of the polymer sample at different frequencies makes it possible to identify the chemical bonds and functional groups within the polymer, providing insight into the polymer's chemical structure and composition. The instrument used was Perkin-Elmer 1605 FT-IR spectrometer.

# 3.6 Nuclear Magnetic Resonance (NMR)

Nuclear magnetic resonance spectroscopy (NMR) is an important and widely used technique to identify molecular structures due to the magnetic properties of nuclei. When an external magnetic field is applied, some nuclei exist in specific nuclear spin states. NMR would observe the transitions of particular nuclei between these spin states and the chemical environment that is around those nuclei. If a nucleus has a spin I=0, then NMR spectroscopy could not detect it. In

other words, only those nuclei with a spin I  $\neq$  0 are "visible" to NMR spectroscopy. Due to these properties, NMR has been utilized in many areas, such as medicine, biochemistry and physics. In this project, regular NMR tests were conducted on Bruker Avance Neo 700 MHz and the ssNMR was collected from Solid-state NMR spectrometer with a widebore 7 T magnet, Avance 300 console, magic-angle spinning multinuclear probes.

#### 3.7 Transmission Electron Microscopy (TEM)

Transmission electron microscopy (TEM) is an advanced imaging technique widely used in physics, biology, and materials science. The mechanism of TEM involves the use of a high-energy electron beam that is passed through a thin sample. As the beam interacts with the atoms and electrons within the sample, it generates a complex diffraction pattern. This pattern can be used to determine the crystal structure, defects, and atom distribution of the sample. The electrons that pass through the sample are then captured on a detector, producing a high-magnification image of the sample. As a result, TEM can provide valuable information on the morphology, crystal structure, and chemical composition of materials at the nanoscale, making it a crucial tool for nanotechnology research and materials science. JEOL JEM-F200 was used for TEM images in this project.

# 3.8 X-ray Photoelectron Spectroscopy (XPS)

X-ray photoelectron spectroscopy (XPS), also known as electron spectroscopy for chemical analysis (ESCA), is a widely used analytical technique for characterising the surface chemical composition and electronic state. The mechanism of XPS involves irradiating a sample with high-

energy X-rays, causing the emission of photoelectrons from the surface of the sample. These photoelectrons have energies specific to the element and chemical environment they originated from, allowing for the identification and quantification of the elements present and their oxidation state. Also, the number of electrons detected at a given energy can provide information on the chemical state and electronic structure of the atoms within the sample. In addition, depth profiling into the bulk is possible using ion etching. XPS is commonly used in a wide range of fields, including materials science, chemistry, and physics, to study the composition and electronic structure of surfaces and interfaces. In this project, the XPS test was performed on Thermoscientific XPS K-alpha surface analysis machine using an Al source.

#### 3.10 Electron Paramagnetic Resonance (EPR)

Electron paramagnetic resonance (EPR) is a powerful spectroscopic technique used to study the properties of materials with unpaired electrons, such as radicals, transition metal ions, and defects in solids. The mechanism of EPR involves the application of a magnetic field to a sample containing unpaired electrons, causing the electrons to align themselves with the field. A microwave frequency is then applied to the sample, causing the electrons to absorb energy and transition to higher energy levels. The energy absorbed by the electrons is detected by measuring changes in the microwave absorption spectrum, providing information on the electronic and magnetic properties of the sample. EPR is used in a variety of fields, including chemistry, physics, and biology, to study materials and their properties, such as the electronic structure and bonding of paramagnetic species, the kinetics of chemical reactions, and the behavior of biomolecules. Electron paramagnetic resonance (EPR) was measured by a MS-5000 spectrometer at ambient temperature (288 K). Microwave power was set at 10 microwatts, while the frequency was 9.485

GHz (X-band). The modulation frequency was 100 kHz. For the in-situ EPR test, a 365 nm LED (80 mW cm-2) was applied for irradiation.

# **3.11** Temperature-programmed Desorption (TPD)

Temperature-programmed desorption (TPD) is a commonly used technique in surface science and catalysis to investigate the adsorption and desorption behavior of gases on solid surfaces. The mechanism of TPD involves exposing a sample to a gas, typically an inert gas such as helium or argon, at a low temperature to adsorb the gas molecules onto the surface. The temperature is then increased, causing the gas molecules to desorb from the surface. The desorbed gas molecules are detected and quantified by a mass spectrometer, providing information on the desorption kinetics and energetics of the surface-gas interactions. TPD is a useful tool for studying the properties of catalysts, such as the strength and distribution of active sites, and for optimizing catalytic processes by understanding the reaction mechanisms involved. It can also be used to investigate the surface properties of materials, such as porosity and surface area. Micromeritics AutoChem II 2920 was used for the TPD test in this project.

Chapter 4 Control Selectivity Among Acetalisation, Pinacol Coupling and Hydrogenation Reactions of Benzaldehyde via Catalytic and Photochemical Pathways at Ambient Temperature

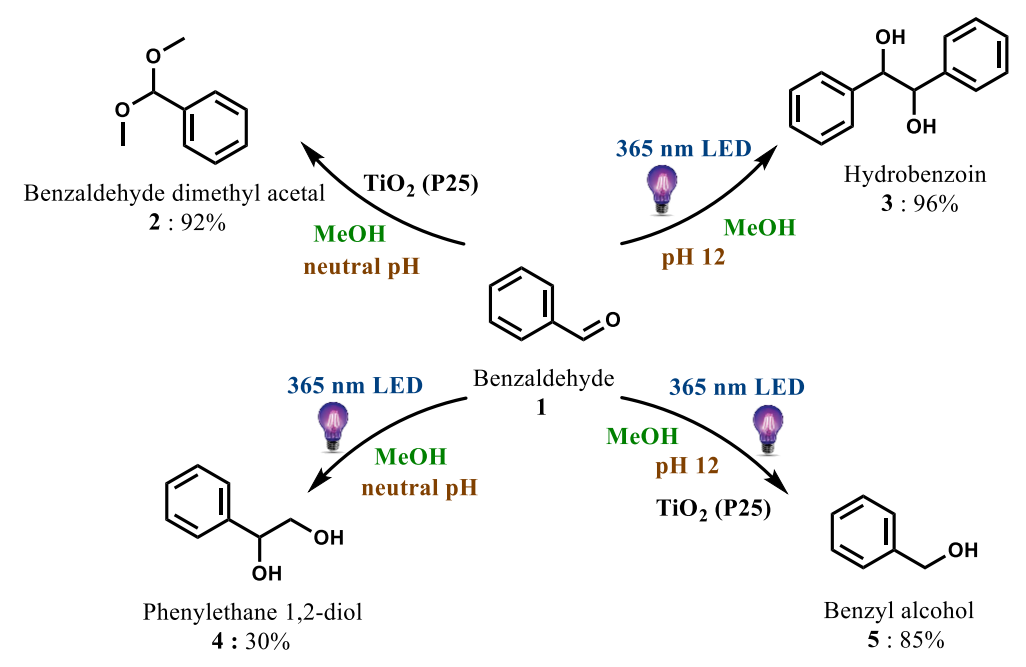
#### 4.1 Introduction

Benzaldehyde is the simplest aromatic aldehyde, which is often derived from renewable biomass (e.g. cheery, peach seeds). It is also one of the most abundant building blocks in chemical industry<sup>[119]</sup>. It was first successfully isolated in 1803, and since then, many types of valuable chemicals have been produced using benzaldehyde as the raw material, including various aldehydes, alcohols, diols, acetals, rendering wide applications in pharmaceutical, fragrance and flavour industries<sup>[120]</sup>.

Despite the relatively mature benzaldehyde transformation technologies that have been widely used so far, most processes still suffer from harsh reaction conditions (e.g. high temperature [121]), complex multi reaction steps and complicated post-treatments. Acetals are common intermediates in organic synthesis, while the conventional method for acetalisation of aldehyde often requires a homogeneous system with strong Brønsted mineral acids [122–124]. As a result, facing a series of concerns, e.g. complex product separation, catalyst recycle and the induced system corrosion [125],[126] leading to high capital and operation costs. The construction of C–C bonds via pinacol coupling is of paramount significance in organic chemistry, and photochemistry could offer a mild and efficient pathway driven by solar energy [127]. However, it is challenging due to the very negative reduction potential (E<sub>1/2red</sub> = -1.42 vs. normalised hydrogen electrode) of direct aldehyde conversion required [128]. This reaction could happen with precious metals and/or

homogenous metallic complexes catalyst<sup>[129]</sup>, while it normally suffers from limited stability and low solubility. Moreover, some toxic reagents are inevitably involved in these methods, raising economic and environmental concerns. Diols, such as 1-phenylethane-1,2-diol, are widely recognised as readily accessible building blocks in organic chemistry<sup>[130]</sup>, while often require multi-step synthetic protocols, resulting in low carbon atom utilisation efficiency<sup>[131]</sup>. Hydrogenation of aldehyde by the thermal catalysis has been well investigated <sup>[132],[133]</sup>, always involving the pure hydrogen gas, which is highly combustible<sup>[134]</sup>. Besides, they are mainly carried out in homogeneous systems in most cases<sup>[120]</sup>, leading to time-consuming recycling and separation processes.

Herein, a green and reliable approach has been developed to transfer benzaldehyde into four valuable chemical products with both high yield and high selectivity. Through manipulation of general experimental parameters, including adjusting pH, presence/absence of light irradiation, the use of a photocatalyst TiO<sub>2</sub> (P25), smart pathways to specific value-added products have been established (Scheme 37 Four different pathways for benzaldehyde transformations and corresponding product yield (%)(Scheme 37). Moreover, the mechanisms have been investigated, and isotopic labelling experiment was conducted to identify an efficient pinacol coupling pathway. This work provided a simple but effective method to synthesise different compounds with high selectivity from benzaldehyde, which gives new insight for further development of photocatalysis and photochemistry.



Scheme 37 Four different pathways for benzaldehyde transformations and corresponding product yield (%)

#### **4.2 Experimental section**

#### 4.2.1 Characterisation of bare P25

The powder X-ray diffraction (XRD) was carried out on bare P25 using a Bruker D4 diffractometer equipped with a Cu-K $\alpha$  source (K $\alpha$ 1 =1.540562 Å and K $\alpha$ 2 = 1.544398 Å), and the result is shown in **Figure 11**. UV-vis spectrum (UV-vis) was also carried out on bare P25 using a Shimadzu UV-2550 UV-vis spectrophotometer (**Figure 12**).

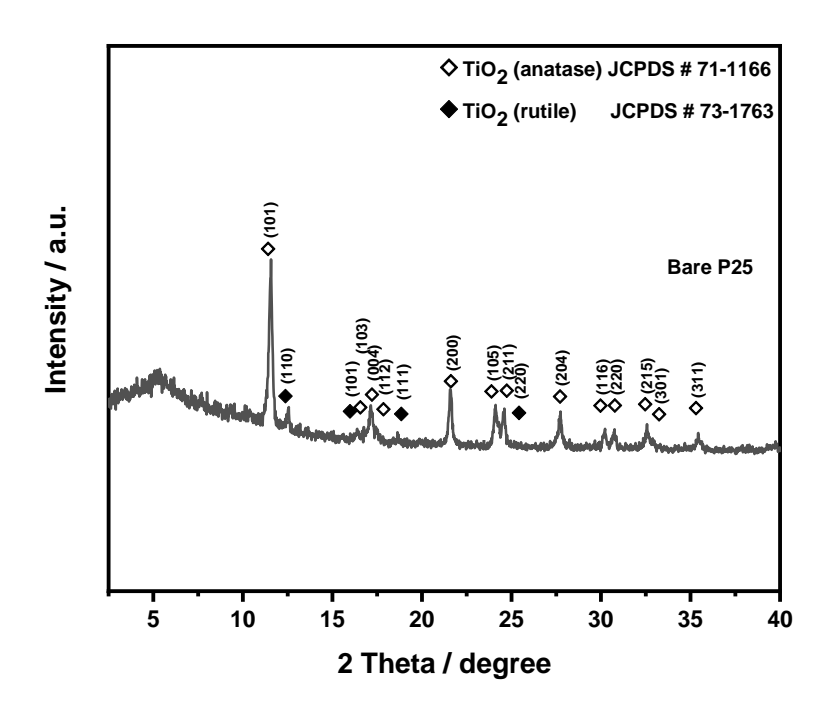


Figure 11 XRD result of  $TiO_2$  (bare P25)

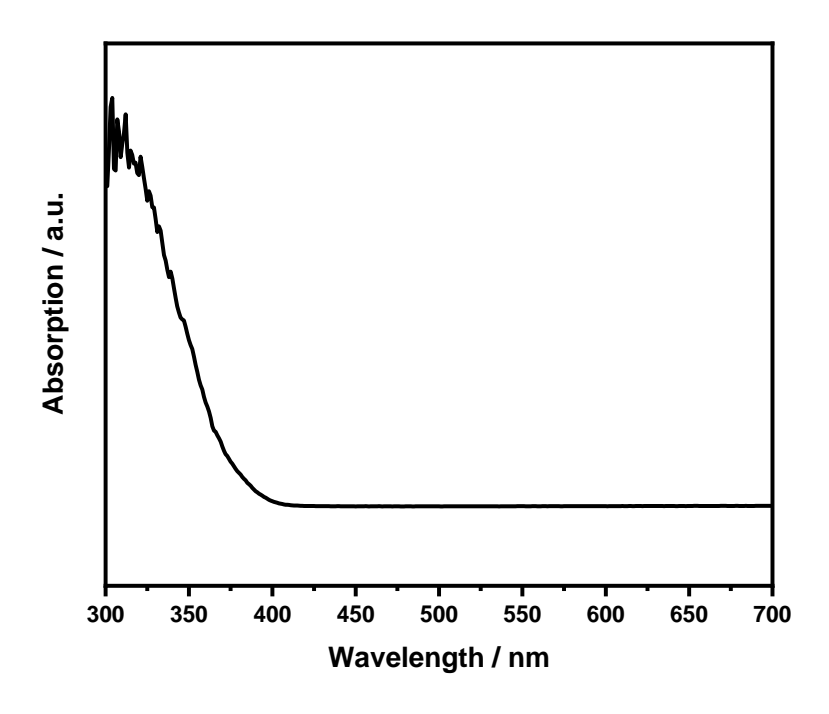


Figure 12 UV-vis spectrum of P25

#### 4.2.2 Catalytic performance evaluation.

All the materials used were commercially available without any further purification once received.

Acetalisation (benzaldehyde dimethyl acetal): in a typical catalytic acetalisation reaction, the reactor contained 15 ml methanol, 1 mmol benzaldehyde and 30 mg TiO<sub>2</sub> (P25). The mixture was stirred at 25 °C for 2 h in air. The products were analysed by GC-MS (Shimadzu QP2010 SE).

Pinacol coupling (hydrobenzoin): in a typical photochemical pinacol coupling reaction, the reactor contained 15 ml 0.01 M KOH methanol solution (15 ml methanol in the case of 1-phenylethane-1,2-diol) and 1 mmol benzaldehyde. The mixture in the sealed reactor was firstly purged by Ar for 20 min and then irradiated by 365 nm LED (Perfectlight PCX50C Discover multichannel system) at 25 °C for 2 h. The products were analysed by GC-MS (Shimadzu QP2010 SE).

Hydrogenation (benzyl alcohol): in a typical photocatalytic hydrogenation reaction, the reactor contained 15 ml 0.01 M potassium hydroxide (KOH) methanol solution, 1 mmol benzaldehyde and 30 mg TiO<sub>2</sub> (P25). The mixture in the sealed reactor was firstly purged by Argon (Ar) for 20 min and then irradiated by 365 nm LED (Perfectlight PCX50C Discover multichannel system) at 25 °C for 2 h. The products were analysed by GC-MS (Shimadzu QP2010 SE).

For the above 3 mentioned pathways they all could be achieved at ambient conditions with excellent/stable activity, leading to scale-up potential. Further experiments may need to be conducted to confirm this.

# 4.3 Results and discussion

Table 1 Experimental conditions for the transformations of benzal dehyde  $\mathbf{1}^a$ 

Entry	Cataly st (mg)	Atmospher e	$pH^b$	Light source	Con. (%) <sup>c</sup>	$S_2$ . (%) $^c$	S <sub>3</sub> . (%) <sup>c</sup> (meso : dl)	S4. (%) <sup>c</sup>	S <sub>5</sub> . (%) <sup>c</sup>
1	-	Argon	Neutral	-	-	-	-	_	-
2	P25	Argon	Neutral	-	92%	> 99%	-	-	-
3	P25	Air	Neutral	-	91%	> 99%	-	-	-
4	P25	Argon	12	-	-	-	-	-	-
5	-	Argon	Neutral	365 nm LED	76%	12%	48% (53% : 47%)	40%	-
6	-	Argon	Neutral	> 420 nm (Xe)	-	-	-	-	-
7	-	Argon	Neutral	Xe full arc	73%	72%	16% (57% : 43%)	12%	-
8	-	Argon	Neutral	450 nm LED	-	-	-	-	-
9	-	Argon	12	365 nm LED	96%	-	> 99% (59%:	-	-
10	P25	Argon	12	365 nm LED	98%	-	41%) 6% (47%: 53%)	-	94%
11	PC50	Argon	12	365 nm LED	97%	-	14% (51% : 49%)	-	86%
12	Al <sub>2</sub> O <sub>3</sub>	Argon	12	365 nm LED	91%	-	> 99% (55% : 45%)	-	-
13 <sup>d</sup>	-	Argon	12	365 nm LED	-	-	-	-	-

<sup>&</sup>lt;sup>a</sup>Substrate 1 (1 mmol), catalyst (30 mg), solvent (15 ml methanol), 25 °C, 2h. <sup>b</sup>pH 12: 0.01 M KOH in methanol. <sup>c</sup>Determined by GC-MS. <sup>d</sup>Substrate changed to benzil (1 mmol),  $S_2$  is the selectivity to benzaldehyde dimethyl acetal,  $S_3$  is the selectivity to hydrobenzoin,  $S_4$  is the selectivity to phenylethane 1.2-diol,  $S_5$  is the selectivity to benzyl alcohol as illustrated in **Scheme 37**.

I found that it is very interesting to tune conversion, in particular selectivity in four different reaction processes, by only change one or two experimental parameters. As illustrated in Scheme 37, four reaction pathways have been achieved with four different products, including benzaldehyde dimethyl acetal, hydrobenzoin, phenylethane 1.2-diol and benzyl alcohol.

Acetalization of benzaldehyde. In the presence of P25 TiO<sub>2</sub> (about 20 nm particle size and 50 m<sup>2</sup>/g surface area), the formation of benzaldehyde dimethyl acetal (product 2) could be realised within 2 h at room temperature, with a surprising selectivity (nearly 100%) and yield (92%) (Table 1, entry 2). It was clear that the gas atmosphere did not affect the acetalisation of benzaldehyde as a similar yield could be achieved when the experiment was exposed to air (Table 1, entry 3). In contrast, no conversion of the reactant was observed in the absence of P25 (Table 1, entry 1), indicating the important role of the catalyst P25. Actually, the acetal formation mechanism was widely investigated in organic chemistry<sup>[122]</sup>, the conversion process with the assistance of P25 was proposed(Figure 13).

 $Figure~13~(a)~structure~of~Br \emptyset nsted~acid~site~on~P25~surface.~(b)~mechanism~of~acetalisation~of~benzalde hyde$ 

When the benzaldehyde was adsorbed on the surface of P25, it could be activated by the Brønsted acid sites (H<sup>+</sup>) on the surface of P25 to form a protonated intermediate<sup>[135]</sup>. Afterwards, this intermediate reacted with methanol to generate a hemiacetal, accompanying by deprotonation. Subsequently, the hydroxyl group of the hemiacetal underwent protonation, following by a dehydration process, resulting into the formation of a highly reactive oxonium ion. The next step was the addition of another methanol to the unstable oxonium ion, and after removing a proton again, the final product acetal generated. Therefore, the formation of acetal was a typical two-steps process, in which the formation of hemiacetal was a reversible reaction. However, the corresponding hemiacetal was not detected by the GC-MS either in the published or our study, suggesting that the subsequent generation of the acetal product was faster than the formation of the hemiacetal<sup>[122]</sup>. The lack of observation of hemiacetal was also previously reported in other reaction systems<sup>[122],[136]</sup>. According to the proposed mechanism, pH was important to provide accessible H<sup>+</sup> for the protonation of hemiacetal. The pH of the solution was adjusted to 12 by the addition of alkaline in order to support the hypothesis. Notably, no conversion of benzaldehyde could be observed as expected (**Table 1, entry 4**), consistent with previous reports<sup>[122]</sup> and the proposed mechanism.

Table 2 pH influence on the transformations of benzaldehyde  $1^a$ 

Entry	Cataly	Atmospher	$pH^b$	Light source	Con.	$S_2$ .	$S_3$ .	$S_4$ .	$S_5$ .
	st (mg)	e			$(\%)^{c}$	$(\%)^c$	$(\%)^{c}$	$(\%)^{c}$	$(\%)^{c}$
1	-	Argon	4.5	365 nm LED	96%	52%	6%	42%	-
2	P25	Argon	4.5	365 nm LED	>99%	58%	4%	6%	32%

<sup>&</sup>lt;sup>a</sup>Substrate 1 (1 mmol), catalyst (30 mg), solvent (15 ml methanol), 25 °C, 2h. <sup>b</sup>pH 4.5: HCl in methanol. <sup>c</sup>Determined by GC-MS.  $S_2$  is the selectivity to benzaldehyde dimethyl acetal,  $S_3$  is the selectivity to hydrobenzoin,  $S_4$  is the selectivity to phenylethane 1.2-diol,  $S_5$  is the selectivity to benzyl alcohol.

**Photochemical pinacol coupling of benzaldehyde.** As mentioned above, pinacol coupling is important in the synthesis of pharmacologically important agents. Interestingly, in the absence of a photocatalyst, 76% of benzaldehyde could be converted into products 2, 3 and 4 (selectivities: 12%, 48% and 40%, respectively) under irradiation of 365 nm LED (**Table 1, entry 5**). The pH influence was also investigated and from the results (Table 2, entry 1), acid condition could not prevent the formation of acetalisation<sup>[137]</sup>, leading to a very low selectivity to the pinacol coupling. KOH was then introduced to adjust the pH to 12 (**Table 1, entry 9**). Surprisingly, when the pH increased to 12, the acetalisation process was successfully prevented<sup>[138]</sup>, and the formation of product 4 also disappeared. The formation of 4 was supposed to be a simple addition process between benzaldehyde and methanol, and highly likely under alkaline condition the cleavage occurred<sup>[139],[140]</sup>. As such the reaction exhibited a notable high selectivity (>99%) towards **3** (meso:dl=59:41) with an almost complete conversion of benzaldehyde. This is superior to all the previous results, including both thermo-catalysis and photocatalysis, as all of them required either complex and precious catalysts or complex reaction conditions [128],[141–147]. The mechanism of pinacol coupling was then investigated.

UV-vis absorption spectrum was acquired in order to identify the photosensitive species in this system. As shown in **Figure 14**, benzaldehyde could absorb light with a wavelength less than 400 nm. Thus, the 365 nm LED was able to excite the benzaldehyde molecule to drive the photochemical process, consistent with previous reports<sup>[148],[149]</sup>.

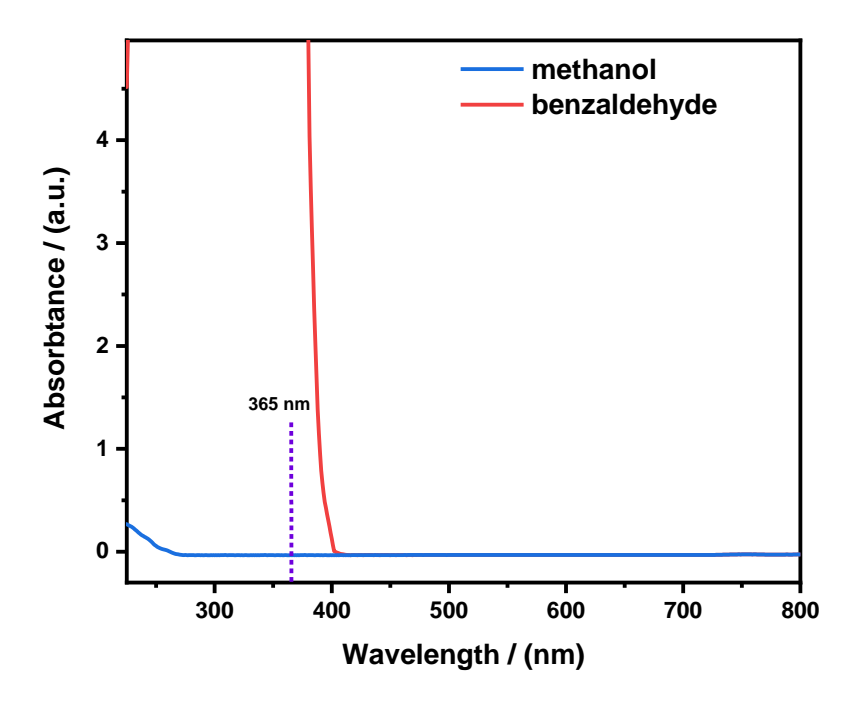


Figure 14 UV-Vis spectrum of methanol and benzaldehyde

To further confirm this process, a series of control experiments were then conducted under irradiation with different wavelengths (**Table 1**, **entries 5-8**). It should be noted that the Xenon light source equipped with a 420 nm long-pass filter (>420 nm) and 450 nm LED could not drive the photochemical processes. In addition, conversion of benzaldehyde was observed when the Xenon lamp with full-arc wavelength was used. All the above results suggested that this photochemical process can be manipulated by UV photons.

It was reported that pinacol coupling of benzaldehyde in alcohol under near-UV light irradiation consisted of two steps<sup>[57]</sup>, the first step was the formation of benzil, and the second step was the hydrogenation of benzil to form hydrobenzoin (this step does not require the participation of a catalyst)<sup>[150]</sup>. However, benzil was not detected in our GC-MS analysis. To further prove this,

benzil was then used as the reactant in methanol solvent, and no conversion was observed with 365 nm LED irradiation in the absence of a catalyst (**Table 1, entry 13**).

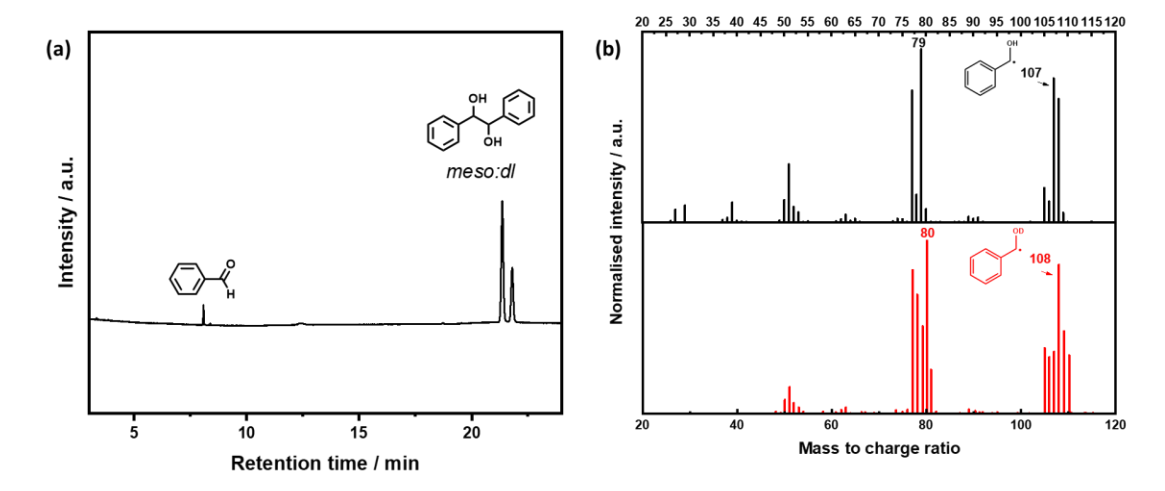


Figure 15 (a) GC-spectrum for isotopic labelling test; (b)Isotopic labelling of pinacol coupling reaction of benzaldehyde. a: Substrate 1 (1 mmol), methanol solvent (15 ml), 365 nm LED, pH 12, 25  $^{\circ}$ C, 2h. b: Substrate 1 (1 mmol), CD<sub>3</sub>OD solvent (15 ml), 365 nm LED, pH 12, 25  $^{\circ}$ C, 2h

The isotopic labelling experiment was further carried out in deuterated methanol (CD<sub>3</sub>OD) to investigate the mechanism. **Figure 15 (a)** indicates that hydrobenzoin was the only product detected in the system and **Figure 15 (b)** shows that only two deuterons were detected and they were each linked with the oxygen atom in hydrobenzoin. This result eliminated the possibility of benzil as an intermediate in the reaction process. This is because if the formation of product **3** was from the reduction of benzil, then when the C=O was reduced, both the protons added onto benzil should be deuterons, and the molecular mass would increase by 4 in total. However, the isotopic labelling result indicated there were only two deuterons on product **3** (two hydroxyl groups), which suggested that the H at -HC=O in benzaldehyde was preserved and the reduction process happened after benzaldehyde became carbon radicals upon absorbing UV photons. Based on the above analysis, a photochemical mechanism has been proposed and shown in **Scheme 38** (left panel).

Initially, benzaldehyde was excited by 365 nm photons and became reduced carbon radicals. Meanwhile, solvent methanol was oxidised into formaldehyde and released H<sub>2</sub> (detected by GC). Consequently, the collision of those reduced carbon radicals resulted in the C–C coupling reaction and the formation of hydrobenzoin.

**Photocatalytic hydrogenation of benzaldehyde.** A notable shift in selectivity occurred when P25 was introduced into the system as a photocatalyst (Table 1, entry 10). Under alkaline condition, the selectivity towards product 3 dramatically decreased to 6%, while a 94% selectivity towards benzyl alcohol appeared after the introduction of the photocatalyst P25. Anatase TiO<sub>2</sub> (PC50) with a similar surface area to P25 was also tested. The result was shown in Table 1, entry 11. it was found that conversion of benzaldehyde remained similar (97%), but the selectivity to benzyl alcohol was reduced to 86%, which was likely due to the efficient charge separation in P25 compared to the pure single-phase PC50. The pH influence was also investigated (Table 2, entry 2), and the result indicated that acid condition could not inhibit the formation of acetalisation [137], leading to a lower selectivity (32%) towards the hydrogenation product. It was supposed that P25 provided reaction sites for benzaldehyde to be adsorbed on so the carbon radicals would have less possibility to collide with each other. To better understand the interaction between P25 and benzaldehyde, Al<sub>2</sub>O<sub>3</sub> was chosen to replace P25 (**Table 1, entry 12**). Al<sub>2</sub>O<sub>3</sub> is not a photocatalyst and after Al<sub>2</sub>O<sub>3</sub> was added, only pinacol coupling reaction occurred in the system and the formation of product 5 was not observed. This result suggested that the hydrogenation of benzaldehyde was not a simple surface adsorption process. It was a photocatalytic process that happened on the surface of P25. The proposed mechanism was shown in **Scheme 38** (right panel)<sup>[151]</sup>. P25 was excited after absorbing UV light as indicated by its UV-vis absorption spectrum (Figure 12), then electron-hole pairs (e<sup>-</sup> + h<sup>+</sup>) were generated<sup>[152]</sup>. These charges next migrated to corresponding

reaction sites. The adsorbed benzaldehyde on the P25 surface could be reduced by the photoelectrons at the reduction site. I further proved the similar mechanism of hydrogenation of benzaldehyde by the isotopic labelling results (**Figure 16**).

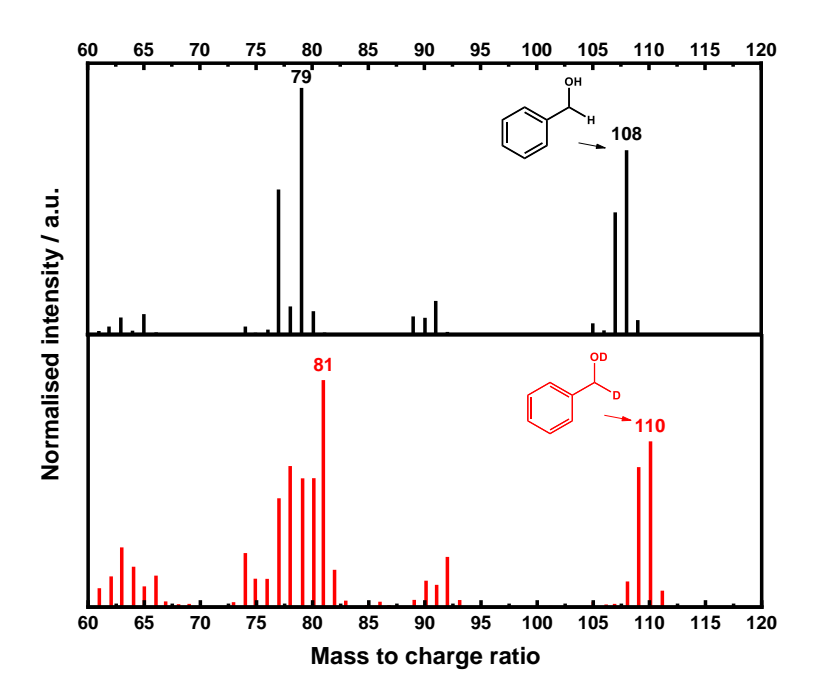
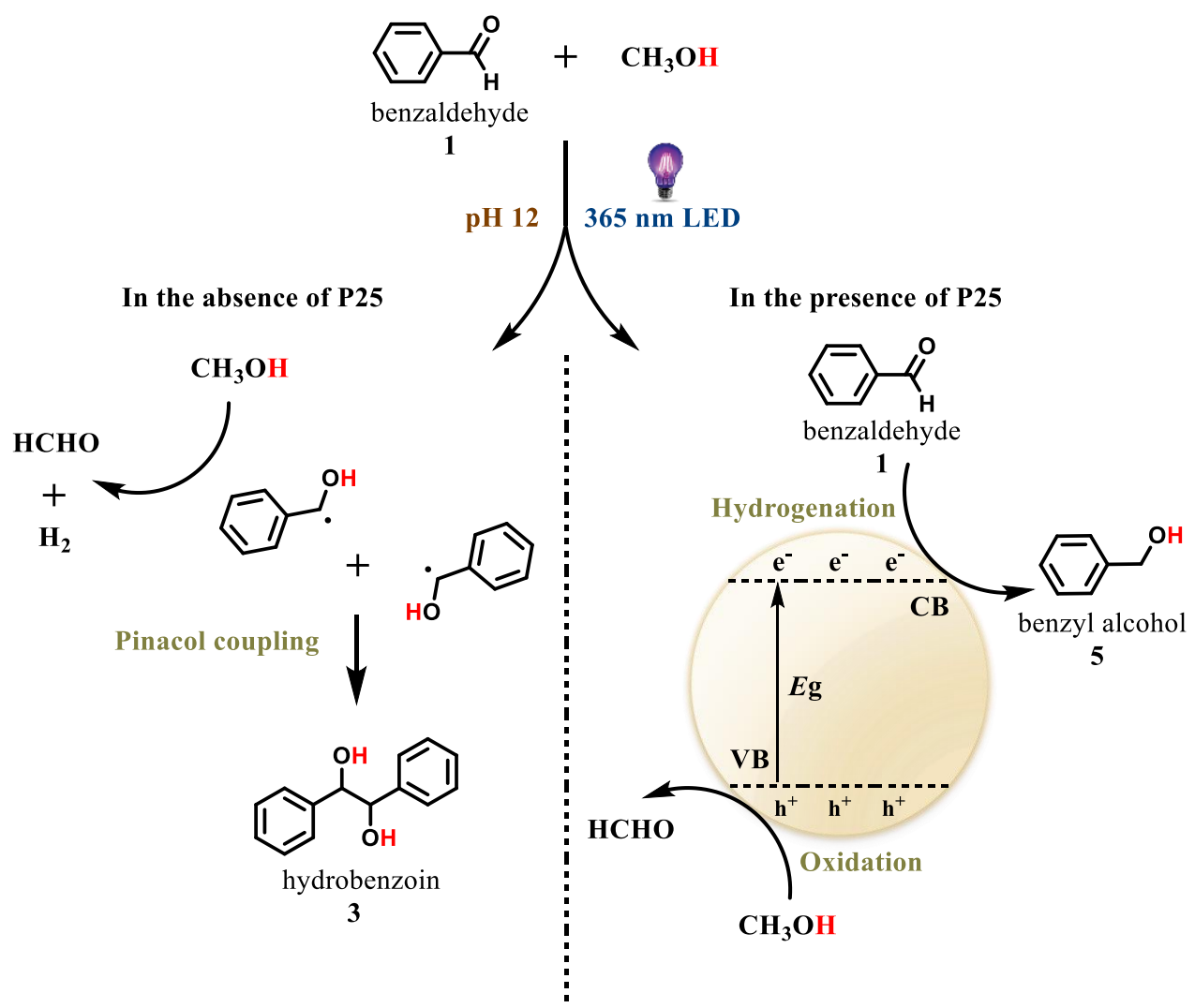


Figure 16 Isotopic labelling result of hydrogenation of benzaldehyde

The methanol solvent behaved as a hole scavenger, was then oxidised by photo-holes. Based on the results, this photocatalytic hydrogenation process was more favourable for carbon radicals compared to collide with each other in the presence of photocatalyst P25, resulting in extremely high selectivity to product 5 other than product 3.



Scheme 38 Purposed mechanisms for photochemical pinacol coupling of benzaldehyde (left panel) and photocatalytic hydrogenation of benzaldehyde (right panel).

# 4.4 Substrate scope

The scope of aldehydes was extended to further prove the above results, which were shown in

Table 3.

Table 3 Scope of different aldehydes

Substrate	Acetalisation <sup>a</sup> (yield / %)	Pinacol coupling <sup>b</sup> (yield / %) (meso:dl)	Hydrogenation <sup>c</sup> (yield / %)
0)	6a, > 99%	6b, 98% (54:46)	HO 6c, > 99%
0,	7a, > 99%	HO OH 7b, 94% (58:42)	HO 7c, > 99%
0	8a, > 99%	8b, 95% (62:38)	HO 8c, > 99%
	9a, 97%	9b, 93% (49:51)	HO 9c, 96%
O F 10	F 0 0 10a, 96%	HO OH F F 10b, 57% (52:48)	HO F 10c, 97%

10a, 96% 10b, 57% (52:48) 10c, 97% All yields were determined by GC-MS. <sup>a</sup>Acetalisation: Substrate (0.5 mmol), P25 (30 mg), solvent (15 ml methanol), 25 °C, 2h. <sup>b</sup>Pinacol coupling: Substrate (0.5 mmol), 15 ml solvent (pH 12: 0.01 M KOH in methanol), 365 nm LED, 25 °C, 2h. <sup>c</sup>Hydrogenation: Substrate (0.5 mmol), P25 (30 mg), 15 ml solvent (pH 12: 0.01 M KOH in methanol), 365 nm LED, 25 °C, 2h.

Several aldehydes have been investigated. It was clear that electron-donating group (-CH<sub>3</sub>) at either para, meta, or ortho position would not affect the proposed selectivities tuning. For substrate **6-8**, 99% yield of desired acetal products and alcohols were obtained (**6a-8a**, **6c-8c**) and all the yields of pinacol coupling products were over 90% (**6b-8b**). For substrate **9**, high yields for all three pathways were observed too (97% yield for **9a**, 93% yield for **9b** and 96% yield for **9c**). However, when the electron-withdrawing group (-F) was added to para position (**10**), the selectivity towards pinacol coupling dropped to 57% (**10b**). In contrast, the selectivities towards acetalization or hydrogenation pathways remained similar, 96% for **10a** and 97% for **10c**, respectively. Cyano group (-CN) was also tested. However, the substrate did not absorb photons at 365 nm, thus could not undertake these transformations (UV-vis spectrum results of those substrates were shown in **Figure 17-Figure 22**). All these are consistent with the proposed reaction pathways.

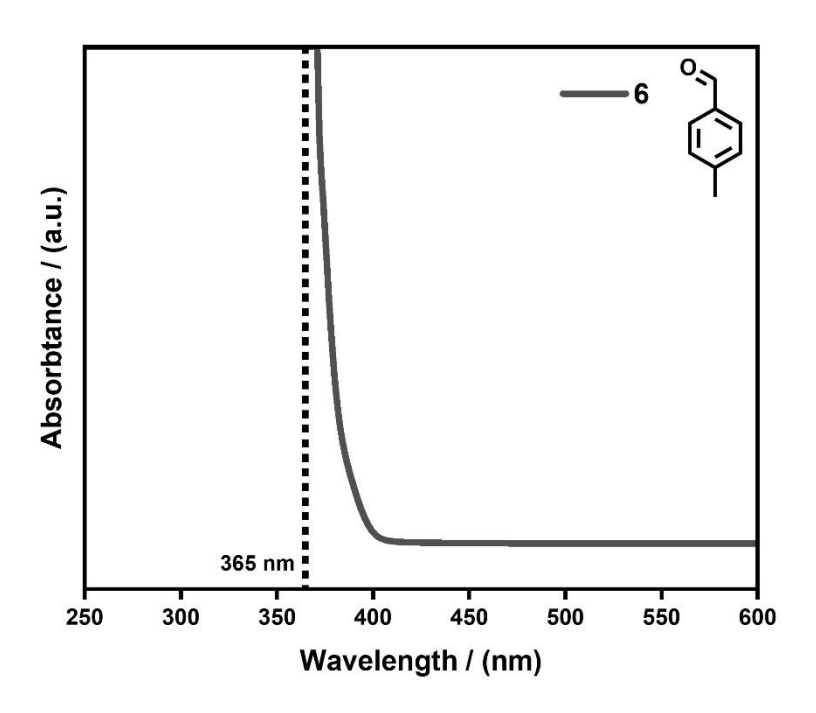


Figure 17 UV-vis spectrum of substrate 6

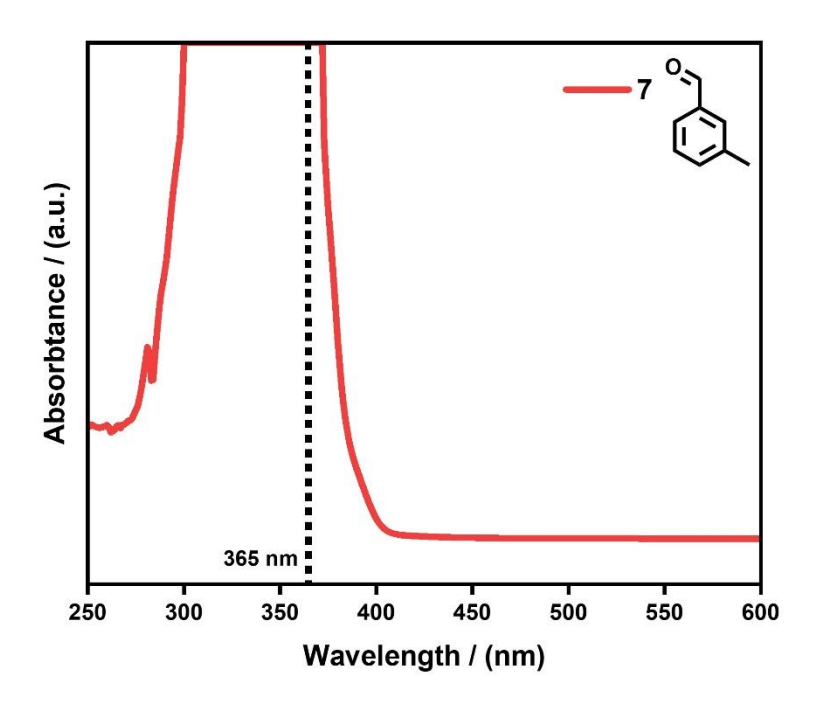


Figure 18 UV-vis spectrum of substrate 7

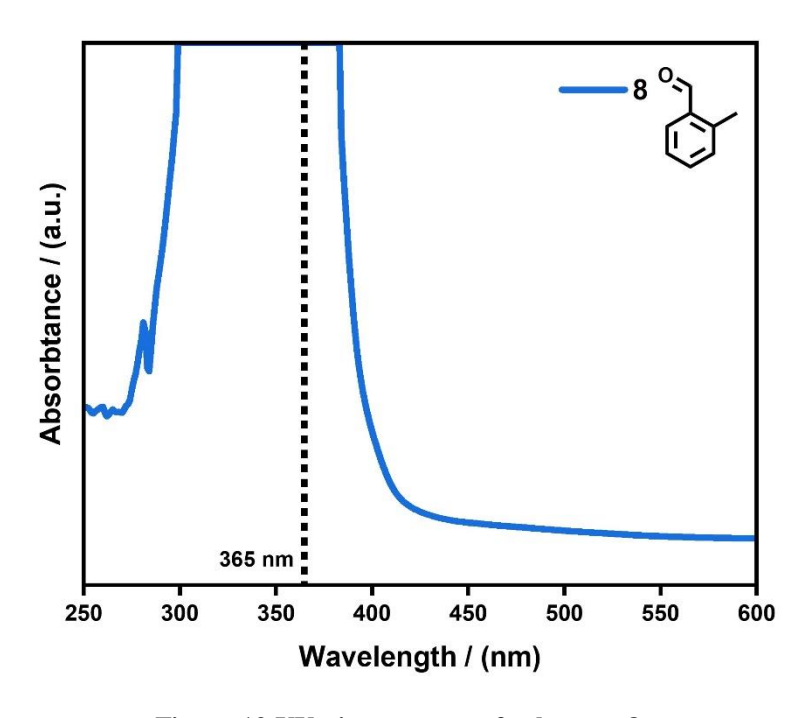


Figure 19 UV-vis spectrum of substrate 8

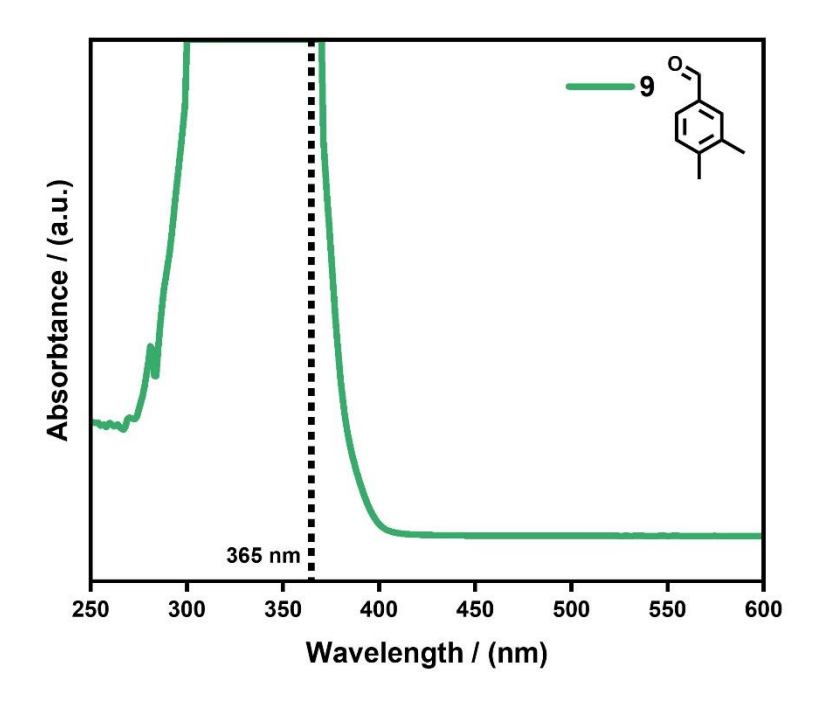


Figure 20 UV-vis spectrum of substrate 9

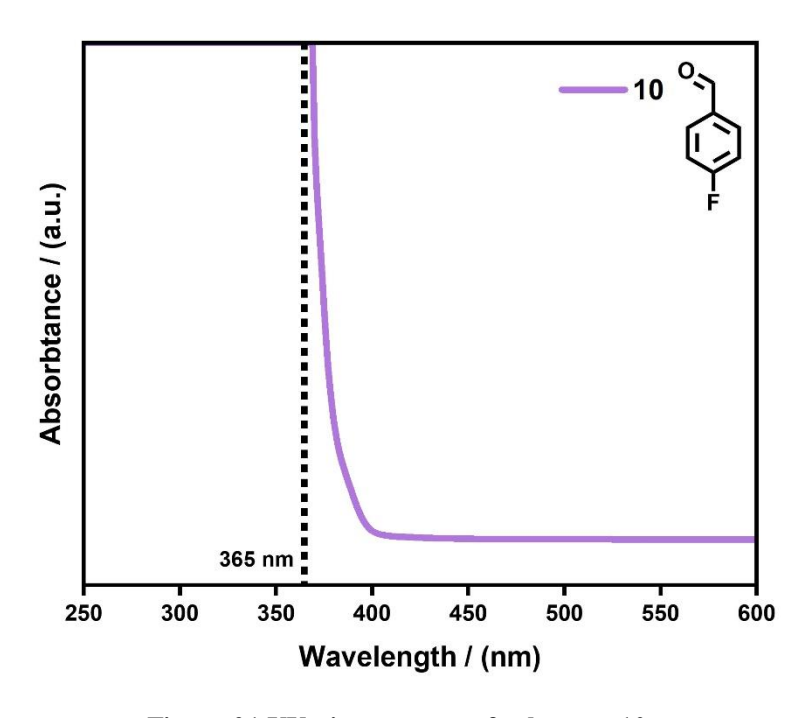


Figure 21 UV-vis spectrum of substrate 10

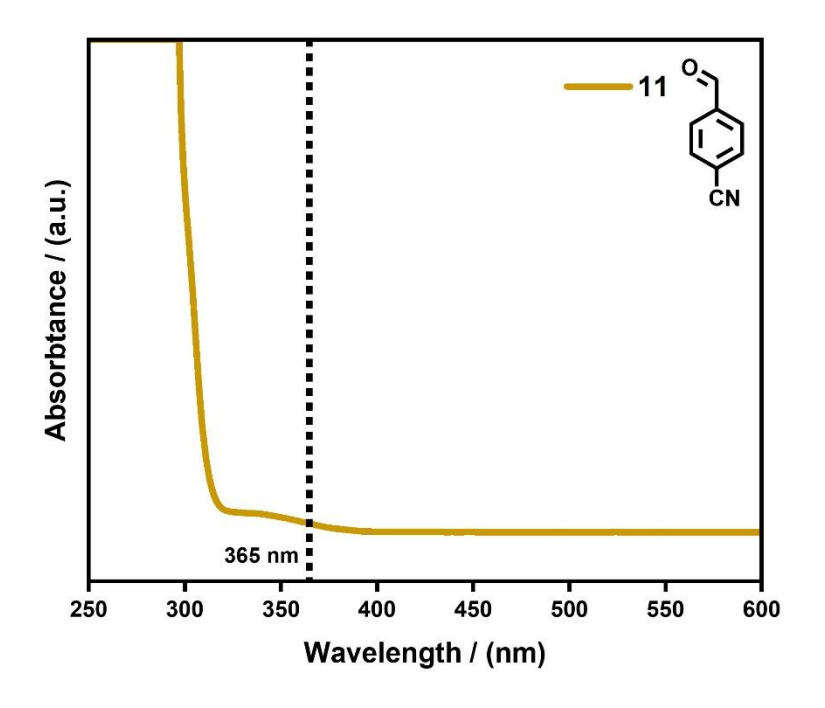


Figure 22 UV-vis spectrum of substrate 11

### 4.4 Conclusion

I developed a green and versatile method to achieve acetalisation, pinacol coupling and hydrogenation of benzaldehyde. Through a photochemical pathway, pinacol coupling of benzaldehyde was achieved in the absence of P25 at pH 12 with 96% conversion and 100% selectivity. The mechanism of this reaction was studied by isotopic labelling experiment and the result indicated that the reaction process was different from the previous report as this was a one-step process without benzil being the intermediate. Compared to other reported systems, this was so far the most economically friendly and efficient method to achieve such high yield product because it did not require any catalyst and complicated experimental conditions. 85% yield for hydrogenation was achieved in the presence of P25 photocatalyst and under 365 nm irradiation. The catalyst could completely shift the selectivity towards pinacol coupling (100%) to benzyl

alcohol (94%) because benzaldehyde radicals prefer to adsorb on the surface of P25 and be reduced by photoelectrons instead of colliding and combining each other. Acetalisation was also achieved using P25 catalyst with a yield of 92% via a low temperature thermal catalytic pathway. These results provided an effective method to synthesise different compounds with high selectivity from benzaldehyde, providing new insight for further development of photocatalysts.

# Chapter 5 Effective Activation of Strong C-Cl Bonds for Robust Homo-Coupling in Photosynthesis of Bibenzyl

In previous chapter, I found that UV light could achieve homo-coupling of benzaldehyde via photochemical pathway. However, for a typical photochemistry process, it is difficult to control the reaction selectivity. In this chapter, I aimed to achieve challenging C–Cl bonds activation and selectivity control of benzyl chloride homo-coupling using photocatalytic system.

### 5.1 Introduction

Carbon-carbon (C–C) coupling is one of the most fundamental reactions in modern organic synthesis<sup>[153,154]</sup>. Dihydrostilbenoids, as natural phenols, are often synthesized using the key chemical of bibenzyl. Due to dihydrostilbenoids' wide applications<sup>[155–158]</sup> in the pharmaceutical and chemical industry and their scarce existence in nature<sup>[159–162]</sup>, the synthesis of bibenzyl compounds has gained significant attention among various coupling reactions in the past decades<sup>[162–164]</sup>. However, harsh reaction conditions (e.g., high temperature) and complicated and high-cost catalysts (e.g., noble metals and designed metal-complex) are often needed to achieve high yield and selectivity of bibenzyls<sup>[162,165–167]</sup>.

Heterogeneous photocatalysis, as a growing field in organic synthesis, has shown great potential for various C–C coupling reactions, where the reactions can proceed under mild conditions with green energy sources (e.g., solar energy). Furthermore, compared to homogenous photocatalysis, heterogeneous photocatalysis also exhibits the superiority of outstanding recyclability, high stability and easy separation of the products from solvents and catalysts. Recently, a series of heterogenous photocatalysts have been reported for the C–C homo-coupling reaction of different alkyl halides.

For example, colloidal CsPbBr<sub>3</sub> perovskite was reported as a photosensitizer for the homocoupling of benzyl bromides (7 examples, yield 42%–83%) with TON as high as 17500, but this perovskite could only be used twice, and aprotic solvent and organic scavenger with a prolonged reaction time were required (20–48 h)<sup>[62]</sup>. Modified AgGaO<sub>2</sub> with shape engineering was synthesized, and the flat AgGaO<sub>2</sub> with electron-rich (001) facets exhibited 20 times higher activity compared to (012) facets stretched AgGaO<sub>2</sub> in dehalogenative homo-coupling of benzyl bromides (5 examples, yield 75%–83%)<sup>[168]</sup>. The hole-rich stretched AgGaO<sub>2</sub>, on the other hand, showed better photocatalytic performance in the oxidative homo-coupling of aniline, extending shape engineering in tuning selectivity for coupling reactions. Surface hydroxylation modified graphitic carbon nitride (gCN-OH) was reported to efficiently activate water and use it as hydrogen donors under mild conditions. It could be applied to a series of coupling reactions, including homocoupling of benzyl bromides (11 examples, yield 80%–91%)<sup>[169]</sup>. All these indicate a clean route for organic synthesis using renewable energy.

Alkyl halides are important reactants in constructing C–C bond for fine chemicals, pharmaceutically active compounds and agricultural chemicals [170]. Compared with alkyl chloride, alkyl bromides have been used and reported more intensively [62,102,168,169,171–174] because C–Br bond has a much lower energy (285 kJ mol<sup>-1</sup>) than that of C–Cl (327 kJ mol<sup>-1</sup>)[175], so the former is more easily activated and the product selectivity is also well controlled. However, alkyl chlorides have superior properties than alkyl bromides [176], such as low-cost and abundant and reduced toxicity. Due to its inert nature, alkyl chlorides have been considered as sluggish reactants in organic synthesis [38,170,177]. It is really challenging to achieve high yield and selectivity using alkyl chloride for the C–C homocoupling reaction.

Herein, after screening a series of noble metals and transition metals, copper was selected as the best co-catalyst to decorate the robust semiconductor ZnO forming the efficient photocatalyst to drive the homo-coupling of benzyl chlorides at room temperature. With the manipulation of electron donors, hydrogen donors and water content, the optimized sample 1.5% Cu/ZnO achieves a 99% conversion with a 93% selectivity to desired product bibenzyl. Such excellent performance is also stable for up to 8 cycles. Furthermore, the university of this low-cost system has been confirmed by 11 various chloride derivatives with a good or very high yield (60% to 96%). The high selectivity is attributed to the synergetic effect between Cu and ZnO, in which benzyl radicals are stabilized on Cu for further coupling and protons are adsorbed on the ZnO support. In addition, the high yield rate is also beneficial from the promoted charge transfer between ZnO and Cu.

## **5.2 Experimental Section**

**Synthesis of ZnO:** The ZnO NPs were prepared by a precipitation method<sup>[178]</sup>, where 0.01 mol Zn(NO<sub>3</sub>)<sub>2</sub> and 0.01 mol oxalic acid were separately dissolved in 100 ml deionised water in two beakers at room temperature. The oxalic acid solution was then dropwise added into Zn(NO<sub>3</sub>)<sub>2</sub> solution to obtain zinc oxalate precipitates. After the precipitates were washed and filtered, the dried powders were calcined at 350 °C in air for 6 h.

## **Synthesis of metal/ZnO photocatalyst:**

**I:** Cu, Pd, Ag, In, Rh, Au, Pt, Ru, Ir NPs were prepared on ZnO via a photo-deposition method. In particular the deposition of Cu on ZnO is described as the following:

200 mg of ZnO powders were dispersed into a methanol water mixture (10 ml methanol and 30 ml water), certain amount of  $Cu(NO_3)_2 \cdot 2.5H_2O(0.1, 0.5, 1, 1.5, 2 \text{ wt\% of Cu})$  was added into the reactor under continuous stirring. The reactor was sonicated for 10min to form a homogeneous suspension and then degassed by argon for 15min to remove dissolved oxygen (O<sub>2</sub>). The purged reactor was later irradiated under 365 nm LED for 2 h in a multi-channel reactor. After irradiation, the reacted suspension (Cu/ZnO) was filtered and washed by deionised water for 3 times, and eventually dried at 60 °C in a vacuum oven.

For the deposition of 1.5 wt% Pd, Ag, In, Rh, Au, Pt, Ru and Ir, PdCl<sub>2</sub> anhydrous, AgNO<sub>3</sub>, InCl<sub>3</sub>, RhCl<sub>3</sub>· 3H<sub>2</sub>O, HAuCl<sub>4</sub>·4H<sub>2</sub>O, H<sub>2</sub>PtCl<sub>6</sub>, RuCl<sub>3</sub>·xH<sub>2</sub>O and IrCl<sub>3</sub>·xH<sub>2</sub>O were used as the metal source, respectively and other procedure is identical to the Cu loading

**II:** Ni, Fe, Co were prepared on ZnO via an impregnation method: certain amount of Ni(NO<sub>3</sub>)<sub>2</sub>·6H<sub>2</sub>O (Co(NO<sub>3</sub>)<sub>2</sub>·6H<sub>2</sub>O and Fe(NO<sub>3</sub>)<sub>3</sub>·9H<sub>2</sub>O for Co and Fe) was firstly dissolved in 500 μl deionised water. 200 mg ZnO was then added to the above solution under vigorous stirring in an alumina crucible. After evaporating water, the crucible was transferred to a muffle furnace and calcined at 400 °C for 2 h with a ramping rate of 5 °C/min.

## Photocatalytic activity tests:

Firstly, 10 mg Cu/ZnO photocatalyst was dispersed into 5 ml solution (2-propanol: water = 1:1) containing 10 mM benzyl chloride, and the solution was then sonicated for 5min to form a homogeneous suspension. The suspension was purged by Argon for 10 min to remove dissolved O<sub>2</sub>. The reactor containing the suspension was eventually placed into a PCX-50C multi-channel photochemical reaction system equipped with 365 nm LEDs and irradiated for 6 h under continuously stirring condition at room temperature (temperature was controlled by a cooling bath

thermostat). The solid photocatalyst was filtered and then the liquid mixture was analysed by Shimadzu GC-MS-QP2010SE using Rxi-5SilMS Column.

# **DFT** calculation (**DFT** calculation was conducted by **Dr** Xiaoyu Han):

The Vienna Ab Initio Package (VASP)[179],[180] was used to perform all the density functional theory (DFT) calculations within the generalised gradient approximation (GGA) using the PBE<sup>[181]</sup> formulation. The projected augmented wave (PAW) potentials were used [182],[183] to describe the ionic cores and take valence electrons into account using a plane-wave basis set with a kinetic energy cut-off of 450 eV. Partial occupancies of the Kohn-Sham orbitals were allowed using the Gaussian smearing method and a width of 0.05 eV. The on-site corrections (DFT+U) have been applied to the 3d electron of Ti atoms (U<sub>eff</sub>=4.5 eV) by the approach from Dudarrev et al. [184] The electronic energy was considered self-consistent when the energy change was smaller than 10<sup>-5</sup> eV. Geometry optimisation was considered convergent when the force change was smaller than 0.02 eV/Å. Grimme's DFT-D3 methodology<sup>[185]</sup> was used to describe the dispersion interactions. The equilibrium lattice constants wurtzite ZnO unit cell were optimised to be a=b=3.272 Å and c=5.291 Å when using a 15×15×9 Monkhorst-Pack k-point grid for Brillouin zone sampling. It was then used to construct a ZnO(100) surface model with  $p(4\times2)$  periodicity in the X and Y directions and three stoichiometric layers in the Z direction by vacuum depth of 15 Å in order to separate the surface slab from its periodic duplicates. In another model, a Cu<sub>10</sub> cluster resides onto ZnO(100). During structural optimisations, a  $2\times2\times1$  in the Brillouin zone was used for k-point sampling, and the bottom stoichiometric layer was fixed while the rest were allowed to relax fully. The equilibrium lattice constants of anatase TiO<sub>2</sub> unit cell were optimised to be a=b=3.858 Å and c=9.652 Å when using a 10×10×4 Monkhorst-Pack k-point grid for Brillouin zone sampling. It

was then used to construct a  $TiO_2(101)$  surface model with  $p(1\times3)$  periodicity in the X and Y directions and two stoichiometric layers in the Z direction by vacuum depth of 15 Å in order to separate the surface slab from its periodic duplicates. A  $Cu_{10}$  cluster resides onto  $TiO_2(101)$ . During structural optimisations, a  $2\times1\times1$  in the Brillouin zone was used for k-point sampling, and the bottom stoichiometric layer was fixed while the rest were allowed to relax fully.

The adsorption energy (E<sub>ad</sub>) was defined as

$$E_{ad} = E_{total} - E_{sub} - E_{adsorbent}$$

where  $E_{total}$ ,  $E_{sub}$  and  $E_{adsorbent}$  is the energy of the adsorbate adsorbed on the polyimide, the energy of clean polyimide, and the energy of adsorbent molecule in a cubic periodic box with a side length of 20 Å and a  $1\times1\times1$  Monkhorst-Pack k-point grid for Brillouin zone sampling, respectively.

## **DFT** for Mulliken population analysis

The DFT calculation was performed with the Gaussian 16 package using the hybrid B3LYP functionals. The 6-311++G\*\* basis set was used for C, H and Cl elements, and SDD pseudo potential basis set for Cu element<sup>[186,187]</sup>.

## **5.3 Result and Discussion**

## **5.3.1 Catalytic Performance**

The ZnO powders were prepared by a precipitation method<sup>[178]</sup>. The metal-loaded ZnO samples were prepared by either photo-deposition or impregnation methods described above. From the X-ray diffraction (XRD) results (**Figure 23**), ZnO NPs with excellent crystallinity were successfully

synthesized, which indexed to ZnO (JCPDS no: 043-0002). Various metals were then loaded on this ZnO support with a similar amount of 1.5 wt%. No extra peaks for the other metal species can be observed in the spectra, probably due to either low concentration and/or high dispersion on the support of  $ZnO^{[188]}$ .

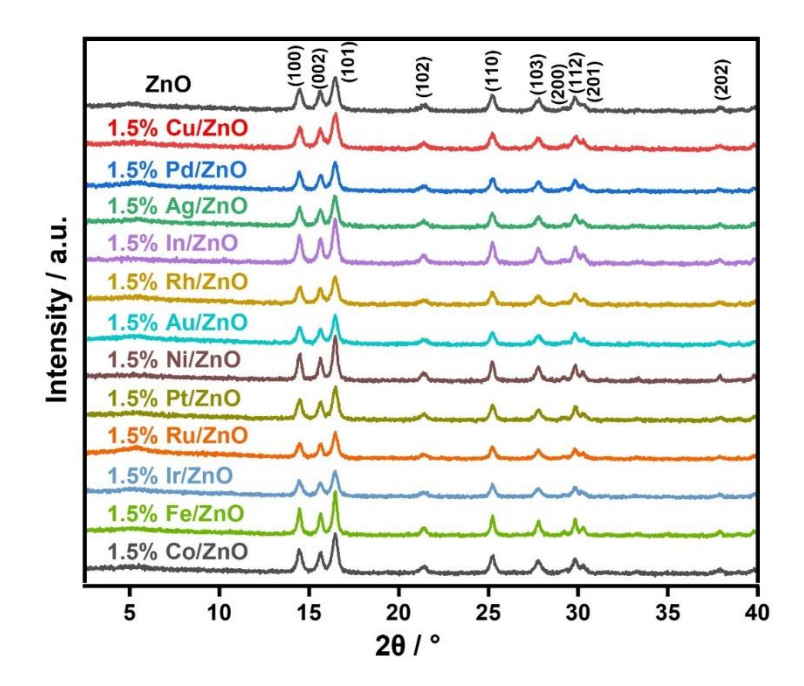


Figure 23 XRD patterns of bare ZnO, 1.5% M/ZnO (M= Cu, Pd, Ag, In, Rh, Au, Ni, Pt, Ru, Ir, Fe, Co) samples

Then, their photocatalytic activity toward homo-coupling of benzyl chloride was evaluated, as shown in **Figure 24**.

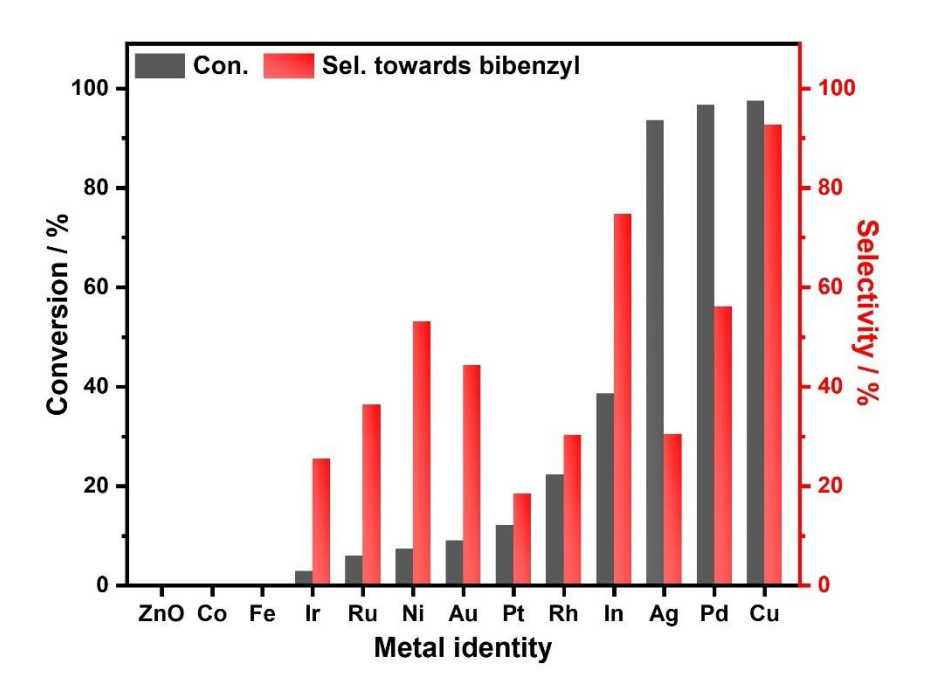


Figure 24 Photocatalytic benzyl chloride coupling using a series of selected metals decorated ZnO, 1.5 wt% M/ZnO (M=Cu, Pd, Ag, In, Rh, Au, Ni, Pt, Ru, Ir, Fe, Co). Reaction conditions: 10mM reactant, 10 mg photocatalyst in 5 ml solvent (2-propanol: water = 1:1) under 365 nm LED irradiation for 6 h in Ar at room temperature

Table 4 Performance of bibenzyl synthesis over different photocatalysts.

Entry	Catalyst	Metal concentration	Con. (%)	Sel.1a (%)	Sel.1b (%)	Sel.1c (%)
1	ZnO	-	-	-	-	-
2	Co/ZnO	1.5%	-	-	-	-
3	Fe/ZnO	1.5%	-	-	-	-
4	Ir/ZnO	1.5%	3%	26%	40%	34%
5	Ru/ZnO	1.5%	6%	37%	34%	29%
6	Ni/ZnO	1.5%	7%	53%	12%	35%
7	Au/ZnO	1.5%	9%	44%	31%	25%
8	Pt/ZnO	1.5%	12%	18%	65%	17%

9	Rh/ZnO	1.5%	22%	31%	62%	7%
10	In/ZnO	1.5%	38%	75%	13%	12%
11	Ag/ZnO	1.5%	94%	31%	68%	1%
12	Pd/ZnO	1.5%	96%	49%	44%	4%
13	Cu/ZnO	1.5%	97%	93%	3%	2%
14	Cu/ZnO	0.1%	86%	78%	7%	8%
15	Cu/ZnO	0.5%	88%	86%	3%	2%
16	Cu/ZnO	1%	91%	87%	4%	2%
17	Cu/ZnO	2%	98%	86%	3%	2%
18	Cu/ZnO	2.5%	99%	84%	3%	3%

Reaction conditions: 10mM reactant, 10 mg photocatalyst in 5 ml solvent (2-propanol: water = 1:1) under 365 nm LED irradiation for 6 h in Ar at room temperature.

After 6 h light irradiation (λ = 365 nm), ZnO exhibits negligible conversion of benzyl chloride, likely owing to the high recombination rate of photoinduced electrons and holes. Among 12 metal co-catalysts tested, most of them display low conversion of benzyl chloride (< 22%) and low selectivity (< 50%) towards bibenzyl (detailed activity is summarized in **Table 4**, entries 1-13). Two possible reasons are behind this result. Some metals (i.e., Ir, Rh, Ni, Pt) show high performance for the dehydrogenation of alcohols<sup>[189,190]</sup>, so there is a great possibility that the adsorbed benzyl radical would undergo hydrogenation and generate toluene as a side reaction. Some metals, such as Fe, Co and Ru, exhibit strong interactions with halides<sup>[33][191]</sup>, which could lead to poisoning effects of co-catalysts, hence the low activity. Surprisingly, Indium (In) displays relatively high selectivity towards bibenzyl (75%), but the conversion of benzyl chloride is only 38%. This may due to lower charge separation/transfer efficiency in the photocatalytic process.

Ag, Pd and Cu show excellent conversion of over 90% of benzyl chloride. In particular, Cu shows both a very high conversion of 98% and selectivity of 93% to bibenzyl (reaction equations are shown in **Equation 6**).

Equation 6 Overall equation for photocatalytic homo-coupling of benzyl chloride

As for Pd and Ag, the dehalogenation product toluene is the main byproduct with up to 44% and 68% selectivity, respectively, and a small amount (3% selectivity) of benzyl alcohol, which is another byproduct from hydrolysis, is observed in every experiment (GC spectra of products over 3 photocatalysts are shown in **Figure 25**).

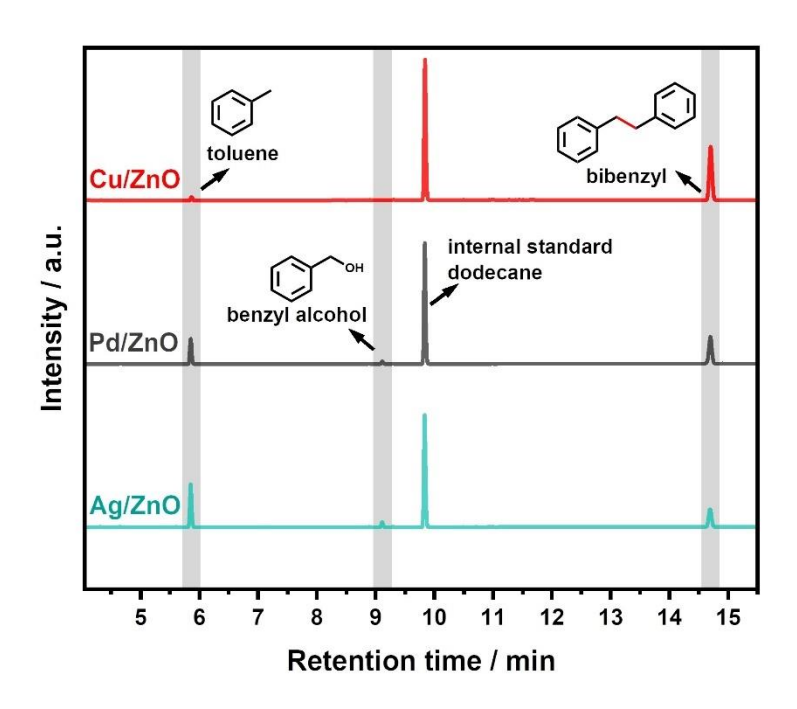


Figure 25 GC spectra of products over 1.5% M/ZnO (M= Cu, Pd, Ag)

The temporal study of benzyl chloride homo-coupling over 1.5% M/ZnO (M=Cu, Pd, Ag) was then conducted. For Cu decorated ZnO (**Figure 26**), the conversion of benzyl chloride exhibits a linear increase and the selectivity towards bibenzyl well remains above 90% throughout the reaction time while only small amounts of toluene and benzyl alcohol are detected.

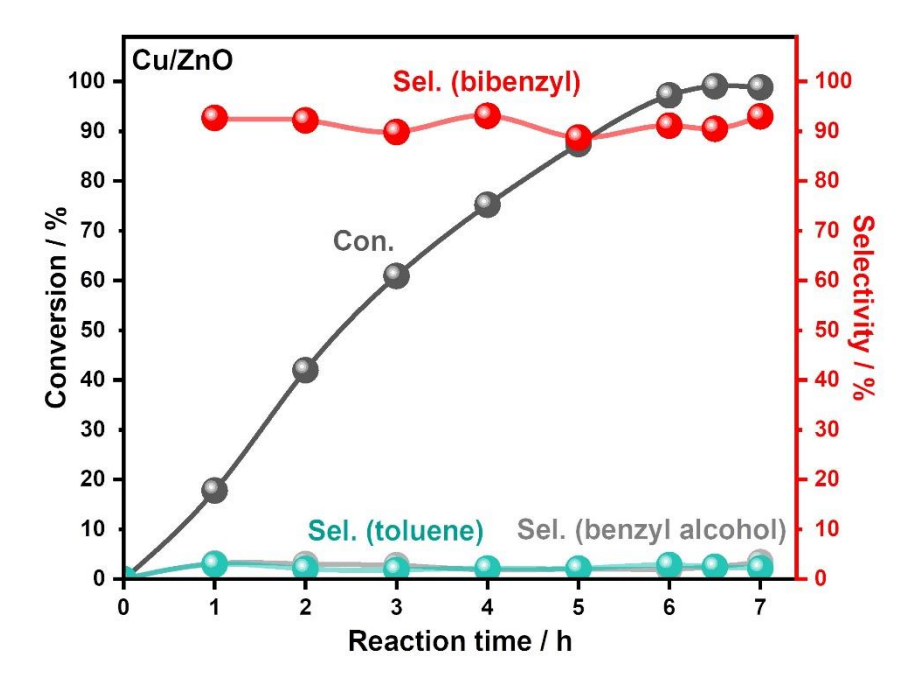


Figure 26 Temporal study of photocatalytic benzyl chloride conversion over 1.5 wt% Cu/ ZnO. Reaction conditions: 10 mM reactant, 10 mg photocatalyst in 5 ml solvent (2-propanol: water = 1:1) under 365 nm LED irradiation for 6h, Ar, room temperature

For Pd species (**Figure 27**), the temporal study result shows that the selectivity to bibenzyl and toluene remain constant at around 55% and 43% during the reaction time, respectively. The adsorption energy of hydrogen atoms on Pd is ~ -0.43 eV<sup>[189]</sup>, which is much negative compared to on Cu (~0.05 eV), so the low selectivity to bibenzyl may be attributed to the excessive amount of surface-adsorbed protons, which favours the conversion of the intermediate (benzyl radical) to the dehalogenation product (toluene).

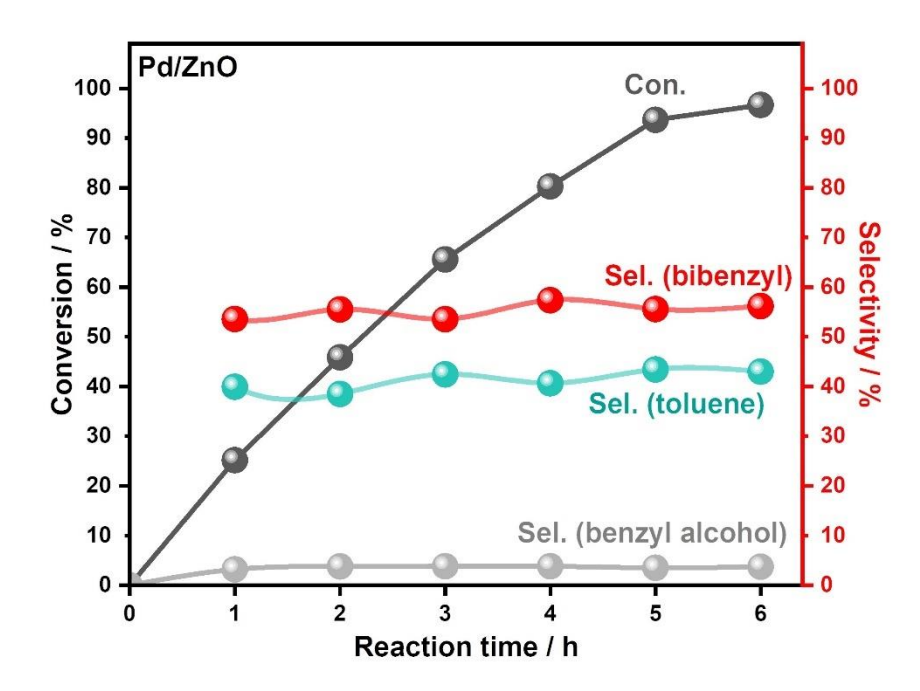


Figure 27 Temporal study of photocatalytic benzyl chloride conversion using Pd/ ZnO. Reaction conditions: 10 mM reactant, 10 mg photocatalyst in 5 ml solvent (2-propanol: water = 1:1) under 365 nm LED irradiation for 6h, Ar, room temperature

In addition, from the temporal study result of Ag/ZnO (**Figure 28**), the selectivity to bibenzyl gradually drops from 52% to 31% after 6 h irradiation while the selectivity towards toluene increases accordingly (from 47% to 68%).

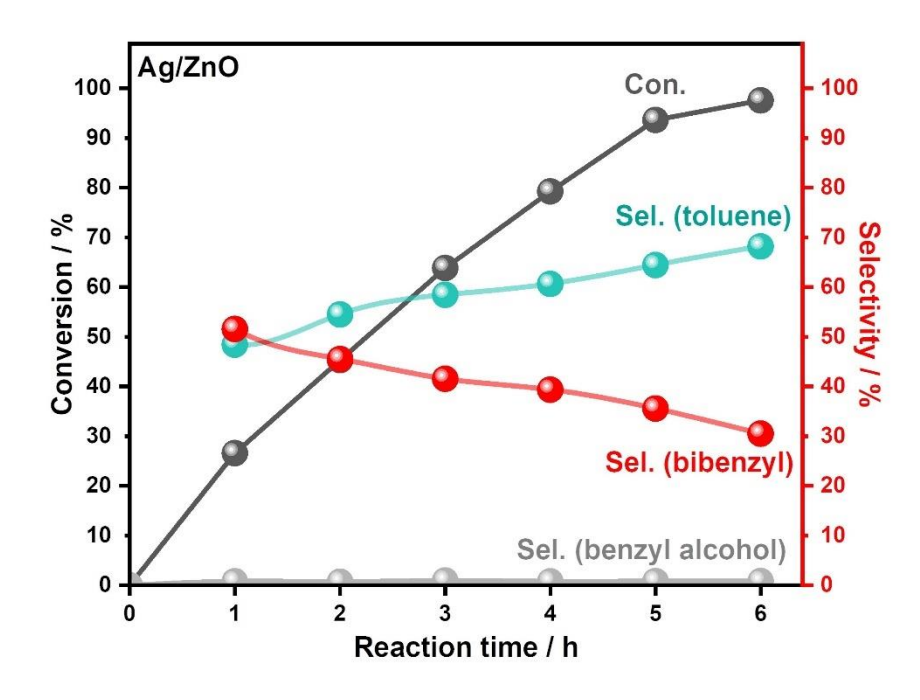


Figure 28 Temporal study of photocatalytic benzyl chloride conversion using Ag/ ZnO. Reaction conditions: 10 mM reactant, 10 mg photocatalyst in 5 ml solvent (2-propanol: water = 1:1) under 365 nm LED irradiation for 6h, Ar, room temperature

The reason behind the poor selectivity of Ag co-catalyst is likely due to the poison by Cl<sup>-</sup> ions that gradually convert silver species into AgCl, which has a more decisive influence on the coupling process (bibenzyl production) than on the hydrogenation process (toluene production). In order to prove this hypothesis, a higher silver concentration (5 wt%) decorated ZnO was therefore prepared. The XRD result (**Figure 29**) of 5% Ag/ZnO sample after reaction shows peaks corresponding to (111), (200) and (222) lattice planes of AgCl, indicating the poison of Ag NPs by Cl<sup>-</sup> ions.

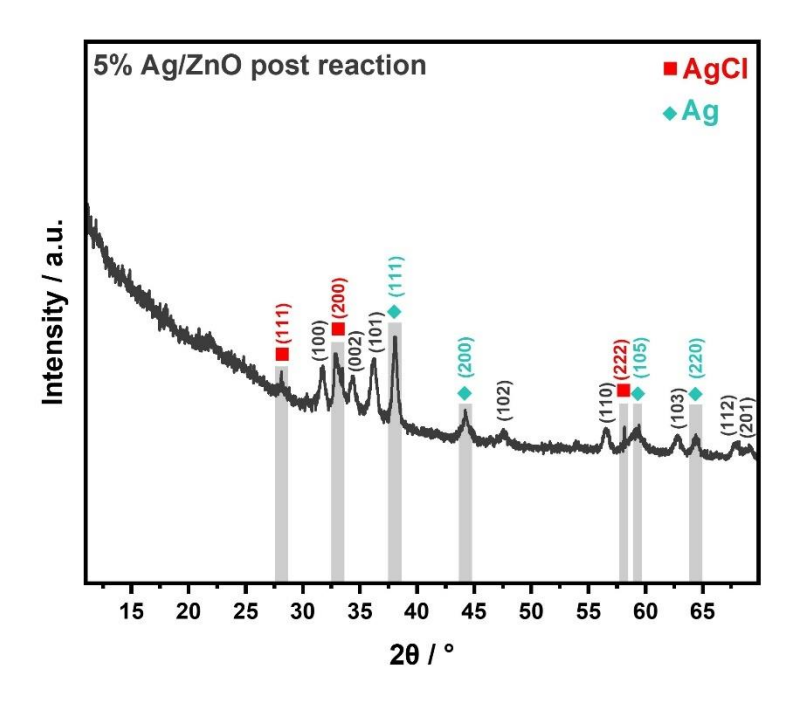


Figure 29 XRD patterns of 5% Ag/ZnO after reaction sample

Based on the screening results, Cu was then selected as the best co-catalyst to further improve bibenzyl production. The loading amount effect of Cu on the catalytic performance was then investigated (detailed activity is summarized in **Table 4**, entries 14-18), as shown in **Figure 30**.

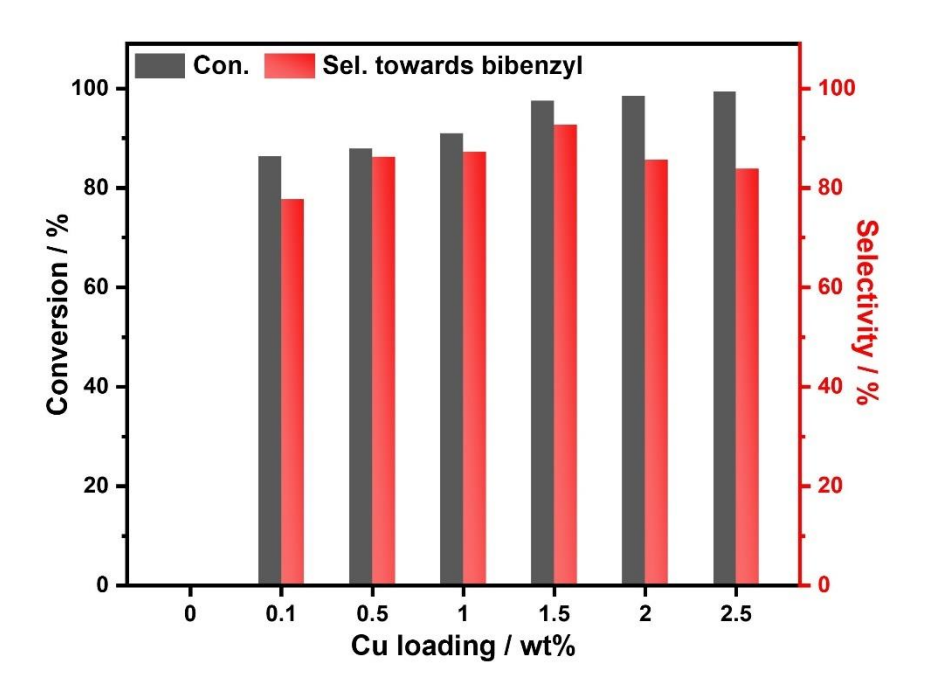


Figure 30 Effect of Cu loading on the photocatalytic coupling of benzyl chloride. Reaction conditions: 10mM reactant, 10mg photocatalyst in 5ml solvent (2-propanol: water = 1:1) under 365mm LED irradiation for 6mm in Ar at room temperature

It should be noted that even a trace amount (low to 0.1 wt%) of Cu loading can increase the selectivity to the desired bibenzyl from 0 % to 78%, together with more than 80% conversion. Further increasing the loading amount of Cu can improve both conversion and selectivity accordingly, and the highest selectivity (93%) towards bibenzyl can be achieved at 1.5 wt% Cu loading with a conversion of 100% after 6 h reaction. Additionally, excessive Cu loading cannot further improve the conversion of benzyl chloride, and the selectivity to bibenzyl shows a gradual decrease. This is likely owing to the increase of CuO<sub>x</sub> particle size with excessive Cu covering on the surface<sup>[192]</sup>. Inductively coupled plasma atomic optical emission spectroscopy (ICP-OES) was used to determine the actual amount of Cu loaded for the 1.5 wt% Cu/ZnO sample, and the loading amount of Cu is measured to be 1.42 wt %, very close to the nominal value. Therefore, 1.5 wt%

Cu/ZnO is selected as the best candidate for the subsequent investigation (denoted Cu/ZnO thereafter)

The effect of solvents was then investigated, as shown in **Figure 31**. After light irradiation for 3 h, the systems using tetrahydrofuran (THF), acetonitrile (MeCN) and dimethylformamide (DMF) show trace or even no yield of bibenzyl. As all three aprotic solvents are not suitable electron donors as reported due to their higher oxidation potentials<sup>[193],[56]</sup>, it is unfavourable to inject electrons into the photocatalyst to facilitate the reduction half-reaction for the dehalogenative process. Then, alcohols as widely used electron donors in photocatalysis [194] were applied, including methanol, ethanol, 1-propanol and 2-propanol. Expectedly, the yield of bibenzyl can be observed after the use of alcohol solvents and the highest selectivity of 63% is achieved when 2propanol is used as the solvent. It is interesting to find that the yield of undesired byproduct toluene decreases with the extension of the carbon chain of the alcohols used (methanol > 1propanol)<sup>[195]</sup>. Longer carbon chains may result in stronger steric effects, offering less interaction opportunities for the alcohol to directly donate the proton to the key intermediate (benzyl radical) to form toluene. Thus, it is reasonable to see 2-propanol as secondary alcohol shows the least selectivity (only 3%) to toluene as its hydroxyl group at the middle carbon atom rather than the terminal position, which is less accessible.

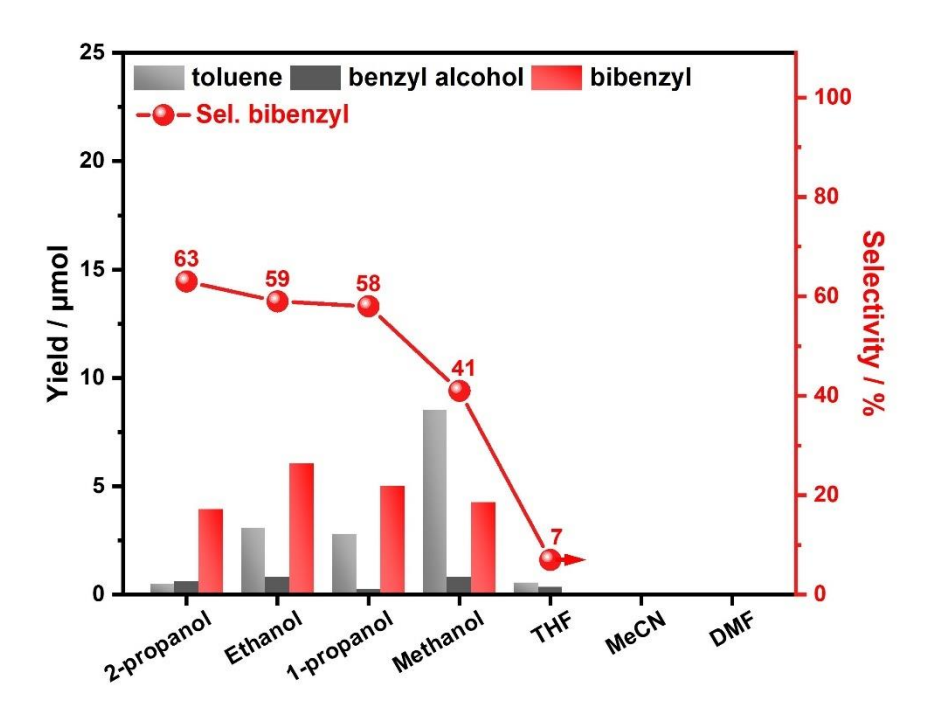


Figure 31 Solvent effect on the photocatalytic coupling of benzyl chloride. Reaction conditions: 10mM reactant, 10 mg photocatalyst in 5 ml pure solvent under 365 nm LED irradiation for 2h in Ar at room temperature

Additionally, different water contents in the solvent (0%, 30%, 50%, 70%) were investigated by taking into account the possible influence of solubility (**Figure 32**). With the addition of water, the selectivity to bibenzyl increases. Notably, high bibenzyl selectivity of 92% with 78% conversion of benzyl chloride can be reached when 50% content of water is added after 3 h reaction. This may be due to the higher solubility of HCl (the other dehalogenation product) in water, likely shifting the reaction equilibrium to form more bibenzyl<sup>[196]</sup>. While too much water (e.g., 70%) may decrease the solubility of benzyl chloride in a protic organic solvent, leading to poor dispersion and interaction between the substrate and the catalyst. Moreover, In the presence of 50% water content in the solvent, a small amount of benzyl chloride would undergo hydrolysis and react with water to form benzyl alcohol (3% yield) and hydrochloric acid<sup>[197]</sup>. The yield of benzyl alcohol

increases when the water content reaches 70%, suggesting protonic concentration is critical for hydrolysis of benzyl chloride.

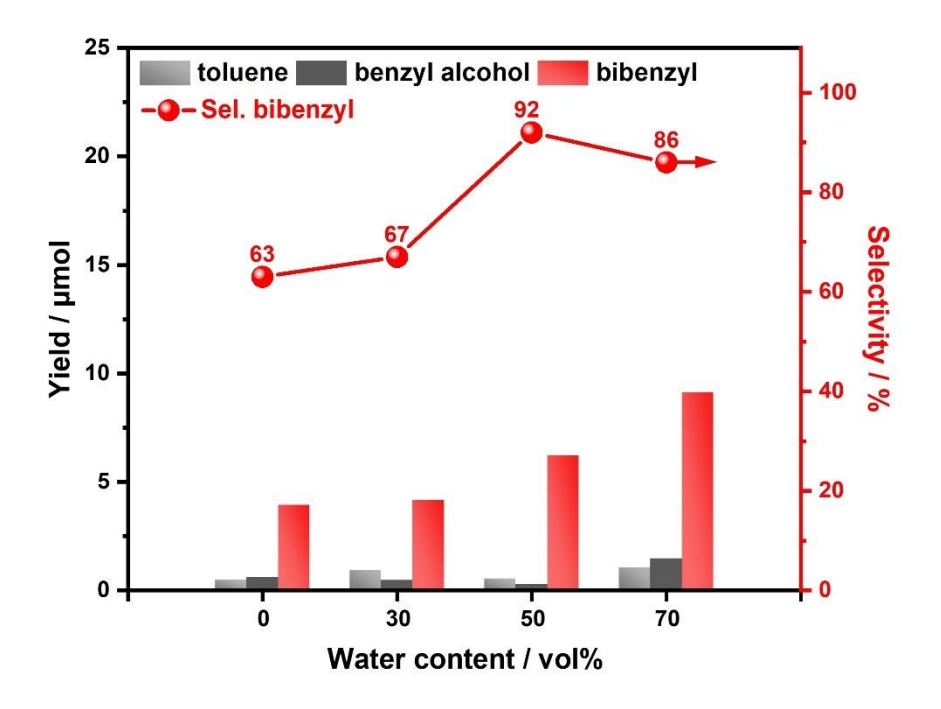


Figure 32 Water contents on the photocatalytic coupling of benzyl chloride. Reaction conditions: 10 mM reactant, 10 mg photocatalyst in 5 ml solvent (2-propanol with different water contents) under 365 nm LED irradiation for 2 h in Ar at room temperature

Finally, the stability and durability of Cu/ZnO were evaluated (**Figure 33**). The Cu/ZnO was separated and collected after each run by filtrating the reaction mixture. After rinsing with water, the catalyst was dried in a vacuum oven. The recycled Cu/ZnO photocatalyst was reused in follow-up reactions under the same conditions. According to stability results, the yield of bibenzyl well remains over 90% with no obvious decay after 8 cycles, indicating high stability of Cu/ZnO photocatalyst for homo-coupling of benzyl chloride. At low light intensity (27 mW cm<sup>-2</sup>), the Cu/ZnO photocatalyst possesses an apparent quantum efficiency (AQE) of 2%, suggesting no

convincing evidence for the radical propagation process. The low AQE value also indicates the challenge of activating C–Cl bonds.

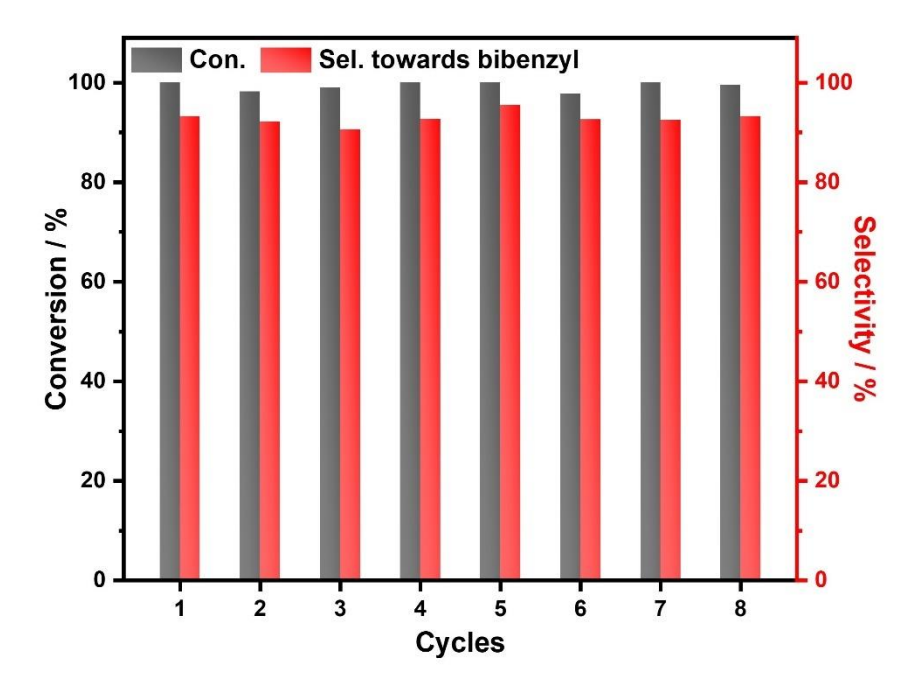


Figure 33 Stability test of 1.5 wt% Cu/ZnO. Reaction conditions: 10mM reactant, 10 mg photocatalyst in 5 ml solvent (2-propanol: water = 1:1) under 365 nm LED irradiation for 6 h in Ar at room temperature

Furthermore, In the presence of a higher benzyl chloride concentration (40 mM, **Figure 1**), the high conversion of benzyl chloride can be achieved by simply extending the irradiation time (40 h). Notably, the higher reactant concentration and prolonged irradiation do not compromise the selectivity towards bibenzyl, which remains consistently high at 90%. These results suggest that this approach has the potential for practical implementation in industrial settings.

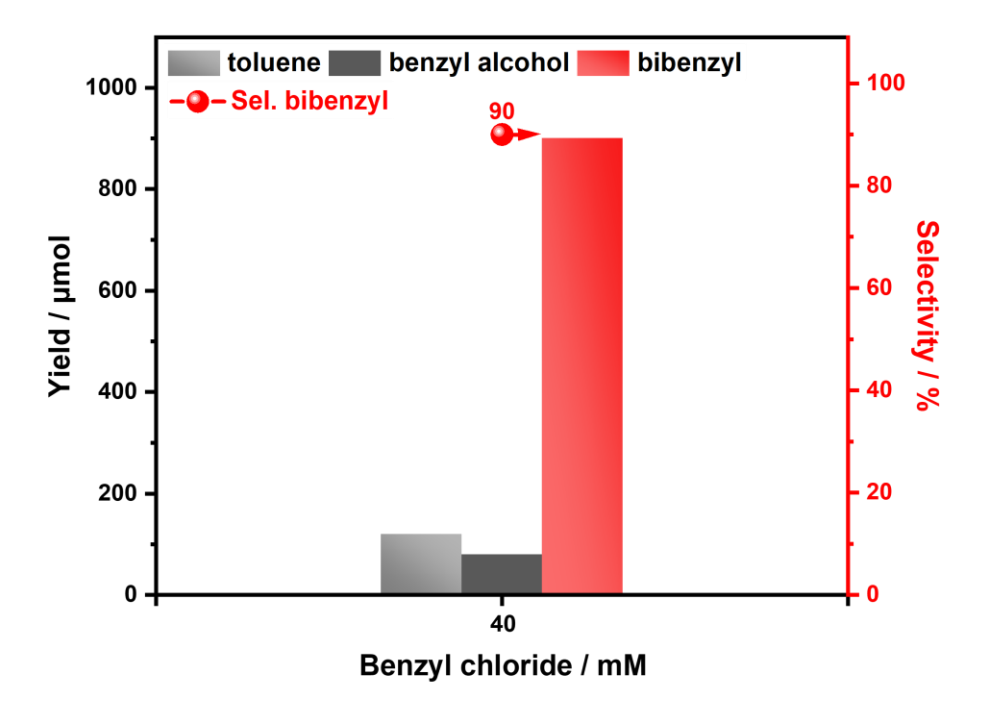


Figure 34 Scaling-up experiment with higher benzyl chloride concentration. Reaction conditions: 40mM reactant, 50 mg photocatalyst in 50 ml solvent (2-propanol: water = 1:1) under 365 nm LED irradiation for 40 h, Ar, room temperature.

## **5.3.2 Substrate Scope**

The reaction system was further extended to 10 alkyl chlorides with various functional groups to examine the general applicability of Cu/ZnO for photocatalytic C–C homo-coupling reactions, as shown in **Figure 35**. The Cu/ZnO photocatalyst can efficiently drive the homo-coupling of the benzylic chlorides with different methyl-groups. For example, both 3-methylbenzyl chloride (2) and 4-methylbenzyl chloride (3) can be efficiently converted to the corresponding coupling products **2a** and **3a**, with a high yield of 96% and 93%, respectively. However, with increasing numbers of methyl groups on the substrates, such as (2,4-dimethylbenzyl chloride (4), 2,5-dimethylbenzyl chloride (5) and 2,6-dimethylbenzyl chloride (6)), a slight decrease in the yields

has been observed (78%, 85%, 80% yields for 4a, 5a and 6a). Furthermore, 2,4,6-trimethylbenzyl chloride (7) with three methyl groups shows a relatively moderate yield of 7a (72%). The observed decrease in yield can be attributed to the steric hindrance effect<sup>[97]</sup>. Then, the electronic effect of different substituents was also studied. When a strong electron-donating group, methoxy, is added to the benzene ring, the corresponding coupling product 8a is obtained with a very high selectivity of 96%. This is because the higher electron density of the benzene ring can facilitate the reduction reaction to release the Cl substituent, which is a rate-determining step in this process<sup>[198]</sup>. In contrast, when electron-withdrawing groups are introduced (e.g., -Cl, -OOMe), the yields of desired products 9a and 10a show a slight decrease, but it is still as high as 82% and 93%. Furthermore, 4-trifluoromethylbenzylchloride (11) with the strongest electron-withdrawing group -CF<sub>3</sub> can still give a product yield of 60% towards **11a**. Electron-withdrawing groups change the reactivity of a molecule by reducing the electron density on adjacent carbon atoms<sup>[199]</sup>, leading to a more electron deficient carbon centre and a weaker reactivity. The observed yields of 9a, 10a and 11a (93% for -Cl, 82% for -COOMe and 60% for -CF<sub>3</sub>) align with their respective electronwithdrawing abilities ( $-Cl < -COOMe < -CF_3$ ). The above results show that electron-donating groups favor this synthetic process. It also indicates that Cu/ZnO shows excellent tolerance to a wide substrate scope, and both the <sup>1</sup>H NMR and <sup>13</sup>C NMR results are shown in Figure 36-Figure **45**.

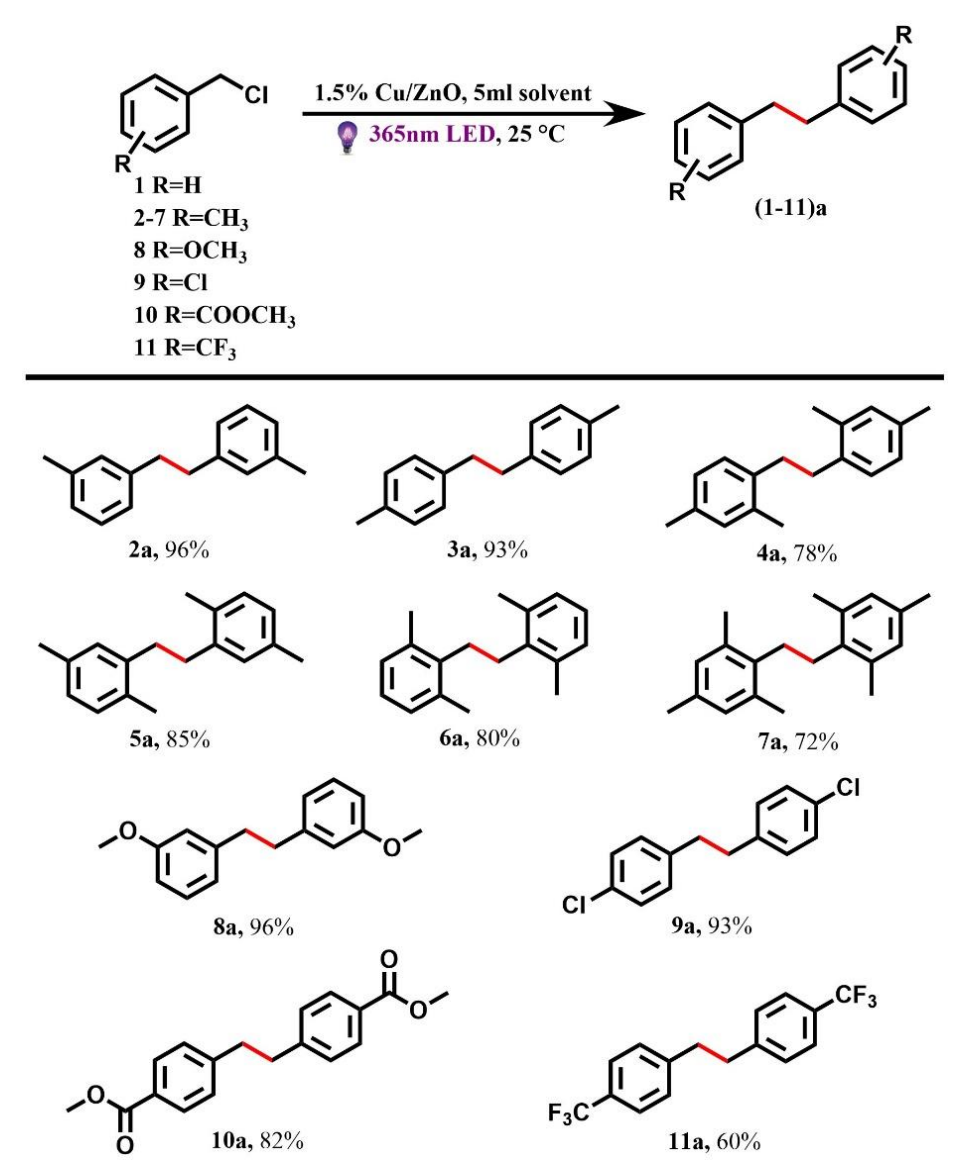
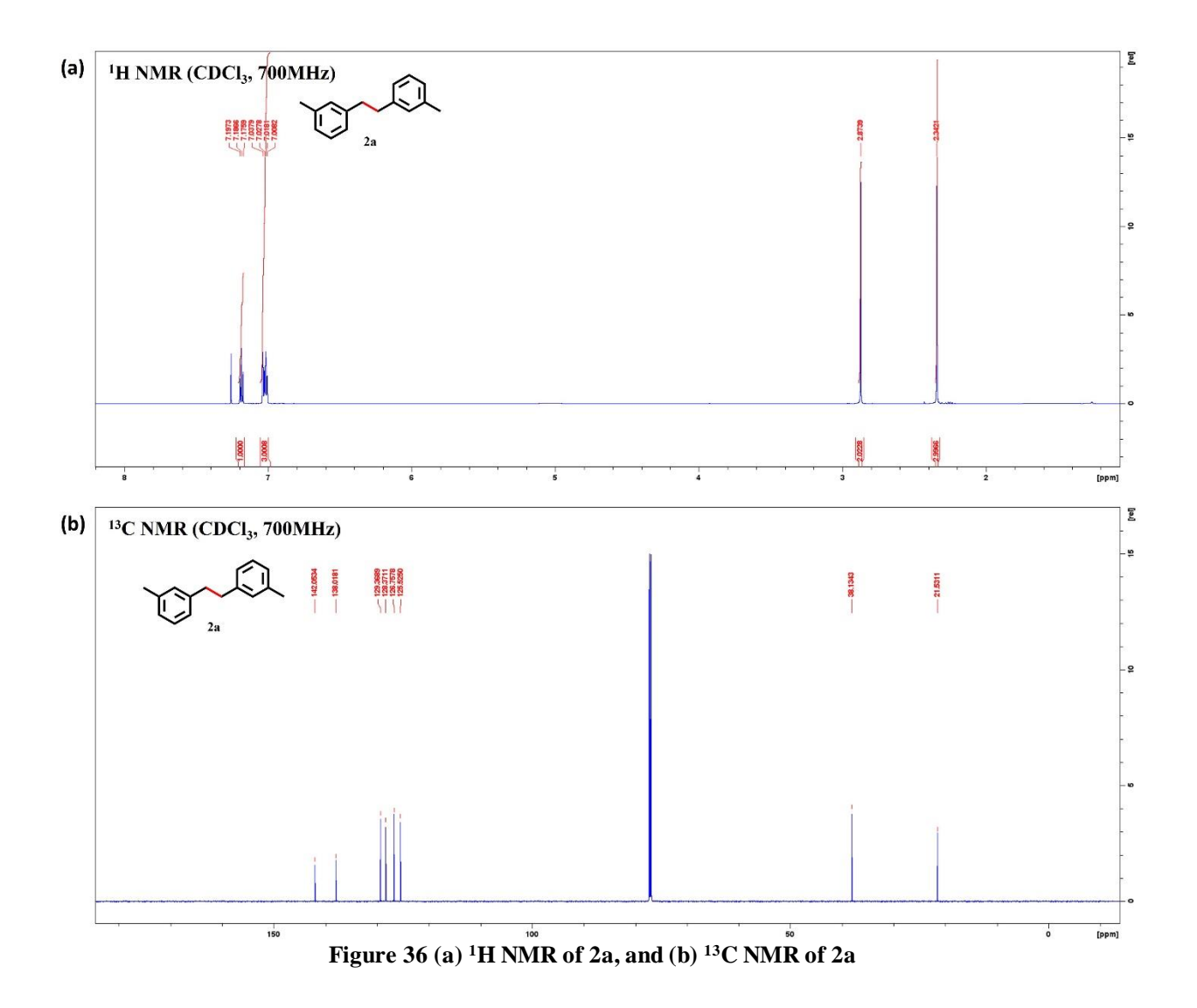
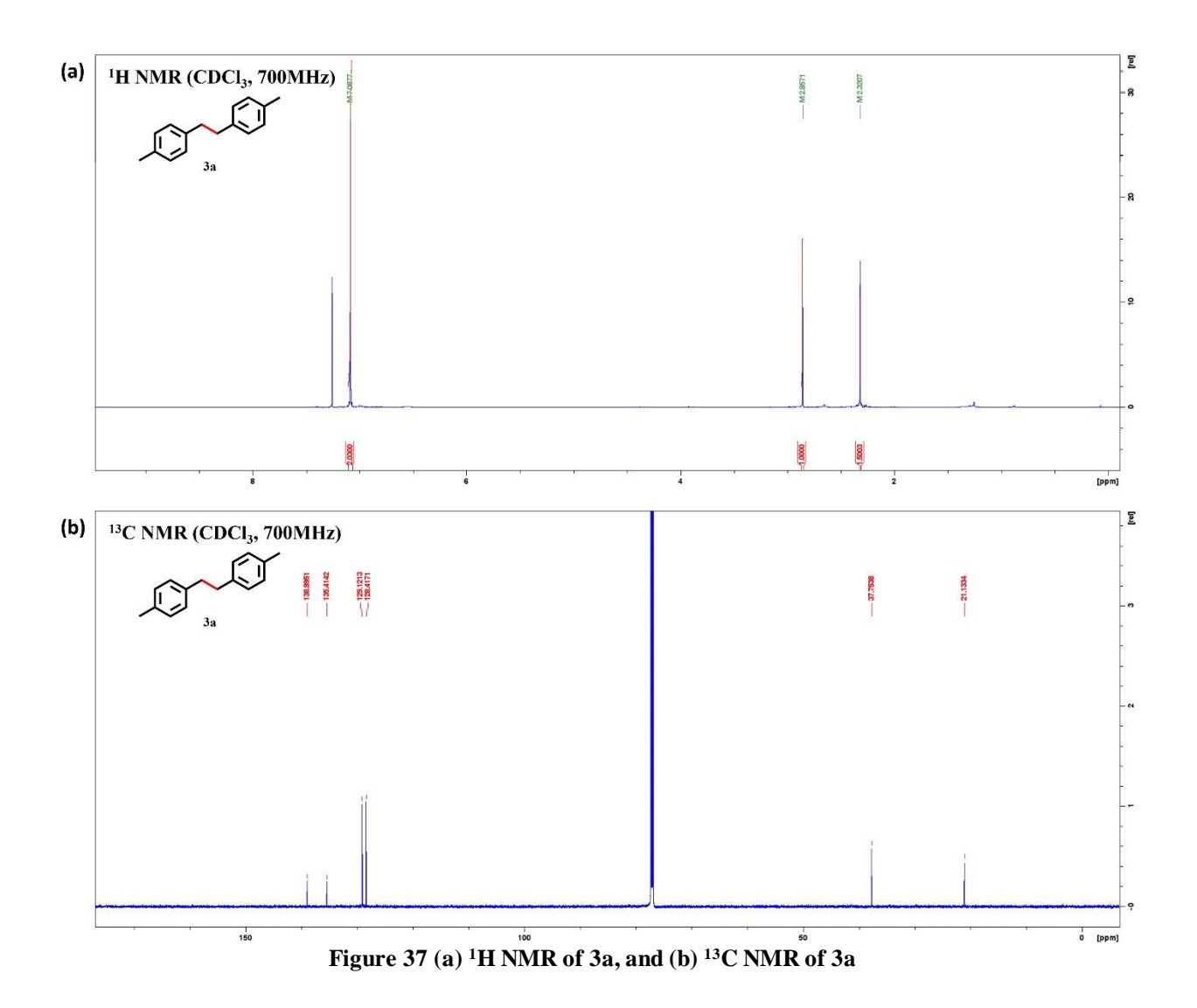


Figure 35 Extension to different substrates. Photocatalytic homo-coupling of various benzylic chlorides to the corresponding bibenzyl using Cu/ZnO photocatalyst.  $^a$ Reaction conditions: 10mM reactant, 10 mg photocatalyst in 5 ml solvent (2-propanol: water = 1:1) under 365 nm LED irradiation for 6 h, Ar, room temperature.  $^b$ Analysed by GC-FID, and all conversions  $\geq$  99%, the percentage indicates its yield, the equation for calculating yield is shown in Equation 2



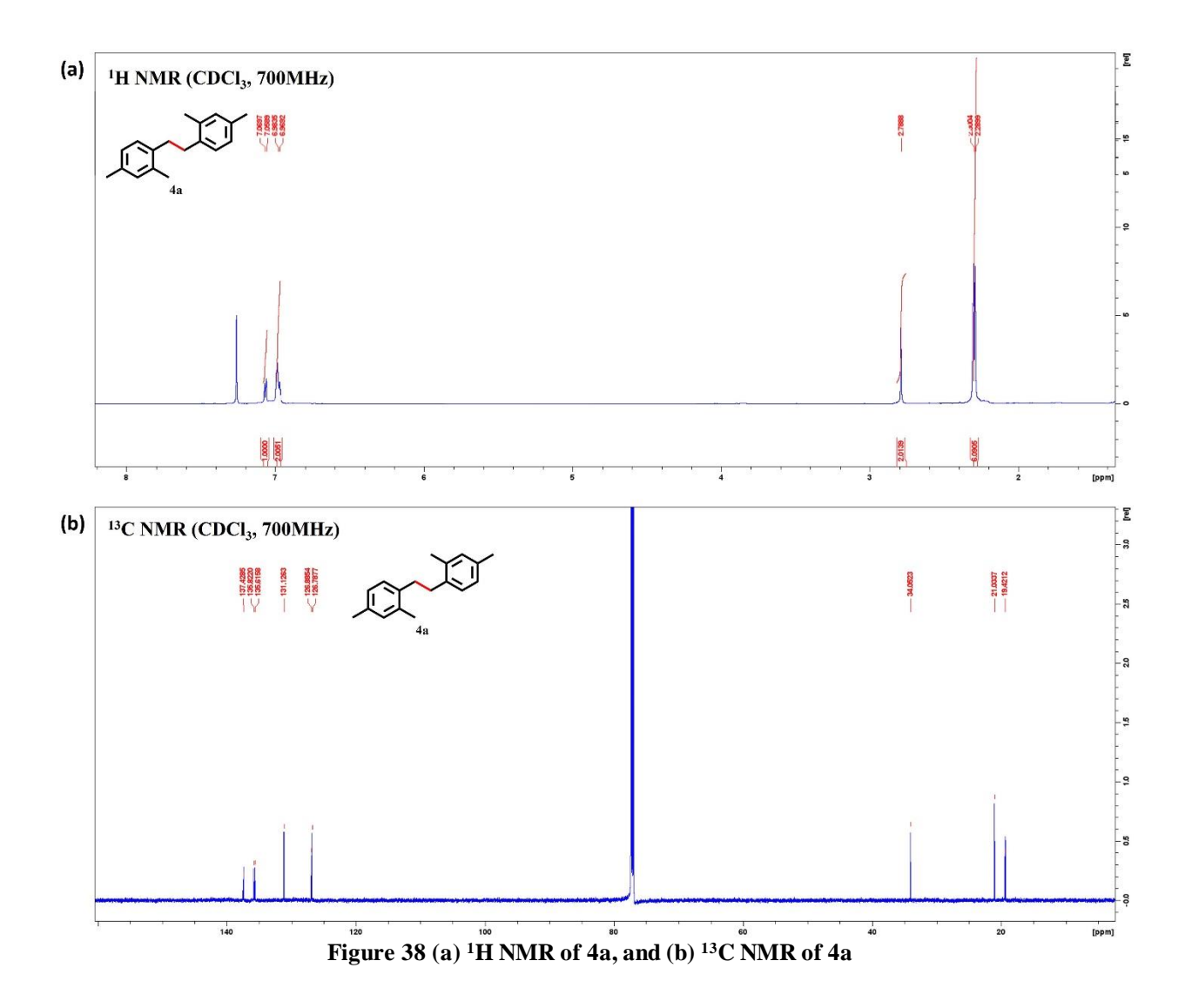
 $^{1}$ H NMR (700 MHz, CDCl<sub>3</sub>):  $\delta$  = 2.34 (s, 6H), 2.88 (s, 4H), 7.02 (m, 6H), 7.19 (m, 2H)

 $^{13}\text{C NMR}$  (700 MHz, CDCl<sub>3</sub>):  $\delta$  21.5, 38.1, 125.5, 126.7, 128.3, 129.3, 138.0, 142.0



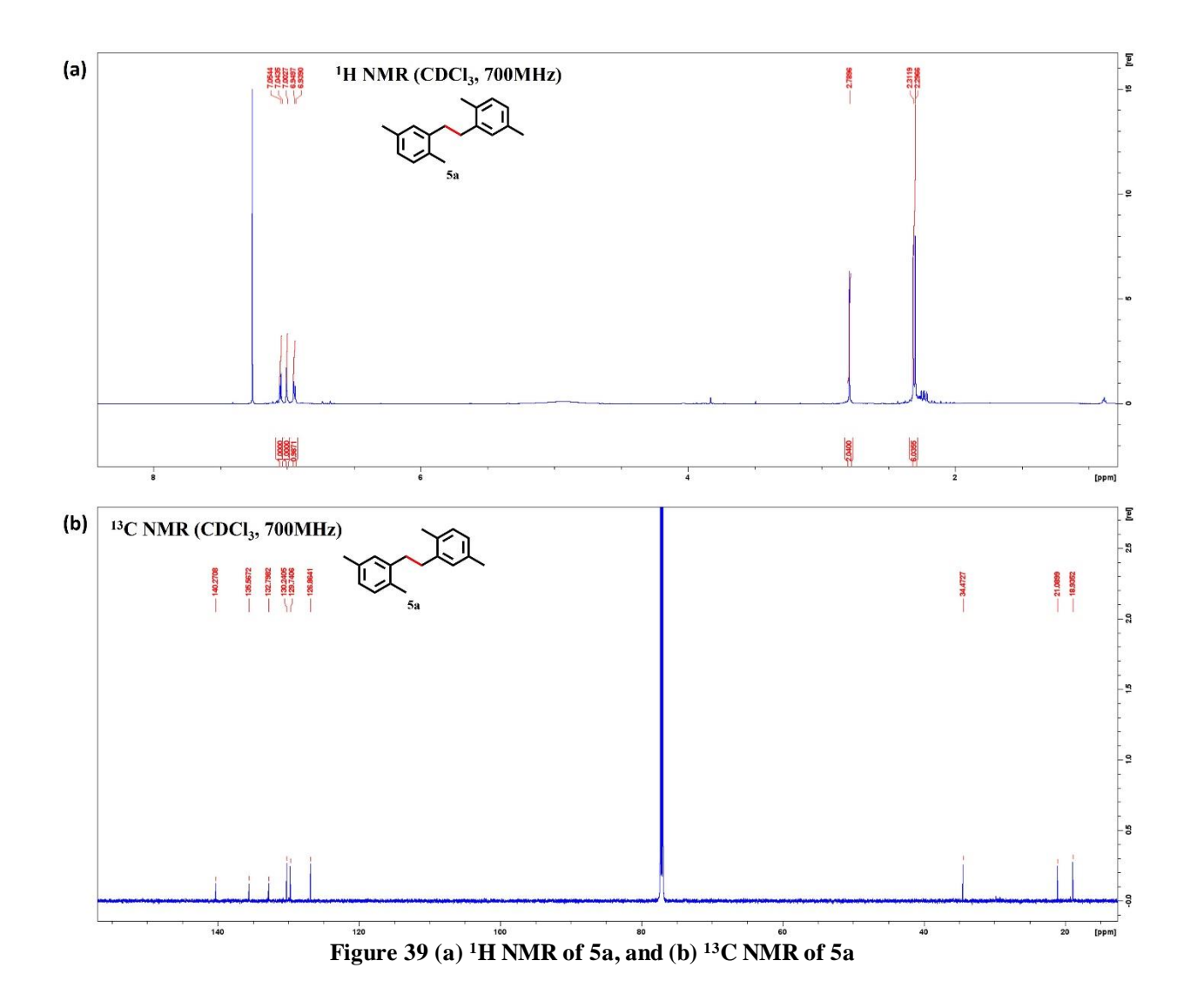
<sup>1</sup>H NMR (700 MHz, CDCl<sub>3</sub>):  $\delta$  = 2.32 (s, 6H), 2.86 (s, 4H), 7.09 (s, 8H)

 $^{13}\text{C NMR}$  (700 MHz, CDCl<sub>3</sub>):  $\delta$  21.1, 37.3, 128.4, 129.1, 135.4, 138.9



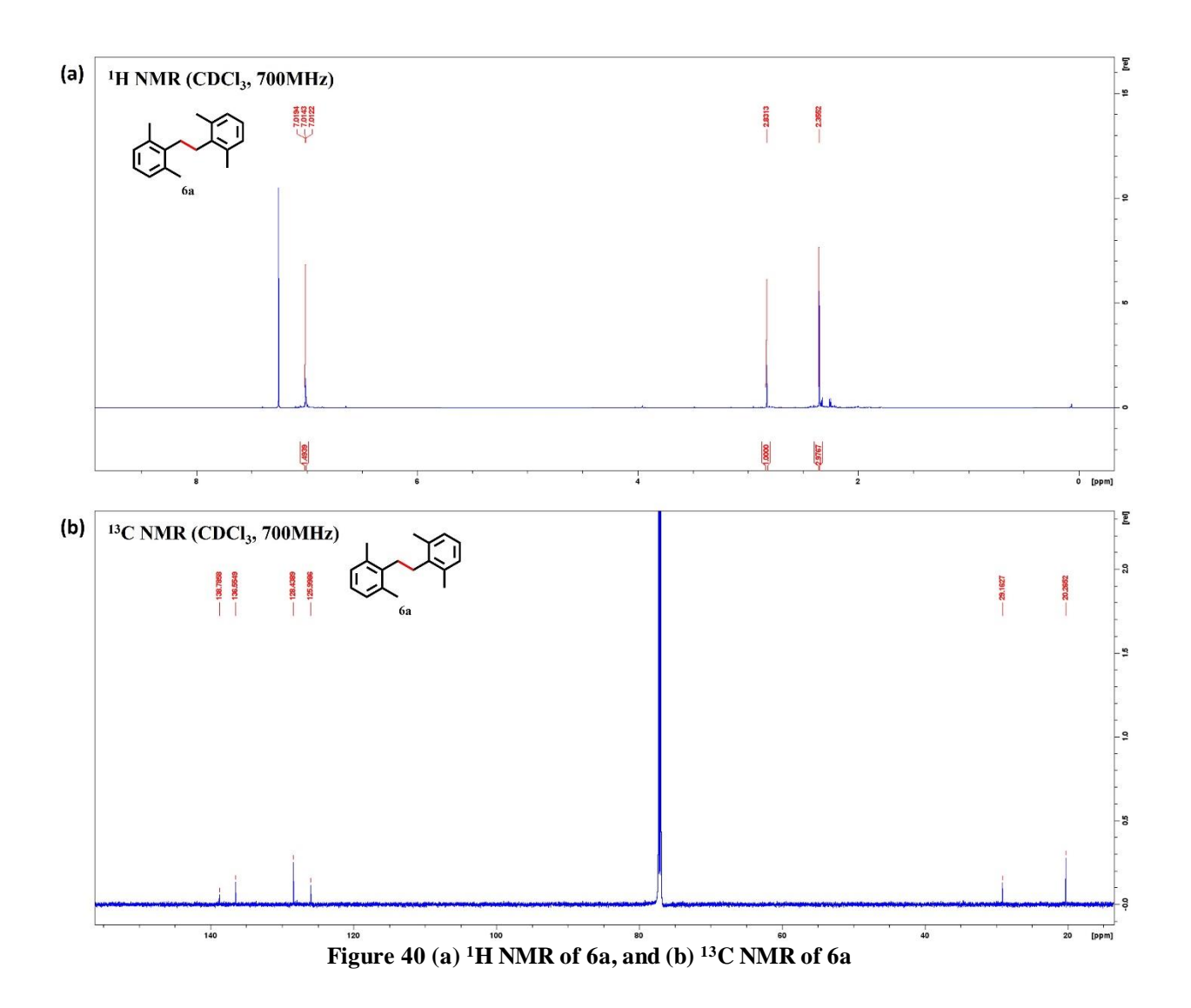
 $^{1}$ H NMR (700 MHz, CDCl<sub>3</sub>):  $\delta$  = 2.35 (s, 12H), 2.83 (s, 4H), 7.01 (s, 6H)

 $^{13}\mathrm{C}$  NMR (700 MHz, CDCl<sub>3</sub>):  $\delta$  19.4, 21.0, 34.1, 128.8, 128.9, 131.1, 135.6, 135.8, 137.4



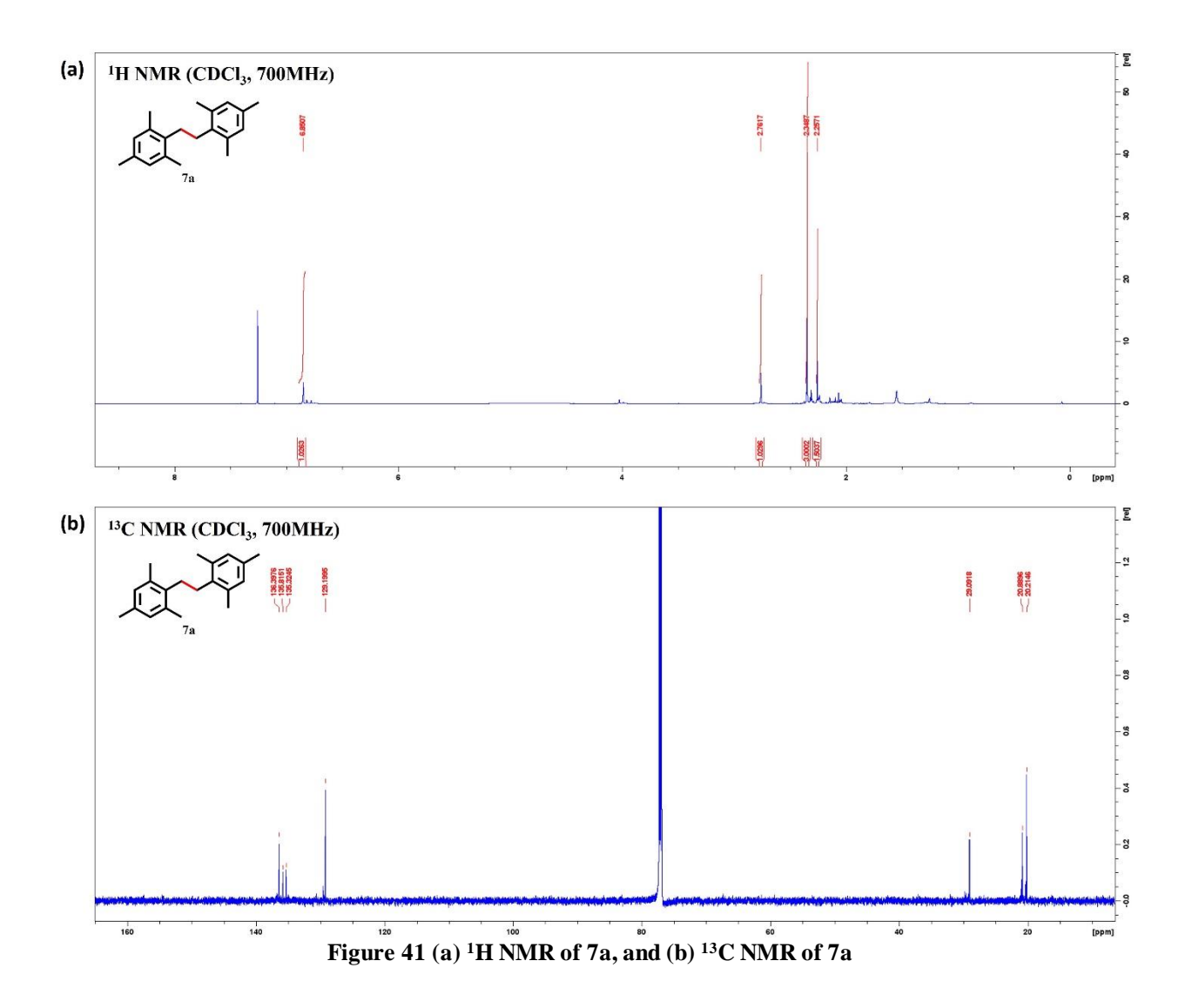
<sup>1</sup>H NMR (700 MHz, CDCl3):  $\delta$  = 2.29 (s, 6H), 2.31 (s, 6H), 2.78 (s, 4H), 6.94 (s, 2H), 7.00 (s, 2H), 7.05 (s, 2H)

 $^{13}\mathrm{C}$  NMR (700 MHz, CDCl3):  $\delta$  18.9, 21.1, 34.5, 126.8, 129.7, 130.2, 132.8, 135.5, 140.2



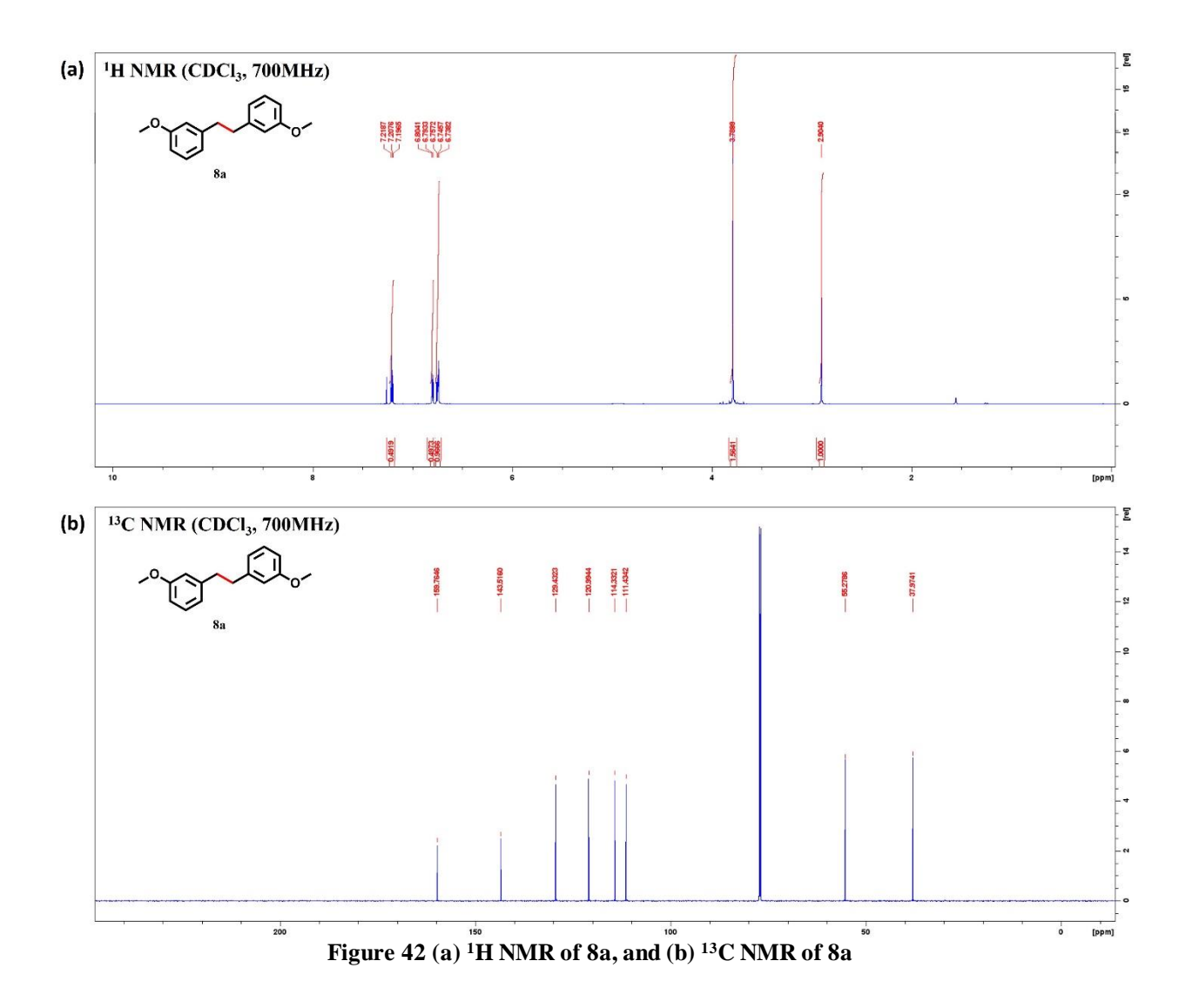
<sup>1</sup>H NMR (700 MHz, CDCl<sub>3</sub>):  $\delta$  = 2.35 (s, 12H), 2.83 (s, 4H), 7.01 (s, 6H)

 $^{13}\text{C NMR}$  (700 MHz, CDCl<sub>3</sub>):  $\delta$  20.2, 29.2, 125.9, 128.4, 135.5, 138.7

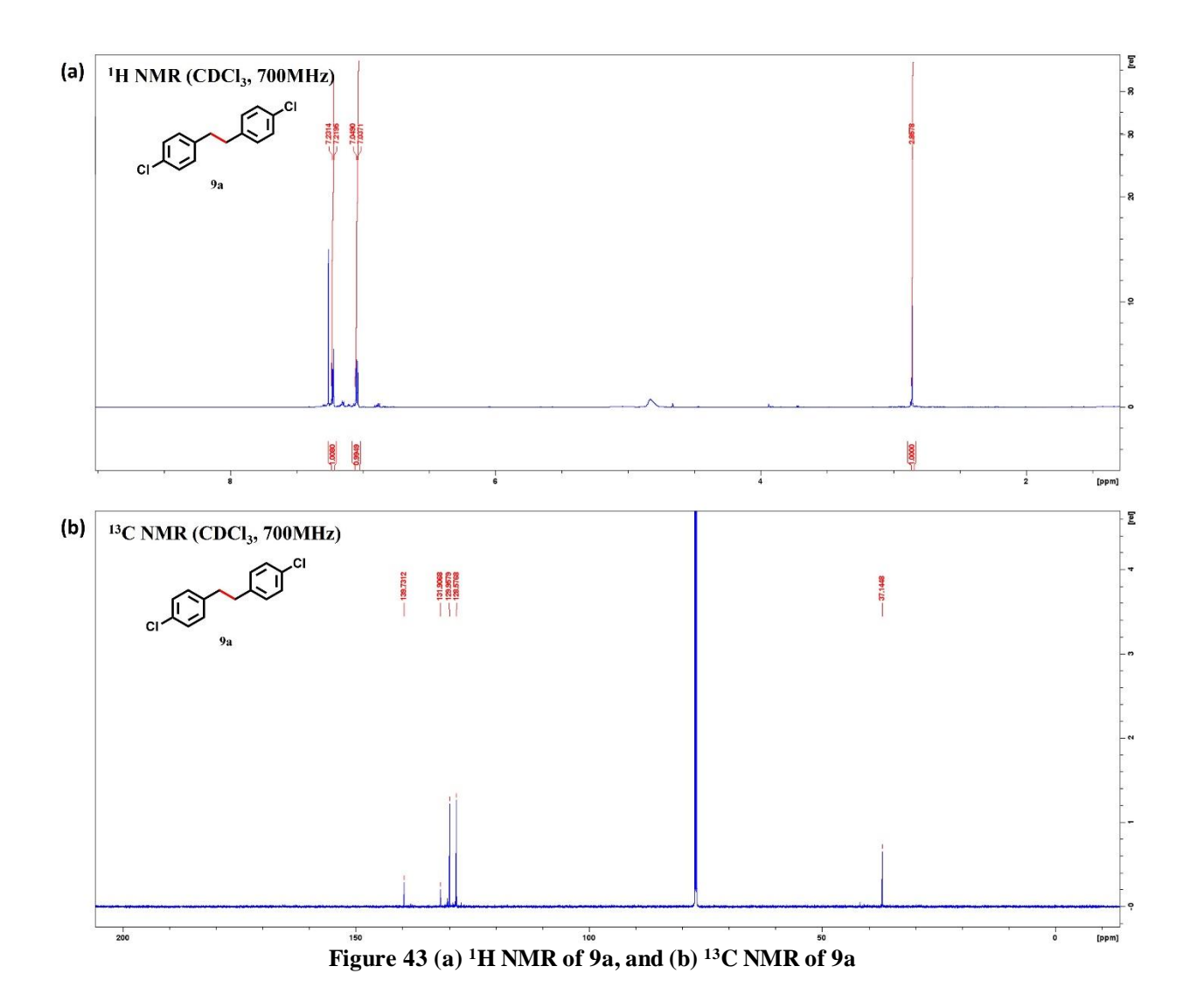


 $^{1}$ H NMR (700 MHz, CDCl<sub>3</sub>):  $\delta$  = 2.25 (s, 6H), 2.35 (s, 12H), 2.76 (s, 4H), 6.85 (s, 4H)

 $^{13}\text{C NMR}$  (700 MHz, CDCl<sub>3</sub>):  $\delta$  20.2, 20.9, 29.1, 129.1, 135.3, 135.8, 136.4

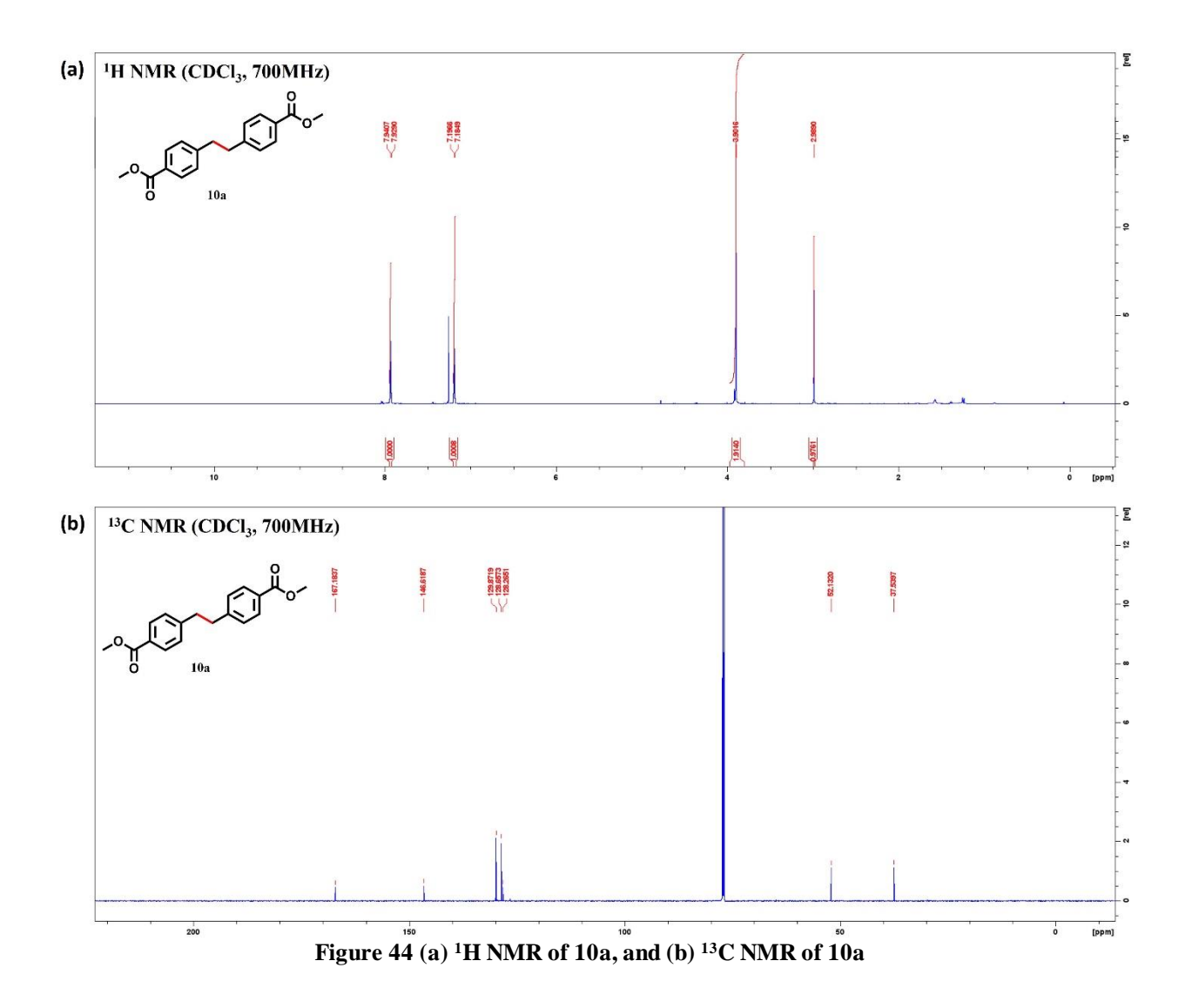


<sup>1</sup>H NMR (700 MHz, CDCl<sub>3</sub>):  $\delta$  = 2.90(s, 4H), 3.79 (s, 6H), 6.73-6.80 (m, 6H), 7.19-7.21 (m, 2H) <sup>13</sup>C NMR (700 MHz, CDCl<sub>3</sub>)  $\delta$  37.9, 55.2, 111.4, 114.3, 120.9, 129.4, 143.5, 159.7



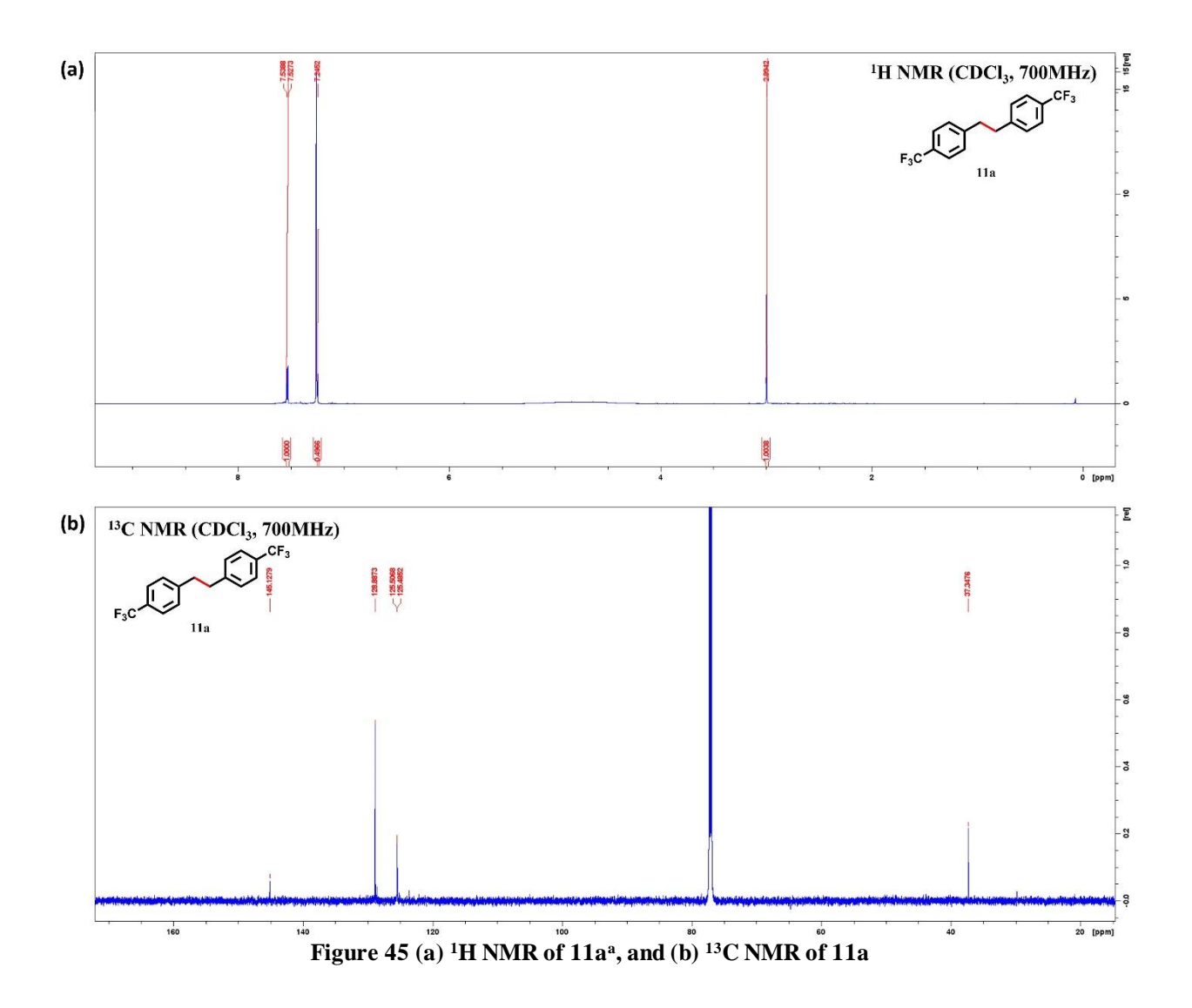
<sup>1</sup>H NMR (700 MHz, CDCl<sub>3</sub>):  $\delta$  = 2.85 (s, 4H), 7.03 (d, 4H), 7.21 (d, 4H)

 $^{13}\text{C NMR}$  (700 MHz, CDCl<sub>3</sub>)  $\delta$  37.1, 128.5, 129.9, 131.9, 139.7



 $^{1}$ H NMR (700 MHz, CDCl<sub>3</sub>):  $\delta$  = 2.98(s, 1H), 3.90 (s, 2H), 7.19 (s, 1H), 7.93 (s, 1H)

 $^{13}\text{C NMR}$  (700 MHz, CDCl<sub>3</sub>)  $\delta$  37.5, 52.1, 128.2, 128.6, 129.8, 146.6, 167.1



<sup>1</sup>H NMR (700 MHz, CDCl<sub>3</sub>):  $\delta$  = 2.99(s, 4H), 7.24 (d, 4H)<sup>a</sup>, 7.53 (d, 4H)

<sup>a</sup>One peak overlapped with CDCl<sub>3</sub>

 $^{13}\text{C NMR}$  (700 MHz, CDCl<sub>3</sub>)  $\delta$  37.3, 125.4, 125.5, 128.8, 145.1

## 5.3.3. Catalyst characterizations

A series of characterizations were carried out to obtain structural information on the active Cu/ZnO photocatalyst. As the XRD spectra (**Figure 23**) displays no extra peaks for the 1.5% Cu/ZnO sample mentioned above, a higher loading amount (5 wt%) of Cu was used for detailed analysis. As shown in **Figure 46**, the peaks assigned to (002) and (-202) lattice planes of crystalline CuO are observed for the sample before a reaction, while only peaks corresponding to (111), (200) and (220) lattice planes of crystalline Cu are observed after 2 h and 6 h irradiation. This result suggests that the Cu species can be reduced in situ by the photoelectrons during the reaction (denoting an activation process) and metallic Cu may be the active catalytic species.

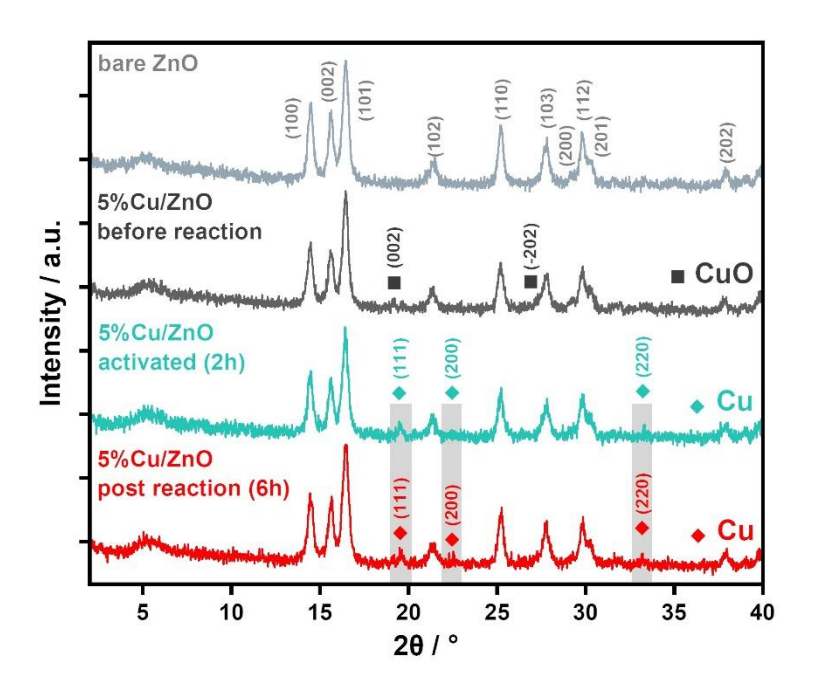


Figure 46 XRD patterns of bare ZnO, 5%Cu/ZnO samples (before, activated and post reaction)

Transmission electron microscopy (TEM) and energy dispersive spectroscopy (EDS mapping) were conducted on the post-reaction Cu/ZnO sample, as shown in **Figure 47**. The Cu nanoparticles

are homogeneously deposited on the ZnO support. The diameters of ZnO range from 10 to 20 nm, while the diameter of Cu NPs is roughly 10 nm, respectively. These nanoparticles are further identified by the d spacing of fringes, with 0.283 nm for ZnO (100)<sup>[194]</sup> and 0.207 nm for Cu (111)<sup>[200]</sup>, respectively.

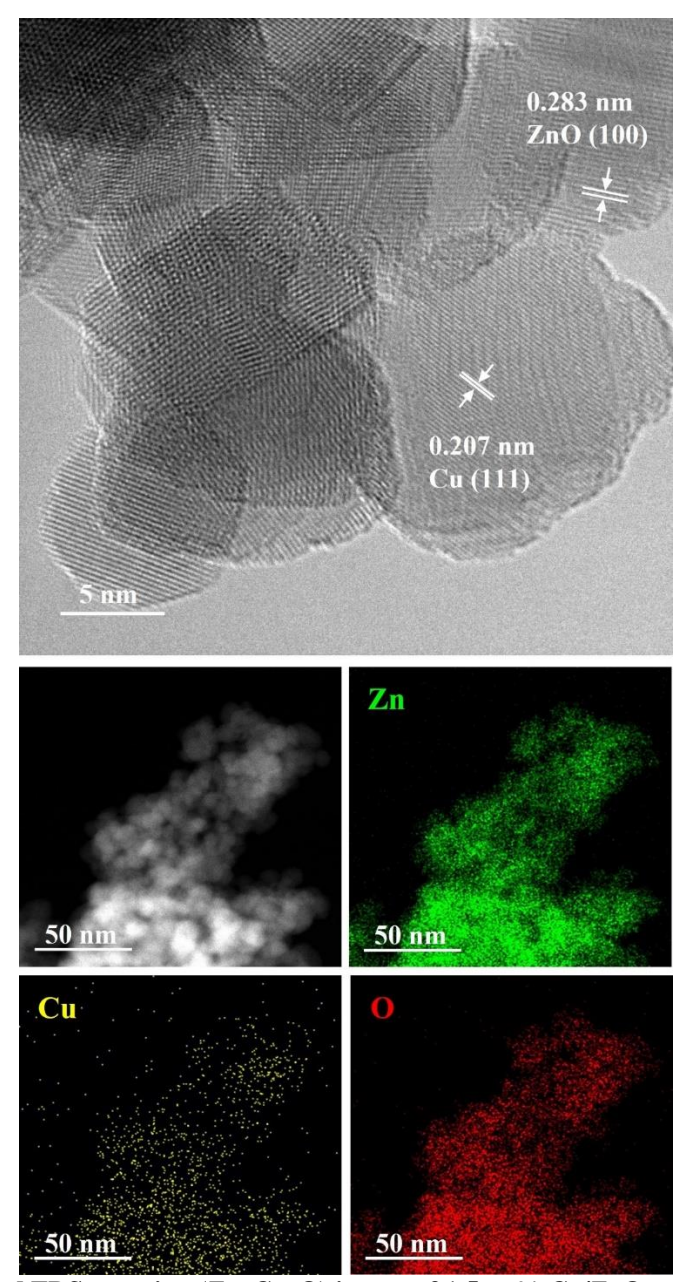


Figure 47 TEM and EDS mapping (Zn, Cu, O) image of 1.5 wt% Cu/ZnO post-reaction sample

The EPR results (**Figure 48**) show a sharp peak for the sample before the reaction, which is owing to I=3/2 of Cu<sup>2+</sup>, so CuO hyperfine structure ( $g_{//}=2.27$ ,  $A_{//}\approx90$  G) can be observed by EPR spectra, which agrees with the distorted octahedral coordination of Cu<sup>2+</sup> ions in CuO clusters<sup>[201],[202],[203]</sup>. The intensity of Cu<sup>2+</sup> peak decreases after 2 h irradiation and remains similar after 6h reaction, suggesting that the Cu<sup>2+</sup> species is likely reduced at the beginning of the photoreaction and the reduced Cu metal is EPR-silent. Thus, there is an in-situ activation process where most of Cu<sup>2+</sup> is photo-reduced to copper, which then acts as the reaction sites.

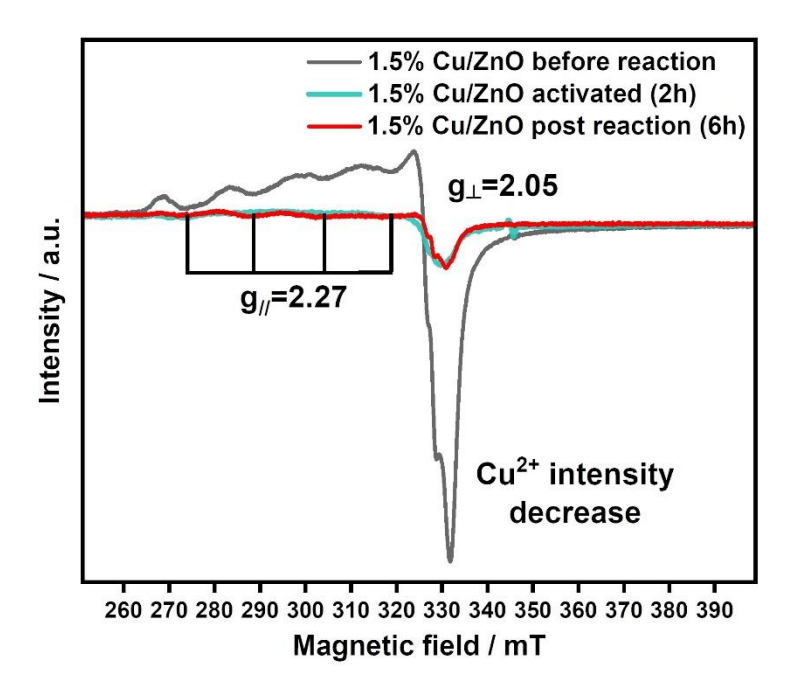


Figure 48 EPR spectra of 1.5% Cu/ZnO samples (before, activated and post reaction)

A similar trend can also be observed from the EPR results on the 5% Cu loading samples (**Figure 49**).

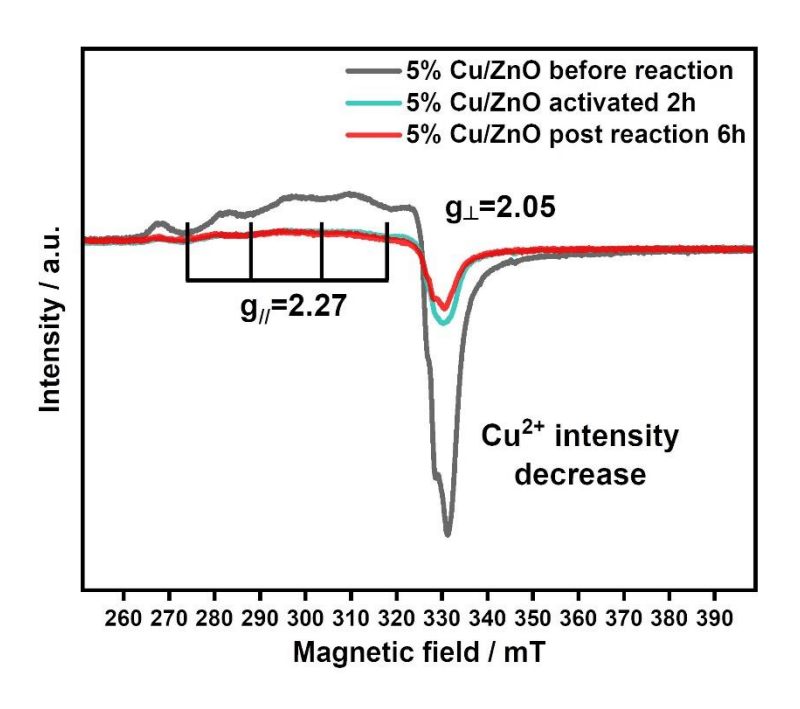


Figure 49 EPR spectra of 5% Cu/ZnO samples (before and post reaction)

Some lattice fringes corresponding to the CuO can also be found with 0.251 nm of (002)<sup>[204]</sup>, as shown in **Figure 50**.

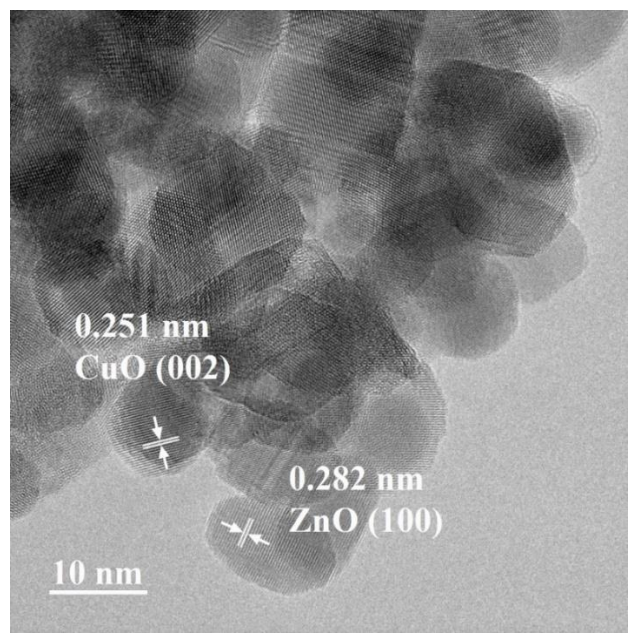


Figure 50 TEM image of Cu/ZnO post reaction sample

Taking into account the above XPS and EPR analysis, some CuO still remains in the sample after the in-situ activation process. In order to further investigate the function of metallic Cu in the system, in-situ EPR was conducted on the Cu/ZnO post-reaction sample as it is similar to the sample after 2 h activation and the results are shown in **Figure 51**. A weak Cu<sup>2+</sup> peak with  $g_{//} = 2.27$  and  $A_{//} \approx 90$  G can be observed in the EPR spectra, while upon in-situ irradiation for 0 min to 10 min, the intensity of this Cu<sup>2+</sup> peak gradual decreases, suggesting that the metallic Cu may function as electron acceptors during the photocatalytic process.

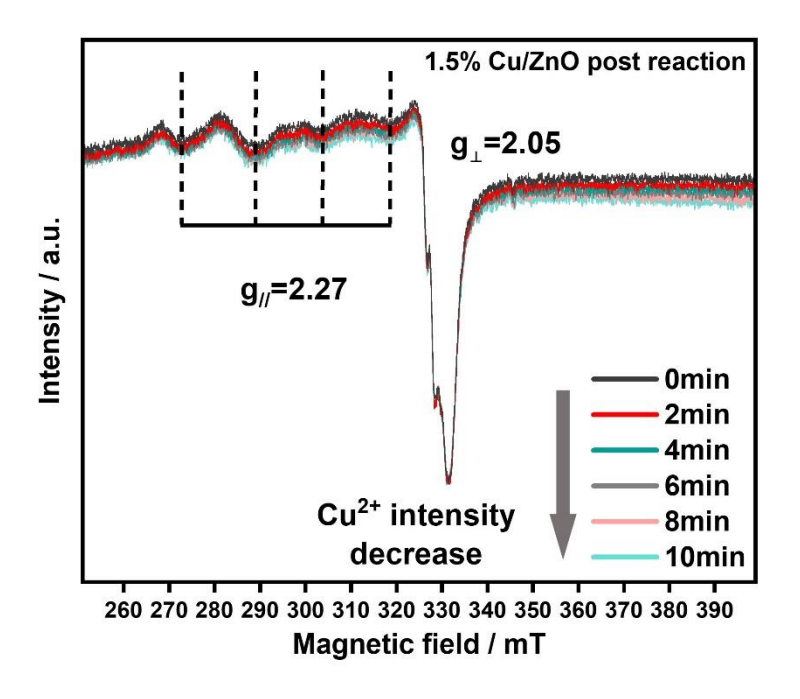


Figure 51 in-situ EPR spectra of 1.5% Cu/ZnO post reaction sample

**Figure 52** shows the deconvolution of XPS spectra in the Cu  $2p_{3/2}$  region of Cu/ZnO sample before, after 2 h activation and after 6 h reaction. The peak observed at around 933.7 eV can be attributed to CuO, and the other peak that appears at 932.2 eV can be assigned to the mixture of Cu/Cu<sub>2</sub>O<sup>[205]</sup>. It is clear that the concentration of Cu<sup>2+</sup> decreases (21% to 10%) in the sample after 2 h light

irradiation, suggesting the reduction of  $Cu^{2+}$  during the activation process, after which the concentration of  $Cu^{2+}$  remains around 8% at the end of reaction, further indicating the electron acceptors during the photocatalytic process may be metallic Cu.

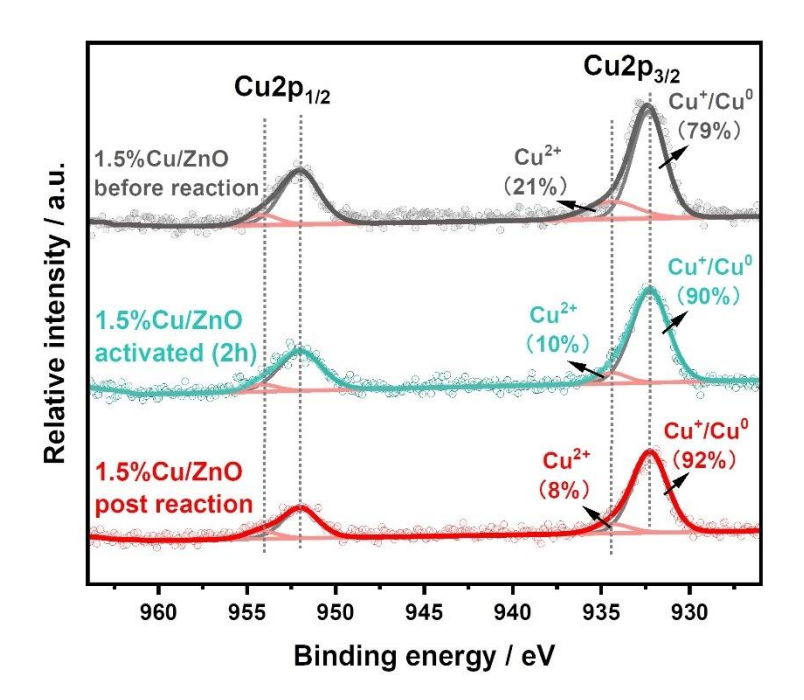


Figure 52 Deconvolution of XPS spectra in the Cu  $2p_{3/2}$  region for 1.5% Cu/ZnO samples (before, activated and post reaction)

The same sequence is also observed on the 5% Cu loading sample (32% to 9% to 10%, **Figure 53**). The above structural characterizations indicate that the active photocatalyst is composed of Cu species and ZnO and the active sites are probably metallic Cu NPs, which act as electron acceptors during the reaction.

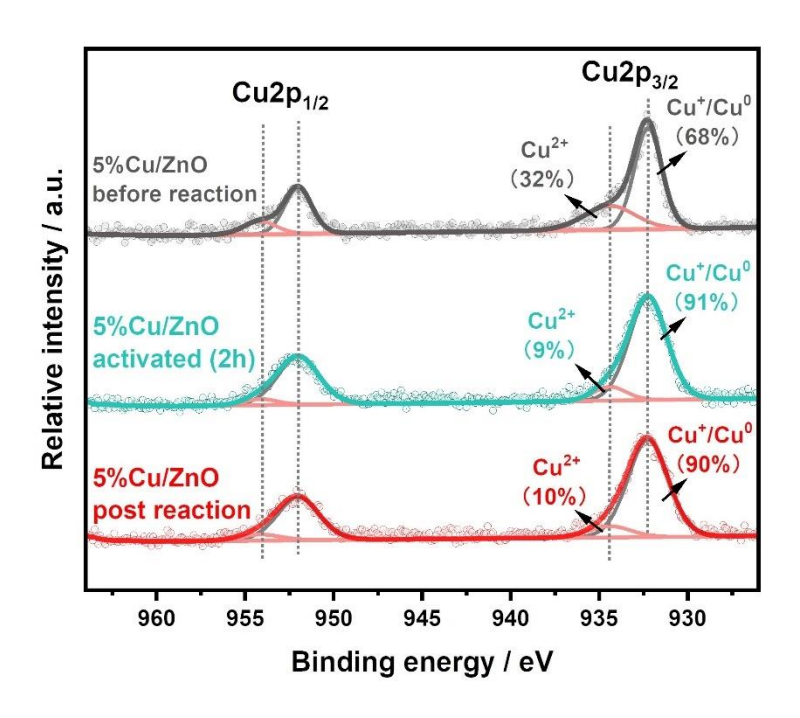


Figure 53 Deconvolution of XPS spectra in the Cu  $2p_{3/2}$  region for 5% Cu/ZnO samples (before, activated and post reaction)

## 5.3.4. Reaction Mechanism

The first step of the photocatalytic process is the reactant adsorption, so benzyl chloride-TPD was carried out to monitor the reactant desorption on the 6h reaction sample as it is similar to the 2h reaction one. From the TPD results (**Figure 54**), the desorption peak of benzyl chloride shifts to a higher temperature after the loading of Cu species. This result suggests the existence of a stronger interaction between the catalyst and the reactant, which is induced by the Cu species.

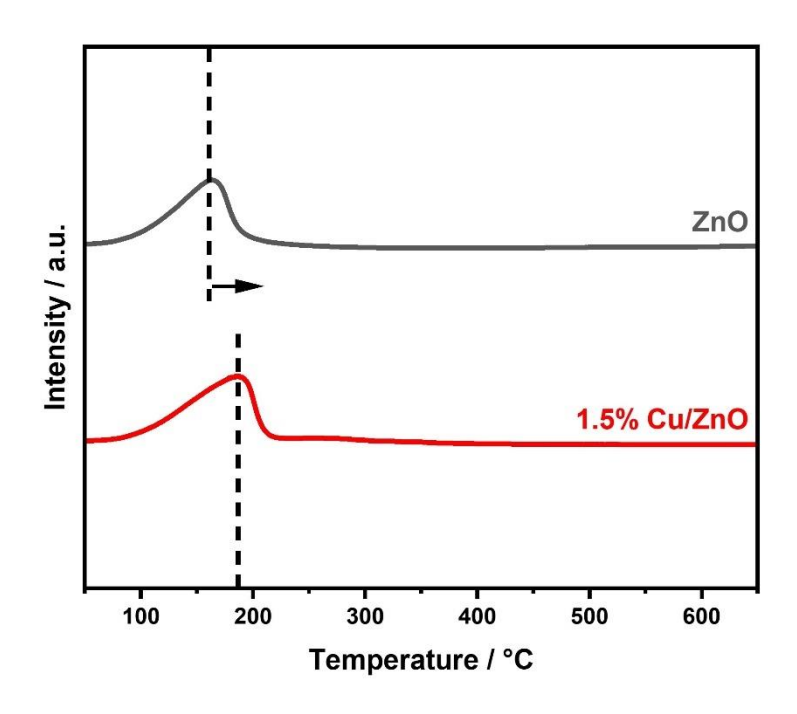


Figure 54 TPD spectra of benzyl chloride on bare ZnO and 1.5% Cu/ZnO 6h reaction sample

The photoabsorption properties of bare ZnO and Cu/ZnO were also investigated by UV-vis spectroscopy (**Figure 55**). After introducing copper onto ZnO, the photoabsorption remains similar at the wavelength below 400 nm, indicating the intact band structure of ZnO. In contrast, an enhancement is observed in the range  $\geq$  400 nm for the post-reaction sample. The broadened enhancement throughout the visible range may be attributed to CuO<sup>[206]</sup>, while the stronger absorption at around 625 nm can be contributed by LSPR effect from the Cu NPs<sup>[207,208]</sup>.

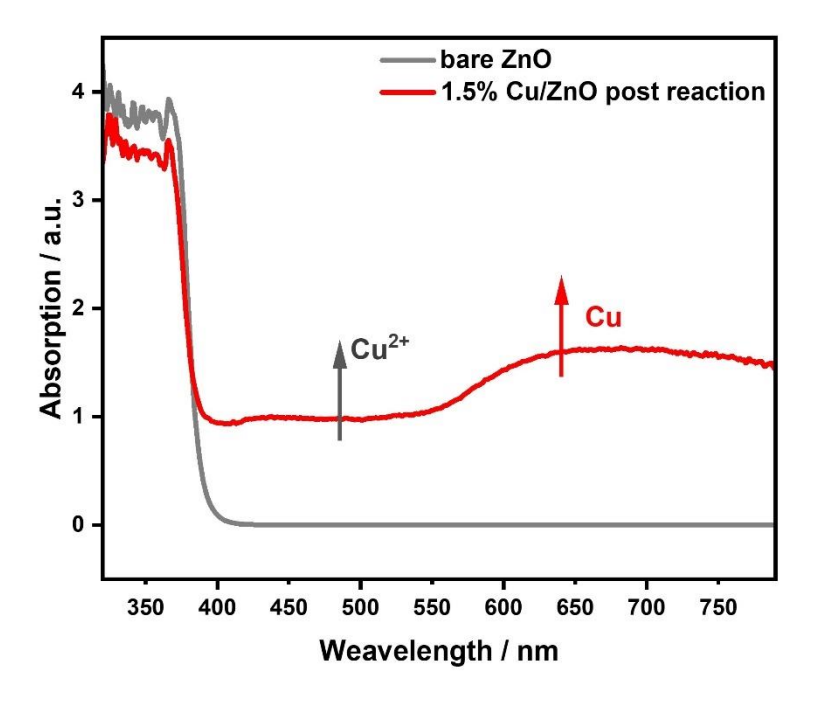
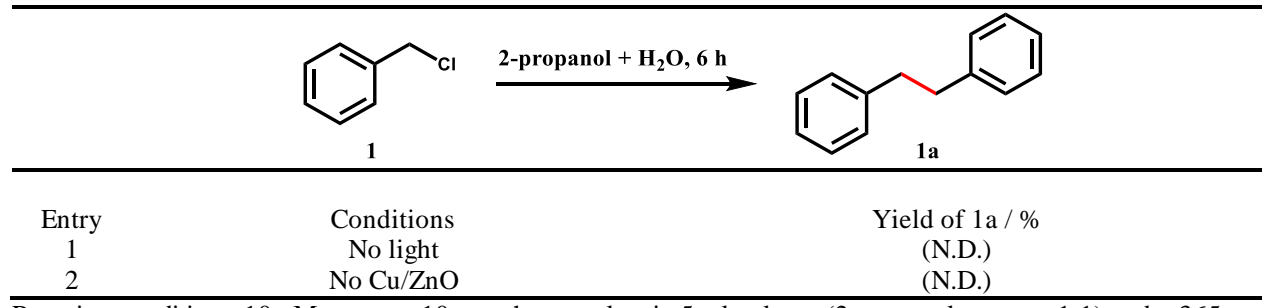


Figure 55 UV-vis spectra of bare ZnO, 1.5% Cu/ZnO after 6 hour reaction sample

Control experiments were conducted, and the results are shown in **Table 5**. In the absence of either light irradiation or Cu/ZnO photocatalyst, no conversion of benzyl chloride and generation of bibenzyl are detected.

Table 5 Control experiments for photocatalytic Ullmann homo-coupling of benzyl chloride



Reaction conditions: 10mM reactant, 10 mg photocatalyst in 5 ml solvent (2-propanol: water = 1:1) under 365 nm LED irradiation for 6 h, Ar, room temperature

It has been reported that C–Cl bond activation is an electron-assisted reduction process<sup>[209]</sup>. Thus, the electron capture experiment was carried out to examine this reaction pathway of benzyl chloride in our photocatalytic system. After 2 h 365 nm LED irradiation, there is no conversion of benzyl chloride observed with the addition of electron scavenger sodium iodate (NaIO<sub>3</sub>) (**Figure 56**). These results suggest the homo-coupling of benzyl chloride is indeed a photocatalytic process requiring the presence of photoelectrons generated by light irradiation on a photocatalyst.

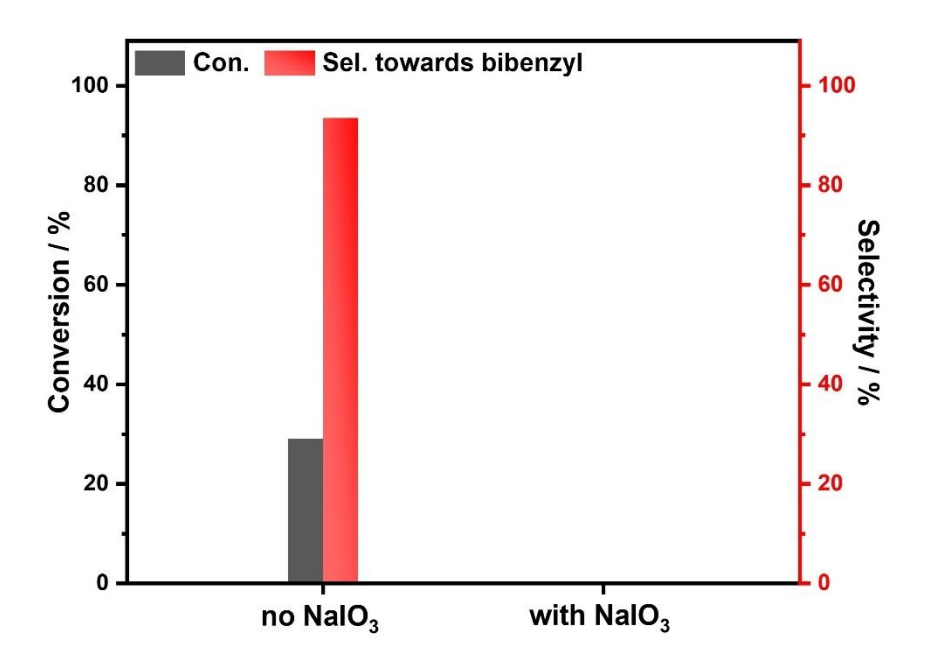


Figure 56 Electron capture experiments. Reaction conditions: 10 mM reactant, with/without NaIO<sub>3</sub>, 10 mg photocatalyst in 5 ml solvent (2-propanol: water = 1:1) under 365 nm LED irradiation for 1.5h

The pathway of the C–Cl decomposition was further investigated by chemical precipitation, as shown in **Figure 57**. Initially, the transparent reaction solution of benzyl chloride in the mixture of 2-propanol and water solution remains colourless in the absence of Cu/ZnO catalyst (bottle A) and in the presence of Cu/ZnO catalyst under 365 nm LED irradiation for 2 h (bottle C), and 4 h (bottle E), respectively. Upon adding silver nitrate (AgNO<sub>3</sub>) dropwise into bottle C and bottle E,

white precipitates appear in both bottles (bottle D and bottle F), which suggests the existence of Cl anions (Cl<sup>-</sup>) in the solution. Moreover, it is reasonable to observe more white precipitates in bottle F (4 hours) than in bottle D (2 hours), as a longer reaction time results in higher Cl<sup>-</sup> concentration. In contrast, bottle B remains transparent after adding AgNO<sub>3</sub>, excluding the existence of Cl<sup>-</sup> without the photoreaction. The production of Cl anions often leads to the formation of HCl in the solution, thus the pH was also monitored. Expectedly, a decreasing trend in pH is obtained with increasing reaction time from 0 h to 4 h (pH: 6.5> 6.04> 5.84). This result indicates that the C–Cl group cleavage is the important step.

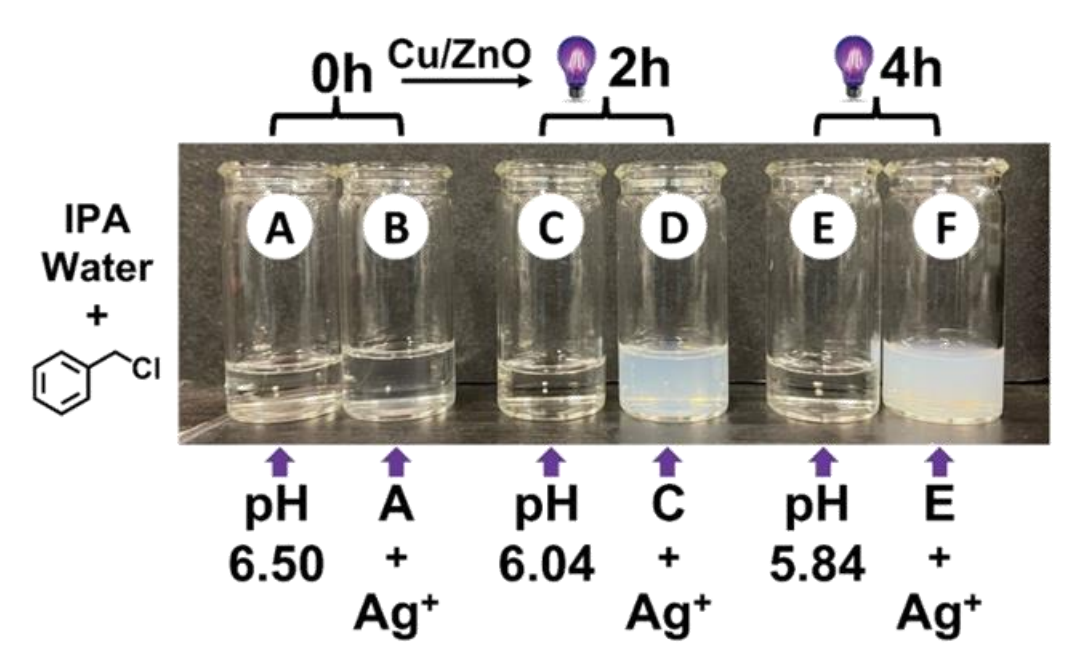


Figure 57 Images of reaction solutions for identifying reaction intermediates. A: benzyl chloride in isopropanol/water mixture. C and E: photoreduction of benzyl chloride using 1.5% Cu/ZnO after irradiated by 365nm LED for 2 h and 4 h, respectively under deaerated conditions. B, D and F: photos after adding the same amount of AgNO3 into A, C and E

Both the precursor PhCH<sub>2</sub>Cl and the key intermediate PhCH<sub>2</sub> on both bare ZnO(100) and Cu<sub>10</sub>/ZnO(100) surfaces (**Figure 58** and **Figure 59**, respectively) were then studied by density

functional theoretical (DFT) calculations (detailed calculation can be found in experimental section).

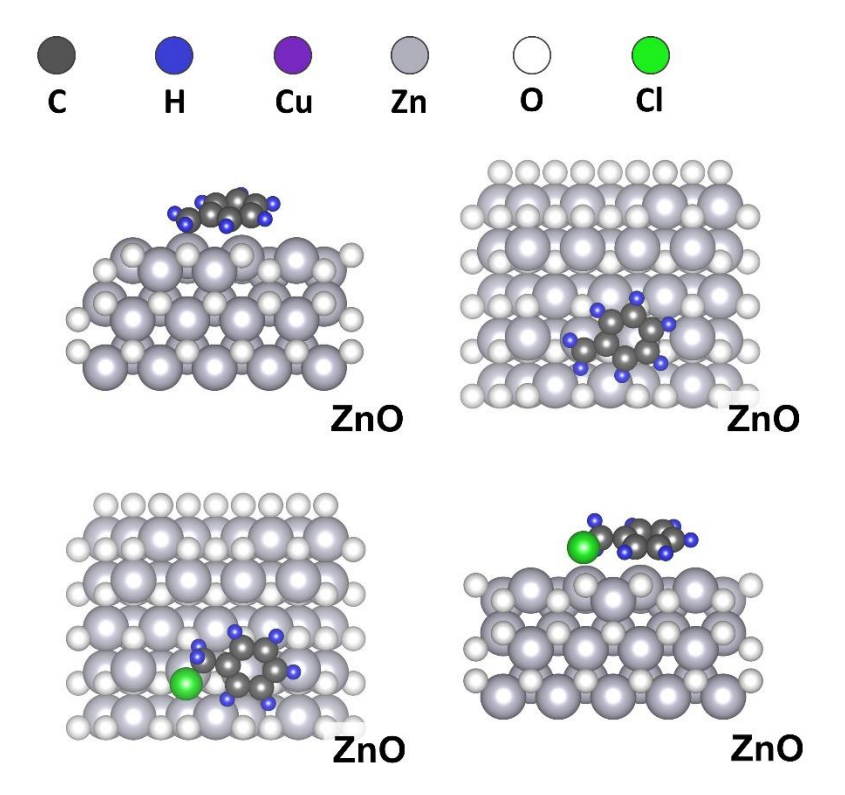


Figure 58 benzyl radical and benzyl chloride on selected surfaces of ZnO(100)

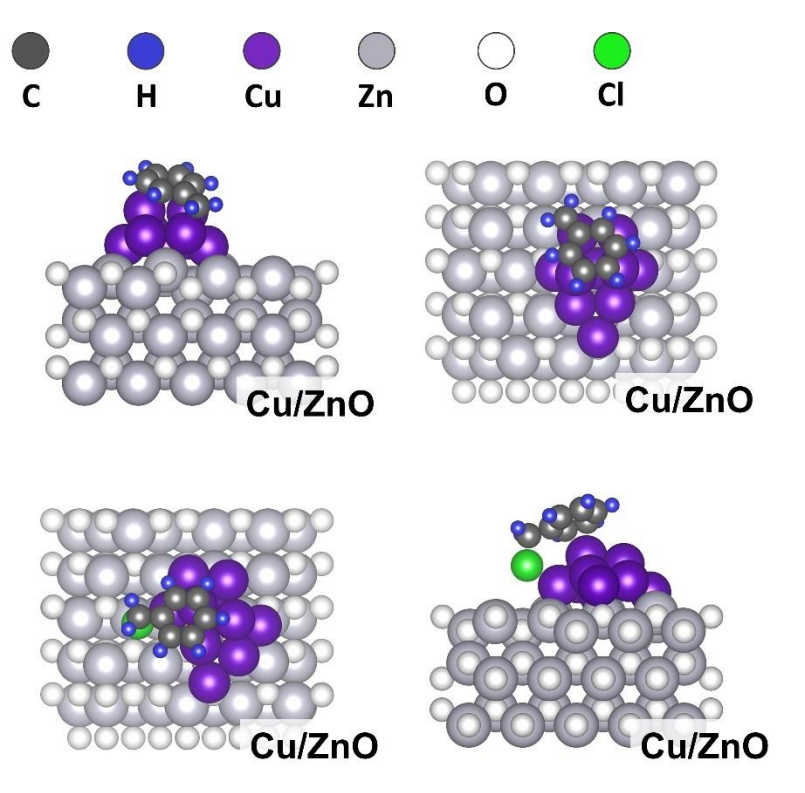


Figure 59 benzyl radical and benzyl chloride on selected surfaces of Cu/ZnO(100)

Both bare ZnO(100) and Cu<sub>10</sub>/ZnO(100) surfaces attracts the precursor PhCH<sub>2</sub>Cl (**Table 6**). In particular, the introduction of copper loading can significantly enhance the adsorption of benzyl radical PhCH<sub>2</sub>' on Cu decorated ZnO(100) (-2.39 eV on Cu<sub>10</sub>/ZnO(100) and -1.19 eV on ZnO(100), suggesting an enhanced stabilization of the intermediate on the surface of the catalyst, which is crucial for the further coupling reaction to produce bibenzyl with high selectivity. TiO<sub>2</sub>, as a most widely-used semiconductor with a similar band structure<sup>[210]</sup>, was used to compare with ZnO. It should be noted that Cu/TiO<sub>2</sub> has been reported to be an efficient photocatalyst in driving homocoupling of a relatively easy process of benzyl bromide with a good yield<sup>[33]</sup>. However, it is reported that Cu/TiO<sub>2</sub> exhibits a very moderate yield (53%) and selectivity (57%) towards the coupling product with the corresponding chloride substrate.

Table 6 Energy data of benzyl chloride and benzyl radicals on different model surface for DFT

Gas molecules				
Molecule	E <sub>tot</sub> (eV)			
Ph-Ch <sub>2</sub> Cl(g)	-91.289			
Ph-Ch <sub>2</sub> (g)	-87.685			

	ZnO(100)		$Cu_{10}/ZnO(100)$		$Cu_{10}/TiO_2(101)$	
Adsorbate	E <sub>tot</sub> (eV)	E <sub>ads</sub> (eV)	E <sub>tot</sub> (eV)	E <sub>ads</sub> (eV)	E <sub>tot</sub> (eV)	E <sub>ads</sub> (eV)
*	-425.941	-	-457.157	-	-597.048	-
Ph-CH <sub>2</sub> Cl*	-518.511	-1.28	-549.540	-1.09	-689.342	-1.00
Ph-CH <sub>2</sub> *	-514.813	-1.19	-547.228	-2.39	-687.105	-2.37

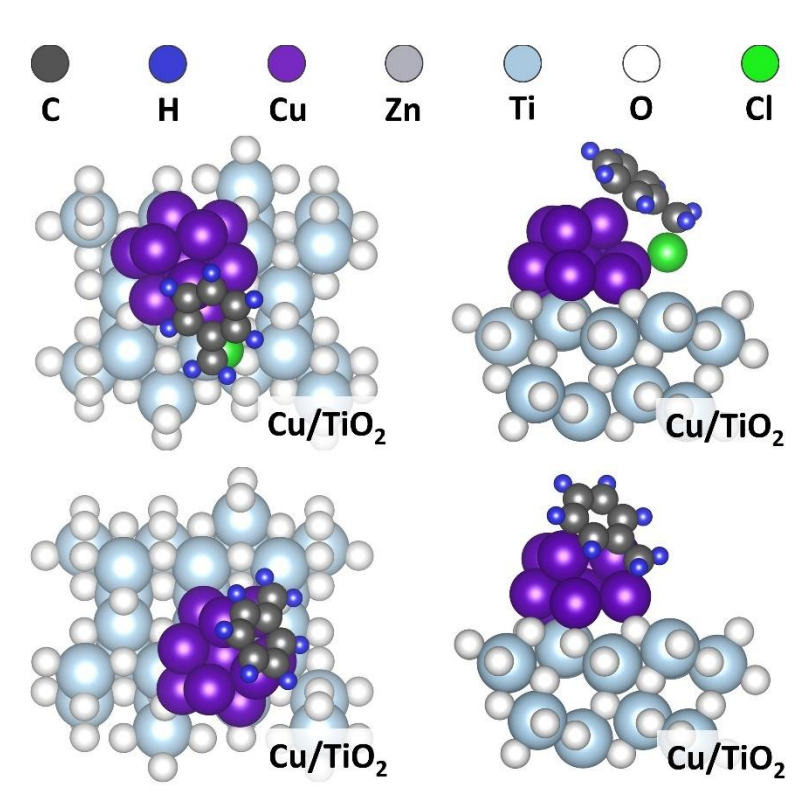


Figure 60 benzyl radical and benzyl chloride on selected surfaces of  $\text{Cu/TiO}_2(101)$ 

As a reference, the adsorption energy of PhCH<sub>2</sub> on Cu<sub>10</sub>/TiO<sub>2</sub>(101) was also calculated by DFT (**Figure 60**). Compared to  $Cu_{10}/ZnO(100)$  (-2.39 eV), the adsorption energy of benzyl radicals on is comparable (-2.37 eV, **Table 6**), suggesting that apart from the  $Cu_{10}/TiO_2(101)$ adsorption/desorption of benzyl radicals, there is another factor to dominate the bibenzyl selectivity. According to kinetic studies of 2-propanol adsorption on ZnO and TiO<sub>2</sub>, the adsorption capacity of 2-propanol in dark on TiO<sub>2</sub> is 6.3 times higher than on ZnO<sup>[211]</sup>. Meanwhile, the photooxidation rate of 2-propanol under UV irradiation on TiO<sub>2</sub> is 2.6 times higher than on ZnO<sup>[212]</sup>. Furthermore, I studied the photo-oxidation rate of 2-propanol on both TiO<sub>2</sub> and ZnO, and the capture experiment of alkoxy radicals produced from 2-propanol was then conducted, and the results are shown in **Figure 61**. 2-nitroso-2-niethylpropane (t-BuNO) was used as the trapping agent following the reaction **Equation 7**. The trapped nitroxides show strong signals  $(g_{//}=2.85, A)$  $\approx$  60 G) on the EPR spectrum after 30 s irradiation, and the integral of nitroxides generated on TiO<sub>2</sub> is roughly 3 times higher than that on ZnO, which is similar to the reference result (2.6 times), indicating a faster photo-oxidation of 2-propanol on TiO<sub>2</sub> surface. Therefore after the formation of alkoxy radicals due to the reaction between photoholes and 2-propanol, the amount of the surface adsorbed H on TiO<sub>2</sub> would be much higher than that on ZnO, resulting in the formation of dehalogenation byproduct (toluene).

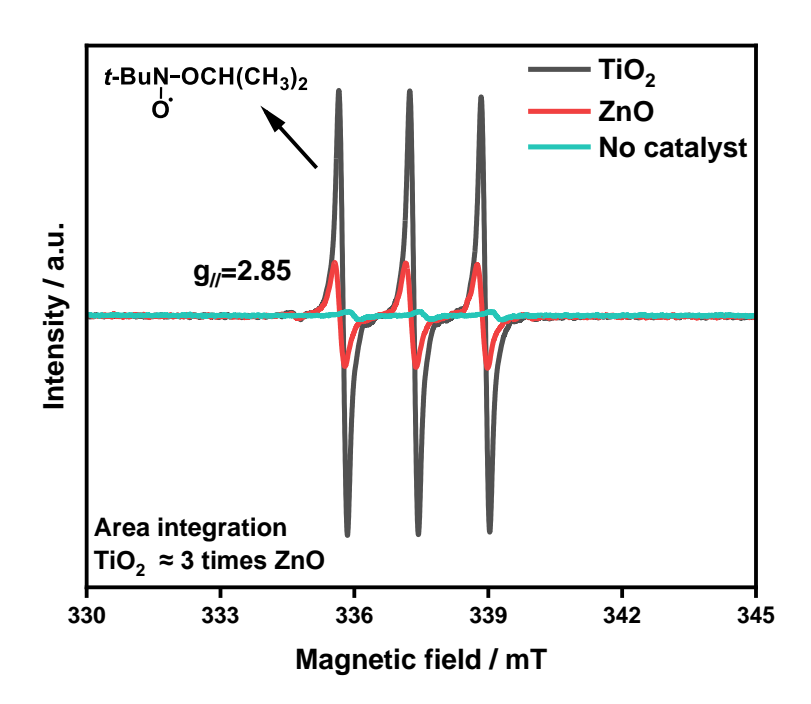


Figure 61 EPR spectra for capture experiment of alkoxy radicals from 2-propanol over TiO<sub>2</sub>, ZnO and no catalyst. The EPR measurement was conducted at room temperature, with a modulation frequency of 100 kHz, a microwave frequency of 9.46 GHz, a sweep time of 60 s, a microwave power of 10 mW, and swept from 330 to 345 mT. irradiation for 20s using 465 nm LED.

$$(CH_3)_2CHO$$
 +  $t$ -BuNO  $\longrightarrow$   $t$ -BuN-OCH $(CH_3)_2$   $O$ .

Equation 7 Representation of capturing alkoxy radicals from 2-propanol using t-BuNO

The temporal study on Cu/TiO<sub>2</sub> (**Figure 62**) indeed shows that after 1 h irradiation, Cu/TiO<sub>2</sub> exhibits nearly 80% selectivity towards bibenzyl. However, this selectivity continuously decreases in the following 2 h irradiation and maintains around 57% afterwards. The gradually increasing amount of surface adsorbed H on Cu/TiO<sub>2</sub> could be responsible for this decrease. By the end of experiment, almost 40% of benzyl radicals react with the surface adsorbed H to generate toluene. In contrast, the selectivity to bibenzyl remains as high as 90% with negligible formation of toluene during the term of 6 h reaction when Cu/ZnO is used as the photocatalyst. These results indicate

that the moderate photo-oxidation half reaction is also critical in achieving high selectivity of bibenzyl from benzyl chloride.

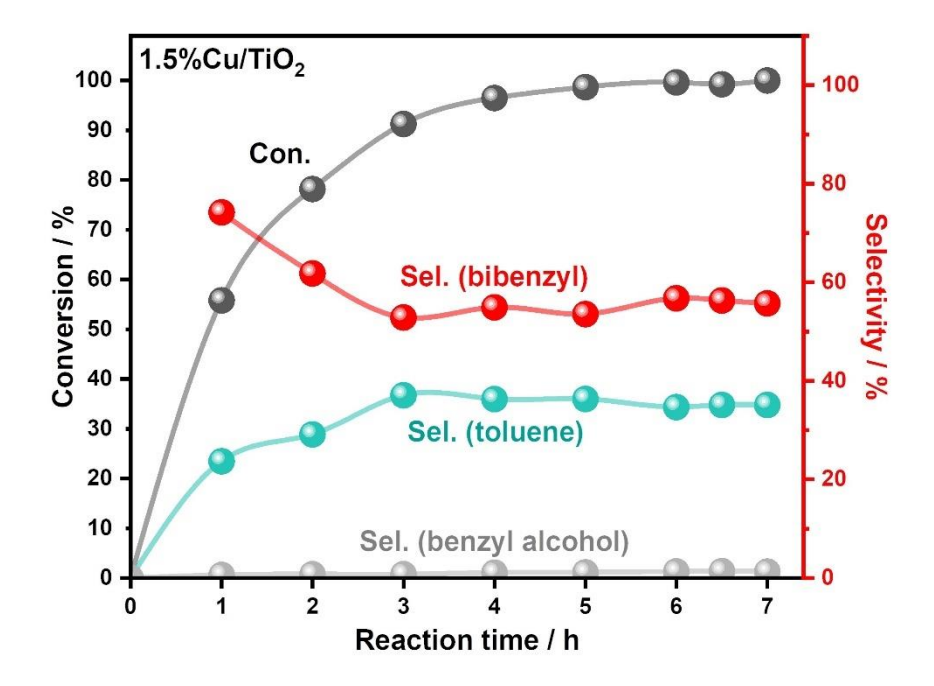


Figure 62 Temporal study of photocatalytic benzyl chloride conversion using  $Cu/TiO_2$ . Reaction conditions: 10mM reactant, 10 mg photocatalyst in 5 ml solvent (2-propanol: water = 1:1) under 365 nm LED irradiation for 7h, Ar, room temperature.

Finally, besides the enhanced adsorption of the reactant by Cu and moderate oxidation ability of ZnO, the charge transfer on ZnO and Cu/ZnO was also investigated by PL (**Figure 63**). There are two peaks observed in the PL spectra of bare ZnO. The strong peak at around 400 nm in the ultraviolet (UV) region is attributed to the near-band-edge emission of ZnO, and the broad peak at around 550 nm can be assigned to the oxygen vacancies-related emission<sup>[213]</sup>. A remarkable decrease of both emissions in PL intensity is observed on Cu/ZnO compared to bare ZnO, indicating the effective inhibition of recombination of charge carriers by the copper loading.

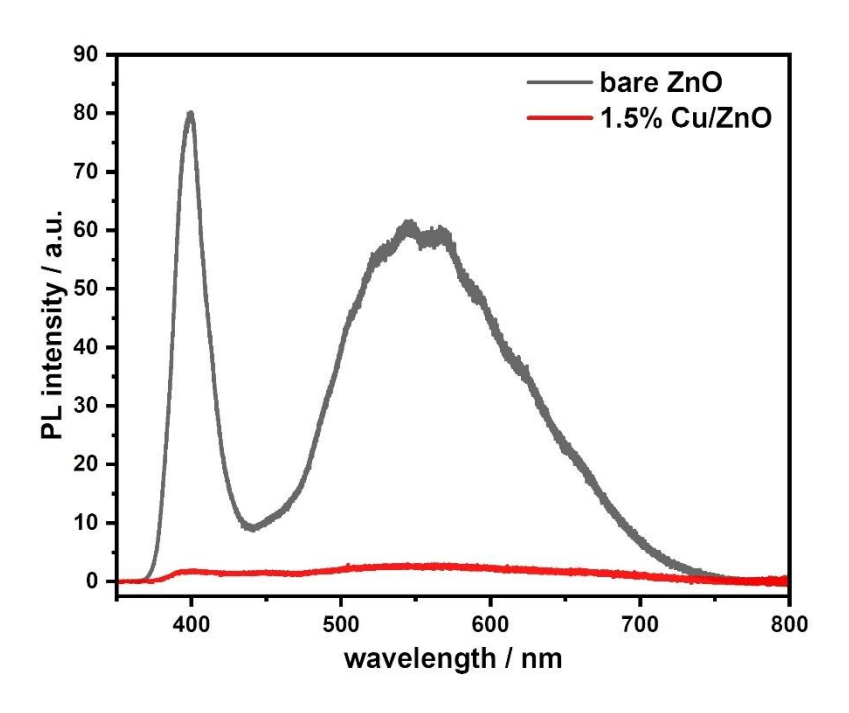


Figure 63 PL spectra of bare ZnO and Cu/ZnO post reaction sample.

Mulliken population analysis was also performed to study the charge transfer direction (**Table 7**, detailed calculation can be found in experimental section). Benzyl chloride on electrically neutral  $Cu_{10}$  cluster or on  $Cu_{10}$  cluster with one extra electron,  $Cu_{10}^-$ , were optimized. When benzyl chloride adsorbs on the  $Cu_{10}^-$  cluster, -0.111 e of the Mulliken charge of benzyl chloride indicates the electron transfer from  $Cu_{10}^-$  cluster to benzyl chloride. Also, compared to the  $Cu_{10}$  cluster, the Mulliken charge on the  $Cu_{10}^-$  cluster is more negative (-0.111 e < -0.086 e), suggesting that the negatively charged Cu cluster can benefit the activation of benzyl chloride  $^{[80]}$ .

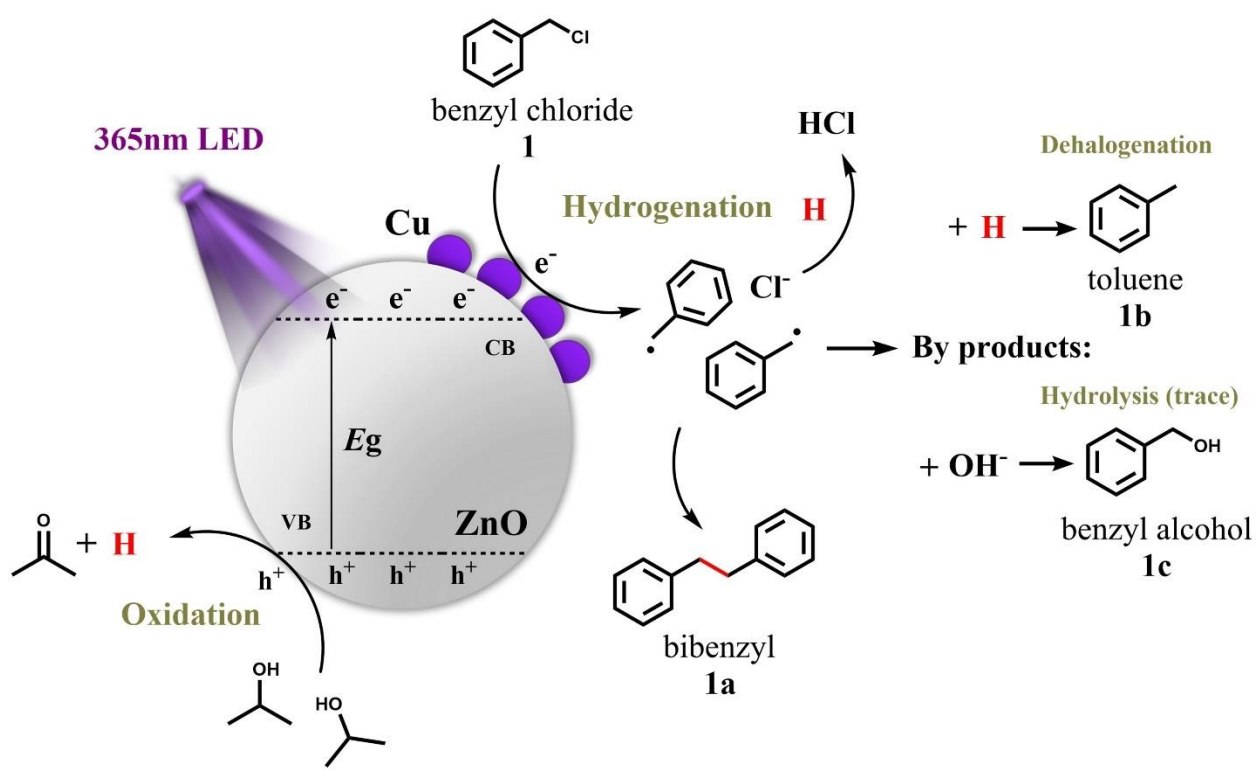
Table 7 Mulliken charge of C7H7Cl

Calculated system	Optimised structure <sup>[a]</sup>	Mulliken charge of C <sub>7</sub> H <sub>7</sub> Cl / e
C <sub>7</sub> H <sub>7</sub> Cl on Cu <sub>10</sub> cluster		-0.086



 $^{[a]}$  The grey, white, green, and purple spheres represent carbon atoms, hydrogen atoms, chlorine atoms and copper atoms, respectively.

Based on the results mentioned above, the possible reaction mechanism is proposed and illustrated in **Scheme 39**. The ZnO semiconductor is firstly excited by the irradiation of 365 nm LED, and the photo-generated electrons would then migrate to the surface of ZnO. The CuO NPs decorated on the surface are in-situ reduced to Cu<sup>+</sup>/Cu by the electrons, which is the activation process. Then this metallic copper loading can not only significantly alleviate the recombination between photogenerated electrons and holes by working as an electron sink but also enhance the adsorption of benzyl chloride onto the catalyst surface. The adsorbed benzyl chloride accepts electrons from Cu and breaks its C–Cl bond, and 2-propanol acts as an electron donor, which is moderately oxidized by the photo-generated holes on the valence band of ZnO and provides limited amount of protons. Those benzyl radicals can be stabilized on the surface of Cu, thus coupling with each other to generate bibenzyl (1a), while the released Cl atoms in water would form HCl, resulting in a decreased pH. Meanwhile, benzyl radical can either react with protons to generate toluene (1b) or hydroxy radical to generate trace amounts of benzyl alcohol (1c). The high selectivity to 1a is due to the abundant formation of benzyl radicals without excessive presence of protons.



 $Scheme\ 39\ Proposed\ mechanism\ for\ photocatalytic\ reductive\ homo-coupling\ of\ benzyl\ chloride\ over\ Cu/ZnO\ catalyst$ 

#### **5.4 Conclusion**

Bibenzyl, as the major raw material for pharmaceutical synthesis, has higher natural abundance of organic chlorides over others e.g. bromides and iodides. Therefore, the coupling of benzyl chlorides is highly sought-after. However, high selectivity and high yield towards bibenzyl using chlorides have not been realized by photocatalysis because of the strong C–Cl bonds. I developed a strategy for heterogeneous photocatalytic homo-coupling of benzyl chlorides, leading to the first successful case with a 92% yield. A series of transition metal co-catalysts were first screened and the reaction conditions (including solvents, Cu loading and water content) were then optimized. The unprecedented high yield towards bibenzyl can be achieved over Cu/ZnO photocatalyst with 1.5 wt% copper loading using 2-propanol and water mixture as the solvent. Furthermore, the

photocatalytic activity is very stable during the term of 8 cycles without obvious decay in the yield of bibenzyl. The Cu/ZnO photocatalyst can also be applied to 11 benzyl chloride derivatives to achieve their homo-couplings, among which 10 derivatives have gained excellent yields (72% to 96%), which shows its potential for wide application. Fundamentally, the TPD result indicates Cu can improve interaction between benzyl chloride and the catalyst. By comparing Cu/ZnO with Cu/TiO<sub>2</sub> using EPR measurement, I found that photo-oxidation rate of 2-propanol on TiO<sub>2</sub> is 3 times higher than that on ZnO, indicating the moderate oxidation ability of ZnO is another key to achieving high bibenzyl yield from chloride substrates.

# Chapter 6 CuOx and PdO Co-decorated CTF-1 for Efficient Suzuki-Miyaura Coupling Reaction

For the first two chapters, I studied the homo-coupling of benzaldehyde and benzyl chloride. However, cross-coupling is another subset when constructing C–C bonds. These reactions demand the use of two distinct fragments, posing a challenge in controlling the selectivity throughout the process. My research plan cantered around investigating the renowned Suzuki-Miyaura cross-coupling reaction within a photocatalytic system. The primary goal is to achieve enhanced control over the selectivity towards the coupling pathway while simultaneously reducing the usage of noble co-catalysts (Pd).

#### **6.1 Introduction**

Covalent triazine frameworks (CTFs), a new type of porous organic polymers, are usually fabricated from cyclotrimerisation of aromatic nitriles under different conditions. These CTFs often exhibit great properties, such as excellent chemical stability, and responsive to visible light. Therefore, it has gained considerable attention in the last decade owing to its potential for extensive applications, especially in photocatalysis<sup>[214]</sup>. The current research focus of CTFs in photocatalysis includes water splitting<sup>[215],[216]</sup>, CO<sub>2</sub> reduction<sup>[217],[218]</sup>, environmental remediation<sup>[219],[220]</sup> and organic synthesis. Among these research areas, the organic synthesis is appealing since the direct utilisation of solar energy to drive organic reactions is considered an efficient and highly sustainable pathway compared to traditional thermal catalysis. Due to the properties mentioned above, CTFs have been applied to a series of organic reactions. Photocatalytic selective oxidation of alcohols over CTF-Th@SBA-15 has been reported, in which the thiophene containing CTF was added onto the mesoporous silica SBA-15 through a superacid-catalysed method, and

corresponding aldehydes were obtained with 99% yields<sup>[221]</sup>. Photocatalytic cycloaddition of *trans*-anethol and mequinol was carried out by CTF-2BT and it was found smaller particle sizes of CTFs could enhance the activity<sup>[222]</sup>. Photocatalytic Ugi reaction and functionalisation of thiophenols were achieved by 2,3-dihydrothieno[3,4-b][1,4]dioxine (DD) modified CTF (DD-CTF) with high yields due to significant promotion of charge transfer and separation over DD-CTF<sup>[223]</sup>.

The Suzuki-Miyaura coupling (SMC), one of the most important methods in constructing C–C bonds, was named after A. Suzuki, who was awarded the Nobel Prize in Chemistry in 2010. In most cases, the SMC reaction indicates the coupling between organoboron substrates and aryl halides and requires the participation of Pd catalyst and base. Due to the high selectivity and yield, Pd has been regarded as an excellent catalytic site for SMC reaction, and in photocatalysis, various heterogeneous photocatalysts have been investigated to induce this reaction, including Au–Pd@ZrO<sub>2</sub><sup>[75]</sup>, Pd/ZnO<sup>[74]</sup>, Pd/TiO<sub>2</sub><sup>[72]</sup>, Pd/SiC<sup>[66]</sup>, Pd/C<sub>3</sub>N<sub>4</sub><sup>[96]</sup> and Au-Pd/HPS<sup>[110]</sup>. However, most of these photocatalysts have fairly high palladium loading amount (>3%). Considering palladium is a noble metal, these catalysts are cost-inefficient, and it is desired to find an alternative way to achieve SMC reactions with high performance but low palladium loading amount.

In this study, the commodification of CTF-1 photocatalysts by PdO and CuOx clusters (Pd<sub>0.2</sub>Cu<sub>1</sub>/CTF-1) was investigated to overcome the major drawback mentioned above for photocatalytic SMC reaction. SMC between 4-bromoanisole and phenylboronic acid is achieved under 365 nm light irradiation and the yield of desired coupling product 4-methoxybiphenyl can reach 87%, which is 16 times higher in comparison with the single metal decorated CTF-1 (Pd<sub>0.2</sub>/CTF-1) under the same reaction conditions. This low-cost system has also been confirmed by 8 various aryl bromides with excellent yields (>90%) and the concentration of palladium is only

0.018 mol% with respect to the substrate. The high performance is attributed to the synergistic effect between PdO and CuOx. Palladium functions as a reduction site to activate the C-Br bonds, while copper species accelerate the oxidative half-reaction during the photocatalytic process and further improve the charge separation and transfer in the system.

## **6.2 Experimental section**

## **Fabrication of photocatalysts:**

Synthesis of CTF-1: The covalent triazine based framework CTF-1 was synthesised using a modified microwave-assisted method<sup>[224]</sup>. In this process, 3 g terephthalonitrile (sigma-Aldrich, 98%) and 10 ml of trifluoromethanesulfonic acid (Sigma-Aldrich, reagent grade 98%) were mixed in a 100 ml PTFE liner (CEM), which was then sealed by CEM standard frame support module and placed in a microwave oven (MARS,CEM). After 25 min ramping, the temperature was maintained at 115°C for 60 min. Both the temperature and ramp rate were controlled by automatic output power adjusting. After cooling to room temperature, the resulting yellow solid was ground into particles and then washed with acetonitrile at 70°C three times to remove any unreacted precursor. The particles were then washed with deionised water several times to remove the acid solvent. Finally, the particles were dried overnight at 180°C in a vacuum oven to remove residual water and excess trifluoromethanesulfonic acid.

## **Synthesis of metal/CTF-1 photocatalyst:**

I: for single metal decorated sample, the PdO or CuOx was loaded on CTF-1 via an impregnation method: certain amount of PdCl<sub>2</sub> anhydrous (0.2, 0.5, 1, 1.5, 2 wt% of Pd) was firstly dissolved in 500  $\mu$ l deionised water. The above solution was added to an alumina crucible containing 100 mg CTF-1 under vigorous stirring. After evaporating water, the crucible was transferred to a muffle furnace and calcined at 300 °C for 2 h with a ramping rate of 5 °C/min.

For the deposition of CuOx,  $\text{Cu(NO}_3)_2 \cdot 2.5\text{H}_2\text{O}$  (1 wt% Cu) was used as the metal source while other procedures were identical to the PdO loading

**II:** for dual metal decorated sample Pd<sub>x</sub>Cu<sub>y</sub>/CTF-1, the PdO and CuO<sub>x</sub> were step by step loaded on CTF-1 via the aforementioned impregnation method. Firstly, a certain amount of Cu(NO<sub>3</sub>)<sub>2</sub> · 2.5H<sub>2</sub>O (0.2, 0.5, 1, 1.5 wt% Cu) was dissolved in 500 μl deionised water. The above solution was added to an alumina crucible containing 100 mg CTF-1 under vigorous stirring. After evaporating water, the crucible was transferred to a muffle furnace and calcined at 300 °C for 2 h with a ramping rate of 5 °C/min. The sample after calcination was named Cu<sub>x</sub>/CTF-1. A certain amount of PdCl<sub>2</sub> anhydrous (0.2, 0.5 wt% of Pd) was dissolved in 500 μl deionised water. The solution was added to 100 mg Cu<sub>x</sub>/CTF-1 in an alumina crucible and the previous impregnation and calcination process were repeated to obtain Cu<sub>y</sub>Pd<sub>x</sub>/CTF-1.

## **Photocatalytic activity tests:**

Firstly, 5 mg  $Pd_xCu_y/CTF-1$  photocatalyst was added into a reactor containing 5 ml solvent (EtOH: water = 1:1), 10 mM 4-bromoanisole, 1.3 eq phenylboronic acid and 4 eq  $K_2CO_3$ . The above reactor was then purged by argon under stirring condition for 10 min to remove dissolved  $O_2$ . After that, the reactor containing the suspension was eventually placed into a multi-channel system

equipped with 365 nm LEDs and irradiated for 15 h under continuous stirring at room temperature. The solid photocatalyst was filtered and then the liquid mixture was analysed by Shimadzu GC-MS-QP2010SE using Rxi-5SilMS Column. Reaction equation is illustrated in **Equation 8.** 

**Equation 8 Reaction equation for SMC of 4-bromoanisole** 

#### 6.3 Results and discussion

#### **6.3.1** Materials characterisation

In order to confirm the structure of CTF-1, a series of characterisations was conducted. For the decorated CTF-1 sample, both PdO and CuOx species were introduced via the impregnation method and the as-prepared sample was designated as Pd<sub>x</sub>Cu<sub>y</sub>/CTF-1, in which *x* and *y* represent the nominal weight ratio of Pd species and Cu species to CTF-1, respectively. X-ray diffraction (XRD) results for Pd<sub>0.2</sub>Cu<sub>1</sub>/CTF-1 and bare CTF-1 are shown in **Figure 64**. For the bare CTF-1 sample, the first peak located at 7.9° is assigned as (100), indicating the hexagonal cages. One additional small peak at 11.9° (200) is observed. The multi-layer structure can be attributed to the peak at 26.1° (001), and according to Bragg's law, the interlayer distance of CTF-1 is calculated as 3.4 Å<sup>[225]</sup>. Compared to bare CTF-1, all 3 peaks (100), (200) and (001) can also be observed, indicating the structure of Pd<sub>0.2</sub>Cu<sub>1</sub>/CTF-1 remained stable after the heat treatment during the metal loading process. Meanwhile, no extra peak for Pd and Cu co-catalysts can be found in the spectra, probably due to either low concentration and/or high dispersion on the support of ZnO<sup>[188]</sup>.

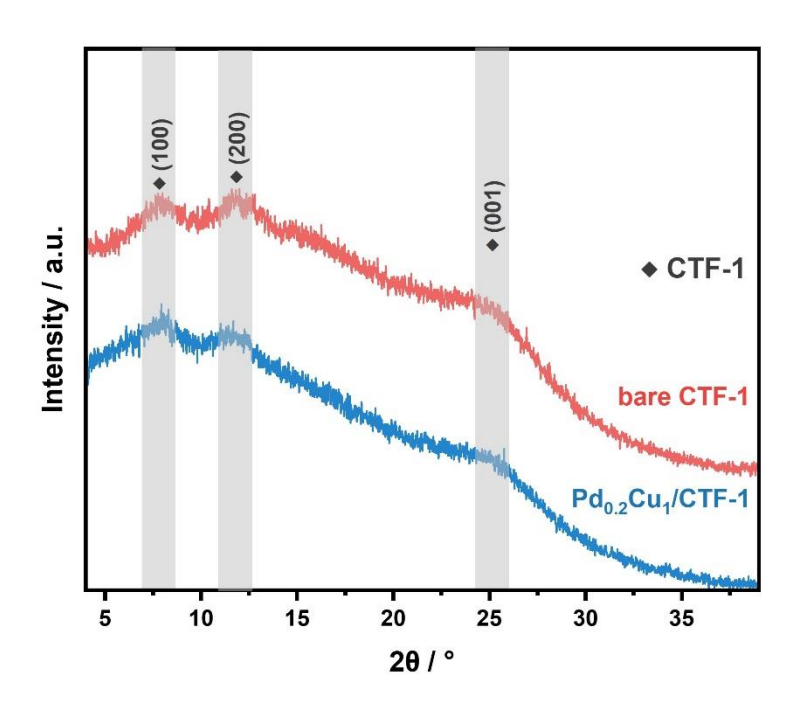


Figure 64 XRD patterns of bare CTF-1 and  $Pd_{0.2}Cu_1/CTF$ -1 samples

The Fourier-transform infrared spectroscopy (FTIR) results of both bare and decorated CTF-1 samples are shown in **Figure 65**. The two strongest peaks at 1345 cm<sup>-1</sup> (benzene ring breathing) and 1501 cm<sup>-1</sup> (C–N bond stretching) for both samples represent the structure of the triazine ring<sup>[226],[227]</sup>. The small peak at 2230 cm<sup>-1</sup> is attributed to the cyanide group ( $-C\equiv N$ )<sup>[228]</sup>. This result also proves the impregnation method of PdO and CuOx loadings did not break the structure of CTF-1.

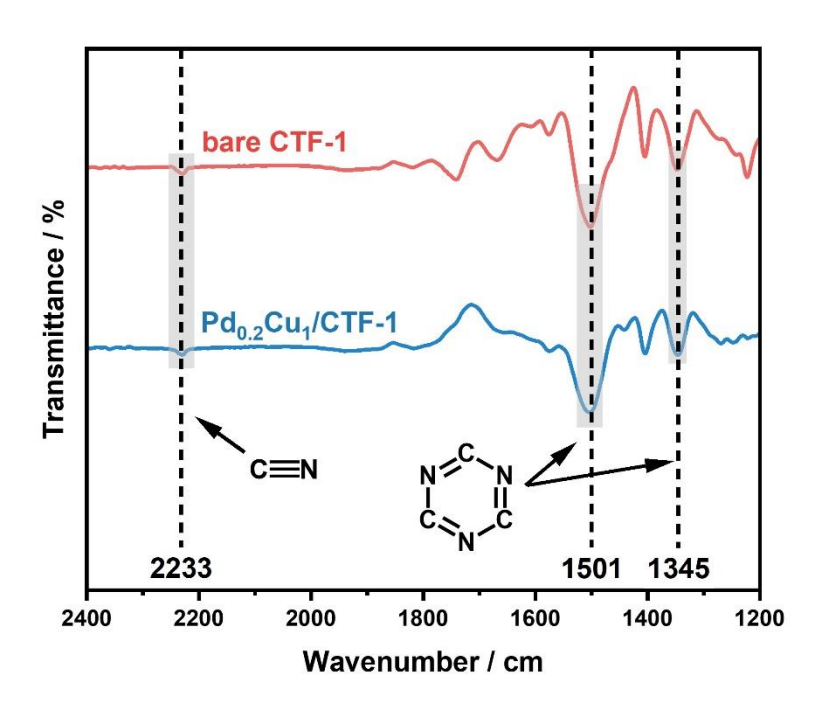


Figure 65 FTIR spectra of bare CTF-1 and Pd<sub>0.2</sub>Cu<sub>1</sub>/CTF-1 samples

The solid-state <sup>13</sup>C NMR (<sup>13</sup>C ssNMR) of CTF-1 is shown in **Figure 66**. Two strong peaks at 129 ppm and 139.1 ppm are assigned to the carbon atoms on the aromatic ring and the carbon atom directly attached to the triazine ring, respectively<sup>[227]</sup>. The peak at 170.5 ppm is related to the carbons within the triazine units. The smallest peak at 116.1 ppm are associated with two different types of carbon atom in the terminating groups, and this weak intensity indicates relatively good polymerisation<sup>[228]</sup>.

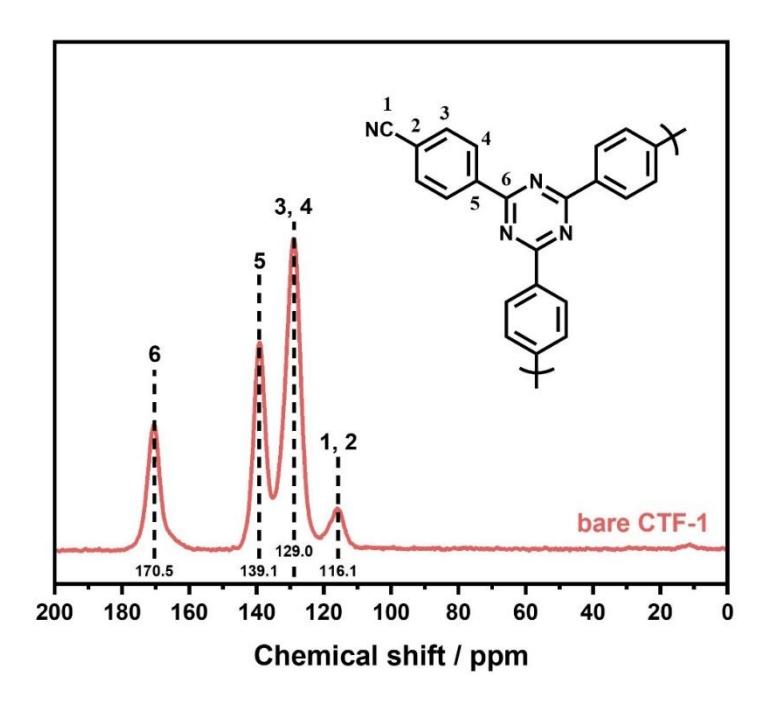


Figure 66 <sup>13</sup>C ssNMR spectrum of CTF-1

The X-ray photoelectron spectroscopy (XPS) result are shown in (**Figure 67**). The existence of triazine units can be confirmed by the peaks at 286.4 eV and 398.8 eV, corresponding to C 1*s* and N 1*s* of the triazine ring, respectively. The peak at 284.5 eV indicates the C 1*s* on the aromatic units, while the small peak at 288.5 eV can be assigned to C=O, and this unanticipated C=O state might be derived from hydrolyzation of marginal –CN on the CTF-1 structure<sup>[229]</sup>. The last peak at 400.2 eV can be attributed to the N atoms in the amide group. The theoretical value of triazine carbon to phenyl carbon for an ideal CTF-1 sample should be 1:3 and based on the XPS result, the ratio of C<sub>triazine</sub>: C<sub>phenyl</sub> of the synthesised CTF-1 is 1:2.54, which is close to the ideal value<sup>[230]</sup>. All these results further indicate the successful synthesis of CTF-1.

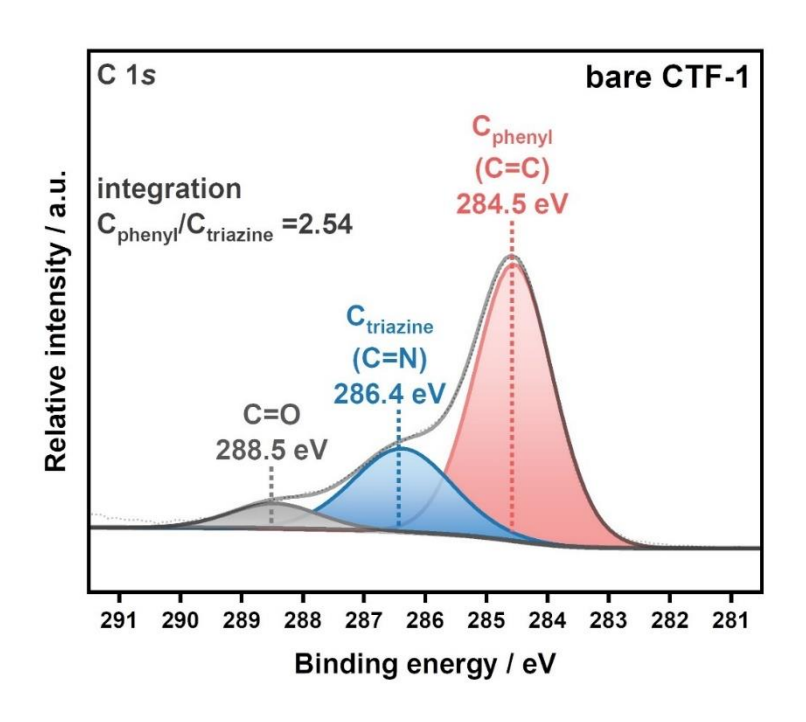


Figure 67 Deconvolution of XPS spectrum of the C 1s in bare CTF-1

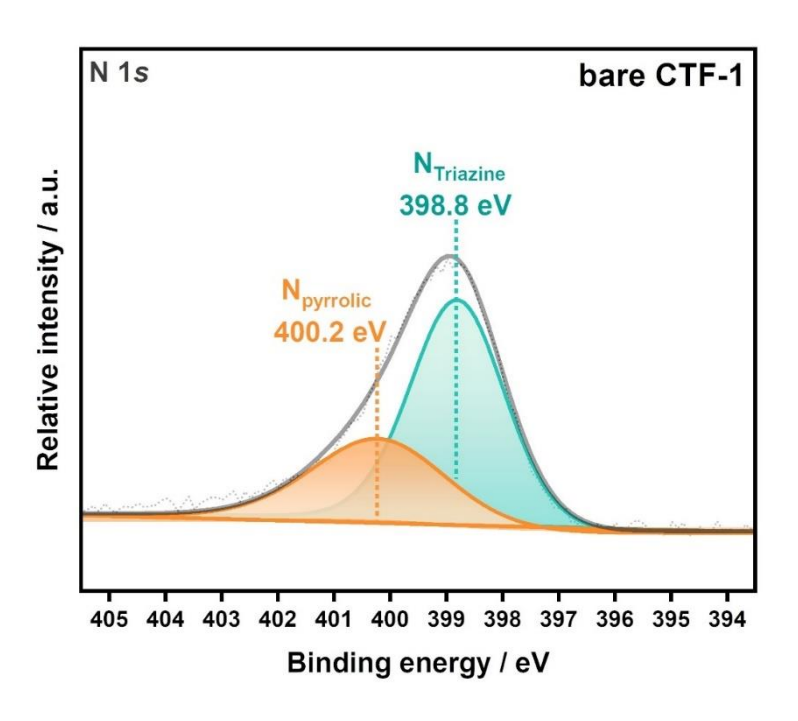


Figure 68 Deconvolution of XPS spectra of the N 1s in bare CTF-1

According to the above characterisations, the polymeric structure and the alternated aromatic units of CTF-1 are confirmed to be successfully synthesised, and the structure remains similar after the dual metal loading process.

## **6.3.2** Photocatalytic activity

After confirming the organic structure of both bare CTF-1 and decorated CTF-1 samples, their photocatalytic activity toward Suzuki-Miyaura coupling of 4-bromoanisole and phenylboronic acid was investigated and the result is shown in **Figure 69**. After 15 h light irradiation ( $\lambda$  = 365 nm), bare CTF-1 exhibits negligible conversion of 4-bromoanisole, likely owing to its high recombination rate of photoinduced electrons and holes. Palladium, as a noble metal, is well-known for its promising catalytic property for driving SMC reactions. Therefore, the loading amount effect of PdO (0.2, 0.5, 1, 1.5, 2 wt% Pd) regarding the catalytic performance was firstly studied and equations for calculating conversion, selectivity and yield are listed below (**Equation 8**):

$$conversion = \frac{mole\ of\ benzyl\ chloride\ reacted}{moles\ of\ benzyl\ chloride\ fed\ into\ the\ system} \times 100\% \tag{6-1}$$

$$selectivity = \frac{mole\ of\ the\ target\ product\ generated}{mole\ of\ benzyl\ chloride\ reacted} \times 100\%\ (times\ 2\ for\ bibenzyl) \tag{6-2}$$

$$yield = conversion \times selectivity$$
 (6 – 3)

Equation 9 for calculating conversion, selectivity and yield

.

It should be noted that low amounts of PdO loading (less than 1 wt%) lead to poor yield (less than 20%) and moderate selectivity (around 50%) toward desired product 4-methoxyphenyl. Further increasing the loading amount of PdO can improve both yield and selectivity accordingly, and the highest yield (89%) towards 4-methoxybiphenyl can be achieved on Pd<sub>2</sub>/CTF-1 with a selectivity of 91% after 15 h reaction. However, anisole and 4,4'-dimethoxybiphenyl, two byproducts from the dehalogenation and homo-coupling process, are observed as well. Excessive generation of anisole radical coupling with each other or protons adsorbed on the PdO surface is likely to be accountable for the generation of the two byproducts.

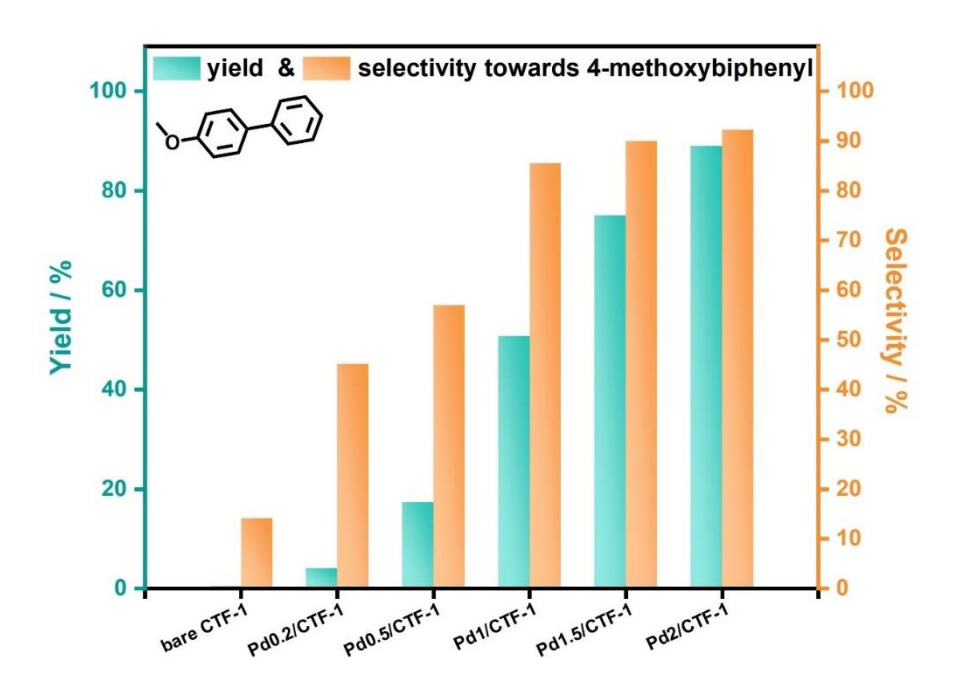


Figure 69 Effect of Pd loading on the photocatalytic SMC reaction of 4-bromoanisole over CTF-1 photocatalysts. Reaction conditions: 0.05 mmol 4-bromoanisole, 1.3 equiv phenylboronic acid, 4 equiv  $K_2CO_3$ , 5 ml solvent (EtOH:  $H_2O=1:1$ ), 5 mg photocatalyst, 365 nm multi-channel LED, 15 h, Ar, room temperature

Interestingly, it is found that introducing CuOx to the catalyst can dramatically reduce the usage of palladium and achieve comparable or even better catalytic performance (**Figure 70**). Among

three bimetallic decorated samples, the highest yield (87%) towards 4-methoxybiphenyl is observed on Pd<sub>0.5</sub>Cu<sub>1</sub>/CTF-1 sample with a selectivity as high as 99%, which means the two byproducts mentioned above are not observed when copper is introduced as the second co-catalyst. This activity is 5 times higher in yield against Pd<sub>0.5</sub>/CTF-1 and is also similar to the Pd<sub>2</sub>/CTF-1 sample, indicating an important synergy between palladium and copper. For the other two samples Pd<sub>0.5</sub>Cu<sub>0.5</sub>/CTF-1 and Pd<sub>0.5</sub>Cu<sub>1.5</sub>/CTF-1, although a slight decrease in the yield is observed (around 75%), the selectivity remains unchanged. As a reference, the performance of Cu<sub>1</sub>/CTF-1 is also tested, but only a trace amount (2% yield) of 4-methoxybiphenyl is generated, suggesting copper alone cannot drive Suzuki-Miyaura cross-coupling reaction and palladium is crucial for this reaction.

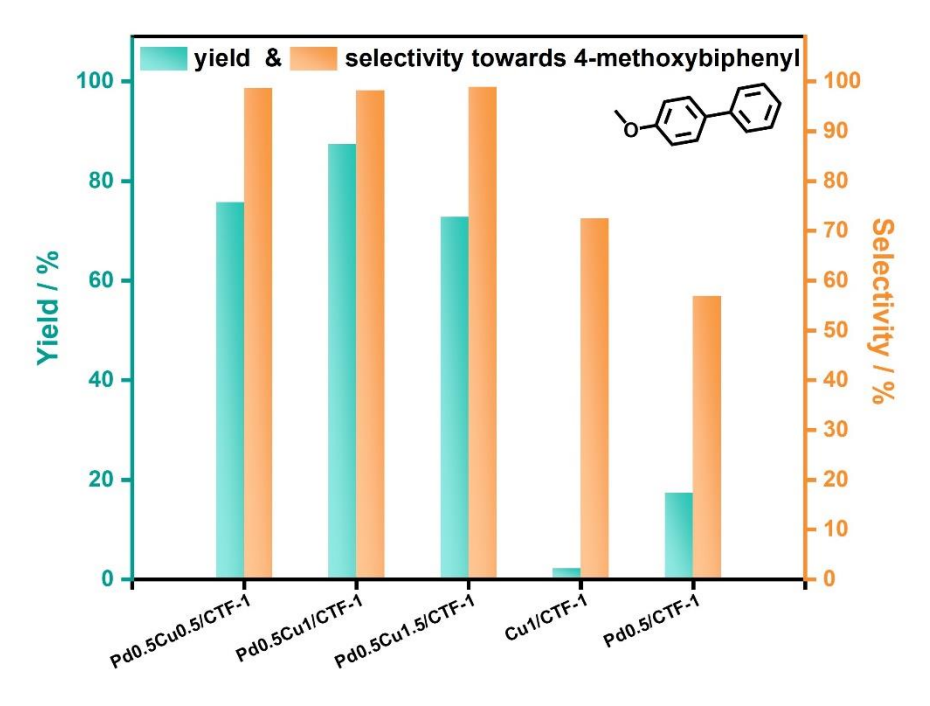


Figure 70 Effect of Cu loading on the photocatalytic SMC reaction of 4-bromoanisole over  $Pd_{0.5}/CTF-1$  photocatalysts. Reaction conditions: 0.05 mmol 4-bromoanisole, 1.3 equiv phenylboronic acid, 4 equiv  $K_2CO_3$ , 5 ml solvent (EtOH:  $H_2O=1:1$ ), 5 mg photocatalyst, 365 nm multi-channel LED, 15 h, Ar, room temperature

In order to figure out the function of cooper loading, the preparation order of the two co-catalysts was investigated. Two other photocatalysts were fabricated and designated as Cu<sub>1</sub>Pd<sub>0.5</sub>/CTF-1(T) and Cu<sub>1</sub>Pd<sub>0.5</sub>/CTF-1, in which (T) represents both Cu and Pd were mixed together and deposited in one go. As for Cu<sub>1</sub>Pd<sub>0.5</sub>/CTF-1, Pd was introduced before Cu. Based on the results (**Figure 71**), the yield of 4-methoxybiphenyl over the two photocatalysts largely decreases compared to Pd<sub>0.5</sub>Cu<sub>1</sub>/CTF-1, emphasising that the deposition sequence may play an important role in their performance. The function of Pd in the SMC reaction is believed to accept photoinduced electrons and break the C–X bond<sup>[56]</sup>, which is the rate-determining step in the SMC reaction<sup>[33]</sup>. If Pd species are introduced before CuOx, some CuOx would block the exposure of PdO and its contact with 4-bromoanisole, resulting in a reduced conversion and yield<sup>[202]</sup>.

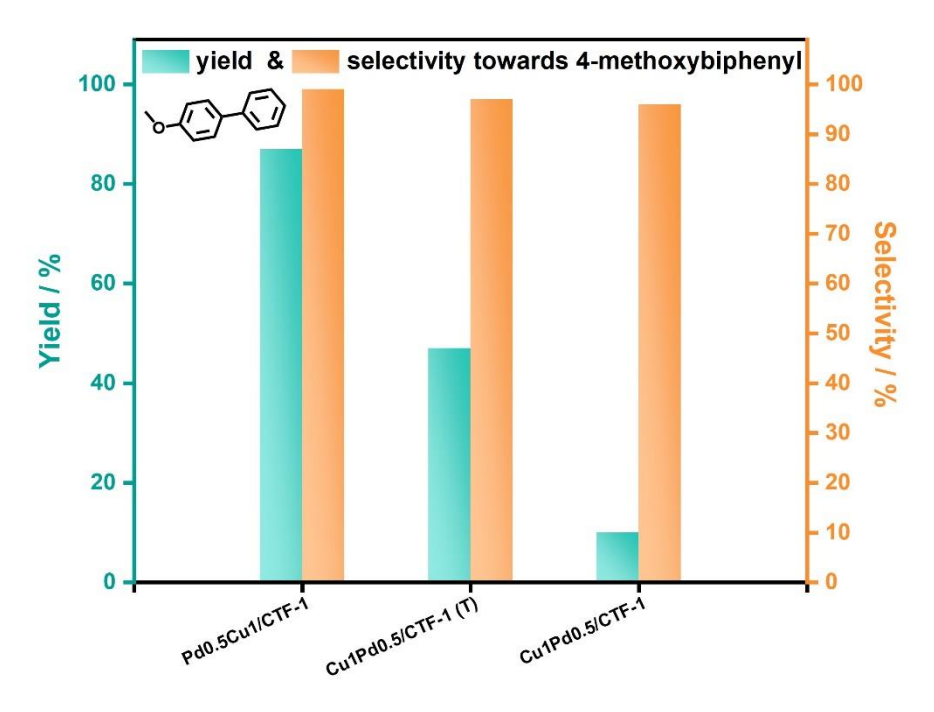


Figure 71 Effect of preparation order of Pd and Cu co-catalysts on CTF-1 for the photocatalytic SMC reaction of 4-bromoanisole. Reaction conditions: 0.05 mmol 4-bromoanisole, 1.3 equiv phenylboronic acid, 4 equiv  $K_2CO_3$ , 5 ml solvent (EtOH:  $H_2O=1:1$ ), 5 mg photocatalyst, 365 nm multi-channel LED, 15 h, Ar, room temperature

Moreover, based on the excellent performance obtained from Pd<sub>0.5</sub>Cu<sub>x</sub>/CTF-1 samples, the concentration of palladium is further reduced to 0.2 wt% (0.018 mol% regarding 4-bromoanisole). After introducing copper species, improved catalytic activity can be observed on all samples as expected (**Figure 72**), and Pd<sub>0.2</sub>Cu<sub>1</sub>/CTF-1 achieves the highest yield of 4-methoxybiphenyl (66%), with the 99% selectivity (so 86% yield after 20 h reaction). Remarkably, compared to Pd<sub>0.2</sub>/CTF-1, bimetallic Pd<sub>0.2</sub>Cu<sub>1</sub>/CTF-1 can improve the selectivity and yield towards the SMC product by 2 and 16 times, respectively (selectivity 45% to 99%, yield 4% to 66%), and its activity is comparable to Pd<sub>1.5</sub>/CTF-1. These results demonstrate a critical synergic effect between palladium and copper decorations, which has the potential to dramatically reduce the consumption of palladium in SMC reactions.

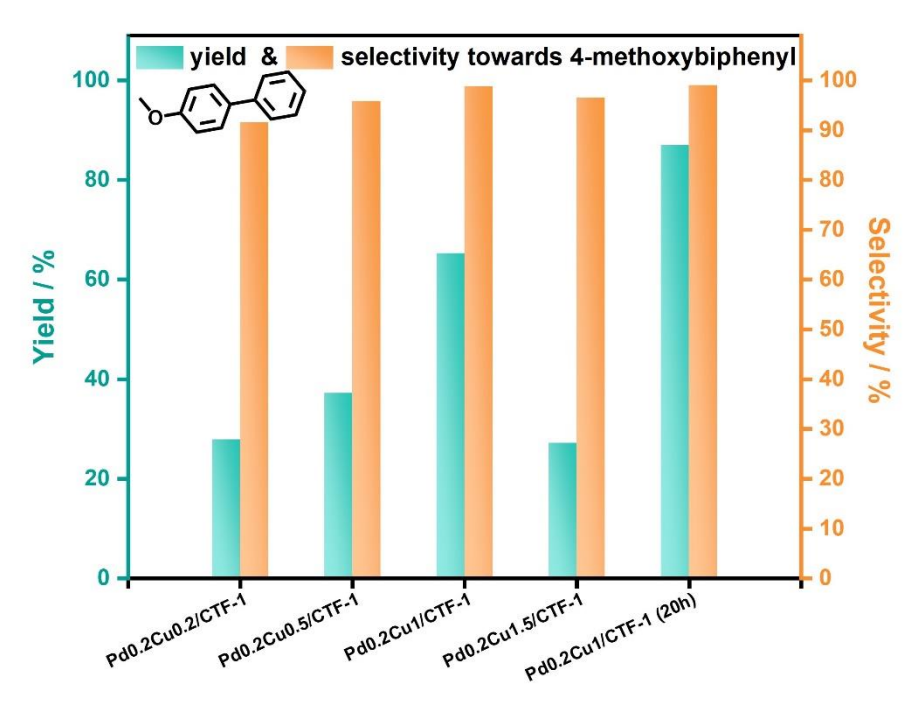


Figure 72 Optimisation of Cu loading on  $Pd_{0.2}/CTF-1$  for the photocatalytic SMC reaction of 4-bromoanisole. Reaction conditions: 0.05 mmol 4-bromoanisole, 1.3 equiv phenylboronic acid, 4 equiv  $K_2CO_3$ , 5 ml solvent (EtOH:  $H_2O=1:1$ ), 5 mg photocatalyst, 365 nm multi-channel LED, 15 h, Ar, room temperature

The stability and durability of  $Pd_{0.2}Cu_1/CTF-1$  were evaluated (**Figure 73**). After each run, the sample was separated and collected by filtrating the reaction mixture. After rinsing with water, the catalyst was dried in a vacuum oven and then reused. According to stability results, the yield of 4-methoxybiphenyl well remains over 80% with a slight decay (8%) after 3 cycles, indicating a good stability of  $Pd_{0.2}Cu_1/CTF-1$  photocatalyst for the SMC of 4-bromoanisole.

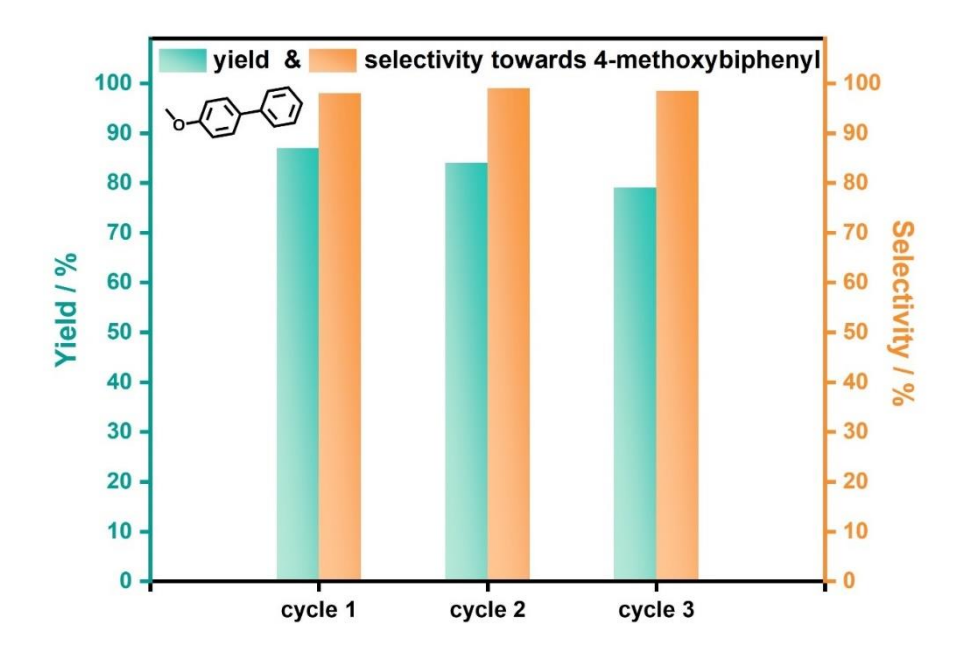


Figure 73 Stability test of  $Pd_{0.2}Cu_1/CTF-1$ . Reaction conditions: 0.05 mmol 4-bromoanisole, 1.3 equiv phenylboronic acid, 4 equiv  $K_2CO_3$ , 5 ml solvent (EtOH:  $H_2O=1:1$ ), 5 mg photocatalyst, 365 nm multi-channel LED, 20 h, Ar, room temperature

Reaction condition optimisation and control experiments of SMC reaction were then conducted over Pd<sub>0.5</sub>Cu<sub>1</sub>/CTF-1, and the results are summarised in **Table 8**. Entry 1-5 demonstrate the effect of solvent and water contents. MeCN, as an aprotic solvent, cannot produce the desired SMC product. This may be due to its higher oxidation potential<sup>[193],[56]</sup>, which is unfavourable to injecting electrons into the photocatalyst to facilitate the reduction half-reaction for the

dehalogenative process. On the other hand, ethanol exhibits 12% yield and 96% selectivity towards 4-methoxybiphenyl, demonstrating its potential as both the solvent and scavenger to drive this coupling reaction. Additionally, specific amounts of water contents in the solvent (30%, 50%, 70%) were investigated by taking into account the possible influence of solubility of organic compounds and the product HBr. With the addition of water, the selectivity to 4-methoxybiphenyl further increases (from 96% to 99%). Notably, a high 4-methoxybiphenyl yield of 87% with the 99% selectivity can be reached after 15 h reaction when 50% water content is added. This may be due to the higher solubility of one dehalogenative product HBr in water, likely shifting the reaction equilibrium to form more 4-methoxybiphenyl<sup>[196]</sup>. While too much water (e.g., 70%) may decrease the solubility of bromobenzene in a protic organic solvent of ethanol, leading to poor dispersion and interaction between the substrate and the catalyst, hence the poor activity. There are two functions of the base in SMC reaction, one is to activate and convert the phenylboronic acid to Ph- $\overline{B}(OH)_3$ , which will be oxidised by photo-generated holes into phenyl radical cation<sup>[113]</sup>. The other function is that excessive base can react with the generated boric acid and HBr to maintain the acid-base equilibrium, therefore protecting the production towards 4-methoxybiphenyl<sup>[231]</sup>. The effect of different bases was then studied (Table 8, Entry 4, 6-7), and among the three bases tested, K<sub>2</sub>CO<sub>3</sub> is the most effective one.

Entry 8 shows the result of SMC carried out under visible light irradiation (Xe lamp with a long-pass filter  $\lambda > 420$  nm). After 7 h irradiation, 50% yield towards 4-methoxybiphenyl is achieved with the 98% selectivity. The photoabsorption properties of bare CTF-1 and Pd<sub>0.5</sub>Cu<sub>1</sub>/CTF-1 were then investigated by UV-vis spectroscopy (**Figure 74**). Bare CTF-1 absorbs photons in the visible region and the absorption decreases when the wavelength increases. After introducing palladium and copper onto CTF-1, the photoabsorption remains similar at the wavelength below 375 nm,

indicating the intact band structure of CTF-1. In contrast, an enhancement is observed in the range  $\geq$  375 nm for the decorated sample. The broadened enhancement throughout the visible range may be attributed to CuO<sup>[207]</sup>, and this result shows the potential of Pd<sub>0.5</sub>Cu<sub>1</sub>/CTF-1 in photocatalysis within the visible region.

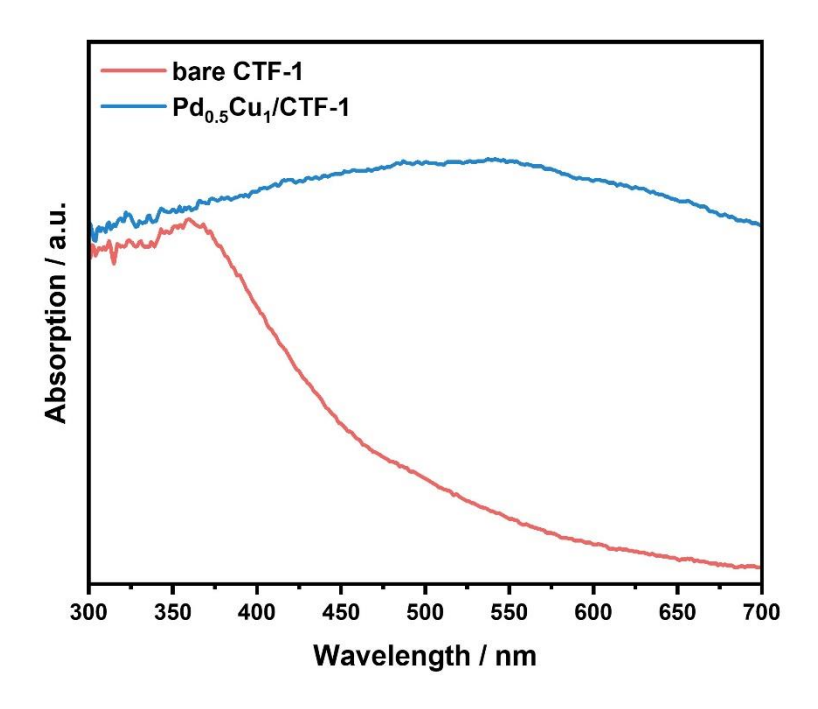


Figure 74 UV-vis spectra results of bare CTF-1 and Pd<sub>0.5</sub>Cu<sub>1</sub>/CTF-1

Control experiments were next conducted (**Table 8**, Entry 9-12). In the absence of Pd<sub>0.5</sub>Cu<sub>1</sub>/CTF-1 photocatalyst, only trace amount of 4-methoxybiphenyl is found in the system. Under dark condition, a moderate yield (28%) can be observed over Pd<sub>0.5</sub>Cu<sub>1</sub>/CTF-1 alone. However, light irradiation can boost the yield more than 3 times higher (87%) compared with the dark condition, which indicates the importance of light energy and confirms a photocatalytic reaction dominates the process. Electron capture and hole capture experiments were then carried out to further confirm this conclusion. After 15 h 365 nm LED irradiation, there is only a small yield (< 5%) of 4-

methoxybiphenyl observed with the addition of either electron scavenger  $NaIO_3$  or hole scavenger NaI. These results suggest that the SMC of 4-bromoanisole and phenylboronic acid is indeed a photocatalytic process, requiring the presence of electron and hole pair generated by light irradiation on  $Pd_{0.5}Cu_1/CTF-1$ .

Table 8 Optimised reaction conditions and control experiments of SMC reaction over Pd <sub>0.5</sub> Cu <sub>1</sub> /CTF-1					
entry	solvent	base	variations	yield (%)	Sel (%)
1	MeCN	K <sub>2</sub> CO <sub>3</sub>	365 nm irradiation	trace	-
2	EtOH	$K_2CO_3$	365 nm irradiation	12	96%
3	EtOH/H <sub>2</sub> O (7:3)	$K_2CO_3$	365 nm irradiation	66	98%
4	EtOH/H <sub>2</sub> O (5:5)	$K_2CO_3$	365 nm irradiation	87	99%
5	EtOH/H <sub>2</sub> O (3:7)	$K_2CO_3$	365 nm irradiation	5	81%
6	EtOH/H <sub>2</sub> O (5:5)	NaOH	365 nm irradiation	29	96%
7	EtOH/H <sub>2</sub> O (5:5)	Na <sub>2</sub> CO <sub>3</sub>	365 nm irradiation	42	98%
8	EtOH/H <sub>2</sub> O (5:5)	$K_2CO_3$	Xe lamp(> 420 nm)	50ª	98%
9	EtOH/H <sub>2</sub> O (5:5)	$K_2CO_3$	No catalyst	trace	-
10	EtOH/H <sub>2</sub> O (5:5)	$K_2CO_3$	No 365 nm irradiation	28	98%
11	EtOH/H <sub>2</sub> O (5:5)	$K_2CO_3$	2 eq NaIO <sub>3</sub> electron capturer	2	97%
12	EtOH/H <sub>2</sub> O (5:5)	K <sub>2</sub> CO <sub>3</sub>	2 eq NaI hole capturer	4	98%

Reaction conditions: 0.05 mmol 4-bromoanisole, 1.3 equiv phenylboronic acid, 4 equiv base, 5 ml solvent, 5 mg photocatalyst, 365 nm multi-channel LED, 15 h, Ar. areaction time 7 h instead of 15 h.

### **6.3.3** Substrates scopes

The reaction system was further extended to 8 aryl bromides with various functional groups to examine the general applicability of Pd<sub>0.2</sub>Cu<sub>1</sub>/CTF-1 for photocatalytic SMC reactions, as shown in **Figure 75**. As expected, in the presence of phenylboronic acid, bromobenzene (1) without any functional group can successfully synthesise biphenyl 1a with the 96% yield in this system. The Pd<sub>0.2</sub>Cu<sub>1</sub>/CTF-1 photocatalyst can efficiently drive the Suzuki-Miyaura coupling of the aryl bromides with different methyl-groups. For example, both 3-bromotoluene (2) and 4bromotoluene (3) can be efficiently converted to the corresponding coupling products 2a and 3a, with a high yield of 91% and 94%, respectively. However, when number of methyl groups on the substrates increases (4-bromo-o-xylene (4)), a slight decrease in the yield of 4a has been observed (89%). The observed decrease in the yield can be attributed to the steric hindrance effect<sup>[97]</sup>. With the strong electron-donating group, methoxy, the lowest yield of corresponding coupling product 5a (87%) is obtained from the reference substrate 4-bromoanisole (5). In contrast, when electronwithdrawing groups are introduced (e.g., -Cl, -F), the yields of desired products **6a** and **7a** are as high as 98% and 99%. Furthermore, 4-Bromobenzotrifluoride (8) with the strongest electronwithdrawing group -CF<sub>3</sub> can also achieve 98% yield of 8a. The above results indicate that Pd<sub>0.2</sub>Cu<sub>1</sub>/CTF-1 shows excellent tolerance to a wide substrate scope, and both the <sup>1</sup>H NMR and <sup>13</sup>C NMR results are shown in **Figure 76-Figure 83**.

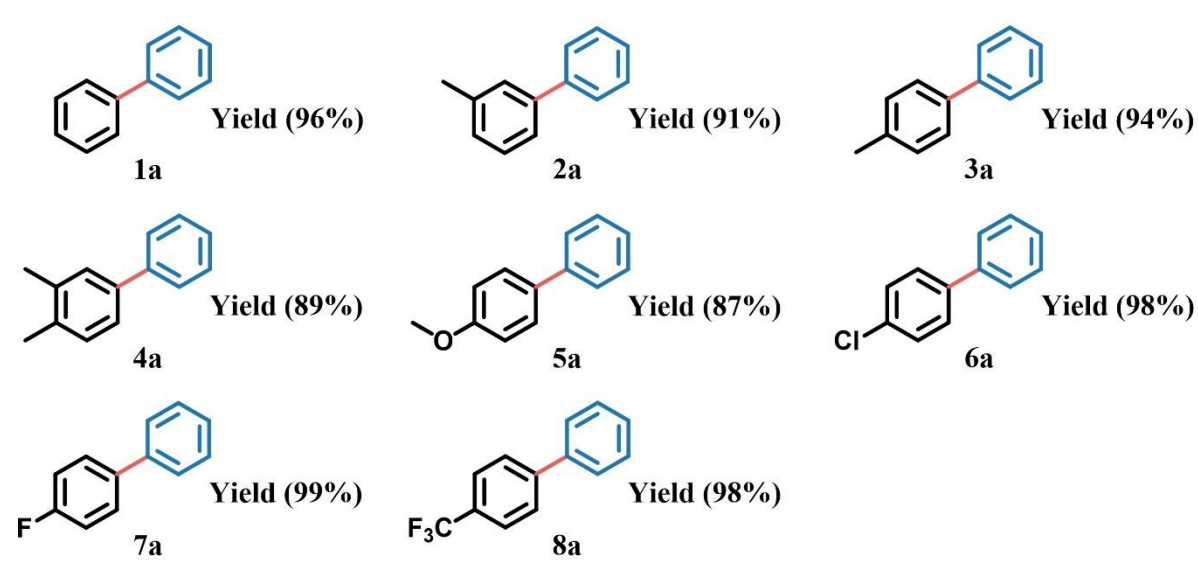
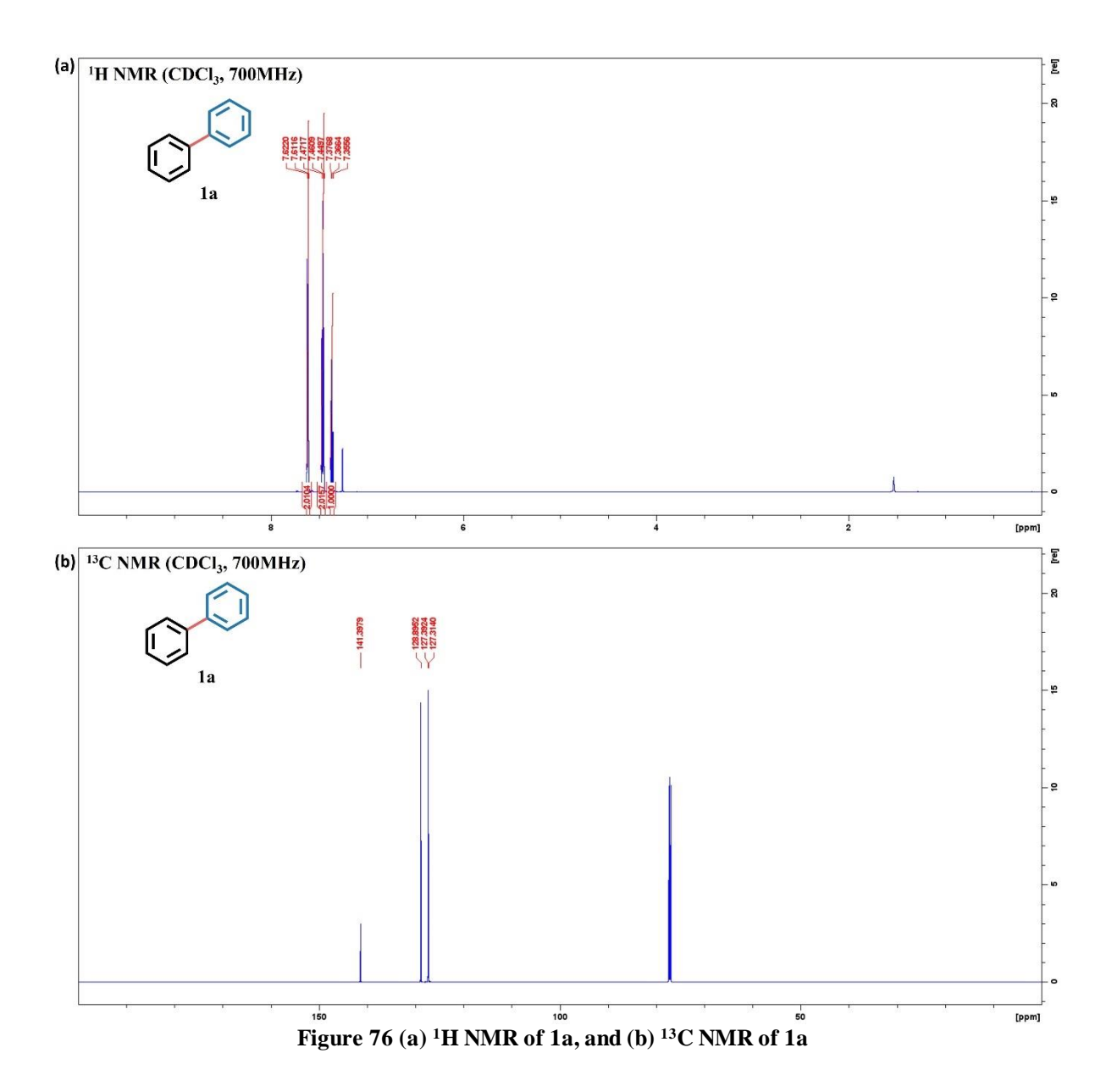
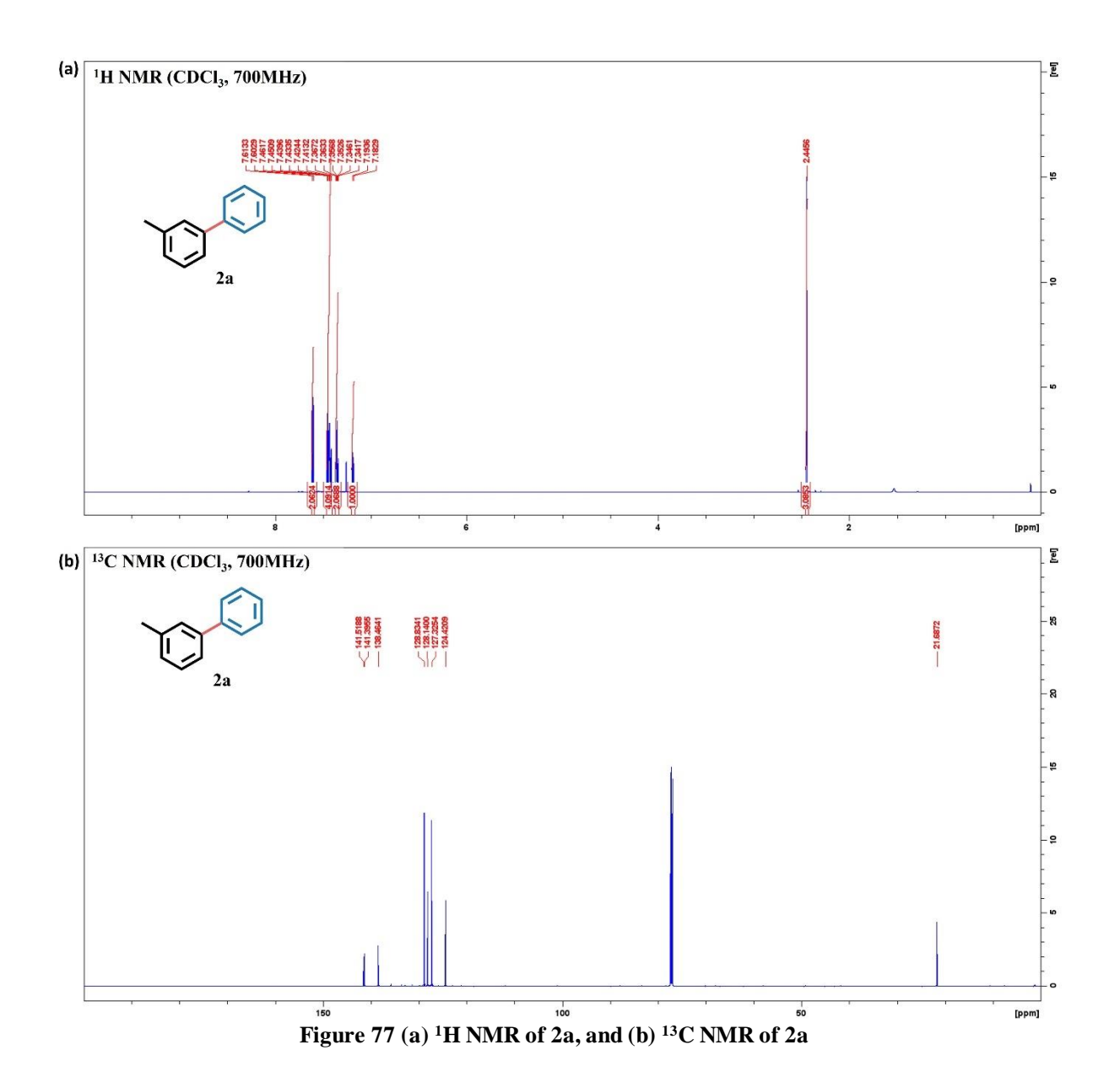


Figure 75 Extension to different substrates. Photocatalytic SMC reaction of various aryl bromides to the corresponding coupling products using  $Pd_{0.2}Cu_1/CTF-1$  photocatalyst. <sup>a</sup>Reaction conditions: 0.05 mmol 4-bromoanisole, 1.3 equiv phenylboronic acid, 4 equiv  $K_2CO_3$ , 5 ml solvent (EtOH:  $H_2O=1:1$ ), 5 mg photocatalyst, 365 nm multi-channel LED, 15 h, Ar, room temperature. <sup>b</sup>Analysed by GC–MS, and all conversions  $\geq 99\%$ , the percentage indicates its yield



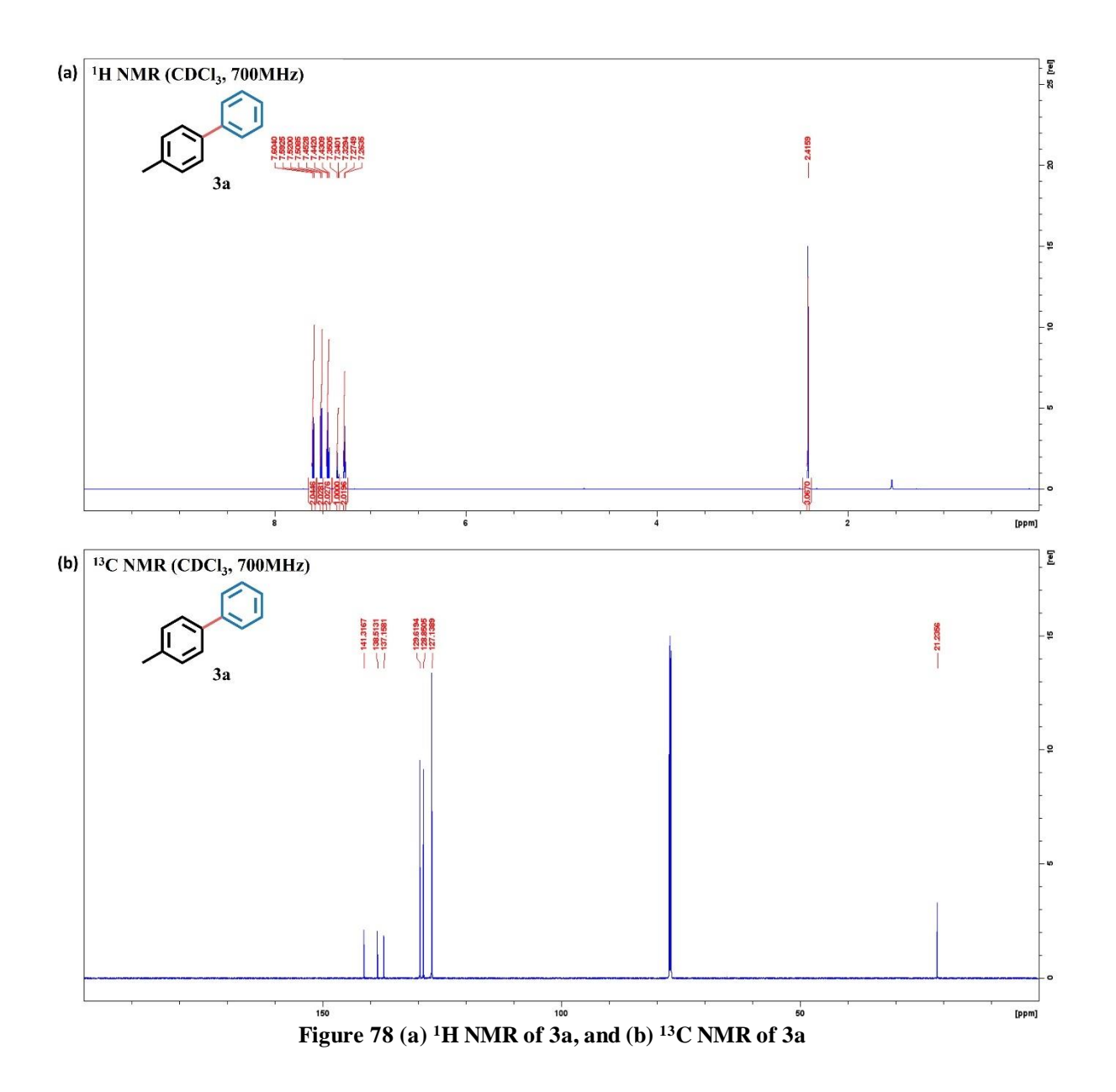
<sup>1</sup>H NMR (700 MHz, CDCl<sub>3</sub>):  $\delta$  = 7.63 (d, J=7.2 Hz, 4H, Ar-H), 7.44 (m, 4H, Ar-H), 7.35 (m, 2H Ar-H)

 $^{13}\text{C NMR}$  (700 MHz, CDCl<sub>3</sub>):  $\delta$  127.31, 127.39, 128.89, 141.39



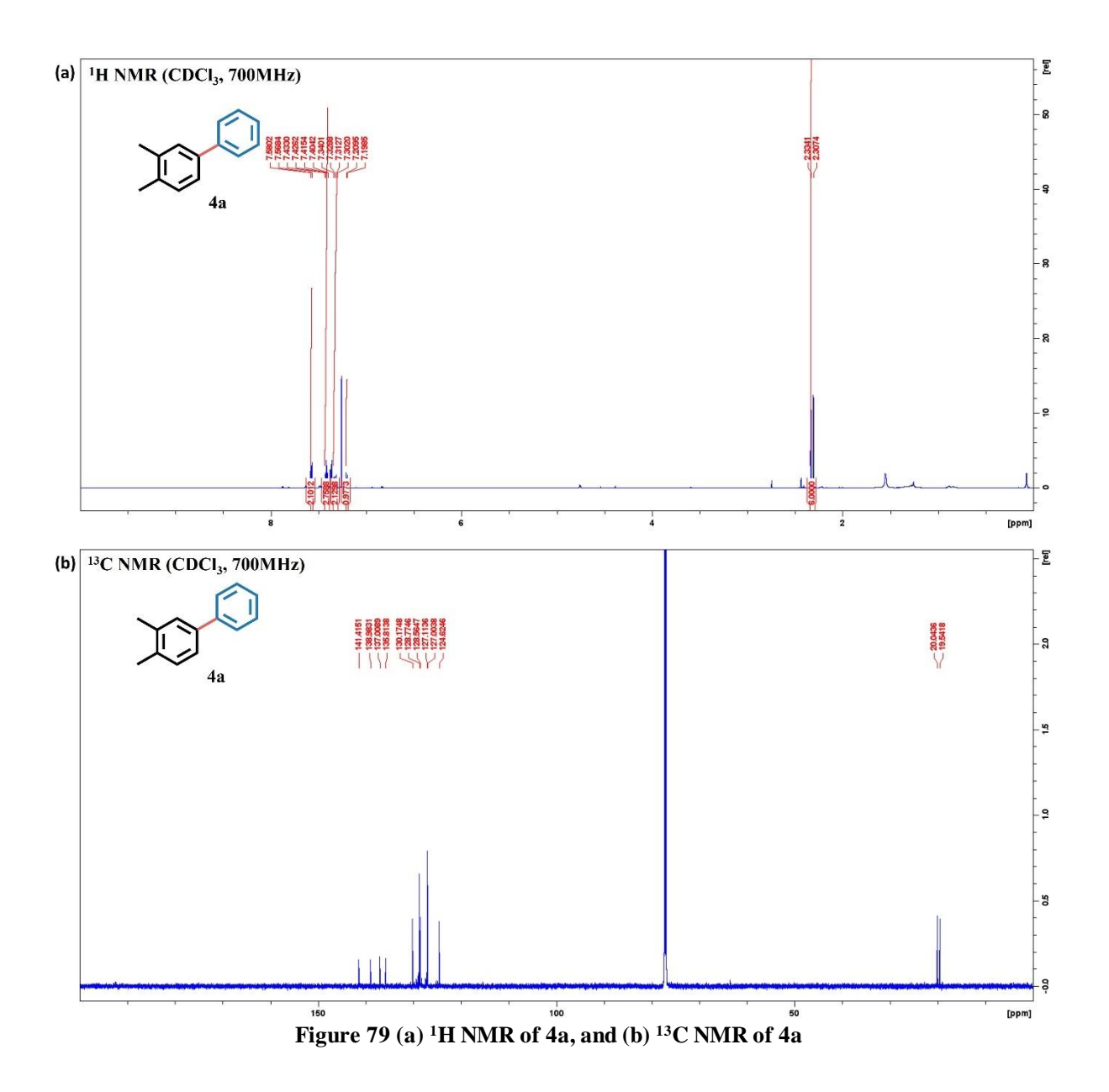
<sup>1</sup>H NMR (700 MHz, CDCl<sub>3</sub>):  $\delta$  = 7.61 (d, J = 7.2 Hz, 2H), 7.41-7.46 (m, 4H), 7.35 (t, J = 7.4 Hz, 2H), 7.19 (d, J = 7.6 Hz, 1H), 2.44 (s, 3H)

 $^{13}\text{C NMR}$  (700 MHz, CDCl<sub>3</sub>):  $\delta$  21.6, 124.4, 127.3, 128.2, 128.8, 138.4, 141.4, 141.5



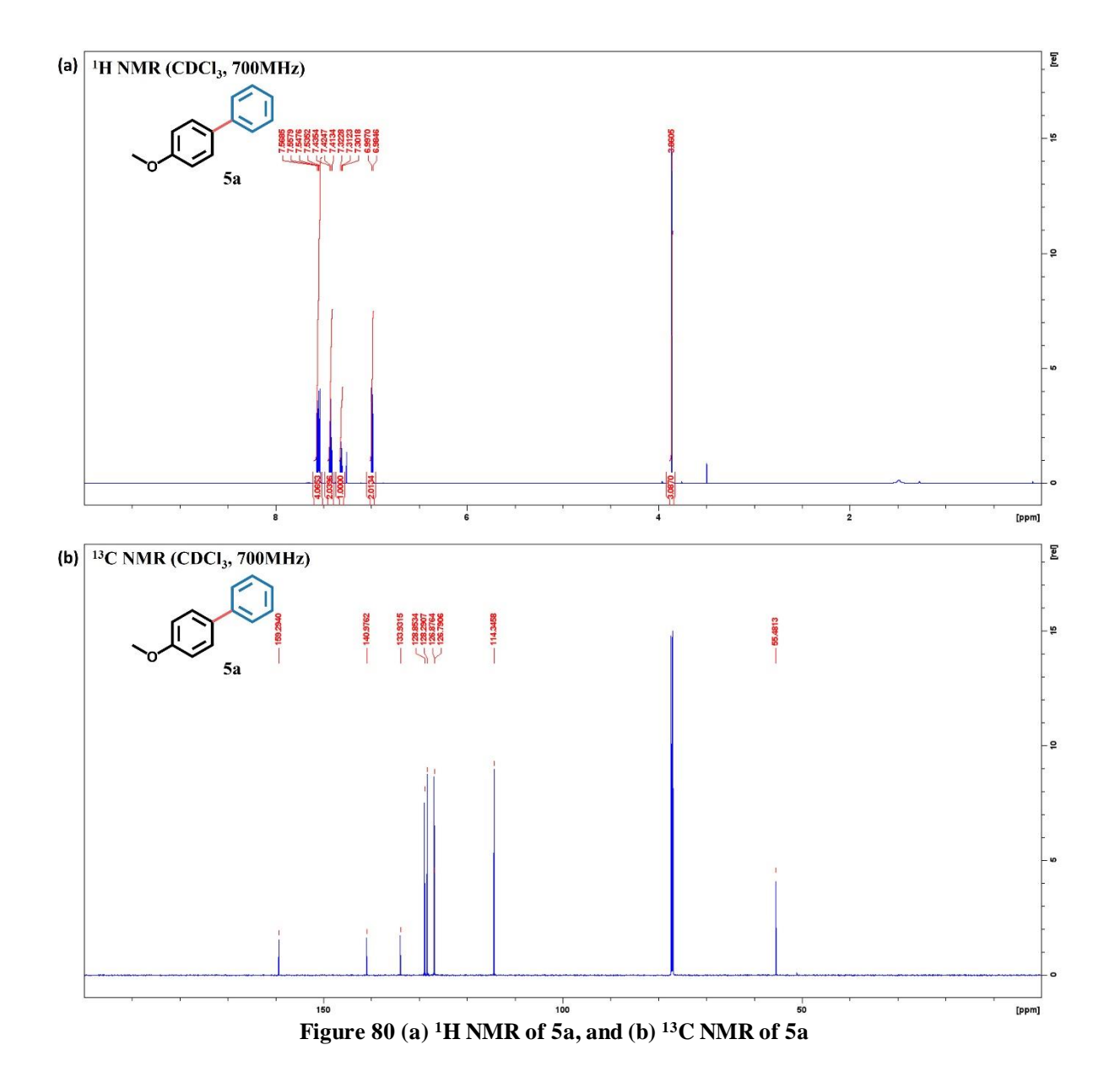
<sup>1</sup>H NMR (700 MHz, CDCl<sub>3</sub>):  $\delta$  = 7.60 (d, J = 7.2 Hz, 2H), 7.51 (d, J = 8.0 Hz, 2H), 7.44 (t, J = 7.6 Hz, 2H), 7.34 (t, J = 7.4 Hz, 1H), 7.26 (d, J = 7.6 Hz, 2H), 2.41 (s, 3H)

 $^{13}\text{C NMR}$  (700 MHz, CDCl3):  $\delta$  21.2, 127.1, 128.8, 129.6, 137.1, 138.5, 141.3



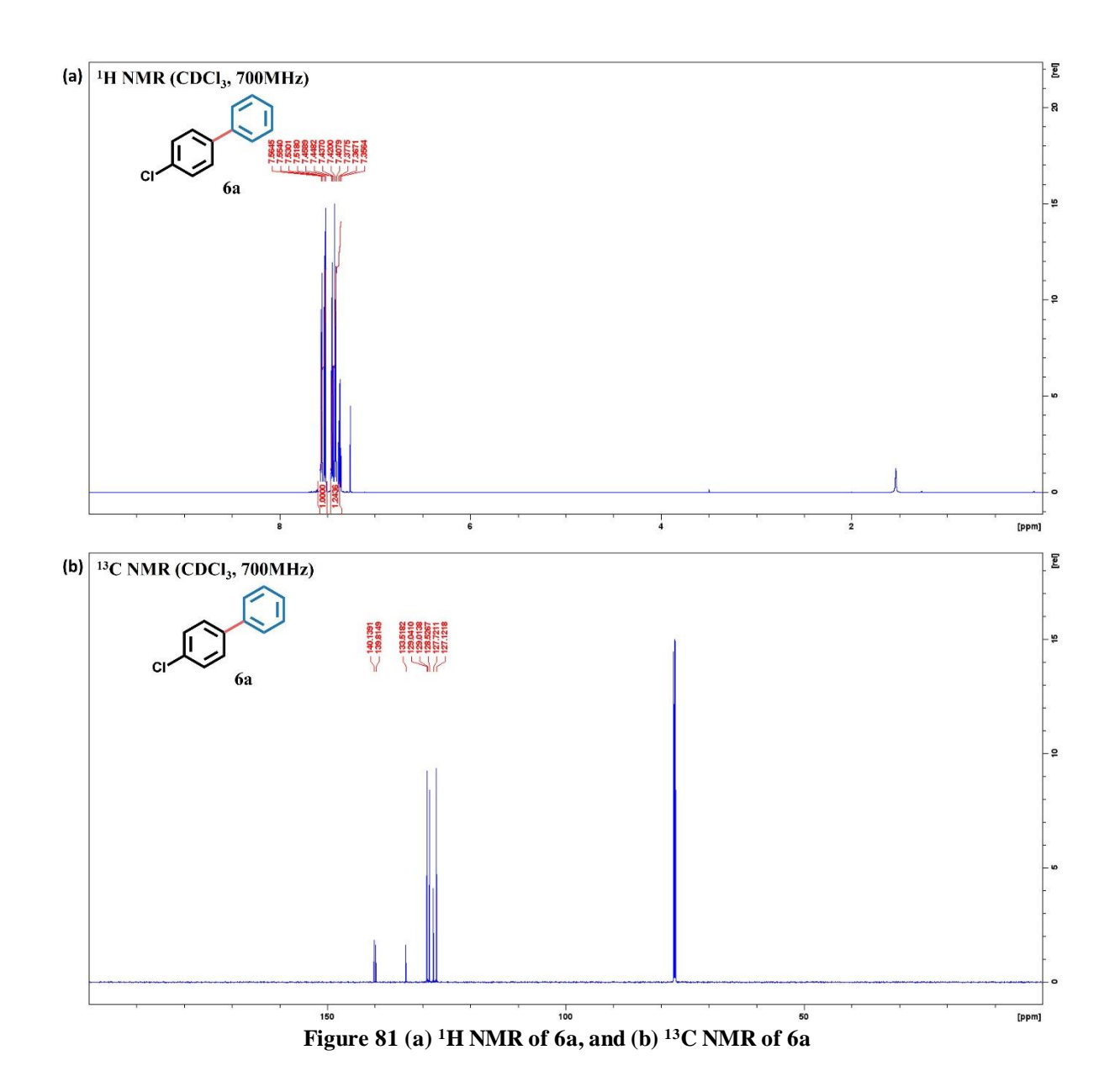
<sup>1</sup>H NMR (700 MHz, CDCl<sub>3</sub>):  $\delta$  = 7.58-7.56 (m, 2H), 7.43-7.30 (m, 5H), 7.21-7.19 (m, 1H), 2.30 (m, 6H)

<sup>13</sup>C NMR (700 MHz, CDCl<sub>3</sub>): δ 19.4, 20.0, 124.6, 127.0, 127.1, 128.5, 128.7, 130.1, 135.8, 137.0, 138.9, 141.4

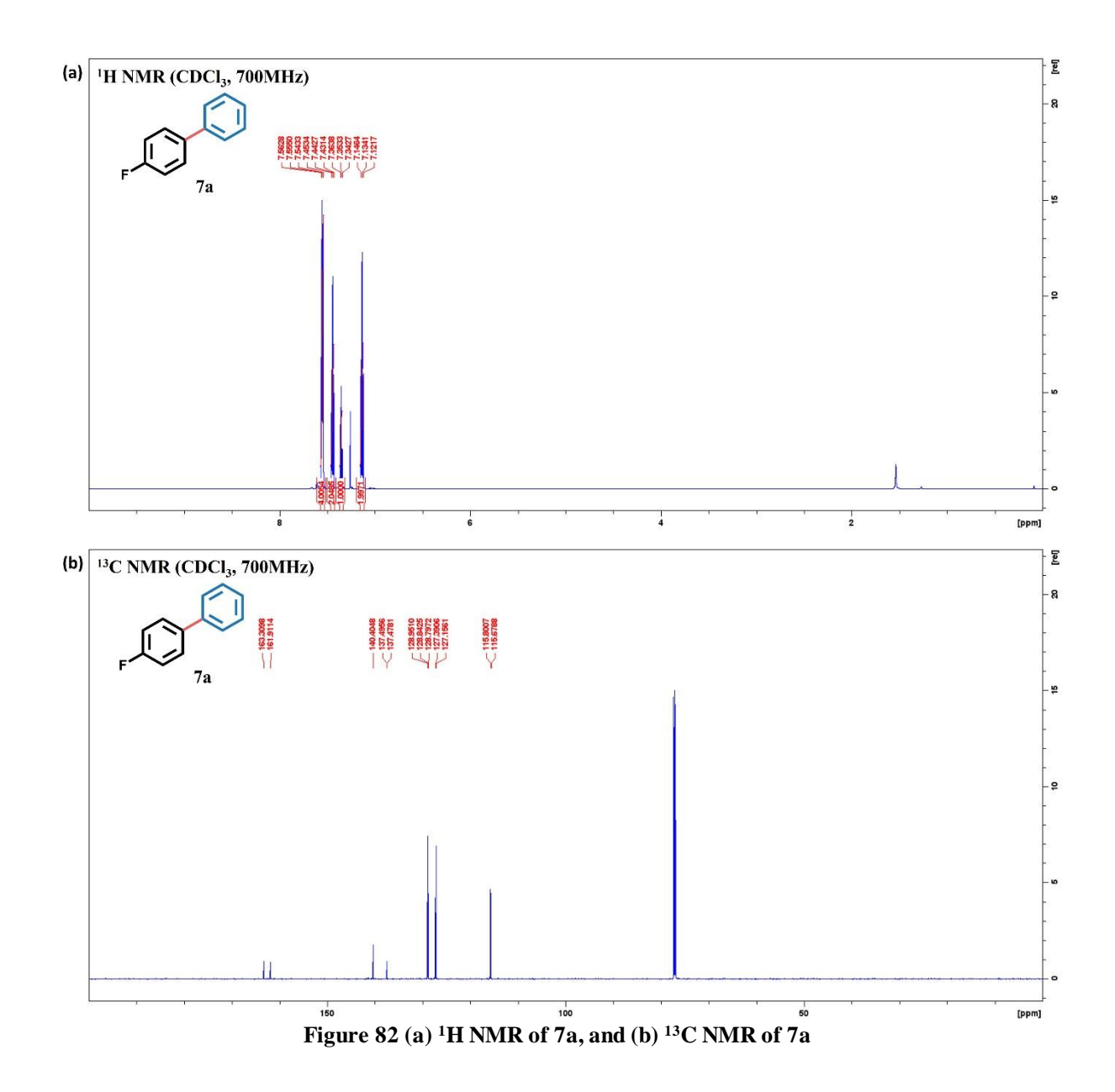


<sup>1</sup>H NMR (700 MHz, CDCl<sub>3</sub>):  $\delta$  = 7.56-7.53 (m, 4H), 7.43-7.41 (m, 2H), 7.32-7.30 (m, 1H), 7.00-6.98 (m, 2H), 3.86 (s, 3H)

 $^{13}\mathrm{C}$  NMR (700 MHz, CDCl<sub>3</sub>):  $\delta$  55.4, 114.3, 126.7, 126.8, 128.2, 128.8, 133.9, 140.9, 159.2

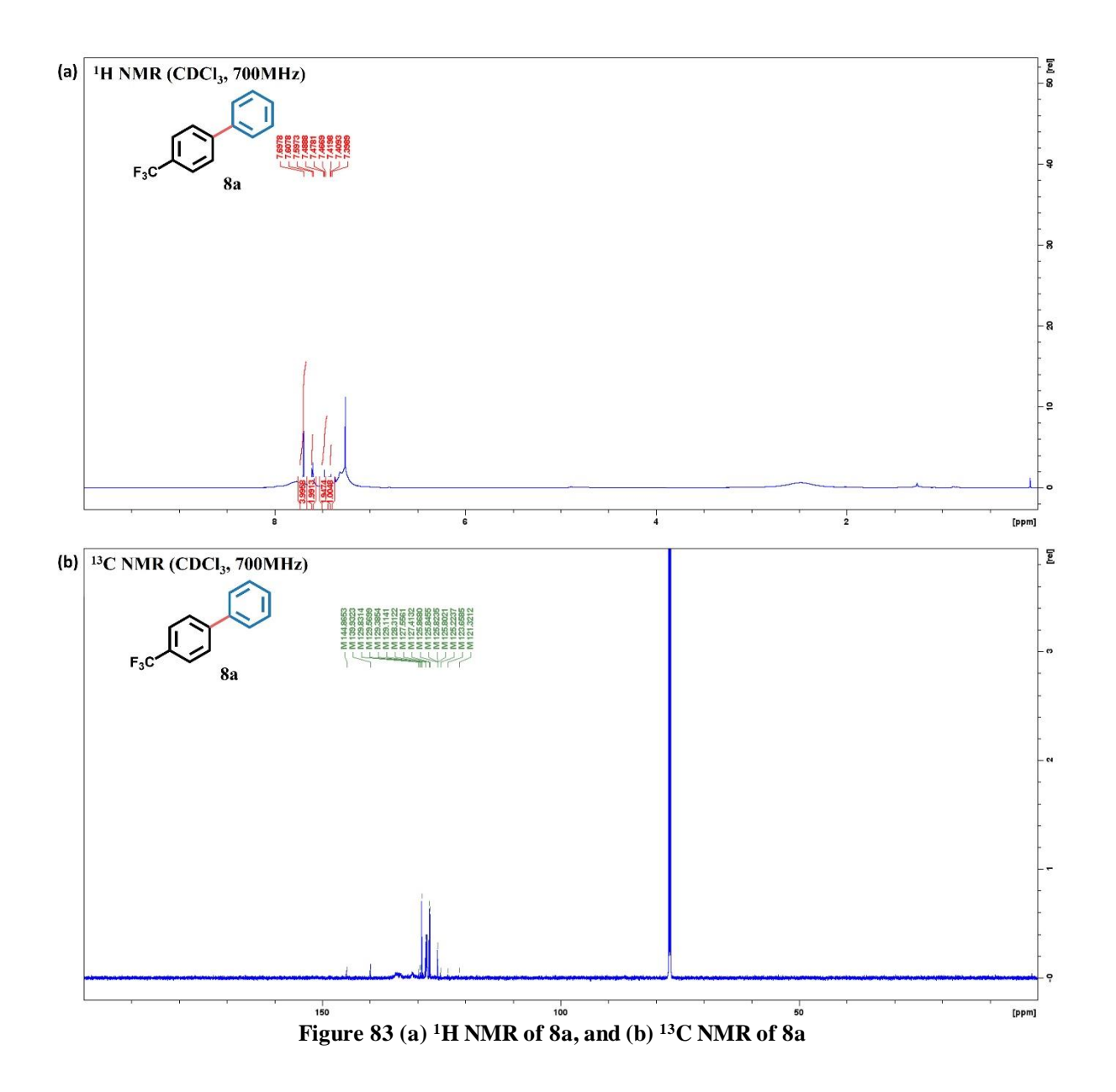


<sup>1</sup>H NMR (700 MHz, CDCl<sub>3</sub>):  $\delta$  = 7.56-7.51 (m, 4H), 7.45-7.40 (m, 4H), 7.36 (t, J = 7.4 Hz, 1H) <sup>13</sup>C NMR (700 MHz, CDCl<sub>3</sub>):  $\delta$  127.1, 127.7, 128.5, 129.0, 129.1, 133.5, 139.8, 140.1



<sup>1</sup>H NMR (700 MHz, CDCl<sub>3</sub>):  $\delta$  = 7.56-7.54 (m, 4H), 7.45-7.43 (m, 2H), 7.36 -7.34 (m, 1H), 7.14-7.12 (m, 2H)

 $^{13}\mathrm{C}$  NMR (700 MHz, CDCl<sub>3</sub>):  $\delta$  115.6, 127.1, 127.3, 128.7, 128.9, 137.4, 140.4, 161.9, 163.3



<sup>1</sup>H NMR (700 MHz, CDCl<sub>3</sub>):  $\delta$  = 7.69 (m, 4H), 7.60-7.59 (m, 2H), 7.48-7.46 (m, 2H), 7.41-7.39 (m, 1H)

 $^{13}\text{C NMR}$  (700 MHz, CDCl<sub>3</sub>):  $\delta$  123.6, 125.8, 127.4, 127.5, 128.3, 129.3, 129.5, 139.9, 144.8

## 6.3.4 Reaction mechanism

The physical and chemical states of co-catalysts on the optimum catalyst Pd<sub>0.2</sub>Cu<sub>1</sub>/CTF-1 were first investigated by transmission electron microscopy (TEM), XPS and electron paramagnetic resonance (EPR). The high-resolution TEM result (**Figure 84**) clearly shows the multi-layer structure with 0.34 nm lattice space, which matches the interlayer distance of the (001) peak of CTF-1 calculated from the XRD spectra<sup>[232]</sup>. However, apart from the lattice planes belonging to CTF-1, both the palladium and copper species cannot be observed at this resolution, suggesting the existence of smaller clusters for both co-catalysts. Energy dispersive spectroscopy (EDS mapping) results confirm the presence of both Pd and Cu, indicating a homogeneous dispersion of both co-catalysts on the surface of CTF-1.

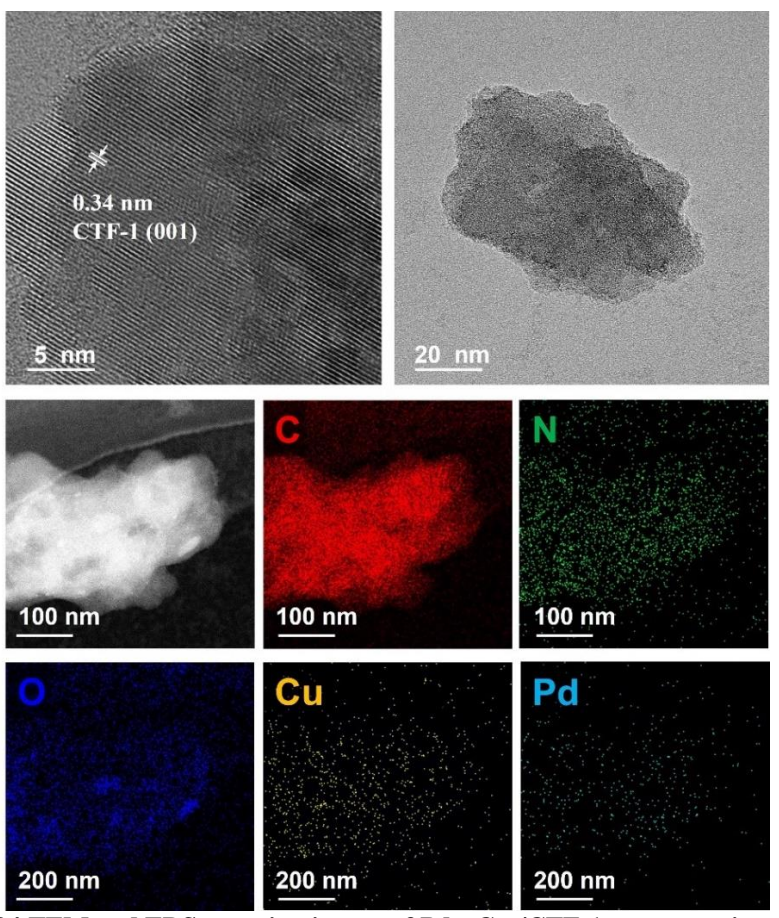


Figure 84 TEM and EDS mapping image of Pd<sub>0.2</sub>Cu<sub>1</sub>/CTF-1 post-reaction sample

From the Pd 3d XPS results of Pd<sub>0.2</sub>Cu<sub>1</sub>/CTF-1 (**Figure 85**), the peaks attributed to Pd 3d<sub>5/2</sub> and Pd 3d<sub>3/2</sub> at around 337.6 and 342.9 eV indicate the existence of PdO<sup>[233]</sup>, and since there is no peak of metallic Pd observed before and after the reaction, palladium species highly likely exist in the form of fully oxidised PdO.

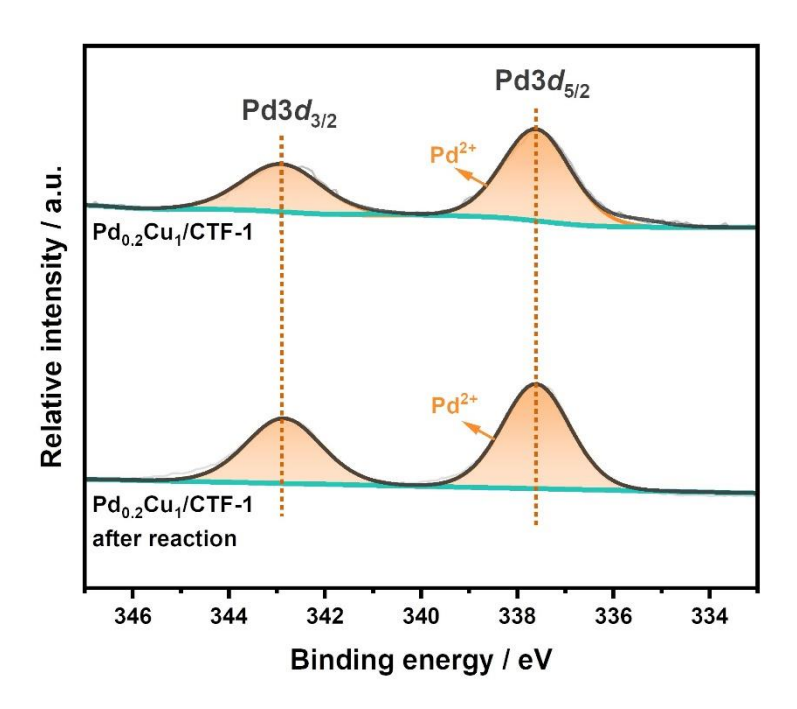


Figure 85 Deconvolution of XPS spectra of the Pd 3d region for  $Pd_{0.2}Cu_1/CTF$ -1samples (before and after reaction)

As for the copper species, from the Cu 2p XPS results (**Figure 86**), copper exists in a mixed status. The peaks at around 934.6 and 953.9 eV, with the shake-up satellite peak at around 943.8 eV, can be assigned to CuO<sup>[206]</sup>, and the concentration of Cu<sup>2+</sup> remains similar before and after the reaction (40% to 44%), indicating a fairly high amount of fully oxidised CuO in the cooper species. Meanwhile, the peaks attributed to Cu  $2p_{3/2}$  and Cu  $2p_{1/2}$  at around 932.2 and 951.9 eV represent the mixture of Cu<sup>+</sup>/Cu<sup>0</sup> with a concentration of around 60%.

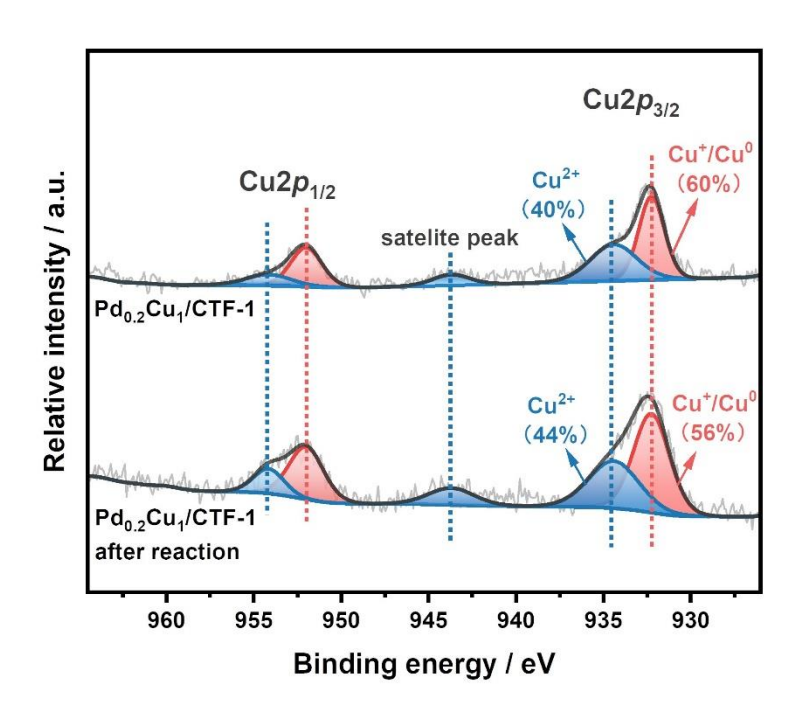


Figure 86 Deconvolution of XPS spectra of the Cu 2p for Pd<sub>0.2</sub>Cu<sub>1</sub>/CTF-1samples (before and after reaction)

The EPR results (**Figure 87**) show a sharp peak for the sample before the reaction, which is attributed to I=3/2 of Cu<sup>2+</sup>, so CuO hyperfine structure ( $g_{//}$ =2.35,  $g_{\perp}$ =2.05 and  $A_{//}\approx$ 100 G) can be observed by EPR spectra<sup>[202],[201]</sup>, which agrees with the distorted octahedral coordination of Cu<sup>2+</sup> ions in CuO clusters<sup>[203]</sup>. The intensity of Cu<sup>2+</sup> after 15 h reaction exhibits a negligible change compared to that before the reaction, suggesting there may be a stable Cu<sup>+</sup>/Cu<sup>2+</sup> cycle which acts as the reaction sites.

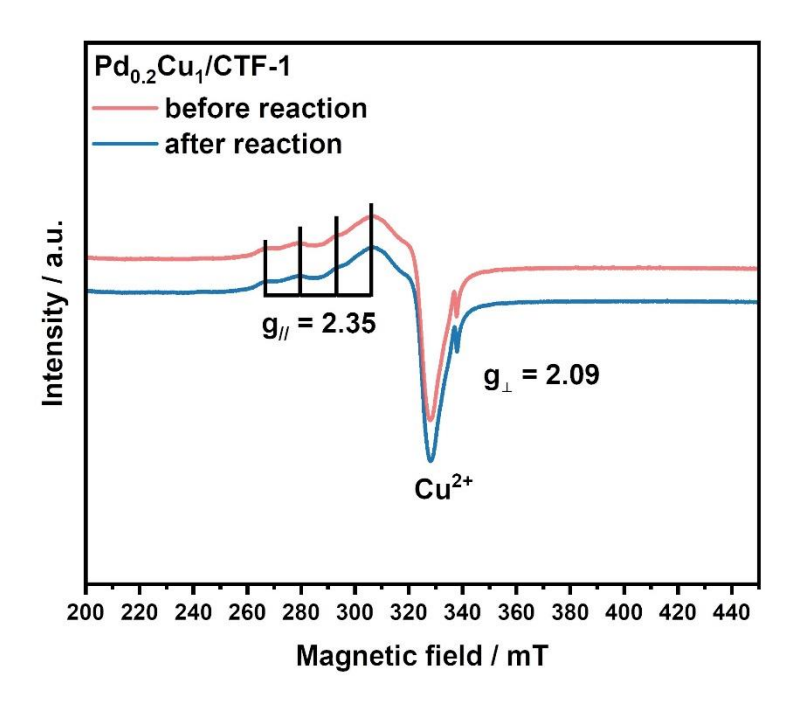


Figure 87 EPR spectra of Pd<sub>0.2</sub>Cu<sub>1</sub>/CTF-1samples

The function of Pd and Cu in the photocatalytic process was further investigated. Results of insitu XPS on Pd 3d and Cu 2p in Pd<sub>0.2</sub>Cu<sub>1</sub>/CTF-1 in the presence and absence of xenon lamp irradiation are shown in **Figure 88** and **Figure 89**. These results are used to confirm the photogenerated charge transfer pathway. According to **Figure 88**, small peaks of metallic Pd can be observed. However, after illuminating under xenon lamp for 20 min, a shift of ~ 0.15 eV to lower binding energy is observed on Pd  $3d_{5/2}$  (337.92 to 337.79 eV) and Pd  $3d_{3/2}$  (342.80 to 342.62 eV) peaks belonging to PdO, unambiguously indicating a reduced palladium species induced by light illumination<sup>[234]</sup>. The intensity of metallic Pd peak slightlt increased from 7% to 10%, also indicating that palladium species likely function as electron acceptors in the SMC reaction.

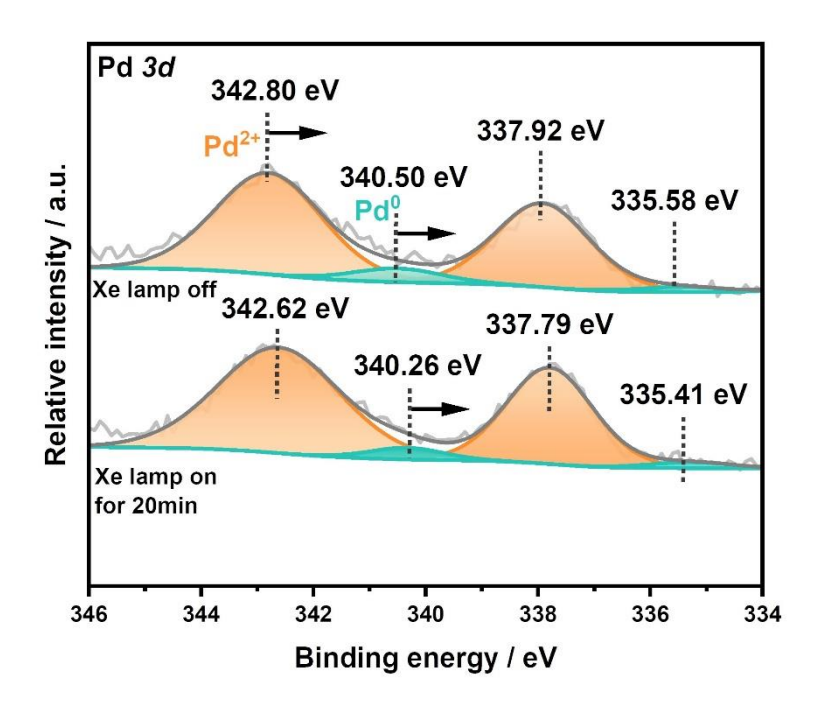


Figure 88 In-situ XPS spectra of the Pd 3d region for Pd<sub>0.2</sub>Cu<sub>1</sub>/CTF-1 samples (Xe lamp off and on for 20min)

The results of Cu 2p are shown in **Figure 89**. Before irradiation, the 932.16 and 951.93 eV peaks are associated with Cu  $2p_{3/2}$  and Cu  $2p_{1/2}$  of Cu<sup>+</sup>, respectively. Two other peaks at 934.57 and 954.52 eV represent Cu<sup>2+</sup>. After 20 min irradiation, all four peaks exhibit a small shift towards higher binding energy and the concentration of Cu<sup>2+</sup> slightly increases from 31% to 36%, which clearly indicates that CuOx may act as a hole acceptor.

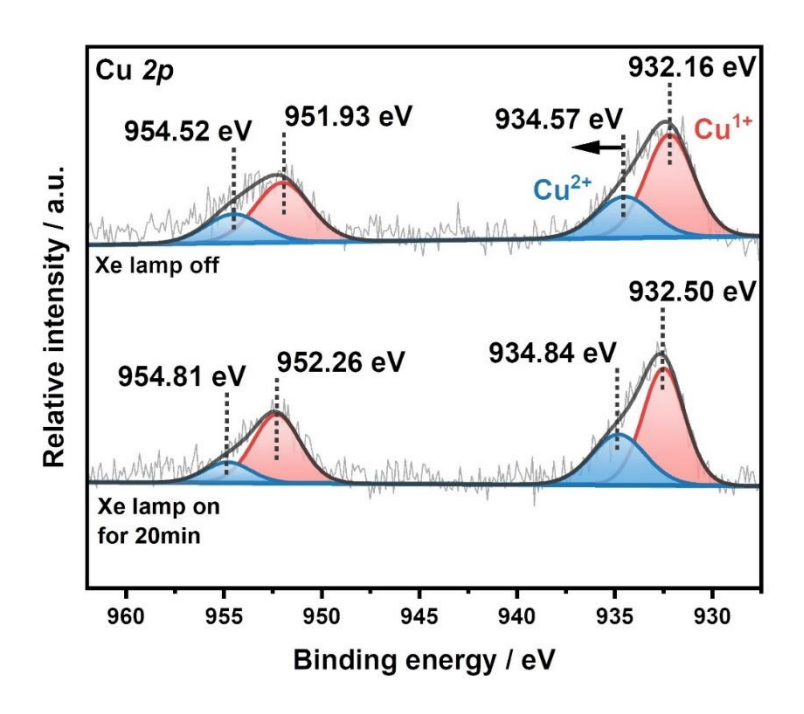


Figure 89 in-situ XPS spectra in the Cu 2p region for Pd<sub>0.2</sub>Cu<sub>1</sub>/CTF-1 samples (Xe lamp off and on for 20min)

The function of copper species in  $Pd_{0.2}Cu_1/CTF-1$  is further confirmed by in-situ EPR (**Figure 90**). A strong  $Cu^{2+}$  peak with  $g_{//} = 2.42$ ,  $g_{\perp} = 2.11$  and  $A_{//} \approx 100$  G can be observed in the EPR spectra, while upon in-situ irradiation for 0 min to 10 min, the intensity of this  $Cu^{2+}$  peak gradual increases, suggesting that the CuOx may work as  $Cu^+/Cu^{2+}$  cycle and responsible for the oxidation half-reaction in the photocatalytic process.

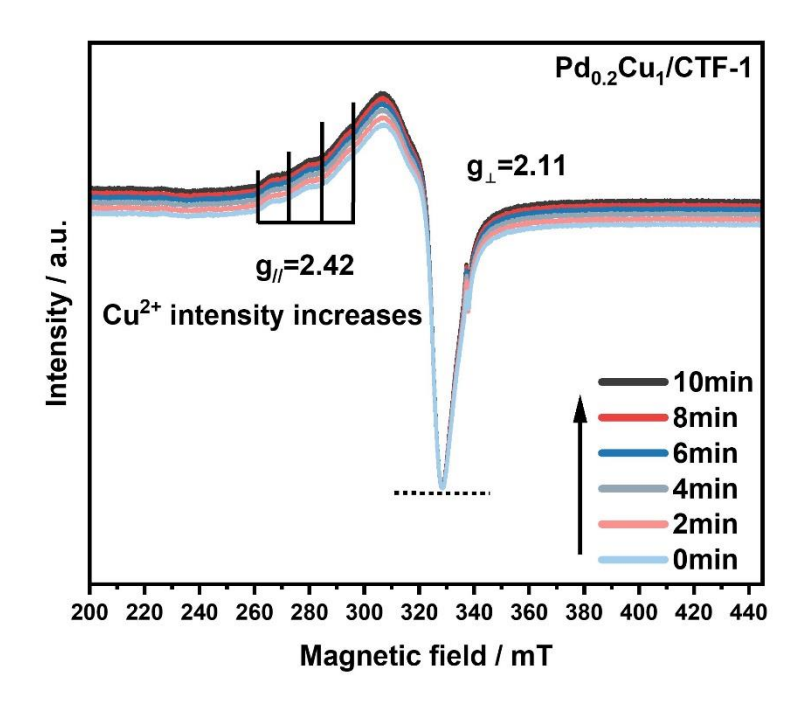


Figure 90 In-situ EPR spectra of Pd<sub>0.2</sub>Cu<sub>1</sub>/CTF-1 sample

Photoluminescence spectroscopy (PL) was finally carried out to study the charge separation over Pd<sub>0.2</sub>Cu<sub>1</sub>/CTF-1, and the result is shown in **Figure 91**. For bare CTF-1, an obvious band is observed at around 590 nm, while the PL intensity decreases notably after loading PdO, suggesting a likely improved charge separation of the photoinduced electron-hole pair over Pd<sub>0.2</sub>/CTF-1. Surprisingly, CuOx loading alone can significantly decrease PL intensity, and if CuOx clusters are decorated on CTF-1 before PdO, an even lower intensity can be obtained over Pd<sub>0.2</sub>Cu<sub>1</sub>/CTF-1. This result suggests that apart from separately driving their responsible photocatalytic half-reactions, a synergistic effect on dramatically boosting the charge separation can be obtained by loading both PdO and CuOx.

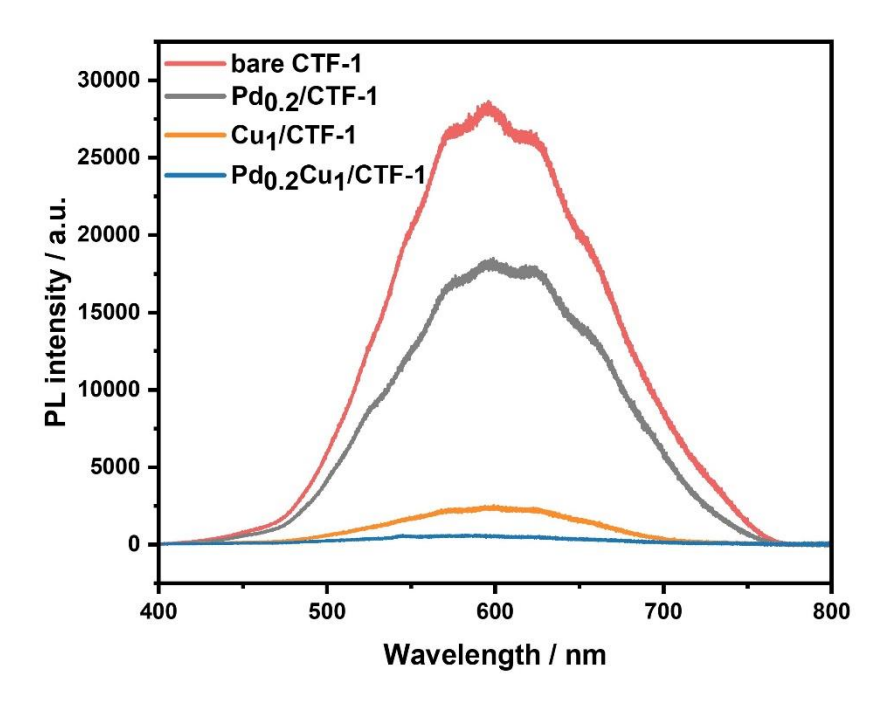


Figure 91 PL spectra for bare CTF-1,  $Pd_{0.2}/CTF$ -1,  $Cu_1/CTF$ -1 and  $Pd_{0.2}Cu_1/CTF$ -1

Based on the above characterisations and investigations, a proposed mechanism of photocatalytic SMC reaction over  $Pd_{0.2}Cu_1/CTF-1$  is illustrated in **Figure 92**. Upon light irradiation, the CTF-1 semiconductor is activated, i.e. the electrons will be excited from the valence band of CTF-1 to the conduction band and then migrate to its surface. The PdO clusters will then alleviate the recombination between photo-generated electrons and holes by acting as an electron sink while adsorbing 4-bromoanisole **5** on the catalyst surface. The adsorbed 4-bromoanisole **5** accepts an electron from reduced PdO and breaks its C–Br bond to generate the corresponding radical anions. The holes remaining on the valence band of CTF-1 will transfer to CuOx. With the assistance of  $K_2CO_3$ , the Ph– $\overline{B}(OH)_3$  activated from phenylboronic acid is ready to be oxidised by the holes on CuOx to generate phenyl radical cations. Meanwhile, the charge recombination is further retarded

by the CuOx loading as the second co-catalyst. In the final step, the radical anions couple with phenyl radical cations to form the desired SMC product 4-methoxybiphenyl 5a.

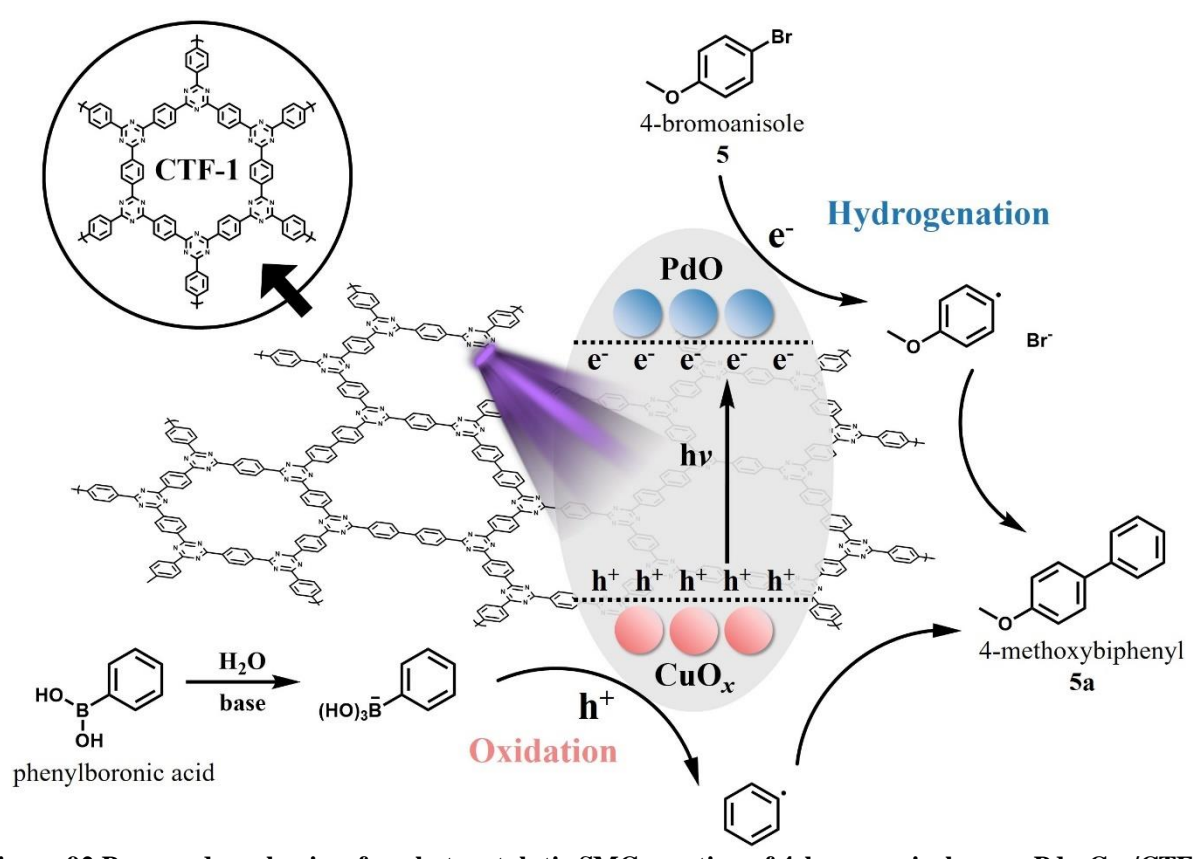


Figure 92 Proposed mechanism for photocatalytic SMC reaction of 4-bromoanisole over  $Pd_{0.2}Cu_1/CTF-1$ 

## **6.4 Conclusion**

Palladium catalysed SMC reaction is a classic reaction to construct C–C bonds. However, most works of heterogeneous photocatalytic SMC reactions reported used a fairly high loading amount of palladium. This work provides a Cu-Pd bimetallic strategy to achieve SMC reaction of aryl bromides with nearly unity selectivity (ca. 98%) towards corresponding coupling products. Reaction conditions, including solvent selection, pH, and co-catalysts loading sequence, were firstly studied and optimised. The ratio of the bimetallic Pd to Cu NPs was then optimised

separately. Compared to the monometallic sample Pd<sub>0.2</sub>/CTF-1, a 16-fold increase in yield was observed over Pd<sub>0.2</sub>Cu<sub>1</sub>/CTF-1, and this activity is comparable to 1.5% Pd loading. Furthermore, the Pd<sub>0.2</sub>Cu<sub>1</sub>/CTF-1 can also be applied to 8 aryl bromide derivatives to achieve their corresponding SMC products, and all yields can be achieved over 87%, indicating a potential for wide application. Fundamentally, the synergy effects between PtO and CuOx clusters as reduction sites and oxidation sites, were responsible for the enhanced catalytic performance of the SMC reaction. Based on in-situ XPS, the loading of CuOx accelerated the photo-oxidation half-reaction, resulting in retarded charge recombination and adequate generation of phenyl radical cations to pair with radical anions reduced on the palladium sites which function as the electron sink. The PL results further indicate that bimetallic loadings can improve charge transfer, consistent with the other characterisations. Overall, SMC reaction of aryl bromide is achieved using Pd<sub>0.2</sub>Cu<sub>1</sub>/CTF-1 with low palladium usage. The selectivity towards desired coupling product is 98% and the photocatalyst exhibits good stability after 3 cycles.

## Chapter 7 Overall conclusion and future works

The progress of C–C bond formation by heterogeneous photocatalysis was reviewed in Chapter 2. Compared to traditional methods, different reactions have been carried out using a variety of photocatalysts under ambient conditions. However, most of the coupling reactions used alkyl/aryl iodides and bromides as the substrates, where the strong C–Cl was rarely investigated. Also, the majority of the photocatalytic systems utilised a high concentration of noble metals as co-catalyst (e.g. Pd, Au) to either tune reaction selectivity or enhance light harvesting. Furthermore, the reaction mechanisms of these photocatalytic transformations were studied, but further investigation is needed to provide an in-depth understanding.

In my project, firstly, the pinacol coupling of benzaldehyde was studied. Through this, a general setup in a multichannel LEDs system for heterogeneous photocatalytic coupling reaction was established, and GC-MS and NMR were utilised to determine substrate conversion and product yield. Different parameters, including pH, light source, temperature, substrates light tolerance, and semiconductors, were studied to gain knowledge in this research field. As a result, A sustainable and eco-friendly method has been developed to convert benzaldehyde into four valuable chemical products with high yield and selectivity. The strategy involves modifying general experimental parameters, such as regulating the pH level, controlling the presence or absence of light irradiation, and utilizing a photocatalyst TiO<sub>2</sub> (P25), which enables the production of specific value-added products. Through a photochemical pathway, pinacol coupling of benzaldehyde was achieved in the absence of P25 at pH 12 with 96% conversion and 100% selectivity (2 h). 85% yield for hydrogenation was achieved in the presence of P25 photocatalyst and under 365 nm irradiation(2 h). The catalyst could completely shift the selectivity towards pinacol coupling (100%) to benzyl alcohol (94%) because benzaldehyde radicals prefer to adsorb on the surface of P25 and be reduced

by photoelectrons instead of colliding and combining each other. Acetalisation was also achieved using P25 catalyst with a yield of 92% via a low-temperature thermal catalytic pathway (2 h). The underlying mechanisms were also investigated, and an isotopic labelling experiment was carried out to identify an efficient pinacol coupling pathway.

Next, the focus of the thesis was towards the breaking of strong C–Cl bonds. The coupling of benzyl chlorides is in high demand due to the abundance of organic chlorides and the use of bibenzyl as a primary raw material in pharmaceutical synthesis. After testing several noble and transition metals, copper was chosen as the ideal co-catalyst to enhance the photocatalytic activity of ZnO and facilitate the homo-coupling of benzyl chlorides at room temperature. With the manipulation of electron donors, hydrogen donors and water content, the optimized sample 1.5% Cu/ZnO achieves a 100% conversion with a 92% selectivity to desired product bibenzyl (6 h, 365 nm LED). Such excellent performance is also stable for up to 8 cycles.

Furthermore, the university of this low-cost system has been confirmed by 10 various chloride derivatives with a good or very high yield (60% to 96%). The high selectivity is attributed to the synergetic effect between Cu and ZnO, in which benzyl radicals are stabilized on Cu for further coupling and protons are adsorbed on the ZnO support. In addition, the high yield rate is also beneficial from the promoted charge transfer between ZnO and Cu. Fundamentally, the TPD result indicates Cu can improve the interaction between benzyl chloride and the catalyst. By comparing Cu/ZnO with Cu/TiO<sub>2</sub> using EPR measurement, I found that photo-oxidation rate of 2-propanol on TiO<sub>2</sub> is 3 times higher than that on ZnO, indicating the moderate oxidation ability of ZnO is another key to achieving high bibenzyl yield from chloride substrates.

Palladium-catalysed SMC reaction is a classic reaction to construct C–C bonds. However, most previous works of heterogeneous photocatalytic SMC reactions used a reasonably high loading

amount of palladium. As a noble metal, Pd is expensive and potentially toxic to the environment. Therefore, reducing palladium usage or even developing palladium-free photocatalysts for SMC reaction is desired. This work provides a Cu Pd bimetallic strategy to achieve SMC reaction of aryl bromides with nearly perfect selectivity (98%) towards corresponding coupling products. Reaction conditions were first studied and optimised, including solvent selection, pH, and cocatalysts loading sequence. The concentration of the bimetallic Pd Cu NPs was then optimised separately. Compared to the monometallic sample Pd<sub>0.2</sub>/CTF-1, a 16-fold increase in yield was observed over Pd<sub>0.2</sub>Cu<sub>1</sub>/CTF-1, and this activity is comparable to 1.5% Pd loading. Furthermore, this low-cost system has also been confirmed by 8 various aryl bromides with excellent yields (>87%, 15 h) and the concentration of palladium is only 0.018 mol% compared to the substrate, indicating a potential for wide application. Fundamentally, the synergy between PdO and CuOx clusters at reduction sites and oxidation sites, respectively, are responsible for the enhanced catalytic performance of the SMC reaction. Based on in-situ XPS, the loading of CuOx accelerates the photo-oxidation half-reaction, resulting in retarded charge recombination and adequate generation of phenyl radical cations to pair with radical anions produced on the palladium sites. The PL results also demonstrate that bimetallic loadings can further improve the charge transfer. There are several promising avenues for future work in the area of heterogeneous photocatalysis for C-C bond formation and organic synthesis. One important direction is the development of new photocatalysts with improved activity, selectivity, and stability, as well as the optimisation of existing photocatalysts. This could involve the design and synthesis of novel catalysts, such as hybrid catalysts, metal-organic frameworks (MOFs), or co-catalysts, that can enhance the performance of photocatalytic reactions. Among these, noble metals such as palladium and gold are heavily used in different photocatalytic systems, and it is desired to develop less noble metal loading or even noble metal free cocatalysts.

Another important direction is extending the reaction ranges and applying photocatalysis to synthesising more complex organic molecules, such as natural products and pharmaceuticals. This could involve the development of new synthetic strategies, such as cascade reactions, multi-component reactions, or tandem reactions, that can be efficiently catalysed by photocatalysts. Though at the current stage, heterogeneous photocatalysts suffer from poor selectivity when multi-substrates (e.g. aryl halides with olefins) are involved in the reaction because the system design cannot satisfy both sides of photoredox cycles.

The more detailed reaction mechanisms of photocatalytic C–C bond formation are worth investigating to understand the reaction pathway and rate-determining step. To further study the reaction mechanism behind heterogeneous photocatalytic C–C coupling, a combination of experimental and theoretical approaches can be used. One experimental approach is to perform kinetic studies to determine the rate and order of the reaction, as well as the effect of different reaction parameters such as catalyst loading, light intensity, and solvent choice. By analyzing the kinetics data, valuable insights can be obtained about the reaction mechanism and the rate-limiting steps involved.

Another experimental approach is to use time-resolved spectroscopy and other cutting-edge spectroscopes such as in-situ infrared spectroscopy, in-situ XPS, in-situ Raman spectroscopy, in-situ EPR, intensity-modulated photocurrent spectroscopies and in-situ X-ray absorption fine structure spectroscopy (XAFS) to study the reaction intermediates and charge dynamics. These techniques can provide information about the active sites on the catalyst surface, the adsorption

and desorption of reactants, and the formation of reaction intermediates and products, thus elucidating the reaction pathway.

In addition to experimental approaches, computational methods such as density functional theory (DFT) calculations and molecular dynamics simulations can be used to provide insight into the reaction mechanism at the molecular level. These calculations can provide information about the reaction pathway, the energy barriers involved, and the electronic structure of the reactants and intermediates.

# **Chapter 8 Reference**

- [1] H.-U. Blaser, C. Malan, B. Pugin, F. Spindler, H. Steiner, M. Studer, *ChemInform* 2003, 34,DOI 10.1002/chin.200318260.
- [2] D. Ravelli, M. Fagnoni, A. Albini, *Chem. Soc. Rev.* **2013**, *42*, 97–113.
- [3] C. Minero, G. Mariella, V. Maurino, D. Vione, E. Pelizzetti, *Langmuir* **2000**, *16*, 8964–8972.
- [4] X. Lang, X. Chen, J. Zhao, *Chem. Soc. Rev.* **2014**, *43*, 473–486.
- [5] E. Properties, S. Interfaces, *Springer Handbook of Electronic and Photonic Materials*, Springer International Publishing, Cham, **2017**.
- [6] AndrewMills, J. Photochem. Photobiol. A Chem. 1997, 108, 1–35.
- [7] M. A. Lazar, W. A. Daoud, RSC Adv. 2013, 3, 4130–4140.
- [8] D. W. Manley, R. T. McBurney, P. Miller, R. F. Howe, S. Rhydderch, J. C. Walton, J. Am. Chem. Soc. 2012, 134, 13580–13583.
- [9] V. T. Bhat, P. A. Duspara, S. Seo, N. S. B. Abu Bakar, M. F. Greaney, *Chem. Commun.*2015, 51, 4383–4385.
- [10] Z. Chen, J. Xu, Z. Ren, Y. He, G. Xiao, *Catal. Commun.* **2013**, *41*, 83–86.
- [11] K. Inumaru, M. Yasui, T. Kasahara, K. Yamaguchi, A. Yasuda, S. Yamanaka, J. Mater. Chem. 2011, 21, 12117.
- [12] B. Srinivas, B. Shubhamangala, K. Lalitha, P. Anil Kumar Reddy, V. Durga Kumari, M. Subrahmanyam, B. R. De, *Photochem. Photobiol.* **2011**, *87*, 995–1001.

- [13] Q. Liu, Y. Zhou, Y. Ma, Z. Zou, RSC Adv. 2012, 2, 3247–3250.
- [14] J. Mao, T. Peng, X. Zhang, K. Li, L. Ye, L. Zan, Catal. Sci. Technol. 2013, 3, 1253–1260.
- [15] W. Tu, Y. Zhou, Q. Liu, S. Yan, S. Bao, X. Wang, M. Xiao, Z. Zou, Adv. Funct. Mater.2013, 23, 1743–1749.
- [16] S. Ghosh-Mukerji, H. Haick, Y. Paz, J. Photochem. Photobiol. A Chem. 2003, 160, 77–85.
- [17] S. Ghosh-Mukerji, H. Haick, M. Schvartzman, Y. Paz, J. Am. Chem. Soc. 2001, 123, 10776– 10777.
- [18] S. Liu, J. Yu, M. Jaroniec, J. Am. Chem. Soc. 2010, 132, 11914–11916.
- [19] Q. Xiang, J. Yu, M. Jaroniec, Chem. Commun. 2011, 47, 4532–4534.
- [20] P. S. Fier, J. F. Hartwig, **2020**, *342*, 956–960.
- [21] M. J. Koh, R. K. M. Khan, S. Torker, M. Yu, M. S. Mikus, A. H. Hoveyda, *Nature* 2015, 517, 181–186.
- [22] Á. Molnár, Chem. Rev. 2011, 111, 2251–2320.
- [23] Y. Zhang, N. Zhang, Z. R. Tang, Y. J. Xu, Chem. Sci. 2012, 3, 2812–2822.
- [24] O. Tomita, B. Ohtani, R. Abe, *Catal. Sci. Technol.* **2014**, *4*, 3850–3860.
- [25] J. Tripathy, K. Lee, P. Schmuki, *Angew. Chemie* **2014**, *126*, 12813–12816.
- [26] Z. Yu, E. R. Waclawik, Z. Wang, X. Gu, Y. Yuan, Z. Zheng, J. Mater. Chem. A 2017, 5, 4607–4615.
- [27] Y. Shiraishi, N. Saito, T. Hirai, J. Am. Chem. Soc. 2005, 127, 12820–12822.

- [28] Y. Shiraishi, D. Tsukamoto, T. Hirai, *Langmuir* **2008**, *24*, 12658–12663.
- [29] N. Zhang, X. Li, H. Ye, S. Chen, H. Ju, D. Liu, Y. Lin, W. Ye, C. Wang, Q. Xu, J. Zhu, L. Song, J. Jiang, Y. Xiong, J. Am. Chem. Soc. 2016, 138, 8928–8935.
- [30] S. Linic, P. Christopher, D. B. Ingram, *Nat. Mater.* **2011**, *10*, 911–921.
- [31] Q. Gu, Q. Jia, J. Long, Z. Gao, ChemCatChem 2019, 11, 669–683.
- [32] W. Shi, C. Liu, A. Lei, Chem. Soc. Rev. 2011, 40, 2761.
- [33] M. C. D'Alterio, È. Casals-Cruañas, N. V. Tzouras, G. Talarico, S. P. Nolan, A. Poater, *Chem. A Eur. J.* **2021**, *27*, 13481–13493.
- [34] T. Niwa, Y. Uetake, M. Isoda, T. Takimoto, M. Nakaoka, D. Hashizume, H. Sakurai, T. Hosoya, Nat. Catal. 2021, 4, 1080–1088.
- [35] G. C. Castillo, I. C. Vila, E. Neild, *Environ. Toxicol.* **2000**, *15*, 370–375.
- [36] N. Marina, A. E. Lanterna, J. C. Scaiano, ACS Catal. 2018, 8, 7593–7597.
- [37] A. Elhage, A. E. Lanterna, J. C. Scaiano, *Chem. Sci.* **2019**, *10*, 1419–1425.
- [38] A. Tyagi, A. Yamamoto, H. Yoshida, Catal. Sci. Technol. 2018, 8, 6196–6203.
- [39] H. S. Kim, J. D. Kim, H. C. Choi, S. Lee, *Mol. Catal.* **2017**, *441*, 21–27.
- [40] S. S. Soni, D. A. Kotadia, *Catal. Sci. Technol.* **2014**, *4*, 510–515.
- [41] Y. Li, P. Ren, D. Zhang, W. Qiao, D. Wang, X. Yang, X. Wen, M. H. Rummeli, H. Niemantsverdriet, J. P. Lewis, F. Besenbacher, H. Xiang, Y. Li, R. Su, ACS Catal. 2021, 11, 4338–4348.

- [42] G. K. Hodgson, J. C. Scaiano, ACS Catal. 2018, 8, 2914–2922.
- [43] P. Riente, M. A. Pericàs, ChemSusChem 2015, 8, 1841–1844.
- [44] H. R. Choe, S. S. Han, Y.-I. Kim, C. Hong, E. J. Cho, K. M. Nam, ACS Appl. Mater. Interfaces 2021, 13, 1714–1722.
- [45] Y. Li, Z. Zhang, L. Pei, X. Li, T. Fan, J. Ji, J. Shen, M. Ye, *Appl. Catal. B Environ.* **2016**, 190, 1–11.
- [46] Z. Lou, Q. Gu, Y. Liao, S. Yu, C. Xue, Appl. Catal. B Environ. 2016, 184, 258–263.
- [47] H. Tang, Z. Tang, J. Bright, B. Liu, X. Wang, G. Meng, N. Wu, ACS Sustain. Chem. Eng.2021, 9, 1500–1506.
- [48] K. Sharma, M. Kumar, V. Bhalla, Chem. Commun. 2015, 51, 12529–12532.
- [49] K. P. McClelland, E. A. Weiss, ACS Appl. Energy Mater. 2019, 2, 92–96.
- [50] A. Pal, I. Ghosh, S. Sapra, B. König, *Chem. Mater.* **2017**, 29, 5225–5231.
- [51] Z. W. Xi, L. Yang, D. Y. Wang, C. W. Feng, Y. Qin, Y. M. Shen, C. Pu, X. Peng, J. Org. Chem. 2021, 86, 2474–2488.
- [52] M. Y. Qi, Y. H. Li, M. Anpo, Z. R. Tang, Y. J. Xu, ACS Catal. 2020, 10, 14327–14335.
- [53] G. Han, X. Liu, Z. Cao, Y. Sun, ACS Catal. **2020**, 10, 9346–9355.
- [54] N. Luo, T. Hou, S. Liu, B. Zeng, J. Lu, J. Zhang, H. Li, F. Wang, ACS Catal. 2020, 10, 762–769.
- [55] H. H. Shin, E. Kang, H. Park, T. Han, C.-H. Lee, D.-K. Lim, J. Mater. Chem. A 2017, 5, 24965–24971.

- [56] F. Raza, D. Yim, J. H. Park, H.-I. Kim, S.-J. Jeon, J.-H. Kim, J. Am. Chem. Soc. 2017, 139, 14767–14774.
- [57] Y. Wang, P. Ren, X. Gu, X. Wen, Y. Wang, X. Guo, E. R. Waclawik, H. Zhu, Z. Zheng, Green Chem. 2016, 18, 1482–1487.
- [58] Y. Zhou, J. Zhao, Appl. Catal. B Environ. 2022, 300, 120721.
- [59] M. Dabiri, R. Nikbakht, S. K. Movahed, *Mater. Chem. Phys.* **2021**, 258, 123908.
- [60] Y. Yuan, Y. Q. Wang, G. Zhuang, Q. Li, F. L. Yang, X. Wang, X. Han, J. Mater. Chem. A 2021, 9, 24909–24914.
- [61] J. Cai, Y. Li, M. Zhang, Z. Li, *Inorg. Chem.* **2019**, *58*, 7997–8002.
- [62] I. Rosa-Pardo, C. Casadevall, L. Schmidt, M. Claros, R. E. Galian, J. Lloret-Fillol, J. Pérez-Prieto, *Chem. Commun.* **2020**, *56*, 5026–5029.
- [63] B. W. Crabbe, O. P. Kuehm, J. C. Bennett, G. L. Hallett-Tapley, *Catal. Sci. Technol.* 2018, 8, 4907–4915.
- [64] B. Y. Cao, S. Xu, Y. L. Ren, Y. Yu, J. Y. Guo, L. Zhang, N. Li, G. C. Zhang, C. S. Zhou, Chem. Lett. 2017, 46, 1773–1776.
- [65] S. Gao, N. Shang, C. Feng, C. Wang, Z. Wang, RSC Adv. 2014, 4, 39242–39247.
- [66] Z. Jiao, Z. Zhai, X. Guo, X.-Y. Guo, J. Phys. Chem. C 2015, 119, 3238–3243.
- [67] B. Wang, X. Guo, G. Jin, X. Guo, Catal. Commun. 2017, 98, 81–84.
- [68] M. Sahoo, S. Mansingh, S. Subudhi, P. Mohapatra, K. Parida, Catal. Sci. Technol. 2019, 9, 4678–4692.

- [69] M. D. Kärkäs, J. A. Porco, C. R. J. Stephenson, Chem. Rev. 2016, 116, 9683–9747.
- [70] N. Kaur, Synth. Commun. 2018, 48, 1259–1284.
- [71] P. Li, J. A. Terrett, J. R. Zbieg, ACS Med. Chem. Lett. **2020**, 11, 2120–2130.
- [72] M. Koohgard, M. Hosseini-Sarvari, Catal. Commun. 2018, 111, 10–15.
- [73] F. Feizpour, M. Jafarpour, A. Rezaeifard, Catal. Letters 2019, 149, 1595–1610.
- [74] M. Hosseini-Sarvari, Z. Bazyar, ChemistrySelect 2018, 3, 1898–1907.
- [75] S. Sarina, H. Zhu, E. Jaatinen, Q. Xiao, H. Liu, J. Jia, C. Chen, J. Zhao, J. Am. Chem. Soc.2013, 135, 5793–5801.
- [76] A. M. Lacerda, I. Larrosa, S. Dunn, *Nanoscale* **2015**, *7*, 12331–12335.
- [77] K. H. Leong, H. Y. Chu, S. Ibrahim, P. Saravanan, *Beilstein J. Nanotechnol.* **2015**, *6*, 428–437.
- [78] D. Han, Z. Bao, H. Xing, Y. Yang, Q. Ren, Z. Zhang, *Nanoscale* **2017**, *9*, 6026–6032.
- [79] S. Rohani, A. Ziarati, G. M. Ziarani, A. Badiei, T. Burgi, Catal. Sci. Technol. 2019, 9, 3820–3827.
- [80] S. Zhang, C. Chang, Z. Huang, Y. Ma, W. Gao, J. Li, Y. Qu, ACS Catal. 2015, 5, 6481–6488.
- [81] Q. Xiao, S. Sarina, E. Jaatinen, J. Jia, D. P. Arnold, H. Liu, H. Zhu, Green Chem. 2014, 16, 4272.
- [82] Q. Xiao, S. Sarina, A. Bo, J. Jia, H. Liu, D. P. Arnold, Y. Huang, H. Wu, H. Zhu, ACS Catal.
  2014, 4, 1725–1734.

- [83] M. Wen, S. Takakura, K. Fuku, K. Mori, H. Yamashita, Catal. Today 2015, 242, 381–385.
- [84] P. Verma, Y. Kuwahara, K. Mori, H. Yamashita, J. Mater. Chem. A 2015, 3, 18889–18897.
- [85] C. Han, D. E. Gómez, Q. Xiao, J. Xu, J. Catal. 2021, 397, 205–211.
- [86] E. Kang, H. Shin, D.-K. Lim, *Catalysts* **2018**, 8, 463.
- [87] T. Yoshii, Y. Kuwahara, K. Mori, H. Yamashita, J. Phys. Chem. C 2019, 123, 24575–24583.
- [88] A. Elhage, A. E. Lanterna, J. C. Scaiano, ACS Sustain. Chem. Eng. 2018, 6, 1717–1722.
- [89] S. Sarina, H. Y. Zhu, Q. Xiao, E. Jaatinen, J. Jia, Y. Huang, Z. Zheng, H. Wu, Angew. Chemie - Int. Ed. 2014, 53, 2935–2940.
- [90] Z. Zhang, C. Zhao, Y. Duan, C. Wang, Z. Zhao, H. Wang, Y. Gao, Appl. Surf. Sci. 2020, 527, 146693.
- [91] K. Singha, S. C. Ghosh, A. B. Panda, *Chem. An Asian J.* **2019**, *14*, 3205–3212.
- [92] L. Möhlmann, M. Baar, J. Rieß, M. Antonietti, X. Wang, S. Blechert, *Adv. Synth. Catal.*2012, 354, 1909–1913.
- [93] M. Baar, S. Blechert, *Chem. A Eur. J.* **2015**, *21*, 526–530.
- [94] Y. Zhao, M. Antonietti, Angew. Chemie Int. Ed. 2017, 56, 9336–9340.
- [95] J. Khamrai, S. Das, A. Savateev, M. Antonietti, B. König, Green Chem. 2021, 23, 2017– 2024.
- [96] C. Yang, B. Wang, L. Zhang, L. Yin, X. Wang, Angew. Chemie Int. Ed. 2017, 56, 6627–6631.

- [97] Q. Jia, S. Zhang, Q. Gu, J. Energy Chem. 2019, 30, 152–161.
- [98] Q. Jia, S. Zhang, X. Jia, X. Dong, Z. Gao, Q. Gu, Catal. Sci. Technol. 2019, 9, 5077–5089.
- [99] S. K. Movahed, S. Miraghaee, M. Dabiri, J. Alloys Compd. 2020, 819, 152994.
- [100] H. Jiang, J. Xu, S. Zhang, H. Cheng, C. Zang, F. Bian, Catal. Sci. Technol. 2021, 11, 219–229.
- [101] X. Jia, J. Zhao, Y. Lv, X. Fu, Y. Jian, W. Zhang, Y. Wang, H. Sun, X. Wang, J. Long, P. Yang, Q. Gu, Z. Gao, Appl. Catal. B Environ. 2022, 300, 120756.
- [102] Y. Li, Y. Li, C. Hu, X. Wen, H. Xiang, Y. Li, H. Niemantsverdriet, R. Su, *Green Chem.*2022, 24, 7622–7629.
- [103] A. S. Sharma, V. S. Sharma, H. Kaur, ACS Appl. Nano Mater. 2020, 3, 1191–1202.
- [104] J. Shi, T. Yuan, M. Zheng, X. Wang, ACS Catal. 2021, 11, 3040–3047.
- [105] M. Tian, Y. Wang, X. Bu, Y. Wang, X. Yang, Catal. Sci. Technol. 2021, 11, 4272–4279.
- [106] H. C. Ma, C. C. Zhao, G. J. Chen, Y. Bin Dong, Nat. Commun. 2019, 10, DOI 10.1038/s41467-019-11355-x.
- [107] Y. Zhang, X. Zhang, J. Gao, C. Du, M. Xie, C. Au, J. Chen, L. Wan, *Macromol. Chem. Phys.* 2020, 221, 2000076.
- [108] Z. J. Wang, S. Ghasimi, K. Landfester, K. A. I. Zhang, *Chem. Mater.* **2015**, 27, 1921–1924.
- [109] A. Xie, K. Zhang, F. Wu, N. Wang, Y. Wang, M. Wang, Catal. Sci. Technol. 2016, 6, 1764–1771.
- [110] N. A. Nemygina, L. Z. Nikoshvili, I. Y. Tiamina, A. V. Bykov, I. S. Smirnov, T. LaGrange,

- Z. Kaszkur, V. G. Matveeva, E. M. Sulman, L. Kiwi-Minsker, *Org. Process Res. Dev.* **2018**, 22, 1606–1613.
- [111] G. Singh, M. Kumar, K. Sharma, V. Bhalla, Green Chem. 2016, 18, 3278–3285.
- [112] H. Deol, S. Pramanik, M. Kumar, I. A. Khan, V. Bhalla, ACS Catal. 2016, 6, 3771–3783.
- [113] P. K. Prajapati, S. Saini, S. L. Jain, J. Mater. Chem. A 2020, 8, 5246–5254.
- [114] D. Sun, Z. Li, J. Phys. Chem. C 2016, 120, 19744–19750.
- [115] D. Sun, M. Xu, Y. Jiang, J. Long, Z. Li, Small Methods 2018, 2, 1800164.
- [116] H. Haroon, M. Wahid, K. Majid, ACS Appl. Nano Mater. 2022, 5, 2006–2017.
- [117] H. Li, Y. Yang, C. He, L. Zeng, C. Duan, ACS Catal. 2019, 9, 422–430.
- [118] W. Q. Zhang, Q. Y. Li, Q. Zhang, Y. Lu, H. Lu, W. Wang, X. Zhao, X. J. Wang, *Inorg. Chem.* 2016, 55, 1005–1007.
- [119] T. B. Jayesh, K. Itika, G. V. Ramesh Babu, K. S. Rama Rao, R. S. Keri, A. H. Jadhav, B.
   M. Nagaraja, *Catal. Commun.* 2018, 106, 73–77.
- [120] M. Glatz, B. Stöger, D. Himmelbauer, L. F. Veiros, K. Kirchner, ACS Catal. 2018, 8, 4009–4016.
- [121] M. Billamboz, C. Imbs, E. Banaszak-Léonard, C. Len, *Org. Process Res. Dev.* **2017**, *21*, 835–843.
- [122] J. M. Rubio-Caballero, S. Saravanamurugan, P. Maireles-Torres, A. Riisager, *Catal. Today* **2014**, *234*, 233–236.
- [123] M. J. da Silva, M. G. Teixeira, *Mol. Catal.* **2018**, *461*, 40–47.

- [124] J. L. Dong, L. S. H. Yu, J. W. Xie, ACS Omega 2018, 3, 4974–4985.
- [125] R. Ray, A. D. Chowdhury, G. K. Lahiri, ChemCatChem 2013, 5, 2158–2161.
- [126] B. Zhou, F. Song, X. Ma, L. Wang, ChemSusChem 2021, 14, 2341–2351.
- [127] J. T. Li, J. H. Yang, J. F. Han, T. S. Li, Green Chem. 2003, 5, 433–435.
- [128] T. Luo, L. Li, Y. Chen, J. An, C. Liu, Z. Yan, J. H. Carter, X. Han, A. M. Sheveleva, F. Tuna, E. J. L. McInnes, C. C. Tang, M. Schröder, S. Yang, *Nat. Commun.* 2021, *12*, 1–10.
- [129] R. Naumann, M. Goez, Green Chem. 2019, 21, 4470–4474.
- [130] L. Ma, D. Zhao, L. Chen, X. Wang, Y. L. Chen, J. Shen, *Tetrahedron* **2012**, *68*, 8704–8711.
- [131] S. Shanmuganathan, D. Natalia, L. Greiner, P. Domínguez De María, *Green Chem.* 2012, 14, 94–97.
- [132] D. Ma, S. Zhai, Y. Wang, A. Liu, C. Chen, *Molecules* **2019**, *24*, 330.
- [133] A. H. Aboo, E. L. Bennett, M. Deeprose, C. M. Robertson, J. A. Iggo, J. Xiao, *Chem. Commun.* 2018, 54, 11805–11808.
- [134] M. J. Climent, A. Corma, S. Iborra, *Green Chem.* **2014**, *16*, 516–547.
- [135] Y. Liu, Xuechen, Zhou, D. Zeng, H. Wang, S. Qiao, L. Zhang, W. Wang, *ChemistrySelect* 2021, 6, 8074–8079.
- [136] S. Kohtani, E. Yoshioka, K. Saito, A. Kudo, H. Miyabe, J. Phys. Chem. C 2012, 116, 17705–17713.
- [137] M. J. Taylor, L. J. Durndell, M. A. Isaacs, C. M. A. Parlett, K. Wilson, A. F. Lee, G. Kyriakou, Appl. Catal. B Environ. 2016, 180, 580–585.

- [138] M. J. da Silva, M. G. Teixeira, Mol. Catal. 2018, 461, 40–47.
- [139] H. Luo, L. Wang, S. Shang, J. Niu, S. Gao, Commun. Chem. 2019, 2, DOI 10.1038/s42004-019-0116-5.
- [140] F. Zhang, J. Zhang, S. Guo, *ChemistrySelect* **2018**, *3*, 13638–13640.
- [141] M. Nakajima, E. Fava, S. Loescher, Z. Jiang, M. Rueping, Angew. Chemie Int. Ed. 2015, 54, 8828–8832.
- [142] M. Y. Chernyak, V. E. Tarabanko, A. A. Morosov, A. A. Kondrasenko, J. Sib. Fed. Univ. Chem. 2016, 9, 146–151.
- [143] A. Caron, É. Morin, S. K. Collins, ACS Catal. 2019, 9, 9458–9464.
- [144] F. R. Petronijević, M. Nappi, D. W. C. MacMillan, J. Am. Chem. Soc. 2013, 135, 18323– 18326.
- [145] L. J. Rono, H. G. Yayla, D. Y. Wang, M. F. Armstrong, R. R. Knowles, J. Am. Chem. Soc. 2013, 135, 17735–17738.
- [146] M. Zhang, W. D. Rouch, R. D. McCulla, European J. Org. Chem. 2012, 2012, 6187–6196.
- [147] K. Li, Q. Wan, C. Yang, X.-Y. Chang, K.-H. Low, C.-M. Che, Angew. Chemie 2018, 130, 14325–14329.
- [148] S. J. Ji, M. Matsushita, T. T. Takahashi, C. A. Horiuchi, *Tetrahedron Lett.* **1999**, *40*, 6791–6794.
- [149] E. M. Sharshira, T. Horaguchi, J. Heterocycl. Chem. 1997, 34, 1837–1849.
- [150] J. W. Park, E. K. Kim, K. K. Park, Bull. Korean Chem. Soc. 2002, 23, 1229–1234.

- [151] S. Kohtani, E. Yoshioka, K. Saito, A. Kudo, H. Miyabe, *Catal. Commun.* 2010, 11, 1049–1053.
- [152] J. Xie, R. Jin, A. Li, Y. Bi, Q. Ruan, Y. Deng, Y. Zhang, S. Yao, G. Sankar, D. Ma, J. Tang, Nat. Catal. 2018, 1, 889–896.
- [153] C.-J. Li, Chem. Rev. 2005, 105, 3095–3166.
- [154] J. Hassan, M. Sévignon, C. Gozzi, E. Schulz, M. Lemaire, Chem. Rev. 2002, 102, 1359– 1470.
- [155] H. Yi, G. Zhang, H. Wang, Z. Huang, J. Wang, A. K. Singh, A. Lei, *Chem. Rev.* 2017, 117, 9016–9085.
- [156] D. Ma, A. Liu, S. Li, C. Lu, C. Chen, Catal. Sci. Technol. 2018, 8, 2030–2045.
- [157] D. A. Horton, G. T. Bourne, M. L. Smythe, Chem. Rev. 2003, 103, 893–930.
- [158] A. Grirrane, A. Corma, H. García, *Science* (80-.). **2008**, 322, 1661–1664.
- [159] A. Cirla, J. Mann, Nat. Prod. Rep. 2003, 20, 558.
- [160] D. C. Harrowven, S. L. Kostiuk, Nat. Prod. Rep. 2012, 29, 223–242.
- [161] L. He, Q. Su, L. Bai, M. Li, J. Liu, X. Liu, C. Zhang, Z. Jiang, J. He, J. Shi, S. Huang, L. Guo, Eur. J. Med. Chem. 2020, 204, 112530.
- [162] T. Chen, L. Yang, L. Li, K.-W. Huang, *Tetrahedron* **2012**, *68*, 6152–6157.
- [163] M. Rovira, L. Jašíková, E. Andris, F. Acuña-Parés, M. Soler, I. Güell, M.-Z. Wang, L. Gómez, J. M. Luis, J. Roithová, X. Ribas, Chem. Commun. 2017, 53, 8786–8789.
- [164] T. Chen, B.-T. Chen, K. V. Bukhryakov, V. O. Rodionov, *Chem. Commun.* 2017, 53,

- 11638-11641.
- [165] G. Park, S. Y. Yi, J. Jung, E. J. Cho, Y. You, Chem. A Eur. J. 2016, 22, 17790–17799.
- [166] Y. Zhang, J. L. Petersen, C. Milsmann, J. Am. Chem. Soc. **2016**, 138, 13115–13118.
- [167] K. Sato, Y. Inoue, T. Mori, A. Sakaue, A. Tarui, M. Omote, I. Kumadaki, A. Ando, Org. Lett. 2014, 16, 3756–3759.
- [168] Y. Sun, Y. Li, Z. Li, D. Zhang, W. Qiao, Y. Li, H. Niemantsverdriet, W. Yin, R. Su, ACS Catal. 2021, 11, 15083–15088.
- [169] D. Zhang, P. Ren, W. Liu, Y. Li, S. Salli, F. Han, W. Qiao, Y. Liu, Y. Fan, Y. Cui, Y. Shen, E. Richards, X. Wen, M. H. Rummeli, Y. Li, F. Besenbacher, H. Niemantsverdriet, T. Lim, R. Su, Angew. Chemie Int. Ed. 2022, 61, DOI 10.1002/anie.202204256.
- [170] A. Rudolph, M. Lautens, Angew. Chemie Int. Ed. 2009, 48, 2656–2670.
- [171] D. Li, C.-M. Che, H.-L. Kwong, V. W.-W. Yam, *J. Chem. Soc., Dalt. Trans.* **1992**, 3325–3329.
- [172] Y. Absalan, M. R. Razavi, M. Gholizadeh, A. Ahmadpour, S. Poursabagh, O. Kovalchukova, *Nano-Structures & Nano-Objects* **2022**, *30*, 100858.
- [173] H. Yin, P. J. Carroll, J. M. Anna, E. J. Schelter, J. Am. Chem. Soc. 2015, 137, 9234–9237.
- [174] B. Dam, B. Das, B. K. Patel, Green Chem. 2023, 25, 3374–3397.
- [175] E. T. Martin, C. M. McGuire, M. S. Mubarak, D. G. Peters, *Chem. Rev.* 2016, 116, 15198–15234.
- [176] H. A. Sakai, W. Liu, C. C. Le, D. W. C. MacMillan, J. Am. Chem. Soc. 2020, 142, 11691–

#### 11697.

- [177] T. Yuan, M. Zheng, M. Antonietti, X. Wang, Chem. Sci. 2021, 12, 6323–6332.
- [178] X. Chen, Y. Li, X. Pan, D. Cortie, X. Huang, Z. Yi, Nat. Commun. 2016, 7, 12273.
- [179] G. Kresse, J. Furthmüller, *Comput. Mater. Sci.* **1996**, *6*, 15–50.
- [180] G. Kresse, J. Furthmüller, *Phys. Rev. B* **1996**, *54*, 11169–11186.
- [181] J. P. Perdew, K. Burke, M. Ernzerhof, *Phys. Rev. Lett.* **1996**, 77, 3865–3868.
- [182] G. Kresse, D. Joubert, *Phys. Rev. B* **1999**, *59*, 1758–1775.
- [183] P. E. Blöchl, *Phys. Rev. B* **1994**, *50*, 17953–17979.
- [184] S. L. Dudarev, G. A. Botton, S. Y. Savrasov, C. J. Humphreys, A. P. Sutton, *Phys. Rev. B* 1998, 57, 1505–1509.
- [185] S. Grimme, J. Antony, S. Ehrlich, H. Krieg, J. Chem. Phys. **2010**, 132, 154104.
- [186] M. J. Frisch, G. W. Trucks, H. B. Schlegel, G. E. Scuseria, M. a. Robb, J. R. Cheeseman, G. Scalmani, V. Barone, G. a. Petersson, H. Nakatsuji, X. Li, M. Caricato, a. V. Marenich, J. Bloino, B. G. Janesko, R. Gomperts, B. Mennucci, H. P. Hratchian, J. V. Ortiz, a. F. Izmaylov, J. L. Sonnenberg, Williams, F. Ding, F. Lipparini, F. Egidi, J. Goings, B. Peng, A. Petrone, T. Henderson, D. Ranasinghe, V. G. Zakrzewski, J. Gao, N. Rega, G. Zheng, W. Liang, M. Hada, M. Ehara, K. Toyota, R. Fukuda, J. Hasegawa, M. Ishida, T. Nakajima, Y. Honda, O. Kitao, H. Nakai, T. Vreven, K. Throssell, J. a. Montgomery Jr., J. E. Peralta, F. Ogliaro, M. J. Bearpark, J. J. Heyd, E. N. Brothers, K. N. Kudin, V. N. Staroverov, T. a. Keith, R. Kobayashi, J. Normand, K. Raghavachari, a. P. Rendell, J. C. Burant, S. S. Iyengar, J. Tomasi, M. Cossi, J. M. Millam, M. Klene, C. Adamo, R. Cammi, J. W.

- Ochterski, R. L. Martin, K. Morokuma, O. Farkas, J. B. Foresman, D. J. Fox, **2016**, Gaussian 16, Revision C.01, Gaussian, Inc., Wallin.
- [187] K. Burke, J. Chem. Phys. 2012, 136, 150901.
- [188] X. Li, Y. Pi, Q. Xia, Z. Li, J. Xiao, Appl. Catal. B Environ. 2016, 191, 192–201.
- [189] J. Greeley, T. F. Jaramillo, J. Bonde, I. Chorkendorff, J. K. Nørskov, *Nat. Mater.* **2006**, *5*, 909–913.
- [190] P. Quaino, F. Juarez, E. Santos, W. Schmickler, Beilstein J. Nanotechnol. 2014, 5, 846–854.
- [191] Y. Li, P. Ren, D. Zhang, W. Qiao, D. Wang, X. Yang, X. Wen, M. H. Rummeli, H. Niemantsverdriet, J. P. Lewis, F. Besenbacher, H. Xiang, Y. Li, R. Su, ACS Catal. 2021, 11, 4338–4348.
- [192] J. Ran, M. Jaroniec, S. Qiao, Adv. Mater. 2018, 30, 1704649.
- [193] O. R. Luca, J. L. Gustafson, S. M. Maddox, A. Q. Fenwick, D. C. Smith, *Org. Chem. Front.*2015, 2, 823–848.
- [194] K. Sathiyan, R. Bar-Ziv, V. Marks, D. Meyerstein, T. Zidki, Chem. A Eur. J. 2021, 27, 15936–15943.
- [195] Y. Tamaki, A. Furube, M. Murai, K. Hara, R. Katoh, M. Tachiya, J. Am. Chem. Soc. 2006, 128, 416–417.
- [196] Y. N. Wijaya, J. Kim, S. H. Hur, S. H. Park, M. H. Kim, Sensors Actuators B Chem. 2018, 263, 59–68.
- [197] S. Koshy, R. Anantaraman, J. Am. Chem. Soc. 1960, 82, 1574–1576.

- [198] J. Adisoejoso, T. Lin, X. S. Shang, K. J. Shi, A. Gupta, P. N. Liu, N. Lin, Chem. A Eur. J. 2014, 20, 4111–4116.
- [199] T. Zhang, W. Li, K. Huang, H. Guo, Z. Li, Y. Fang, R. M. Yadav, V. Shanov, P. M. Ajayan, L. Wang, C. Lian, J. Wu, Nat. Commun. 2021, 12, 5265.
- [200] N. Wang, Y. Pan, S. Wu, E. Zhang, W. Dai, RSC Adv. 2017, 7, 43255–43265.
- [201] G. Li, N. M. Dimitrijevic, L. Chen, T. Rajh, K. A. Gray, J. Phys. Chem. C 2008, 112, 19040– 19044.
- [202] X. Li, J. Xie, H. Rao, C. Wang, J. Tang, Angew. Chemie Int. Ed. 2020, 59, 19702–19707.
- [203] M. I. Houchati, N. Chniba-Boudjada, A. H. Hamzaoui, J. Coord. Chem. 2020, 73, 1881– 1894.
- [204] H. Li, Z. Su, S. Hu, Y. Yan, Appl. Catal. B Environ. 2017, 207, 134–142.
- [205] L. Xu, Y. Yang, Z.-W. Hu, S.-H. Yu, ACS Nano 2016, 10, 3823–3834.
- [206] G. Dzido, M. Drzazga, P. Markowski, A. Jarzębski, *Technologies* **2015**, *3*, 37–46.
- [207] S. Peiris, J. McMurtrie, H.-Y. Zhu, Catal. Sci. Technol. 2016, 6, 320–338.
- [208] J. Ramyadevi, K. Jeyasubramanian, A. Marikani, G. Rajakumar, A. A. Rahuman, T. Santhoshkumar, A. V. Kirthi, C. Jayaseelan, S. Marimuthu, *Parasitol. Res.* 2011, 109, 1403–1415.
- [209] M. Cybularczyk-Cecotka, J. Szczepanik, M. Giedyk, Nat. Catal. 2020, 3, 872–886.
- [210] O. R. Fonseca-Cervantes, A. Pérez-Larios, V. H. Romero Arellano, B. Sulbaran-Rangel, C.A. Guzmán González, *Processes* 2020, 8, 1032.

- [211] J. Matos, E. García-López, L. Palmisano, A. García, G. Marcì, *Appl. Catal. B Environ.* **2010**, 99, 170–180.
- [212] J. Cunningham, B. K. Hodnett, A. Walker, Selective Oxidations of Alcohols on UV-Illuminated Metal Oxides, 1977.
- [213] W. Li, G. Wang, C. Chen, J. Liao, Z. Li, Nanomaterials 2017, 7, 20.
- [214] R. Sun, B. Tan, Chem. Res. Chinese Univ. 2022, 38, 310–324.
- [215] J. Bi, W. Fang, L. Li, J. Wang, S. Liang, Y. He, M. Liu, L. Wu, *Macromol. Rapid Commun.*2015, 36, 1799–1805.
- [216] X. Jiang, P. Wang, J. Zhao, J. Mater. Chem. A 2015, 3, 7750–7758.
- [217] R. Xu, X.-S. Wang, H. Zhao, H. Lin, Y.-B. Huang, R. Cao, *Catal. Sci. Technol.* **2018**, 8, 2224–2230.
- [218] S. Zhang, S. Wang, L. Guo, H. Chen, B. Tan, S. Jin, J. Mater. Chem. C 2020, 8, 192–200.
- [219] C. Ayed, W. Huang, K. A. I. Zhang, Front. Chem. Sci. Eng. 2020, 14, 397–404.
- [220] Y. Zhuang, Q. Zhu, G. Li, Z. Wang, P. Zhan, C. Ren, Z. Si, S. Li, D. Cai, P. Qin, Mater. Res. Bull. 2022, 146, 111619.
- [221] W. Huang, B. C. Ma, H. Lu, R. Li, L. Wang, K. Landfester, K. A. I. Zhang, ACS Catal.
  2017, 7, 5438–5442.
- [222] W. Huang, N. Huber, S. Jiang, K. Landfester, K. A. I. Zhang, Angew. Chemie Int. Ed. 2020, 59, 18368–18373.
- [223] W. Zhang, Z. Deng, J. Deng, C.-T. Au, Y. Liao, H. Yang, Q. Liu, J. Mater. Chem. A 2022,

- 10, 22419-22427.
- [224] S. Ren, M. J. Bojdys, R. Dawson, A. Laybourn, Y. Z. Khimyak, D. J. Adams, A. I. Cooper, Adv. Mater. 2012, 24, 2357–2361.
- [225] Z. Yang, H. Chen, S. Wang, W. Guo, T. Wang, X. Suo, D. Jiang, X. Zhu, I. Popovs, S. Dai, J. Am. Chem. Soc. 2020, 142, 6856–6860.
- [226] K. Schwinghammer, S. Hug, M. B. Mesch, J. Senker, B. V. Lotsch, *Energy Environ. Sci.* 2015, 8, 3345–3353.
- [227] P. Kuhn, M. Antonietti, A. Thomas, *Angew. Chemie Int. Ed.* **2008**, 47, 3450–3453.
- [228] J. Xie, S. A. Shevlin, Q. Ruan, S. J. A. Moniz, Y. Liu, X. Liu, Y. Li, C. C. Lau, Z. X. Guo, J. Tang, Energy Environ. Sci. 2018, 11, 1617–1624.
- [229] G. Li, J. Ye, Y. Shen, Q. Fang, F. Liu, Chem. Eng. J. 2021, 421, 127784.
- [230] T. Chen, W.-Q. Li, W.-B. Hu, W.-J. Hu, Y. A. Liu, H. Yang, K. Wen, RSC Adv. 2019, 9, 18008–18012.
- [231] C. F. R. A. C. Lima, A. S. M. C. Rodrigues, V. L. M. Silva, A. M. S. Silva, L. M. N. B. F. Santos, *ChemCatChem* **2014**, *6*, n/a-n/a.
- [232] H. Ou, L. Lin, Y. Zheng, P. Yang, Y. Fang, X. Wang, Adv. Mater. 2017, 29, 1700008.
- [233] X. Wang, J. Chen, J. Zeng, Q. Wang, Z. Li, R. Qin, C. Wu, Z. Xie, L. Zheng, *Nanoscale* 2017, 9, 6643–6648.
- [234] J. Xie, R. Jin, A. Li, Y. Bi, Q. Ruan, Y. Deng, Y. Zhang, S. Yao, G. Sankar, D. Ma, J. Tang, Nat. Catal. 2018, 1, 889–896.